

ERCOFTAC

*Bulletin*

September 2019

120

---

## *European Research Community on Flow, Turbulence and Combustion*

---

ERCOFTAC is a leading European association of research, education and industry groups in the technology of flow, turbulence and combustion. The main objectives of ERCOFTAC are: To promote joint efforts of European research institutes and industries with the aim of **exchanging technical and scientific information**; to promote **Pilot Centres** for collaboration, stimulation and application of

research across Europe; to stimulate, through the creation of **Special Interest Groups**, wellcoordinated European-wide research efforts on specific topics; to stimulate the creation of advanced training activities; and to be influential on funding agencies, governments, the European Commission and the European Parliament.

[www.ercoftac.org](http://www.ercoftac.org)

### **Executive Committee**

<i>Chairman</i>	Von Terzi, D. Delft University of Technology, Netherlands Tel: +31 15 27 83379 D.A.vonTerzi@tudelft.nl
<i>First Deputy Chairman</i>	Tomboulides, A.
<i>Second Deputy Chairman</i>	Hirsch, C.
<i>Treasurer</i>	Geurts, B.
<i>SPC Chairman</i>	Hickel, S.
<i>SPC Deputy Chairman</i>	Salvetti, M. V.
<i>KNC Chairman</i>	Standingford, D.
<i>KNC Deputy Chairman</i>	Hillewaert, K.
<i>Knowledge Base Editor</i>	Rodi, W.
<i>Bulletin Editor</i>	Elsner, W.

### **ERCOFTAC Seat of the Organisation**

<i>Director</i>	Hirsch, C. Chaussée de la Hulpe 189 Terhulpesteenweg B-1170 Brussels, Belgium Tel: +32 2 643 3572 Fax: +32 2 647 9398 ado@ercoftac.be
-----------------	---

### **Scientific Programme Committee**

<i>Chairman</i>	Hickel, S. Delft University of Technology Faculty of Aerospace Engineering Kluyverweg 1 2629 HS Delft The Netherlands Tel: +31 152 789 570 S.Hickel@tudelft.nl
<i>Deputy Chairman</i>	Salvetti, M. V.

### **Knowledge Network Committee**

<i>Chairman</i>	Standingford, D. Zenotech Ltd. 1 Laarkfield Grove Chepstow, NP16 5UF United Kingdom Tel: +44 7870 628 916 david.standingford@zenotech.com
<i>Deputy Chairman</i>	Hillewaert, K.

### **ERCOFTAC Central Administration and Development Office (CADO)**

<i>Admin. Manager</i>	Jakubczak, M. PO Box 53877 London, SE27 7BR United Kingdom Tel: +44 208 117 6170 admin@cado-ercoftac.org Skype: ERCOFTAC-CADO
-----------------------	---

**TABLE OF CONTENTS**

<b>Progress in RANS-based Scale-Resolving Flow Simulation Methods</b> <i>S. Jakirlić</i>	4
<b>Detached-Eddy Simulation: Steps Towards Maturity and Industrial Value EDRFCM-2019</b> <i>P. Spalart and M. Strelets</i>	5
<b>Hierarchical Turbulence and Geometry Modelling of Aeroengine Flows</b> <i>Z-N. Wang, J. Tyacke, Y. Ma and P. Tucker</i>	14
<b>Hybrid RANS/LES Methodologies for External Aircraft Aerodynamics</b> <i>A. Probst, S. Probst and D. G. François</i>	20
<b>A Quick Overview of the Capabilities of ZDES</b> <i>S. Deck and N. Renard</i>	26
<b>Mathematical Framework of the PITM Method for the Simulation of Turbulent Flows</b> <i>B. Chaouat and R. Schiestel</i>	32
<b>Hybrid Temporal LES: Development and Applications</b> <i>R. Manceau</i>	38
<b>Non-Zonal Detached Eddy Simulation Coupled with a Steady RANS Solver in the Wall Region</b> <i>L. Davidson</i>	43
<b>Hybrid RANS/LES Applications at Dassault Aviation</b> <i>F. Billard, F. Chalot, F. Dagrau, L. Daumas M. Mallet, P.E. Normand and P. Yser</i>	49
<b>Use of Anisotropic Linear Forcing for Complex Scale-resolving Simulation</b> <i>S. Lardeau and L. Erbig</i>	55
<b>A Finite-element Viscosity Based Non-slip Wall Modelling Strategy for the Simulation of Industrial Turbulent Flows</b> <i>H. Owen, S. Radhakrishnan, S. Gomez and O. Lehmkuhl</i>	61
<b>Coupled Hybrid RANS-LES Research at The University of Manchester</b> <i>A. Revell, I. Afgan, A. E. A. Ali, M. C. Santasmasas, T. Craft, A. De Rosis, J. Holgate, D. Laurence, B. E. O. Iyamabo, A. Mole, B. Owen, M. Savoie, A. Skillen, J. Wang and X. Zhang</i>	67
<b>Grey-Area Mitigation in Scale-Resolving Simulations with Hybrid RANS-LES Methods</b> <i>S-H. Peng</i>	73

<b>EDITOR</b>	Marek, M.
<b>TECHNICAL EDITOR</b>	Kuban, Ł.
<b>CHAIRMAN</b>	Elsner, W.
<b>EDITORIAL BOARD</b>	Armenio, V. Dick, E. Geurts, B.J.
<b>DESIGN &amp; LAYOUT</b>	Borhani, N. Nichita, B.A.
<b>COVER DESIGN</b>	Aniszewski, W.

**SUBMISSIONS**

ERCOFTAC Bulletin  
Institute of Thermal Machinery  
Częstochowa University of Technology  
Al. Armii Krajowej 21  
42-201 Częstochowa  
Poland  
Tel: +48 343 250 507  
Fax: +48 343 250 507  
Email: [ercoftac@imc.pcz.czest.pl](mailto:ercoftac@imc.pcz.czest.pl)

**HOSTED, PRINTED & DISTRIBUTED BY**



CZĘSTOCHOWA UNIVERSITY OF TECHNOLOGY

ISSN: 2518-0991

The reader should note that the Editorial Board cannot accept responsibility for the accuracy of statements made by any contributing authors

**NEXT ERCOFTAC EVENTS**

*ERCOFTAC Spring Festival*  
16<sup>th</sup> of April, 2020  
Cambridge, UK

*ERCOFTAC Committee Meetings*  
17<sup>th</sup> of April, 2020  
Cambridge, UK



# The ERCOFTAC Best Practice Guidelines for Industrial Computational Fluid Dynamics

The Best Practice Guidelines (BPG) were commissioned by ERCOFTAC following an extensive consultation with European industry which revealed an urgent demand for such a document. The first edition was completed in January 2000 and constitutes generic advice on how to carry out quality CFD calculations. The BPG therefore address mesh design; construction of numerical boundary conditions where problem data is uncertain; mesh and model sensitivity checks; distinction between numerical and turbulence model inadequacy; preliminary information regarding the limitations of turbulence models etc. The aim is to encourage a common best practice by virtue of which separate analyses of the same problem, using the same model physics, should produce consistent results. Input and advice was sought from a wide cross-section of CFD specialists, eminent academics, end-users and, (particularly important) the leading commercial code vendors established in Europe. Thus, the final document can be considered to represent the consensus view of the European CFD community.

Inevitably, the Guidelines cannot cover every aspect of CFD in detail. They are intended to offer roughly those 20% of the most important general rules of advice that cover roughly 80% of the problems likely to be encountered. As such, they constitute essential information for the novice user and provide a basis for quality management and regulation of safety submissions which rely on CFD. Experience has also shown that they can often provide useful advice for the more experienced user. The technical content is limited to single-phase, compressible and incompressible, steady and unsteady, turbulent and laminar flow with and without heat transfer. Versions which are customised to other aspects of CFD (the remaining 20% of problems) are planned for the future.

The seven principle chapters of the document address numerical, convergence and round-off errors; turbulence modelling; application uncertainties; user errors; code errors; validation and sensitivity tests for CFD models and finally examples of the BPG applied in practice. In the first six of these, each of the different sources of error and uncertainty are examined and discussed, including references to important books, articles and reviews. Following the discussion sections, short simple bullet-point statements of advice are listed which provide clear guidance and are easily understandable without elaborate mathematics. As an illustrative example, an extract dealing with the use of turbulent wall functions is given below:

- Check that the correct form of the wall function is being used to take into account the wall roughness. An equivalent roughness height and a modified multiplier in the law of the wall must be used.
- Check the upper limit on  $y^+$ . In the case of moderate Reynolds number, where the boundary layer only extends to  $y^+$  of 300 to 500, there is no chance of accurately resolving the boundary layer if the first integration point is placed at a location with the value of  $y^+$  of 100.
- Check the lower limit of  $y^+$ . In the commonly used applications of wall functions, the meshing should be arranged so that the values of  $y^+$  at all the wall-adjacent integration points is only slightly above the recommended lower limit given by the code developers, typically between 20 and 30 (the form usually assumed for the wall functions is not valid much below these values). This procedure offers the best chances to resolve the turbulent portion of the boundary layer. It should be noted that this criterion is impossible to satisfy close to separation or reattachment zones unless  $y^+$  is based upon  $y^*$ .
- Exercise care when calculating the flow using different schemes or different codes with wall functions on the same mesh. Cell centred schemes have their integration points at different locations in a mesh cell than cell vertex schemes. Thus the  $y^+$  value associated with a wall-adjacent cell differs according to which scheme is being used on the mesh.
- Check the resolution of the boundary layer. If boundary layer effects are important, it is recommended that the resolution of the boundary layer is checked after the computation. This can be achieved by a plot of the ratio between the turbulent to the molecular viscosity, which is high inside the boundary layer. Adequate boundary layer resolution requires at least 8-10 points in the layer.

All such statements of advice are gathered together at the end of the document to provide a 'Best Practice Checklist'. The examples chapter provides detailed expositions of eight test cases each one calculated by a code vendor (viz FLUENT, AEA Technology, Computational Dynamics, NUMECA) or code developer (viz Electricité de France, CEA, British Energy) and each of which highlights one or more specific points of advice arising in the BPG. These test cases range from natural convection in a cavity through to flow in a low speed centrifugal compressor and in an internal combustion engine valve.

Copies of the Best Practice Guidelines can be acquired from:

ERCOFTAC (CADO)  
PO Box 53877  
London, SE27 7BR  
United Kingdom  
Tel: +44 208 117 6170  
Email: [admin@cado-ercoftac.org](mailto:admin@cado-ercoftac.org)

The price per copy (not including postage) is:

ERCOFTAC members		
First copy		<i>Free</i>
Subsequent copies		75 Euros
Students		75 Euros
Non-ERCOFTAC academics		
Non-ERCOFTAC industrial		140 Euros
EU/Non EU postage fee		230 Euros
		10/17 Euros

---

# *BPG for CFD in Turbulent Combustion*

---

## **ERCOFTAC**

*Best Practice Guidelines for CFD of Turbulent Combustion*

Editors: Profs. Luc Vervisch, & Dirk Roekaerts

Foreword: Dr. Richard E. Seoud

The aim of this Best Practice Guide (BPG) is to provide guidelines to CFD users in a wide range of application areas where combustion is an essential process. Its overall structure is as follows:

Chapters 1-3 summarize the key issues in model formulation, Chapter 4 is addressing the validation of modeling using available experimental databases. Then, two application areas are elaborated in separate chapters: Chapter 5 on Internal Combustion Engines, and Chapter 6 on Gas Turbines. Best practice guidelines by the nature of technology development are always temporary. New insights and approaches will take over after some time. Therefore this BPG ends with a Chapter 7 on Emerging Methods, providing a preview of approaches so far only useful for simulating canonical configurations or requiring further developments.

A comprehensive CFD approach to turbulent combustion modeling relies on appropriate submodels for flow turbulence, chemistry and radiation, and their interactions. In the framework of this BPG, knowledge of turbulent flow modeling is a pre-requisite and only briefly explained. Instead the discussion on models is divided in three parts: turbulence-chemistry interaction (Chapter 1), chemistry (Chapter 2) and radiative heat transfer (Chapter 3). Many of the models introduced in the first three chapters will reappear in the discussion in Chapters 4 to 6 and comments on challenges, advantages and disadvantages are formulated in all chapters. Those looking for immediate advices to tackle a specific application may want to proceed immediately to the application chapters (IC engines in Chapter 5 and Gas Turbines in Chapter 6) and return to the basic chapters when necessary. But everyone not finding in these chapters an immediate answer to the basic question: What is the best model for my specific application? should certainly spend some time on Chapter 4, because it addresses the mandatory preliminary steps that have to be considered to validate a simulation involving any sort of turbulent flames.

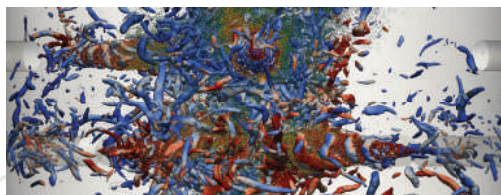
We hope that many readers will find this BPG useful. Feedback on possible improvements is welcome. Instructions on how to provide such feedback is available on the ERCOFTAC webpages ([www.ercoftac.org](http://www.ercoftac.org)). When appropriate, the information received will be included in the courses promoting the use of this BPG and in future additions or updates.



**ERCOFTAC**  
*Best Practice Guidelines*



*Computational Fluid Dynamics of  
Turbulent Combustion*



**Luc Vervisch & Dirk Roekaerts**

**Editors**

**Richard E. Seoud**

**Foreword**

### **Table of Content**

- 1-Introduction to Turbulent Combustion Modelling
- 2-Combustion Chemistry
- 3-Thermal Radiation
- 4-RANS and LES validation
- 5-Internal Combustion Engines
- 6-Gas Turbine
- 7-Emerging Methods

To order please visit

[www.ercoftac.org/publications/ercoftac\\_best\\_practice\\_guidelines/](http://www.ercoftac.org/publications/ercoftac_best_practice_guidelines/)

Or from:

ERCOFTAC (CADO)

PO Box 53877

London, SE27 7BR

United Kingdom

Tel: +44 208 117 6170

Email: [admin@cado-ercoftac.org](mailto:admin@cado-ercoftac.org)

The price per copy (not including postage) is:

ERCOFTAC members

First copy Free

Subsequent copies 75 Euros

Students 75 Euros

Non-ERCOFTAC academics, 140 Euros

Non-ERCOFTAC industrial, 230 Euros

EU / Non EU postage fee 10/ 17 Euros

# Progress in RANS-based Scale-Resolving Flow Simulation Methods

S. Jakirlić

*Institute of Fluid Mechanics and Aerodynamics*

*Technische Universität Darmstadt, Alarich-Weiss-Straße. 10, 64287 Darmstadt, Germany*

s.jakirlic@sla.tu-darmstadt.de

The procedure of hybridizing the RANS (Reynolds-Averaged Navier-Stokes) and LES (Large-Eddy Simulation) computational frameworks aimed at combining their advantages - with RANS exhibiting weaker sensitivity against grid non-uniformities being especially affordable in the attached near-wall regions and LES being capable of capturing the flows dominated by the organized large-scale coherent structures with a broader spectrum, as encountered for instance in the flows involving separation - has been experiencing intensified developments over the past two decades since the appearance of the DES (Detached-Eddy Simulation) methodology (Spalart et al., 1997, [1]) - finally numerous relevant sessions at major conferences, even the entire symposiums on Hybrid RANS-LES Methods (Hoarau et al., 2020, [2]) have been organized. Analogously to the role of the Smagorinsky-related subgrid-scale (SGS) models in LES, the dynamics of the residual turbulence in Hybrid LES/RANS computational schemes is described by an appropriately sensitized RANS-based model.

Contrary to the LES framework utilizing mostly the SGS models of the Smagorinsky type (0-equation models), where the grid spacing  $\Delta$  represents the characteristic size of the largest unresolved scales (Sub-Grid-Scales), the representative length (and time) scales of the residual turbulence entering the relevant equations of motion in the hybrid LES/RANS methodologies are determined by solving respective equations describing the dynamics of corresponding turbulence quantities. In these introductory remarks just a few popular hybrid schemes will be briefly mentioned (the nominally grid-spacing-free SAS formulation, representing actually an eddy-resolving Unsteady RANS model, are purposefully introduced here within the same methodological concept): whereas the unresolved turbulence in the DES (Spalart et al., 1997, Spalart, 2009; Annu. Rev. Fluid Mech. 41: 181-202), PANS (Partially-Averaged Navier-Stokes; Girimaji, 2006; ASME J. Appl. Mech. 73: 413-421, Basara et al., 2011; AIAA J. 49(12): 2627-2636), PITM- $k - \epsilon$  (Partially Integrated Transport Model; Schiestel and Dejoan, 2005; Theoret. Comput. Fluid Dynamics 18: 443-468) and SAS- $k - \omega$  (Scale-Adaptive Simulations; Menter and Egorov, 2010; Flow Turbulence Combust. 85:113-138) methods is represented by an appropriately

modelled turbulent viscosity, the PITM- $\overline{u_i u_j} - \epsilon$  (Chaouat and Schiestel, 2005; Phys. Fluids 17(065106): 1-19) and SAS- $\overline{u_i u_j} - \omega$  (Jakirlic and Maduta, 2015; Int. J. Heat Fluid Flow 51: 175-194) methods utilize the solutions of model equations governing the entire turbulent stress tensor. Accordingly, the RANS-based sub-scale models of different complexity have been employed. Correspondingly, the grid spacing incorporated into the hybrid LES/RANS models represents just one of several model parameters serving for the determination of the unresolved turbulent scales. The relevant model formulations point to complex relationships involving different turbulent quantities exhibiting high level of coherence. Consequently, unlike in the LES method, where the grid size  $\Delta$  influences very directly the final outcome, the grid spacing  $\Delta$  is a less influential factor in Hybrid LES/RANS models - such a model rationale has inherently much more physics, allowing the use of coarser spatial and temporal resolutions.

The present thematic issue of the ERCOFTAC Bulletin (with the second part which will be published in the December 2019 Volume) attempts to give an overview of relevant activities in this very active field of research. We recall the relevant thematic issue on “Wall modelling in LES: method development and application“ published in ERCOFTAC Bulletin No. 72 (March, 2007).

## References

- [1] Spalart, P.R., Jou, W.-H., Strelets, M., Allmaras, S. (1997): Comments on the feasibility of LES for wings and on a hybrid RANS/LES approach, 1st AFOSR Int. Conf. on DNS and LES. In: Liu, C., Liu, Z. (Eds.), Advances in DNS/LES. Columbus, OH, Greyden Press, pp. 137-147
- [2] Hoarau, Y., Peng, S.-H., Schwamborn, D. and Revell, A. (Eds.) (2020): Progress in Hybrid RANS-LES Modelling 7. Notes on Numerical Fluid Mechanics and Multidisciplinary Design, Vol. 143, Springer Verlag (ISBN 978-3-030-27606-5), Contributions to the 7th Symposium on Hybrid RANS/LES Methods, Berlin, Germany, 2018; DOI: <https://doi.org/10.1007/978-3-030-27607-2>

# DETACHED-EDDY SIMULATION: STEPS TOWARDS MATURITY AND INDUSTRIAL VALUE

P. Spalart<sup>1</sup> and M. Strelets<sup>2</sup>

<sup>1</sup>Boeing Commercial Airplanes, P.O. Box 3707, Seattle, WA 98124, USA

<sup>2</sup>Peter the Great St. Petersburg Polytechnic University (SPbPU), Polytechnicheskaya Str. 29, 195251 St. Petersburg, Russia

## Abstract

The paper outlines the status of Detached-Eddy Simulations (DES) [1], which the authors and their co-workers have been working on for over twenty years, and which has a substantial user community. After a discussion of history and versions, recent upgrades of DES are presented with examples illustrating the new possibilities they provide. Along with this, some unresolved problems and directions for further work are discussed.

## 1 Brief historical overview

Twenty years after the first three-dimensional results were published [2] DES enjoys stability, a clear mission, good version control, and a rather wide user community. The original version of DES was motivated by the belief that pure RANS was not accurate enough for massively separated flows (later on, it became clear that this is true even in "challenging" parts of the boundary layer). The further belief that decisive accuracy improvements in RANS would not take place has unfortunately been supported by facts, even now that Reynolds-Stress models are available. Progress has been made in treating curvature, vortices, and corner flows among other areas, but a "universal" RANS model is simply not expected by anyone.

Figure 1 illustrates the power of DES for massively-separated flows (at least, those with relatively easy prediction of separation), including its success in a number of different codes and with different background RANS models.

The initial version, called DES97 and sometimes Natural DES (NDES), is very simple but can be misled by "ambiguous" grids in the boundary layer, leading to Modeled-Stress Depletion (MSD) and premature ("grid-induced") separation. This is prevented to a large extent by Delayed Detached-Eddy Simulation (DDES), which was introduced in 2006 [5]. Minor improvements to DDES are ongoing, to refine the "protection" of the model; this goes in the direction of favoring the RANS mode over the LES mode. Ideally, DDES lessens the need for user-driven zonal decisions, as in the ZDES concepts of Deck [6]. Increasingly, users are applying zonal versions, whether one of Deck's modes, or of their own design. Unfortunately, this inflates the user's burden since the different regions are defined manually.

At the other end of the spectrum, DES is used as a wall model under an LES and, like other wall models, generates two log layers which suffer from some measure of Log-Layer Mismatch (LLM) [7]. This is corrected by Improved DDES (IDDES) [8], which adds complexity but, like other versions, has been successfully applied by many groups outside the core team starting from papers, without any direct help.

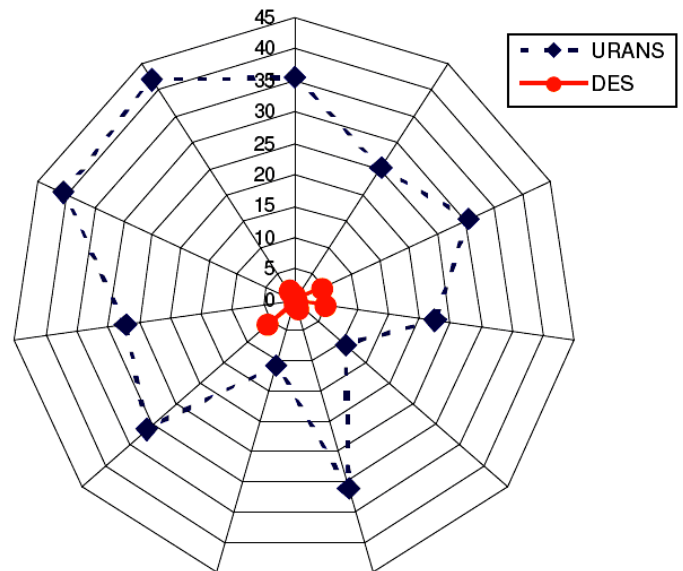


Figure 1: Comparison of two-dimensional URANS and DES (% deviation w.r.t. experiment [3]) for the prediction of mean drag coefficient for the NACA0012 airfoil at  $\alpha = 60^\circ$ . Results of 11 simulations conducted by different partners with different codes and turbulence models within the EU FLOMANIA project [4]

A detailed outline of the DES evolution up to 2008 is available in the review of Spalart [9]. So below we dwell upon only two recent developments.

## 2 Two major upgrades of DES during the last five years

A significant delay of the RANS-to-LES transition (the so called "grey area" issue), which was pointed to in the first DES publication [1], for many years has remained a serious unsolved issue not only in DES and in other non-zonal (DES-like) models but also in zonal Hybrid RANS-LES Methods (HRLM), which treat different areas of a flow by RANS and LES.

In natural applications of DES (massively separated flows, with the boundary layer in RANS mode up to separation or a nozzle lip) a severe delay is observed of the Kelvin-Helmholtz (KH) instability and transition from modelled to resolved turbulence in free and separated shear layers. This is explained by peculiarities of the grids typically used in simulations of such flows: in order to capture, e.g. jet shear-layers, these grids are fine across the shear layer and maybe in the streamwise direction, but coarse in the spanwise/azimuthal direction, which is very different from the nearly isotropic cells as-

sumed when the LES function within DES is applied with the cut-off in the inertial range [2]. The DES97 definition of the grid-cell dimension as the maximum in any direction becomes too conservative, and raises the eddy viscosity too much.

In contrast to pure DES-like approaches, zonal HRLM implying the presence of a user-specified interface between the flow regions treated by RANS and LES could do without the "new instability" mechanism to ensure RANS-to-LES transition in separated flows. Such methods are, in principle, more powerful and capable of predicting both attached and mildly separated flows well (see Section 3 below). However in these methods the issue of delayed RANS-to-LES transition also exists and one of the prerequisites of their success is the injection of artificial ("synthetic") turbulent content at the RANS-LES interface, as needed to trigger a rapid transition from fully modelled turbulence in the RANS region to mostly resolved turbulence in the LES region. Hence, the only possible way to shorten the length of the "adaptation area" required to establish mature 3D resolved turbulence downstream of the interface within the zonal methods is to make the artificial turbulent content as close to real turbulence as possible.

Below we briefly present two upgrades (one for DES-like methods and another for zonal HRLM) developed by our group for mitigation of the delay of RANS-to-LES transition.

## 2.1 Shear Layer Adapted (SLA) subgrid length-scale

The rationale of this length-scale and its detailed formulation are given in Shur et al. [10]. It includes two modifications of the original DES97 definition of the Subgrid Length Scale (SGLS) entering its LES branch, which was  $\Delta_{max} = \max\{\Delta x, \Delta y, \Delta z\}$ .

The first one has been inspired by an idea of Chauvet et al. [11] to sensitize the SGLS to the anisotropic cells in the quasi-2D regions of the separated shear layers by taking into account the direction of the vorticity vector. For a cell with the centre vector  $\mathbf{r}$  and vertices located at  $\mathbf{r}_n (n = 1\dots 8)$ , this modification reads:

$$\tilde{\Delta}_\omega = \frac{1}{\sqrt{3}} \max_{n,m=1,8} |(\mathbf{I}_n - \mathbf{I}_m)| \quad (1)$$

where  $\mathbf{I}_n = \mathbf{n}_\omega \times \mathbf{r}_n$  and  $\mathbf{n}_\omega$  is the unit vector aligned with the vorticity vector.

The quantity  $\tilde{\Delta}_\omega$  represents the diameter of the set of cross-product points,  $\mathbf{I}_n$ , divided by  $\sqrt{3}$  (the  $\sqrt{3}$  is aimed at recovering  $\Delta_{max}$  for 3D turbulence computed on cubic cells).

The advantage of  $\tilde{\Delta}_\omega$  over the standard DES length-scale  $\Delta_{max}$  and, also, over  $\Delta_\omega$  of [11] comes into focus for, e.g., a free shear layer flowing in the  $x - y$  plane, with much larger grid spacing in the  $z$ -direction than in the  $x$ - and  $y$ -directions. Considering that in the initial region of the shear layer the vorticity vector is nearly aligned with  $z$ ,  $\tilde{\Delta}_\omega$  reduces to  $\frac{1}{\sqrt{3}}(\Delta x^2 + \delta y^2)^{1/2}$ , i.e., it is of the order  $O(\max\{\Delta x, \Delta y\})$ , rather than to  $\Delta z$  (as  $\Delta_{max}$  would) or to  $\sqrt{\Delta x \Delta y}$  (as  $\Delta_\omega$  would). This is physically the most plausible behavior when the expected KH eddies have the same scale in the  $x$ - and  $y$ -directions. At the same time, in fully developed 3D turbulence,  $\tilde{\Delta}_\omega$  reduces to the standard DES definition, i.e., it is of the order of  $\max\{\Delta x, \Delta y, \Delta z\}$ , except for the situations when the vorticity vector is aligned with

one of the coordinate-directions, in which case it reduces to  $O(\max\{\Delta x_i, \Delta x_j\})$ . Thus,  $\tilde{\Delta}_\omega$  is always smaller than  $\Delta_{max}$ , which results in reducing the subgrid viscosity on anisotropic grids, but it never experiences a strong effect of the smallest grid-spacing on the SGLS.

On a nearly isotropic (cubic) grid the effect of replacing  $\Delta_{max}$  with  $\tilde{\Delta}_\omega$  is marginal. For this reason, provided that the isotropic grid is not sufficiently fine for a proper resolution of the initial region of a shear layer, which is the case in all practically meaningful simulations, an additional modification to the SGLS is made to ensure the desired decrease of the subgrid viscosity in this region. Unlike the first modification, this modification is based on a purely kinematic measure allowing the identification of quasi-2D flow areas in which nearly implicit LES (ILES) treatment is desirable for facilitating the KH instability, and, therefore, accelerating transition to resolved turbulence.

Such a measure, proposed in [10] and called the Vortex Tilting Measure (VTM), is a normalized cross product of the inviscid vorticity-evolution term  $\hat{\mathbf{S}} \cdot \boldsymbol{\omega}$  and the vorticity vector  $\boldsymbol{\omega}$  itself, and reads as

$$VTM \equiv \frac{\sqrt{6} |(\hat{\mathbf{S}} \cdot \boldsymbol{\omega}) \times \boldsymbol{\omega}|}{\omega^2 \sqrt{3 \text{tr}(\hat{\mathbf{S}}^2) - [\text{tr}(\hat{\mathbf{S}})]^2}} \quad (2)$$

where  $\hat{\mathbf{S}}$  is the strain tensor and  $\text{tr}(\cdot)$  means trace.

This measure is close to zero in the quasi-2D flow regions, where the vorticity vector is nearly an eigenvector of the strain tensor so that the cross product is very small, and close to 1.0 in developed 3D turbulence, where the orientation of the strain eigenvectors and that of the vorticity are not strongly correlated. A key point is that the VTM detects a favorable KH situation even if the shear layer is being stretched in the  $z$ -direction, which is common, e.g. for jets. This is what made us reject a vortex-stretching measure, which was tried first and simpler.

With the use of the VTM quantity, the length-scale  $\Delta = \tilde{\Delta}_\omega$  of equation (1) is further modified as follows:

$$\Delta = \tilde{\Delta}_\omega F_{KH}(< VTM >) \equiv \Delta_{SLA} \quad (3)$$

where the non-dimensional empirical function  $F_{KH}(< VTM >)$  ensures the unlocking the KH instability in the initial part of shear layers independently of the level of grid anisotropy (the angle brackets denote averaging of VTM over the current and closest neighboring cells, which is needed to eliminate possible steep downward excursions experienced by the local values of the VTM in developed turbulence).

Two examples from [10], [12] demonstrating a crucial acceleration of the RANS-to-LES transition in the Delayed DES ensured by the use of the definition of the SGLS in a jet and in a separated shear layer are presented in Figs. 2, 3 and 4, 5 respectively. Observe how for the jet, DDES combined with  $\Delta_{SLA}$  turns out to be far more successful than DES97 and quite competitive with zonal ILES, which was successfully used for jets previously [14] but is not applicable for complex wall-bounded flows. The results on the NASA hump in Figs. 4 and 5 are also very convincing, both in flow visualisations and in quantitative terms. One more example of the performance of DDES combined with  $\Delta = \Delta_{SLA}$  demonstrates its somewhat unexpected positive effect beyond the applications it was proposed for, namely, in Wall-Modelled LES (WMLES) of fully attached flow. Figure 6 shows results of DDES of developed channel



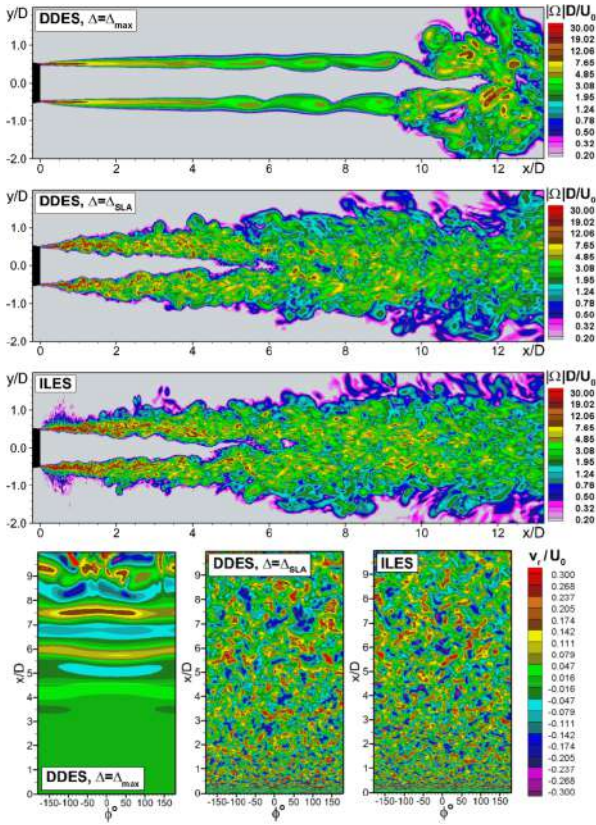


Figure 2: Snapshots of vorticity magnitude in a meridional plane (three upper frames) and of radial velocity on a grid surface inside the mixing layer (three lower frames) for round  $M=0.9$  jet from DDES with  $\Delta = \Delta_{max}$ , DDES with  $\Delta = \Delta_{SLA}$ , and from zonal Implicit LES [10]

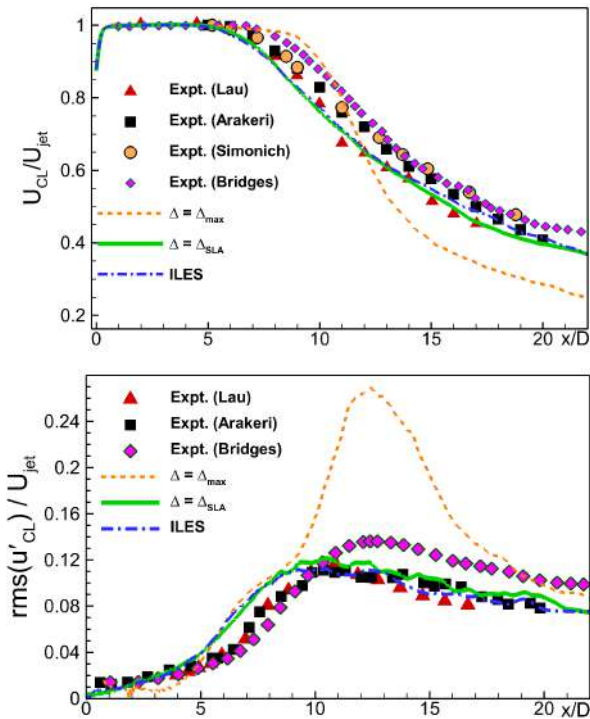


Figure 3: Comparison with experiments of centerline distributions of mean velocity and RMS of its fluctuations predicted by DDES with  $\Delta = \Delta_{max}$ , with  $\Delta = \Delta_{SLA}$ , and with zonal ILES [10]

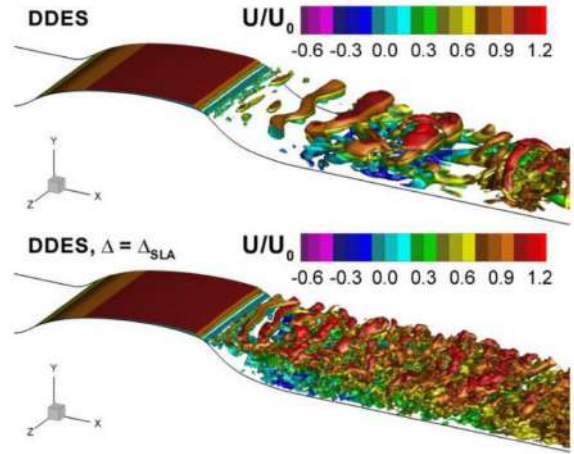


Figure 4: Snapshots of  $Q$ -criterion isosurface from DDES of NASA 2D hump [13] performed with  $\Delta = \Delta_{max}$  (upper frame) and  $\Delta = \Delta_{SLA}$  (lower frame) [12]

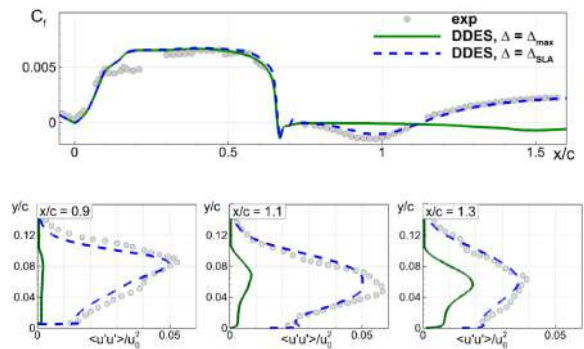


Figure 5: Comparison of skin friction distribution over the NASA hump (upper frame) and profiles of resolved normal stress at different hump-flow cross-sections computed with the use of DDES with  $\Delta = \Delta_{max}$  and  $\Delta = \Delta_{SLA}$  [12] with experiment [13]

flow at the Reynolds number  $Re_\tau = 18000$  carried out with the use of  $\Delta_{max}$  and  $\Delta_{SLA}$ . The simulations were performed on a typical WMLES grid with the step-sizes  $\Delta x/H = 0.05$ ,  $\Delta z/H = 0.025$ ,  $\Delta y_1/H = 10^{-3}$ , where  $H$  is the height of the channel. As seen in the figure, the use of  $\Delta_{SLA}$  results in a significant decrease of the eddy viscosity, caused by the grid anisotropy, especially in the near wall region. This in turn, leads to a much finer turbulence resolution and a mitigation of the LLM compared with the standard (with  $\Delta = \Delta_{max}$ ) DDES. As a result, the DDES with  $\Delta = \Delta_{SLA}$  performs almost as well as the version of DES specially designed for WMLES (namely IDDES [8], see Fig. 7).

## 2.2 Surface and volumetric synthetic turbulence generators for zonal RANS-WMLES methods

As already mentioned, the development of tools for creating turbulent content at the RANS-LES interface is one of the key issues for zonal HRLM. As also noted above, the artificial nature of the synthetic turbulence makes a complete elimination of the adaptation area hardly possible. The problem of suppression of spurious noise sources at the RANS-LES interface caused by the abrupt appearance of resolved unsteady vortical structures arising in aeroacoustic applications is even more challenging.

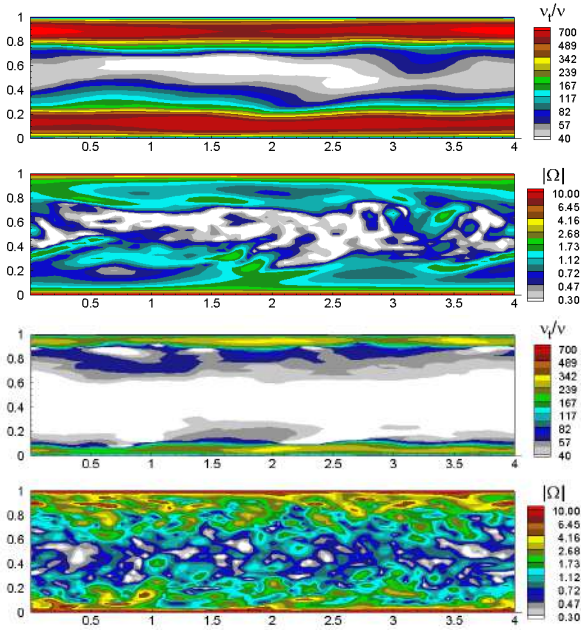


Figure 6: Snapshots of eddy viscosity and vorticity magnitude from DDES of the plane channel flow with the use of  $\Delta = \Delta_{max}$  (two upper frames) and  $\Delta = \Delta_{SLA}$  (two lower frames) [15]

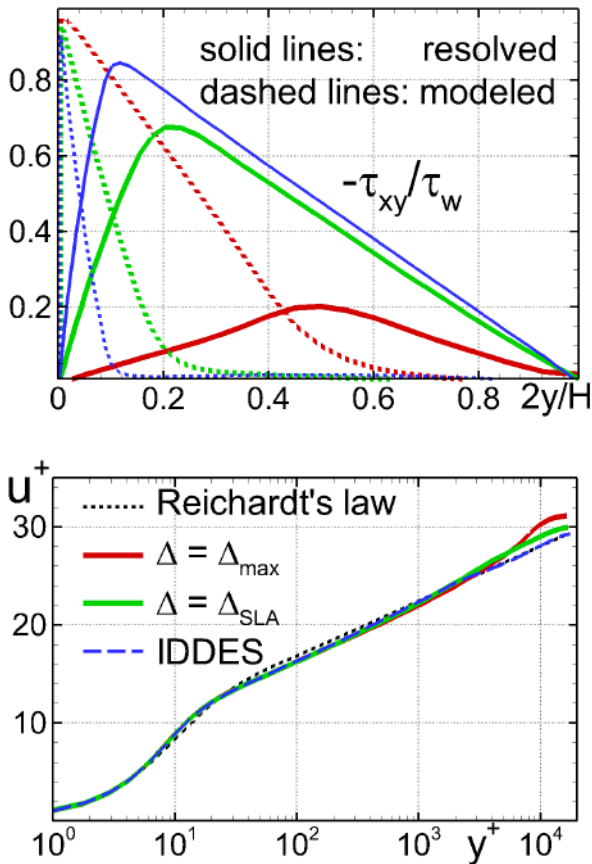


Figure 7: Profiles of resolved and modelled shear stress (upper frame) and of mean velocity (bottom frame) from DDES of the plane channel with the use of  $\Delta_{max}$  and  $\Delta_{SLA}$  and from IDDES [15]

So, the objective of the extensive research carried out in this area is to find ways to minimize the abovementioned negative effects. Below we briefly outline two such ways proposed by our group.

The first one is the "surface" (meaning it is applied directly at the RANS-LES interface) Synthetic Turbulence Generator (STG) developed by Shur et al. [16] and presenting a rather simple and robust but, nonetheless, fairly accurate tool for creating turbulent inflow content within a zonal HRLM. Considering that its detailed formulation is available in [16], we do not present it here, but only outline major features and peculiarities of this STG.

It employs ideas of Kraichnan [17] and has many features in common with other STGs in the literature (e.g. [18]). In particular, it creates velocity fluctuations as a superposition of weighted spatio-temporal Fourier modes satisfying a prescribed (von Karman) shape of the spatial spectrum. However, unlike the other methods, it is capable of a plausible representation of the anisotropy (in space) of the vortical structures, which is an essential feature of near-wall turbulence. This is achieved by a specific definition of the local turbulent length-scale (the size of the most energy containing turbulent structures created by the STG), and by using a global time-scale for setting the time-dependence of the synthetic velocity fluctuations. These features ensure the creation of energy-containing "synthetic eddies" which are small and elongated in the streamwise direction near solid walls, but relatively large and nearly isotropic away from them. Other than that, the method employs a set of wave numbers which is fixed in time and over the entire RANS-LES interface, and ranges from the value corresponding to the largest wavelength of the considered problem to the Nyquist limit. Finally, all the random quantities entering the STG (random phases, directions of the wave vectors, etc), similar to the wave numbers, are generated only once and are then fixed in time. In combination, all these make the method free of the decorrelation issue inherent to many other STGs, which rely on a local definition of turbulence length- and time-scales involved in the wavelength scaling, and suffer from the generation of high-frequency "noise" leading to a partial "re-laminarization" (damping of created turbulence) downstream of the RANS-LES interface.

The last but not least advantage of the STG [16] is that it is adapted to aeroacoustic problems. An inherent feature of virtually all the existing methods developed for creating turbulent content at the RANS-LES interface within zonal hybrid approaches is the sudden formation of energetic vortical structures right at the interface, which inevitably leads to generating strong spurious noise. Therefore, when applied to aeroacoustics, any basic "aerodynamic" algorithm for imposing unsteady turbulent content at the LES inflow should be supplemented by some means of suppressing this spurious noise. In the surface STG [16], the adaptation consists in inserting an Internal Damping Layer (IDL) in the LES sub-domain of the zonal RANS-LES, which effectively suppresses the spurious noise with no noticeable deterioration of the prediction of either mean or fluctuating flow characteristics (see an example in Figs. 8, 9). It should be noted however that the STG procedure assumes that the RANS-LES interface coincides with some grid surface, which makes it not forgiving of the grid structure. This makes difficult or even impossible its application to complex geometries computed on either multi-block structured or unstructured grids. This has motivated the development of a more technologically attractive, volumet-

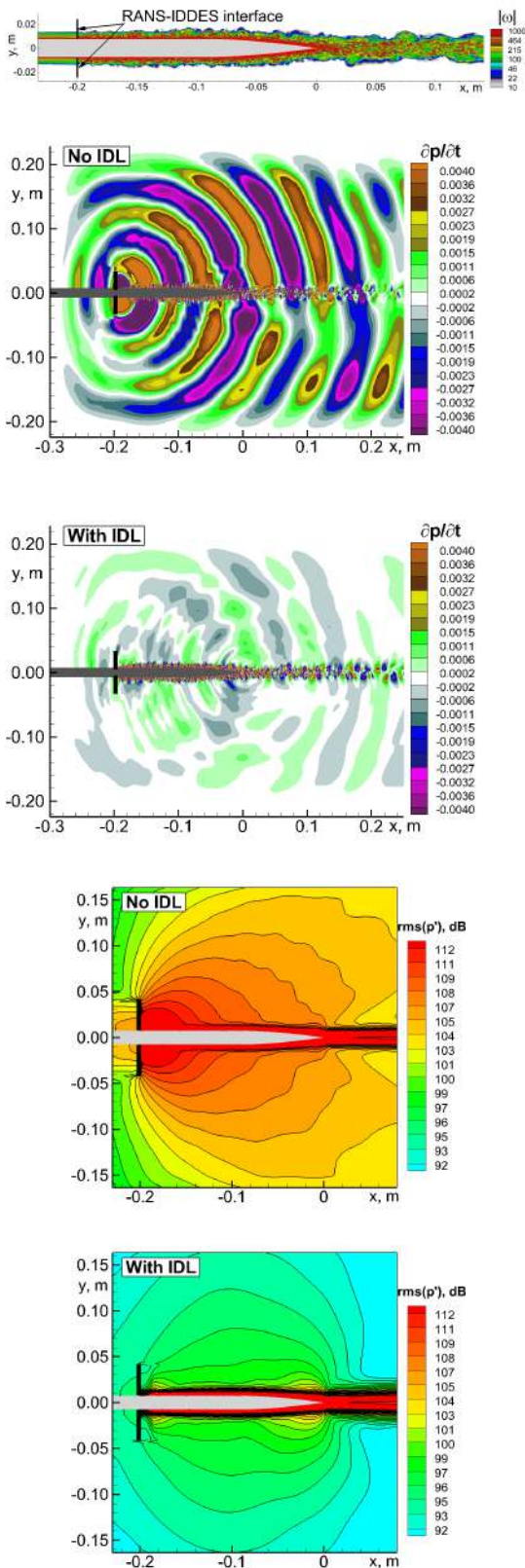


Figure 8: Snapshot of vorticity, instantaneous sound-wave patterns, and contours of RMS of pressure fluctuations from zonal RANS-IDDES of airfoil with the use of surface STG, without and with IDL

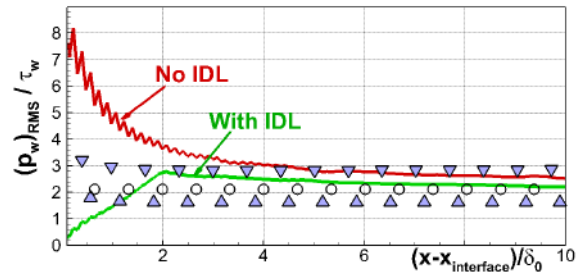


Figure 9: Effect of IDL on RMS of wall pressure fluctuations in the IDDES sub-domain of zonal RANS-IDDES of airfoil

ric, version of this STG (Volumetric STG or VSTG) [19]. This version was developed in the framework of the zonal RANS-IDDES approach with the  $k - \omega$  SST underlying RANS model [20] and is based on introducing specially designed volume source terms ("body forces") in the momentum and turbulent kinetic energy transport equations. The source terms are non-zero only in some (user-specified) region, of which the configuration relies only upon an a priori known "streamwise" flow direction and is not in any way "tied" to the used computational grid. Other than that, the VSTG approach has a high potential in terms of adaptation to aeroacoustic problems without using any supplementary tools (e.g. IDL used in the surface STG [16]). This is achieved thanks to the possibility to gradually increase and decrease the strength of the volume sources in the downstream direction, thus allowing a reduction of the spurious noise caused by the abrupt emergence of turbulence which is typical of the surface STGs.

After a set of numerical experiments with different body forces, a simple, purely empirical formulation was proposed, ensuring synthetic turbulence close to that produced by the original surface STG (see [19] for a detailed formulation and examples of application to generic flows). An example of the VSTG performance within the RANS-IDDES of a complex industrially relevant flow in a contemporary turbofan engine is presented in Figs. 10-12 [21], [22].

### 3 Attached- and Detached-Eddy Simulation (ADES) [24]

This is not a new concept (and the names zonal or embedded LES are just as descriptive), but it represents a significant evolution from the original NDES concept, which could become widespread and serve as a basis for turbulence treatment in high-Reynolds-number applications once the computing power is sufficient.

The idea is to initiate LES or WMLES in the boundary layer, rather than letting it develop only after separation, as in an NDES. It is illustrated by Fig. 13, which suggests that with either of two different locations of the interface (one in the zero pressure gradient boundary layer far upstream of the NASA hump, and another right before the separation) this approach performs equally well with DDES combined with  $\Delta_{SLA}$  (compare Fig. 13 with the upper frame of Fig. 5).

The motivation is pessimism regarding the ultimate accuracy of RANS not only in massively-separated flows (this consideration motivated NDES, and now appears to be a matter of consensus) but also in non-simple boundary layers and separation bubbles.

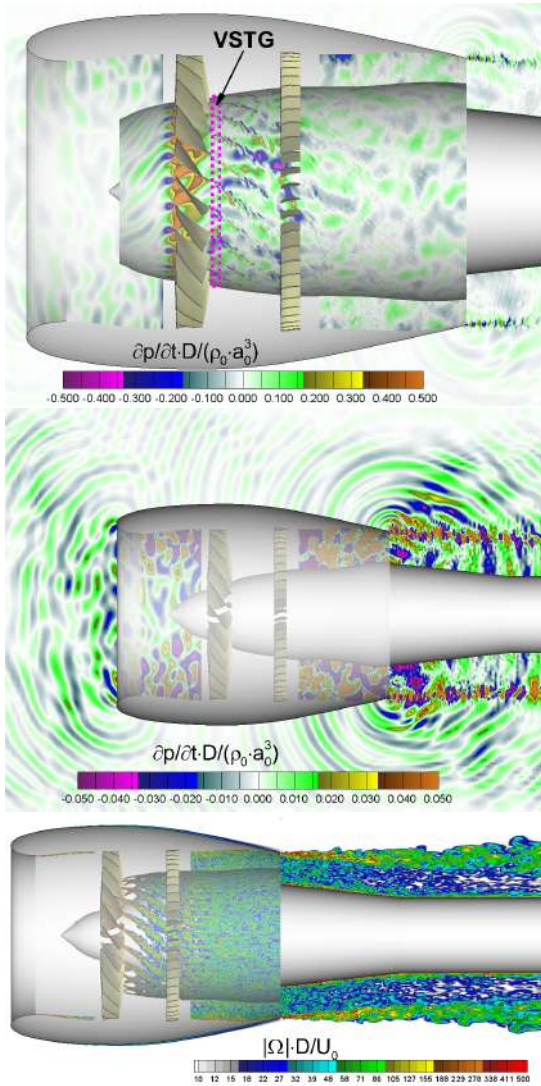


Figure 10: Snapshots of the pressure time-derivative (two upper frames) and vorticity magnitude (bottom frame) from zonal RANS-IDDES [21] of the NASA fan-noise source diagnostic test [23]

The position shift mooted here is that we would abandon RANS models not only for massively-separated regions, but also for any challenging region in a boundary layer. Shock-induced separation would be a prime example. We would admit the existence of a "glass ceiling" for accuracy in RANS, which is not high enough, now that we are well into the 21<sup>st</sup> century and the trend for progress in RANS models is almost imperceptible. In particular, Reynolds-Stress Models (RSM) are becoming more accessible, but arguably not more logical or well-understood, and they are not delivering higher accuracy than modern simpler models "automatically," as could have been expected. We also note that the basic components of the most-used blended RSM, namely the LRR and SSG models, are quite old.

It is essential to position ADES relative to pure LES, which undoubtedly is a conceptually simpler approach, and is considered by some groups as ready for application at flight Reynolds numbers. We are considering the large-airplane problem based on the well-known reasoning of [1]. Assuming WMLES is successful, each cube of the boundary layer with the side equal to the local boundary thickness  $\delta$  will demand a given number, say  $N_0$ , of grid points. The value of  $N_0$  will be debated, but

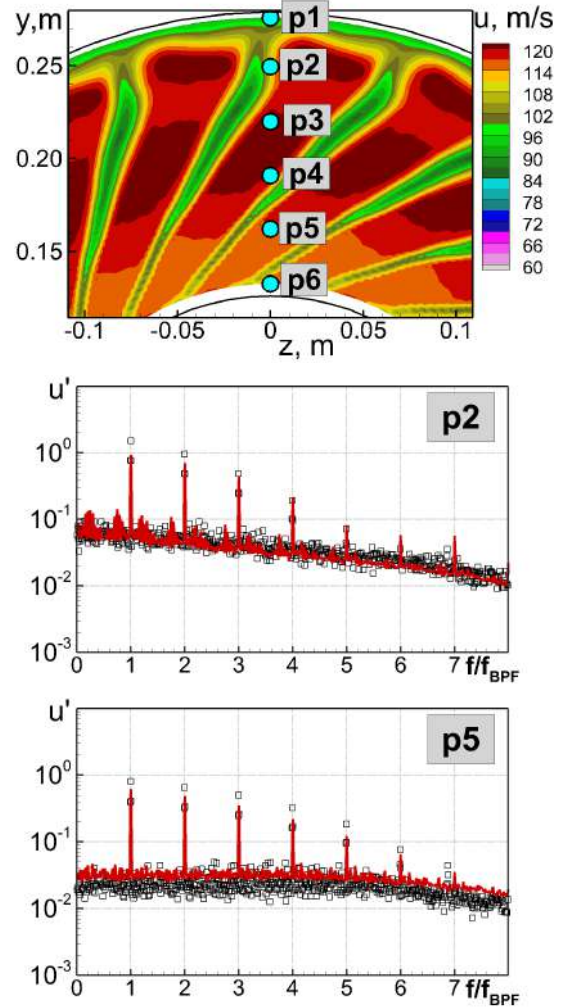


Figure 11: Predicted and measured velocity spectra at a station located in the rotor-stator interstage region [21]

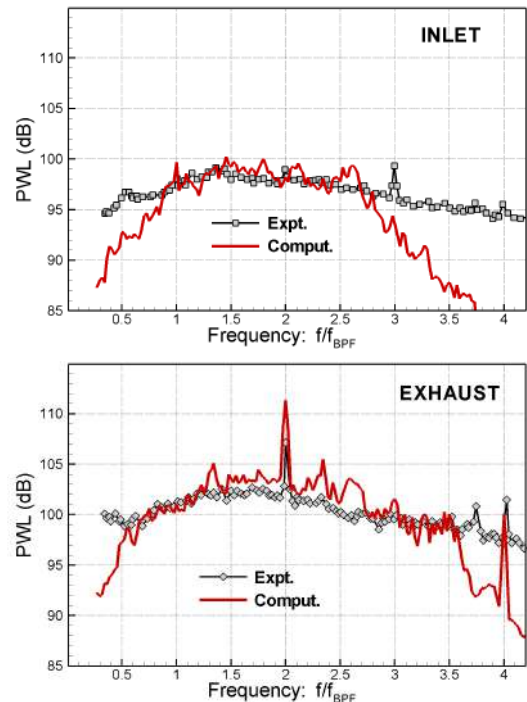


Figure 12: Predicted and measured sound power level spectra of the inlet and exhaust noise [22]

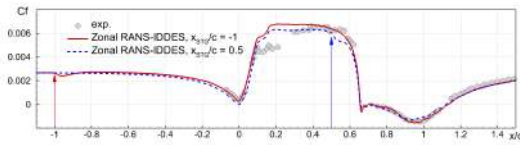


Figure 13: Comparison of skin friction distribution over NASA hump computed with the use of zonal RANS-IDDES with two different locations of the interface[25]

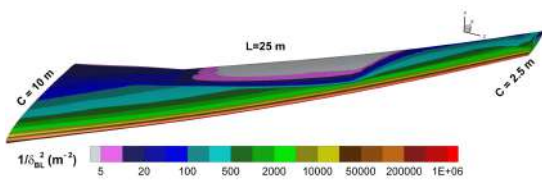


Figure 14: Contour plot of  $1/\delta^2$  over the surface of the CRM wing [24]. Notice the exponential scale for contour levels

for good accuracy, it seems that  $32^3$  would be a plausible minimum. The number of points is then  $N_0 \times N_{cubes}$ , where  $N_{cubes}$  is the number of cubes needed to fill the boundary layer, and (assuming perfect grid generation) is the integral of  $1/\delta^2$  over the surface. In Fig. 14, this quantity is shown over the wing of the Common Research Model of a commercial aircraft (CRM) at flight Reynolds number, with a turbulent attachment line (and therefore a thicker boundary layer there than if it had been laminar).

The figure has two striking features. First, the integrand takes very large values, nearing  $10^6 m^{-2}$ . This is over a band of area roughly  $10 m^2$  for the full wing, leading already to  $N_{cubes}$  in the 25-million range, and roughly  $10^{12}$  points, minimum. This is not doable today, and with the recent trend to a saturation of Moore's law, the estimate made in 2000 [26] that it would be doable in 2045 is probably too optimistic. In other words, practical methods will be RANS-WMLES hybrids rather than pure WMLES.

The second feature is how rapidly the integrand  $1/\delta^2$  falls, away from the attachment line. By the 10% chord line, it is down by a factor of 500, and therefore the local cost of WMLES has become manageable (in addition, the time step is proportional to the grid spacing). Based on  $1/\delta^2 \sim 2000 m^{-2}$  and a wetted area of  $600 m^2$ ,  $N_{cubes}$  becomes about 1 million and, if  $N_0 = 32^3$  is sufficient, the grid count is  $4 \times 10^{10}$  [26], which is in the "grand challenge" range today. Hence, a zonal approach combining RANS in the very thin region and WMLES for the rest (i.e., ADES) is possible already today.

A fortunate feature of this strategy is that the regions of the boundary layer that are treated by RANS are relatively easy to predict, often having zero or favorable pressure gradients. Also, by nature the thinnest regions have the weakest pressure gradients, if the gradient is normalized by the skin friction and the thickness; the same applies to curvature effects. In other words, the demands on the RANS model in the ADES framework become fairly low. In addition, a RANS model that is active only in boundary layers could be calibrated specifically for such flows, forsaking good performance in free shear flows.

While very plausible, this strategy leads to at least two questions, both difficult. The first is the logistics of implementing ADES, especially in an industrial context, and the second is the probability of truly "breaking the

glass ceiling" we contend RANS has in terms of accuracy, and/or the resolution required to achieve that.

The implementation as a reliable and non-expert-user engineering tool will require many non-trivial achievements and, in simple terms, much artificial intelligence. The system has not only grid sequencing, but "turbulence treatment sequencing." It will include preliminary steady (possibly not fully converged) RANS solutions as needed to establish the inviscid part of the flow, and the trailing vortices. This must be done with acceleration to steady state, rather than at the low computing speed of (time-accurate) WMLES. These solutions should involve automatic grid adaptation, including the important task of matching the region with RANS or LES resolution to the boundary layers and to the turbulent wakes and vortices. Based on the boundary-layer thickness, the system will then set the RANS and the LES zones, and generate grids accordingly. These will not be ambiguous. Other than that, in order to produce rapid transition from modelled to resolved turbulence with almost no gap in skin friction, an STG will be installed along the RANS-LES interface (as demonstrated by Fig. 12, this is, in principle, possible). All these steps need to be robust, and free of specific user inputs, while providing clear information in post-processing, such as marking the RANS and LES regions on the surface. Another difficulty will appear when the ADES solutions differ a lot from the preliminary RANS solutions, e.g. move the shock, or the separation line and wakes. The system will need to adapt the grid again. In extreme cases, separation could appear where it did not at first, or else disappear, causing large-scale changes in the flow, so that the re-adaptation would be extensive.

In summary, the implementation of ADES will be very involved, but we have failed to envision any simpler strategy that would have the same ultimate potential at high Reynolds numbers.

The accuracy question is also daunting. Just like RSMs have so far negated the hopes for "automatic" improvement over simpler RANS models, could WMLES fail to reward all our efforts and "logical" expectations?

In Fig. 15, we show an example of this possibility from recent work [27]. The Bachalo-Johnson flow [28] contains shock-induced separation over an axisymmetric bump, and has been a primary validation case since the 1980's. For this flow ADES (RANS-IDDES) gives inaccurate shock positions and post-shock pressure distributions, even though it was conducted on two grids, with a large number of points and with quite a significant difference between the two. Grid refinement which normally is discriminating for WMLES approaches gives no warning that the solutions are not very accurate. Grid 2 has about  $5 \times 10^5$  points in a cube of boundary layer, which is far larger than  $32^3$ , and therefore the resolution is not marginal by any standard. DNS with the same code, and a reduced domain size, agrees much better with experiment. Auxiliary tests of the WMLES system show that the flat-plate boundary layer is simulated accurately on a similar grid at the same Mach and Reynolds number, leaving the pressure gradient as the likely cause of the discrepancy. Hence, if this is the case, WMLES which was supposed, precisely, to accurately render the effects of pressure gradients and compressibility once the grid was fine enough, does not fulfill this mission. It appears that the very strong favorable pressure gradient creates an internal boundary layer, which dramatically increases the resolution needed. Of course, the SGS and wall models used in [27] are only one of many available, and we are hoping to read competing studies in the near future, but

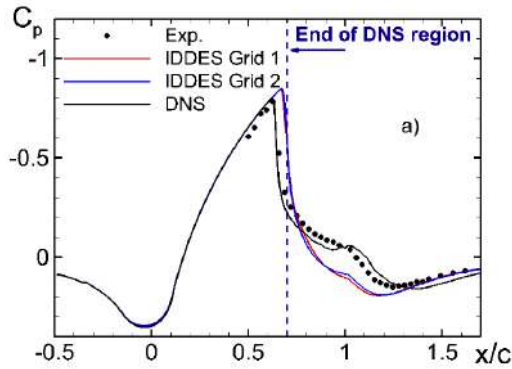


Figure 15: Pressure distribution for Bachalo-Johnson flow. IDDES Grid 1:  $4.7 \times 10^8$  cells, IDDES Grid 2:  $1.6 \times 10^9$  cells, DNS grid:  $8 \times 10^9$  cells [27]

the results of this exercise are worrisome. A possibility is that safe grid resolutions for WMLES will turn out to be very costly, say of the order of  $10^6$  for each cube, rather than  $10^4$  to  $10^5$  as some observers are hoping. Whether for RANS or LES, testing in simple flows, even at high Reynolds number, can be misleading.

To conclude, the ADES CFD strategy extends DES in that it begins with RANS and leads to WMLES initiated in the boundary layer as soon as it is thick enough not to make  $N_{cubes}$  unmanageable. We believe such an approach will impose itself over the years (maybe under another name) due to the realities of turbulent shear layers at high Reynolds numbers and the well-known weaknesses of both RANS and LES, but we also pointed out how complex it will be to implement, and how much remains to be learned about the grid resolution which will be needed to reach the desired level of accuracy.

## References

- [1] Spalart P. R., Jou W. H., Strelets M., Allmaras S. R., Comments on the feasibility of LES for wings, and on a hybrid RANS/LES approach, Proceedings of first AFOSR international conference on DNS/LES, 1997.
- [2] Shur M, Spalart PR, Strelets M, Travin A. Detached-eddy simulation of an airfoil at high angle of attack, In: Rodi W., Laurence D. (eds.), Engineering Turbulence Modelling and Experiment. Elsevier, Amsterdam, pp 669-678, 1999.
- [3] Hoerner S., Fluid-dynamic drag. Hoerner Fluid Dynamics, New Jersey, 1965.
- [4] Haase W., Aupoix B., Bunge U., Schwamborn D. (Eds.), FLOMANIA - A European Initiative on Flow Physics Modelling, Notes on Numerical Fluid Mechanics and Multidisciplinary Design, v. 94, 2006.
- [5] Spalart P. R., Deck S., Shur M. L., Squires K. D., Strelets M. Kh., Travin A., A new version of detached-eddy simulation, resistant to ambiguous grid densities, Theoretical and Computational Fluid Dynamics, 20(3), pp. 181-195, 2006.
- [6] Deck S., Recent improvements in the Zonal Detached Eddy Simulation (ZDES) formulation, Theoretical and Computational Fluid Dynamics, 26(6), pp. 523-550, 2012.
- [7] Nikitin N., Nicoud F., Wasistho B., Squires K. D., Spalart P. R., An approach to wall modeling in large-eddy simulations, Physics of Fluids, 2(7), pp. 1629-1632, 2000.
- [8] Shur M. L., Spalart P. R., Strelets M. K., Travin A. K., A hybrid RANS-LES approach with delayed-DES and wall-modeled LES capabilities, International Journal of Heat and Fluid Flow, v. 29, pp. 1638-1649, 2008.
- [9] Spalart P.R., Detached-Eddy Simulation, Annual Review of Fluid Mechanics, v. 41, pp. 181-202, 2009.
- [10] Shur M. L., Spalart P. R., Strelets M. Kh., Travin A. K., An enhanced version of DES with rapid transition from RANS to LES in separated flows, Flow, Turbulence and Combustion, 95(4), pp. 709-737, 2015.
- [11] Chauvet, N., Deck, S., Jacquin, L., Zonal detached eddy simulation of a controlled propulsive jet. AIAA Journal, 45 (10):pp. 2458-2473, 2007.
- [12] Guseva E. K., Garbaruk A. V., Strelets M. Kh. Assessment of Delayed DES and Improved Delayed DES Combined with a Shear-Layer-Adapted Subgrid Length-Scale in Separated Flows, Flow, Turbulence and Combustion, 98 (2), pp.481-502, 2017.
- [13] Greenblatt D., Paschal Y. C., Harris J. K., Schaeffer N., Washburn A., A separation control CFD validation test case. Part 1: Baseline & steady suction, AIAA Paper, AIAA-2004-2220, 2004.
- [14] Shur M. L., Spalart P. R., Strelets M. K., Noise prediction for increasingly complex jets. Part I: Methods and tests, International Journal of Aeroacoustics, v. 4, pp. 213-246, 2005.
- [15] Strelets M., Shur, M., Travin A., Spalart P.R., The delay of RANS-to-LES transition in hybrid RANS-LES approaches and some recently proposed remedies, Notes on Numerical Fluid Mechanics and Multidisciplinary Design, Advances in Simulation of Wing and Nacelle Stall, v. 131, Radespiel R. Niehuis R., Kroll N., Behrends K. (eds.), pp. 3-21, 2016.
- [16] Shur M. L., Spalart P. R., Strelets M. K., Travin A. K., Synthetic Turbulence Generators for RANS-LES Interfaces in Zonal Simulations of Aerodynamic and Aeroacoustic Problems, Flow, Turbulence and Combustion, v. 93, pp. 63-92, 2014.
- [17] Kraichnan R., Diffusion by a random velocity field, Physics of Fluids, v. 13, pp. 22-31, 1970.
- [18] Bechara W., Bailly C., Lafon P., Candel S., Stochastic approach to noise modeling for free turbulent flows, AIAA Journal, v. 32, pp. 455-463, 1994.
- [19] Shur M., Strelets M., Travin A., et al., Improved embedded approaches, Notes on Numerical Fluid Mechanics and Multidisciplinary Design, Vol. 134, 2017, pp. 51-87.
- [20] Menter F. R., Zonal two-equation  $k - \omega$  turbulence model for aerodynamic flows, AIAA-Paper, AIAA-1993-2906, 1993.
- [21] Shur M.L., Strelets M.K., Travin A.K., Spalart P.R., Suzuki T., Unsteady Simulations of a Fan/Outlet-Guide-Vane System: Aerodynamics and Turbulence, AIAA Journal, v. 56, pp. 2283- 2297, 2018.

- [22] Suzuki T., Spalart P.R., Shur M.L., Strelets M.K., Travin A.K., Unsteady Simulations of a Fan/Outlet-Guide-Vane System: Broadband-Noise Computation, *AIAA Journal*, v. 57, 2019.
- [23] Envia E., Fan Noise Source Diagnostic Test Completed and Documented, NASA Technical Report, TR-20050214860, 2003.
- [24] Spalart P. R., Strelets M. Kh., Attached and Detached Eddy Simulation, Notes on Numerical Fluid Mechanics and Multidisciplinary Design, Progress in hybrid RANS-LES Modelling, v. 137, Hoarau Y., Peng S-H., Schwamborn D., Revel A. (eds.), pp. 3-8, 2018.
- [25] Probst A., Schwamborn D., Garbaruk A., Guseva E., Shur M., Strelets M., Travin A., Evaluation of grey area mitigation tools within zonal and non-zonal RANS-LES approaches in flows with pressure induced separation, *International Journal of Heat and Fluid Flow*, v. 68, pp. 237-247, 2017.
- [26] Spalart P. R., Strategies for turbulence modeling and simulations, *International Journal of Heat and Fluid Flow*, v. 21, pp. 252-263, 2000.
- [27] Spalart P.R., Belyaev K.V., Garbaruk A.V., Shur M. L., Strelets M. Kh., Travin A. K., Large-Eddy and Direct Numerical Simulations of the Bachalo-Johnson Flow with Shock-Induced Separation, *Flow, Turbulence and Combustion*, v. 99, pp. 865-885, 2017.
- [28] Bachalo W.D., Johnson, D.A., Transonic, Turbulent Boundary-Layer separation generated on an axisymmetric flow model, *AIAA Journal*, v.24, pp. 437-443, 1986.

# HIERARCHICAL TURBULENCE AND GEOMETRY MODELLING OF AEROENGINE FLOWS

Z-N. Wang<sup>1</sup>, J. Tyacke<sup>2</sup>, Y. Ma<sup>1</sup> and P. Tucker<sup>1</sup>

<sup>1</sup>*Department of Engineering, University of Cambridge, UK*

<sup>2</sup>*Department of Mechanical and Aerospace Engineering, Brunel University London, UK*

## Abstract

For future ultra-high-bypass-ratio engines, strong aerodynamic and aeroacoustic couplings occur at both internal engine component level and external engine-airframe integration level. Direct simulation of these coupling effects is prohibitively expensive using high-fidelity methods only. To properly consider coupling effects, multi-fidelity methods are proposed using hierarchical modelling of turbulence and geometry. Flow zones are treated with methods of various fidelity levels in both turbulence and geometry to reduce the cost for required accuracy. Hierarchical geometry and turbulence modelling methods are outlined in this paper. Three examples are given to demonstrate its success in solving the coupling problems of aeroengine flows.

## 1 Introduction

### 1.1 Motivation

The world aircraft fleet is expected to double by 2036 over the next two decades with increased demand of air transport [1]. It therefore becomes more urgent to increase propulsive efficiency with less environmental impact. In the pursuit of high efficiency and low emissions, jet engine diameter increases as ever with higher bypass ratio. For future ultra-high-bypass-ratio (UHBP) aeroengines, components are designed to be more compact for less weight and drag. This results in stronger interactions between components. To accommodate larger engines under aircraft wings, closer installation is inevitable. This leads to significant interactions between engines and airframes in terms of aerodynamics and aeroacoustics. Designing one component at isolated circumstances is not always guaranteed with the same performance in a closely coupled system. This point has been raised in the NASA CFD vision 2030 [2] and was demonstrated by Cao et al. [3] and Cui et al. [4] on designing short intakes with the effects from fans. It is therefore crucial to incorporate effects of upstream and downstream components properly in the design phase.

However, challenges are faced when modelling this coupled system in full detail. First, high-fidelity eddy resolving simulation is prohibitively expensive at realistic Reynolds numbers for aeroengines. The cost of high-fidelity eddy resolving simulation grows exponentially with Reynolds numbers and the grid requirements of LES and hybrid LES-RANS are estimated by Tucker [5] for each component of an engine. Even simulating one component is challenging, multi-component simulation hence stays out of current computational capability and also out of industrial usefulness. Second, coupling multi-component computation cannot avoid complex geometry meshing. The meshing process of complex ge-

ometries can be very time-consuming if done manually. Meshing complex geometries automatically is still identified as a technical challenge by NASA [2]. Is there any feasible way to consider coupling effects in the simulation?

### 1.2 Hierarchical modelling

The solution could be: treat flow and geometry with various fidelity levels in different zones. This trades off the reliability of a solution with the speed and cost, and will enable the simulation of large-scale aerodynamically coupled systems. Conventionally, the degree of modelling in a computation is described as the fidelity level of a solution, and the fidelity decreases with modelled content. It is worth distinguishing between fidelity and accuracy of a solution. A low-fidelity model, operating in the calibrated space, can reproduce results as well as a much higher fidelity simulation. Rather, an increase in fidelity can improve the trust space with less calibration and provides more flow details. The coupled problem can be solved by integrating models of different fidelity levels in one solution: flow zones with adequate knowledge solved by well-calibrated low-fidelity models while zones with little knowledge solved by high-fidelity eddy resolving and fully geometry resolved methods.

A hierarchy of models representing turbulence and geometry exists from low to high fidelity levels, shown in Figure (1). As the simulation fidelity increases, the modeled content decreases and the resolved content and simulation cost increases. For turbulence modeling, the hierarchy depends on which turbulent scales are modelled: the fidelity ranges from Reynolds Averaged Navier-Stokes (RANS), solving ensemble averaged equations with all turbulent scales modelled, to Large-Eddy Simulation (LES), resolving energy-containing scales with subgrid dissipative scales modelled, and finally to Direct Numerical Simulations (DNS), resolving all turbulent scales with no models. The hierarchy of geometry modelling is less recognised than turbulence modelling. The most common way is to resolve the geometry using body-conformal mesh, which sits at the top fidelity level. This can be challenging for complex geometry and moving body problems. A number of methods have been developed to approximate the geometry to some extents. The Immersed Boundary Methods (IBM) were developed to represent the geometry on cartesian meshes using a distribution of body force [6]. This greatly offloads the mesh generation task. Although this shows advantages in saving meshing effects, it is still very expensive to be used to compute internal flows in turbomachinery at high Reynolds number when boundary layers need to be resolved on blade surfaces. Blade body force methods (BFM) are developed to represent the blade effects in an even lower fidelity, which allows slip wall boundary conditions. The turning angle can be forced locally at each



blade location [7] or globally by smearing blade effects along the circumferential direction [8]. Viscous effects are accounted for separately using a viscous body force parallel to blade camber lines [9].

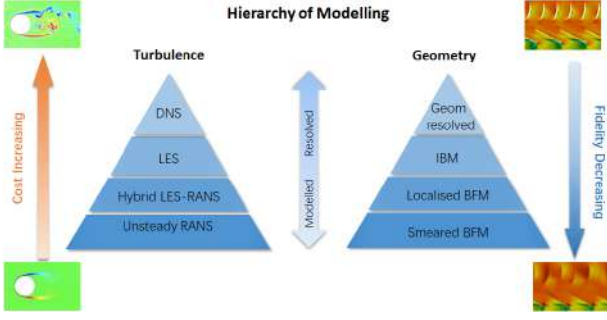


Figure 1: Hierarchy of modelling on geometry and turbulence

### 1.3 Scope of this paper

In this paper, the general framework is outlined to integrate hierarchical turbulence and geometry modelling in one solution. This enables the simulation with zones treated at multi-fidelity levels. Three examples, from aeroengine component interactions to aeroengine-airframe interference, are then given to demonstrate the success of using hierarchical modelling approaches to tackle aerodynamically coupled systems.

## 2 Hierarchical turbulence and geometry modelling

The structural similarities in the governing equations provide theoretical foundation for a hierarchy of turbulence and geometry models. The governing equations can be expressed in a general integral form:

$$\frac{\partial}{\partial t} \int_{\Omega} \mathbf{Q} dV + \oint_{\Gamma} \mathbf{H} \cdot \mathbf{n} dA = \int_{\Omega} \mathbf{F} dV + \frac{1}{\lambda} \int_{\Omega} \mathbf{S} dV \quad (1)$$

where  $\Omega$  and  $\Gamma$  are volume and surfaces of a mesh cell within computational domain, and  $\mathbf{n}$  is a unit vector of surface outwards normal. The conservative variables  $\mathbf{Q}$ , convective and viscous flux  $\mathbf{H}$ , body force  $\mathbf{F}$ , and volume source terms  $\mathbf{S}$  are written as:

$$\mathbf{Q} = \begin{bmatrix} \rho \\ \rho u_1 \\ \rho u_2 \\ \rho u_3 \\ \rho E \end{bmatrix} \quad \mathbf{H} = \begin{bmatrix} \rho u_i \\ \rho u_1 u_i + p \delta_{i1} - \tau_{i1} \\ \rho u_2 u_i + p \delta_{i2} - \tau_{i2} \\ \rho u_3 u_i + p \delta_{i3} - \tau_{i3} \\ \rho H u_i - \tau_{ij} u_j + q_i \end{bmatrix} \quad \mathbf{F} = \begin{bmatrix} 0 \\ f_{b,1} \\ f_{b,2} \\ f_{b,3} \\ f_{b,i} u_i \end{bmatrix} \quad \mathbf{S} = \begin{bmatrix} 0 \\ p \frac{\partial \lambda}{\partial x_1} \\ p \frac{\partial \lambda}{\partial x_2} \\ p \frac{\partial \lambda}{\partial x_3} \\ q_i \end{bmatrix} \quad (2)$$

Definition of  $t_{ij}$  and  $\mathbf{F}$  leads to a hierarchy of turbulence and geometry models.

### 2.1 Turbulence modelling

The hierarchical modelling of turbulence is reflected in the definition of the stress tensor  $\tau_{ij}$ . It can be expressed as

$$\tau_{ij} = \tau_{ij}^{lam} + \tau_{ij}^{turb} \quad (3)$$

where  $\tau_{ij}^{lam}$  is physical viscous stress caused by molecular motion and  $\tau_{ij}^{turb}$  represents the modelled stress of turbulent motion. For DNS,  $\tau_{ij}^{turb} = 0$  as all turbulent scales are directly resolved in the computation. Because of structural similarity shared by LES and RANS equations, modelled turbulent stress of LES and RANS can be framed in a general form:

$$\tau_{ij}^{turb} = (1 - f) \tau_{ij}^{RANS} + f \tau_{ij}^{LES} \quad (4)$$

where  $f = 1$  for LES and  $f = 0$  for RANS. It is worth noting that  $\mathbf{Q}$  is ensemble averaged in RANS and spatially filtered in LES, respectively. For hybrid LES-RANS,  $f$  can be a function of spatial location  $\mathbf{x}$  to blend LES zones with RANS [10].  $f(\mathbf{x})$  defines the hybridization strategies and incorporates wall-modelled LES, zonal/embedded LES and DES-type non-zonal methods. The RANS stress  $\tau_{ij}^{RANS}$  and the LES stress  $\tau_{ij}^{LES}$  can be calculated independently by different RANS and LES subgrid models.

### 2.2 Geometry modelling

The hierarchical modelling of geometry is reflected in the definition of  $\mathbf{F}$ . When the body force  $f_{b,i} = 0$  and blocking factor  $\lambda = 1$ , the equation Eq. (1) is used for the simulation with direct mesh-resolved geometries. In a lower fidelity geometry representation, the term  $f_{b,i}$  is used to model the force exerted on fluids by solid boundaries instead of resolving the real geometry by body-conformal mesh. There are two ways to impose body forces at the immersed boundaries: feedback forcing and direct forcing. In feedback forcing, a PI controller is used to drive the computed velocity  $u_i^n$  to the desired velocity  $u_i^D$  at the immersed boundaries [11]

$$f_{b,i} = K_p (u_i^D - u_i^n) + K_I \int_0^{t_n} (u_i^D - u_i^n) dt \quad (5)$$

where  $K_p$  is the coefficient of proportional controllers with dimension of  $s^{-1}$  and controls the convergence speed to the desired value as a damping factor, while  $K_I$  is the coefficient of integral controller with dimension  $s^{-2}$  and used to increase computational stability. The body force terms will vanish when the computed velocity finally converges to the desired velocity. It is verified that both final flow field and convergence speed were the same for the range of values of 0.1-10 for  $K_I$  and  $K_p$  for current simulation cases. However, the integral controller introduces a natural frequency  $(1/2\pi)\sqrt{K_I}$ . For unsteady simulations,  $K_I$  should be adjusted to keep the forcing-introduced frequency away from the interested unsteady frequencies. In the direct forcing strategy, the forcing term is obtained by rearranging the discretised momentum equations and the desired velocities are immediately imposed at the geometry boundaries [12]. If taking the first-order Euler scheme for time stepping as an example, the direct forcing term is

$$f_{b,i} = RHS_i - \frac{u_i^D - u_i^n}{\Delta t} \quad (6)$$

where  $RHS_i$  contains convective and viscous terms, and pressure gradient,  $u_i^D$  is the desired velocity on geometry boundaries and  $u_i^n$  is the computed velocity at the last time step  $n$ . Although direct forcing requires no empirical coefficients to adjust, it needs an implicit scheme to stabilise the computation.

In IBM, it is not necessary that the computational grid nodes lie ideally on the immersed boundaries, therefore an interpolation process needs to be used to distribute the force on the boundaries [12]. In BFM, the body force can be split into two parts

$$f_{b,i} = f_{bn,i} + f_{bp,i} \quad (7)$$

where  $f_{bn,i}$  and  $f_{bp,i}$  are the forces normal to and parallel blade surfaces.  $f_{bn,i}$  is used to impose the non-permeable boundary and  $f_{bp,i}$  depends on the empirical models accounting for viscous losses. To achieve the required flow turning and pressure rise, Cao et al. [3] use direct forcing method to smear the normal force  $f_{bn,i}$  azimuthally in the blade region with the parallel force  $f_{bp,i}$  accounting for losses generated in the blade passage. The blocking factor  $\lambda$  is used to consider the passage blockage caused by the blades. Ma et al. [7] further extend this by localising both normal and parallel forces using a Dirac function inside the blade. This is to approximate blade non-uniformity effects from blades blockage, the parallel force  $f_{bp,i}$  is calibrated to account for friction loss on the blades and mixing loss in the blade wakes.

### 3 Simulation of internal coupling of aeroengine components

In this section, hierarchical modelling approaches are demonstrated to compute aerodynamically coupled components inside aeroengines.

#### 3.1 Intake separation and fan interactions

Flow separation occurs over an intake at a large flow incidence during an aircraft take-off or under crosswinds. It is well known that the distorted inlet flow will severely influence the fan operating stability. However, the fan effects on the wake separation is not traditionally considered in designing the intake shape as the distance between intake lip to fan leading edge is large. The increase of engine diameter for higher efficiency greatly shortens intake length due to the constraint of engine weight and wetted surface area. Hence, the fan effects on the intake separation are becoming significant [3, 4]. The separation is a well-known enemy to RANS models, therefore LES is preferred in this scenario. However, it is far from affordable to extend LES into the fan region by resolving flow structures around fan blades. As all we need to know is the fan response in a large-length scale, the benefits will be very low even if this expensive LES task can be achieved within the blade passage. A better and cost-effective solution is to represent downstream fan blades using a low-fidelity model in the LES context.

The test case used here is the configuration of the Darmstadt rotor [7]. A 1/4 annular distortion generator is placed upstream of the fan tip to reproduce inlet flow distortions generated by intake lip separations at high angles of attack. Figure 2(a) shows the inlet distortion is generated at an annular section upstream of the fan blades. Figure 2(b) shows the computational domain with corresponding simulation strategies. To avoid

meshing complexity, standard IBM is used to model the geometry of the triangular section (distortion generator). The flow separation over the beam is computed by LES. Instead of resolving the blade geometry using mesh, downstream fan blades are modelled by circumferentially smeared blade body force methods. This provides a cost effective solution to simulate downstream fan effects on intake separations.

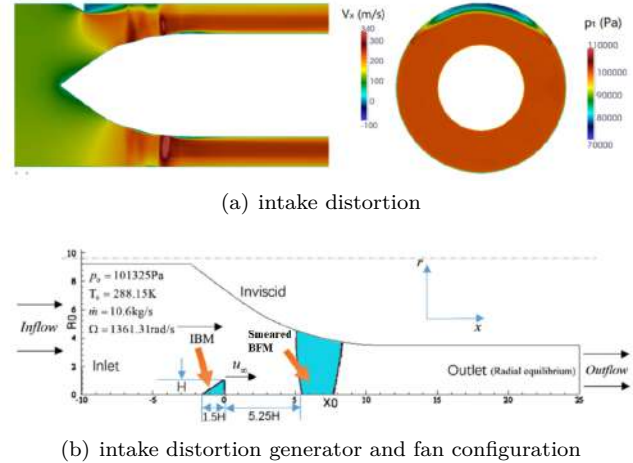


Figure 2: Configuration of simulating intake distortion interactions with fan blades

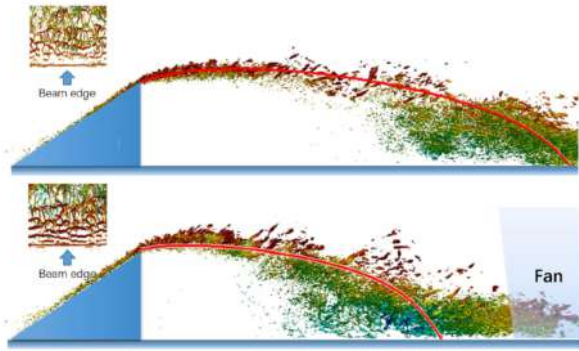
Figure 3(a) shows the inlet separation structures using Q-criterion. Two cases, one with and the other without fan, were simulated to investigate fan effects on the upstream separation. When the fan is present downstream, the trajectory of the shear layer is changed and the separated flow reattaches on the casing much earlier than the no-fan case. This leads to a smaller separation length. Figure 3(b) compares the time-averaged axial velocity at each axial location for both cases. The inflectional points of velocity profiles at axial locations are joined into lines, tracing the shear layers. It quantitatively shows that the fan reduces the separation extent by accelerating the low momentum flows in the separation zone. The separated flow reattaches at an axial location that is around a beam height upstream of the fan leading edge.

Turbulent kinetic energy (TKE) and its production are shown in Figure (4). The fan effects on two regions of the separated flow: flow shear in zone 1 and flow mixing in zone 2. The TKE generation in zone 1 is increased by larger shear introduced via flow acceleration by fan suction. The convection of TKE from upstream causes a high TKE in zone 2. In addition, the streamline curvature is modified by fan suction as seen in the mean flow profile of Figure 3(b). The separated flow reattaches onto the casing wall with a stronger impingement, also leading to more mixing around the reattachment point.

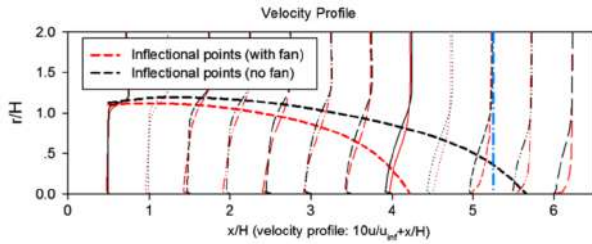
Overall, the low-fidelity geometry modelling of fan blades and distortion generator can not only alleviate mesh generation efforts but also enables simulating coupled aerodynamics in high-fidelity turbulence simulations. The significant fan effects on intake separation, *i.e.* reduced separation size, is well captured in this simulation.

#### 3.2 Fan and OGV interactions

Downstream of intakes, coupling also happens between fan blades and outlet guide vanes (OGV). When the fan operates at off-design conditions, significant separations



(a) q-criterion



(b) axial velocity

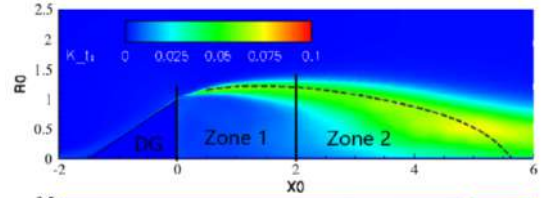
Figure 3: Fan effects on inlet separation sizes

will occur on the fan blade at the presence of the potential flow field set by the downstream OGVs. The case presented here is a high-bypass-ratio fan configuration operating at the approach condition that is half of the design speed. Separation occurs in the upper half span of fan blades, while the flow near hub is relatively clean. Both turbulence and geometry hierarchical modelling are demonstrated here to treat such flows using mixed fidelities.

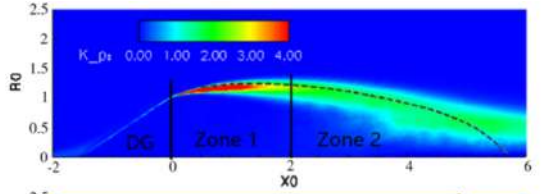
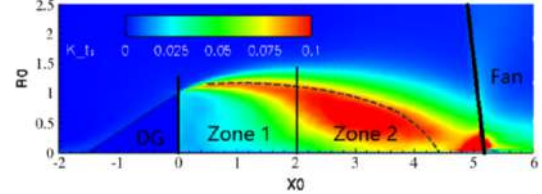
Figure (5) shows hierarchical modelling strategy of this aerodynamically coupled fan and stators (OGV and ESS). Fan tip separation and leakage flows is handled by wall modelled LES (WMLES) in the upper half span, while the attached flows in the lower span is simulated by URANS. As to geometry modelling, the simulation of the fan blades is performed using mesh-resolved geometry as the boundary layers have to be resolved to capture the correct wake velocity deficit. Meanwhile, the OGVs and EESs are modelled by smeared BFM to provide the right downstream potential flow field for fan flows.

Figure (6) shows the implementation for hybridising LES with RANS in the simulation. The function  $f$  defines the blending between LES and RANS. In this case, the Spalart-Allmaras model [13] is used to calculate the RANS stress while the Wall-Adapting Local Eddy-Viscosity (WALE) Subgrid model [14] is used to provide the turbulent stress for the LES. As indicated by Eq. (4), LES ( $f = 1$ ) is zonalised in the fan tip region from 65% span for separation and tip leakage flow while RANS is responsible for the clean hub flow. In the LES zone, a thin RANS layer of  $y^+ \sim 100$  was placed near the fan blade and casing wall as a wall model to further avoid the cost of resolving near-wall turbulent streaks. The maximum grid size in the streamwise and spanwise directions are around 600 and 300, which satisfies hybrid LES-RANS requirements [15]. The total grid number is around 50 million for this hybrid LES-RANS simulation. This saves two orders of grid cells count compared to an estimation of 5 billion for a full-span wall resolved LES.

The ratio of RANS eddy viscosity  $\mu_t$  to physical molecular viscosity  $\mu$  (Figure 7(a)) is shown with vorticity



(a) TKE



(b) TKE production

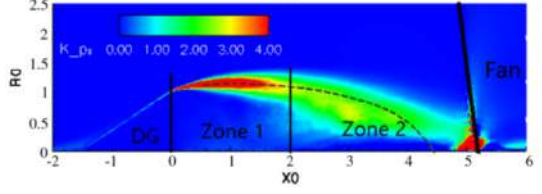


Figure 4: Turbulent kinetic energy (TKE) and its production in the inlet separation

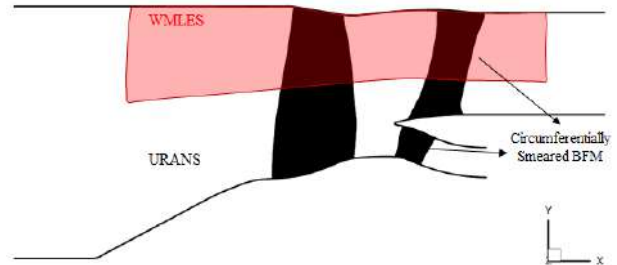


Figure 5: hierarchical modelling strategy in Fan-OGV coupled simulations

magnitude (Figure 7(b)) at the same x-plane downstream of a fan blade. The RANS eddy viscosity is localised in the wake of the lower span region and fades away towards the fan tip for LES. The vorticity shown in Figure 7(b) indicates the effectiveness of zonalised LES by contrasting flow in the upper and lower span. The fan wakes are captured by LES with fine-scale turbulent structures in the upper span while transitioning into the reduced-flow-scale RANS region in the lower span.

Computed velocity profiles from the hybrid LES-RANS are compared with hot-wire measurements in Figure (8). The flows at 90% and 25% span are obtained from WMLES and RANS respectively. LES is capable of capturing the separation at the fan tip and RANS predicts the attached boundary layer correctly. This demonstrates the success of using multi-fidelity turbulence and geometry modelling in one simulation.

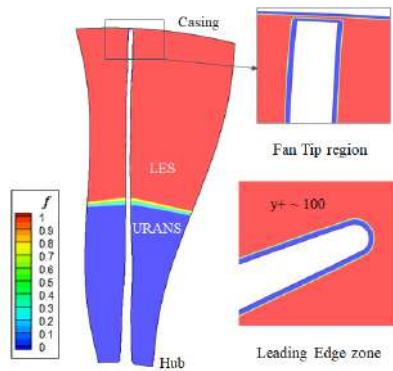


Figure 6: Hierarchical turbulence modelling of fan flows

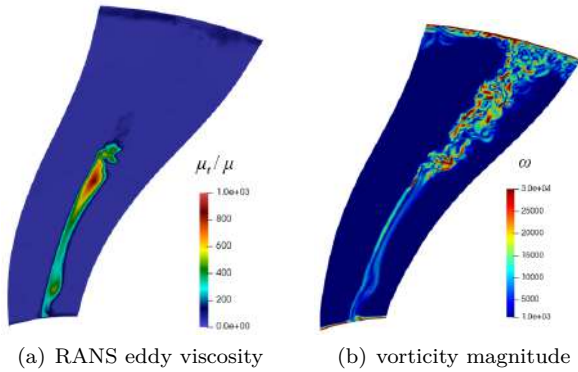


Figure 7: Zonalised LES simulation of fan tip flows at a x-plane downstream a fan blade

## 4 Simulation of external coupling of aeroengine and airframe

The trend towards higher bypass-ratio engines leads to a closer integration with the airframe, which constantly changes the design space. The closer integration introduces strong coupling between aeroengine jets and airframe, where existing aerodynamic and aeroacoustic correlations are no longer valid. There is a direct need to update existing methods of both aerodynamics and aeroacoustics [16]. Experimental facilities are expensive and it is difficult to achieve realistic flight conditions, including flight streams. Numerical simulation of this coupled systems with hierarchical fidelity models provides a promising and cost-effective alternative.

Configuration of an ultra-high-bypass-ratio engine installed under a three-dimensional wing has recently been simulated using hybrid LES-RANS method [17]. Far-field sound is predicted using Ffowcs-Williams Hawkins equations and the prediction agrees well with acoustic measurements. The nozzle and wing are covered by a RANS layer to avoid cost of resolving near-wall streaks. Propulsive jets are simulated using LES to capture large-scale turbulent sound source from first principles. The aerodynamic and aeroacoustic interactions between propulsive jets and wing are directly resolved in this type of simulation. The simulation framework of this jet and wing interactions is presented by Wang et al. [10]. Figure 9(a) shows the predicted flow and acoustics for this installation configuration. Noise, visualised in the background greyscale contour, is generated from the jet itself and its interactions with the wing. Nozzle serrations are designed to reduce installation noise by controlling the jet shear layer development. As indicated by decreased TKE around and downstream of the wing

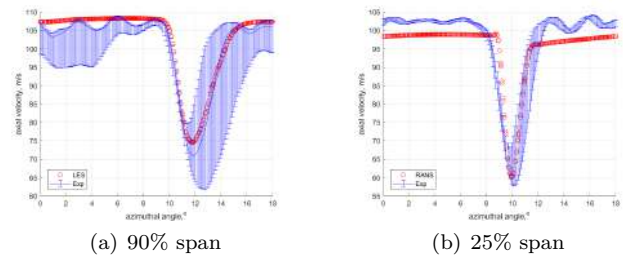
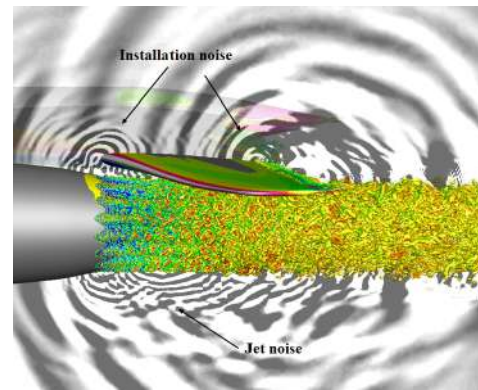
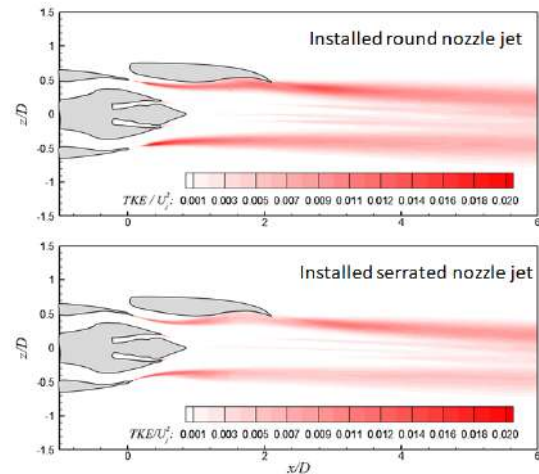


Figure 8: Axial velocity profile across fan blade passage

for serrated nozzle jets in Figure 9(b), serrations reduce jet-wing interactions and hence installation noise.



(a) Installed jet flows and acoustics



(b) TKE of installed round and serrated nozzle jets

Figure 9: Hybrid LES-RANS of installed jet flow and acoustics

In a real engine, there are many components upstream the exhaust nozzle, such as fan, compressor, combustor and turbine. It has been supposed for some time that such upstream flow could excite the jet and generate excess noise [18]. It is not realistic to include all these upstream components directly using high-fidelity simulation with complex geometries resolved by a body-conformal mesh. Figure (10) shows an attempt to incorporate upstream geometry in the bypass using hierarchical modelling approaches to tackle this multi-scale multi-physics problem [19]. The upstream geometry includes fan, OGV, A-frame and gearbox shaft. The fan is modelled by smeared BFM, OGVs are modelled by localised BFM and the rest of the components are modelled by standard IBM. It was found that the introduction of upstream geometry initiated earlier shear layer

development and thickening, as well as greater azimuthal nonuniformity. This may have an impact on overall noise level and directivities.

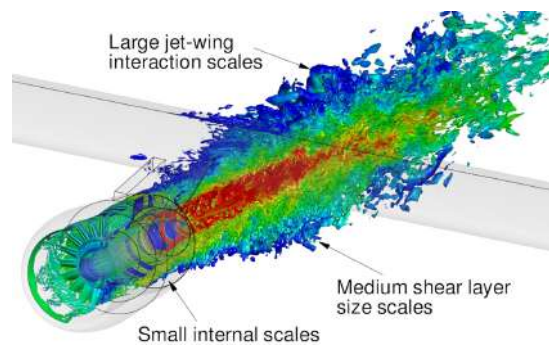


Figure 10: Coupled simulation of Airframe and Aero-engine with internal geometries modelled by BFM and IBM

## 5 Conclusions

There is a high degree of internal and external couplings in aeroengine flows. Challenges are faced to simulate this aero-coupled system. Hierarchical modelling of both turbulence and geometry provides a promising and cost-effective solution. Turbulence and geometry in different flow zones can be modeled in one simulation using methods of different fidelity levels. The multi-fidelity simulation using hierarchical modelling approaches is demonstrated on internally and externally coupled flow systems of aeroengines. The coupling effects are successfully captured by the proposed hierarchical method.

## Acknowledgment

Acknowledge is made for the computational time provided by the UK Turbulence Consortium under EPSRC grant EP/L000261/1 and the EPSRC Leadership project "Coupled, multi-scale modelling of modern installed aeroengine aeroacoustics" on UK national super-computer ARCHER and the DECI resource Sisu based in Finland with support from the PRACE aisbl under the project InJet.

## References

- [1] R. Tinseth, "Current market outlook: 2017-2036," *Boeing Commercial Airplanes, Seattle, USA*, 2017.
- [2] J. Slotnick, A. Khodadoust, J. Alonso, D. Darmofal, W. Gropp, E. Lurie, and D. Mavriplis, "CFD vision 2030 study: a path to revolutionary computational aerosciences," vol. NASA CR-2014-218178, 2014.
- [3] T. Cao, N. R. Vadlamani, P. G. Tucker, A. R. Smith, M. Slaby, and C. T. J. Sheaf, "Fan-intake interaction under high incidence," *Journal of Engineering for Gas Turbines and Power*, vol. 139, 11 2016.
- [4] J. Cui, R. Watson, Y. Ma, and P. Tucker, "Low order modeling for fan and outlet guide vanes in aero-engines," *Journal of Turbomachinery*, vol. 141, 01 2019. 031002.
- [5] P. Tucker, "Computation of unsteady turbomachinery flows: Part 2 - LES and hybrids," *Progress in Aerospace Sciences*, vol. 47, no. 7, pp. 546 – 569, 2011.
- [6] R. Mittal and G. Iaccarino, "Immersed boundary methods," *Annual Review of Fluid Mechanics*, vol. 37, no. 1, pp. 239–261, 2005.
- [7] Y. Ma, J. Cui, N. R. Vadlamani, and P. Tucker, "Hierarchical geometry modelling using the immersed boundary method," *Computer Methods in Applied Mechanics and Engineering*, vol. 355, pp. 323 – 348, 2019.
- [8] T. Cao, P. Hield, and P. G. Tucker, "Hierarchical immersed boundary method with smeared geometry," *Journal of Propulsion and Power*, vol. 33, no. 5, pp. 1151–1163, 2017.
- [9] L. Xu, "Assessing viscous body forces for unsteady calculations," *Journal of Turbomachinery*, vol. 125, pp. 425–432, 08 2003.
- [10] Z.-N. Wang, J. Tyacke, P. Tucker, and P. Boehning, "Parallel computation of aeroacoustics of industrially relevant complex-geometry aeroengine jets," *Computers & Fluids*, vol. 178, pp. 166 – 178, 2019.
- [11] D. Goldstein, R. Handler, and L. Sirovich, "Modeling a no-slip flow boundary with an external force field," *Journal of Computational Physics*, vol. 105, no. 2, pp. 354 – 366, 1993.
- [12] E. Fadlun, R. Verzicco, P. Orlandi, and J. Mohd-Yusof, "Combined immersed-boundary finite-difference methods for three-dimensional complex flow simulations," *Journal of Computational Physics*, vol. 161, no. 1, pp. 35 – 60, 2000.
- [13] P. R. Spalart and S. R. Allmaras, "A one-equation turbulence model for aerodynamic flows," *Recherche Aerospatiale*, vol. 1, pp. 5–21, 1994.
- [14] F. Nicoud and F. Ducros, "Subgrid-scale stress modelling based on the square of the velocity gradient tensor," *Flow, Turbulence and Combustion*, vol. 62, pp. 183–200, Sep 1999.
- [15] P. G. Tucker, *Unsteady computational fluid dynamics in aeronautics*. Springer Science & Business Media, 2014.
- [16] K. Viswanathan, M. J. Czech, and I. C. Lee, "Towards prediction of dual-stream jet noise: Database generation," *AIAA Journal*, vol. 49, no. 12, pp. 2695–2712, 2011.
- [17] J. C. Tyacke, Z.-N. Wang, and P. G. Tucker, "LES-RANS of installed ultra-high-bypass-ratio coaxial jet aeroacoustics with flight stream," *AIAA Journal*, vol. 57, no. 3, pp. 1215–1236, 2019.
- [18] C. J. Moore, "The role of shear-layer instability waves in jet exhaust noise," *Journal of Fluid Mechanics*, vol. 80, no. 2, pp. 321–367, 1977.
- [19] J. C. Tyacke, M. Mahak, and P. G. Tucker, "Large-scale multifidelity, multiphysics, hybrid Reynolds-Averaged Navier-Stokes/Large-Eddy Simulation of an installed aeroengine," *Journal of Propulsion and Power*, vol. 32, no. 4, pp. 997–1008, 2016.

# HYBRID RANS/LES METHODOLOGIES FOR EXTERNAL AIRCRAFT AERODYNAMICS

A. Probst, S. Probst and D. G. François

*German Aerospace Center (DLR), Institute of Aerodynamics and Flow Technology, Göttingen, D-37073, Germany*

## Abstract

An overview of the hybrid RANS/LES methodologies developed and applied at DLR (German Aerospace Center) for external aircraft aerodynamics is provided. Apart from brief descriptions of the methods implemented in the unstructured compressible DLR-TAU solver, a selection of aeronautical applications is presented.

## 1 Introduction

Modern aircraft design relies on the detailed knowledge of flow conditions throughout the whole flight envelope, which is provided not only by measurements but to an increasing extent by numerical simulations (CFD). However, at the borders of the envelope, e.g. during take-off/landing or high-speed flight, there occur complex turbulent flow phenomena like massive or shock-induced separations, which are beyond the nominal validity range of RANS turbulence models. While the step towards turbulence-resolving methods such as Large-Eddy Simulation (LES) appears logical, the large Reynolds numbers of flying aircraft still prohibit the exclusive use of LES in the whole flow field [1]. For this reason, LES for aircraft needs to be augmented by less-expensive modelling, e.g. either just close to the walls (i.e. wall-modelled LES) or even in whole flow regions that are well-computable with RANS models, e.g. attached boundary layers with only mild pressure gradients. Both approaches can be realized with the hybrid RANS/LES method (HRLM) which is therefore considered a promising candidate for accurate border-of-envelope simulations of aircraft.

Over the last years, the DLR (German Aerospace Center) has worked in several national and international projects on the development and application of reliable hybrid RANS/LES approaches for external aircraft aerodynamics. Focusing on the unstructured compressible DLR-TAU code [2], which is widely used in industry and academia, the present paper outlines its basic HRLM capabilities, as well as recent additions to increase the accuracy and applicability range of hybrid methods. For demonstration, a small selection of simulation cases from the field of external aircraft aerodynamics is presented.

## 2 Simulation Method

DLR's simulation strategy for external aerodynamics is founded on flexible unstructured methods, feasible for both fundamental flow cases and complex industrial configurations. The main tool for general aeronautics is the DLR-TAU code [2], which solves the compressible flow equations using a 2nd-order finite-volume approach on meshes with mixed element types (e.g. hexahedra, tetrahedra, prisms). Besides different classes of RANS approaches ranging from eddy-viscosity to differential

Reynolds-stress models, as well as state-of-the-art CFD techniques (e.g. multigrid, explicit/implicit relaxation schemes, Chimera), the TAU code offers dedicated scale-resolving capabilities essentially relying on the hybrid RANS/LES methodology.

### 2.1 Basic Hybrid RANS/LES Method

Among the numerous approaches to combine efficient RANS modelling with more accurate LES, the TAU code focuses on recent variants of the Detached-Eddy Simulation (DES). In DES, an underlying RANS model is seamlessly turned into an LES sub-grid scale model, if certain local grid- and flow-related criteria are met.

Despite its relative complexity, the Improved Delayed DES (IDDES) [3] is considered the standard hybrid model in TAU, thanks to its capability to switch automatically between RANS, LES and wall-modelled LES (WM-LES) modes. In cases without the specific need for WM-LES, the Delayed DES (DDES) is used as simpler alternative. While the IDDES is *non-zonal* by nature, i.e. self-adapting to either RANS or (WM-)LES, it can easily be applied in a *zonal* manner (similar to ZDES [4]) by manually prescribing the local modelling mode.

Besides the hybridization scheme, the underlying RANS model plays an important role as well, as it determines the separation location, computes the inflow for embedded (WM-LES) regions and provides the input statistics for synthetic-turbulence generators. For this reason, we combine DES not only with eddy-viscosity models such as Spalart-Allmaras or Menter's SST model, but also make use of TAU's robust implementations of anisotropy-resolving Reynolds-stress models [5] in the framework of HRLM, see e.g. [6], [7], [8].

### 2.2 Treatment of RANS/LES Interface

One fundamental challenge in HRLM is the ambiguous behaviour at the interface of modelled (RANS) and resolved (LES) turbulence. This issue may affect different aspects, e.g. insufficient *shielding* of RANS boundary layers, the so-called *log-layer mismatch* at the wall-tangential RANS/LES interface in WM-LES, or a delayed streamwise generation of 3D turbulence in the initial LES region. Some remedies implemented in the TAU code are outlined in the following.

**Non-Zonal Grey-Area Mitigation** In typical HRLM applications involving local separations, the flow is sufficiently unstable w.r.t. small disturbances to allow for rapid transition to resolved turbulence. However, in case of large lateral grid anisotropies in the initial LES region, which are often found around trailing edges and other geometrical complexities, the classic DES filter width  $\Delta_{max} = \max(\Delta_x, \Delta_z, \Delta_z)$  leads to unjustified high levels of modelled sub-grid viscosity, which may

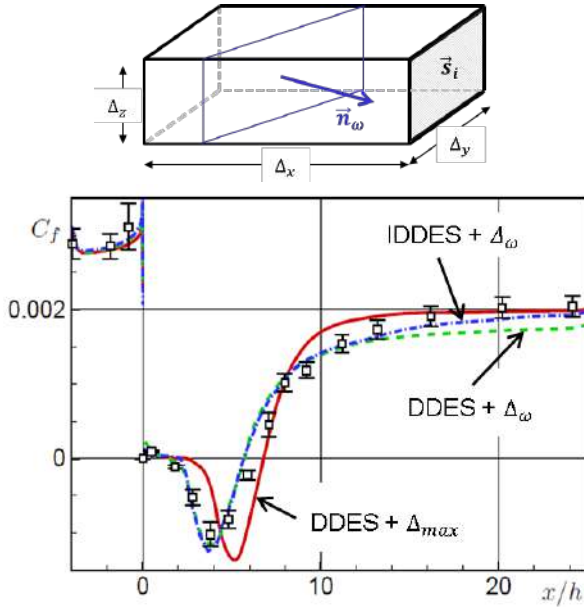


Figure 1: Sketch of cell-area projection on the vorticity plane in  $\Delta_\omega$ -filter (top) and effect of different filters on the skin friction in a backward-facing step flow (bottom)

delay the transition to LES even in unstable flow. As a specific remedy, we adopt the vorticity-sensitive filter width  $\Delta_\omega$  of [9] and transform it into a general expression that is suitable for TAU's unstructured dual-cell approach. As sketched in Figure (1) (top), by projecting the cell faces  $\vec{s}_i$  onto the normalized local vorticity vector  $\vec{n}_\omega$  this filter width only considers the cell areas parallel to the local flow orientation, thus neglecting the possibly large lateral cell dimensions in the initial 2D flow before break-down to turbulence. Its effect is demonstrated for a backward-facing step flow in Figure (1) (bottom), where the original DDES formulation with  $\Delta_{max}$  yields significant deviations from the measured skin friction. This error is minimized by the modified filter width, most notably using IDDES.

**Synthetic turbulence for embedded WM-LES** In order to extend the application range of HRLM to stable flows like attached boundary layers, more powerful methods are needed to model the RANS-to-LES transition. To this end, the TAU code has been supplemented by different synthetic-turbulence (ST) generators, which transform the modelled RANS turbulence into resolved fluctuations with the same statistical properties. Two basic methods are considered: the Synthetic-Eddy Method (SEM) [10] along with its divergence-free variant (DFSEM) and the Synthetic-Turbulence Generator (STG) [11] with extensions due to François et al. [8].

The SEM tracks a number of random vortex elements, which are convected with bulk velocity through a box around the RANS/LES interface. Taking the target Reynolds stresses and integral length scales from the local RANS data into account, these synthetic eddies induce a superimposed field of velocity fluctuations in the requested forcing domain, which can be either a single grid plane or a small volume around the interface. The DFSEM applies the same method to the fluctuating vorticity, which allows enforcing a divergence-free velocity field but restricts the realizable stress anisotropy.

Opposed to convected random eddies, the STG computes velocity fluctuations by superimposing a fixed

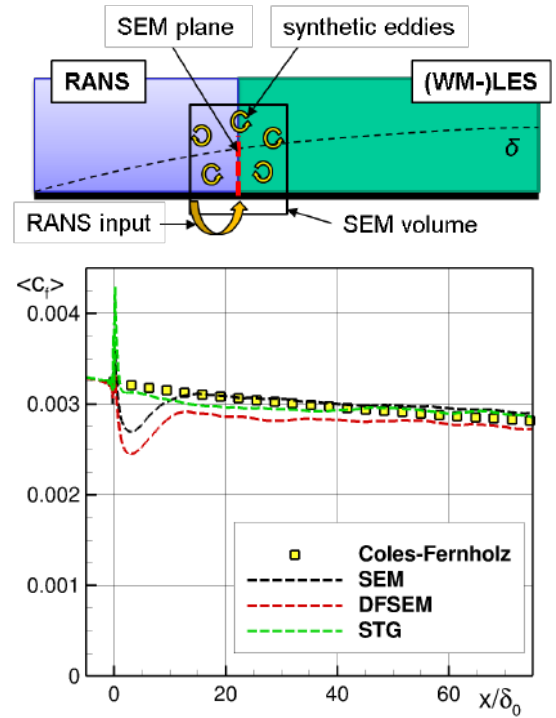


Figure 2: Sketch of the SEM implementation (top) and comparison of synthetic turbulence methods (injected at  $x/\delta_0 = 0$ ) for the skin friction on a flat plate (bottom)

number of stochastic Fourier modes. The modes are weighted to reproduce a von-Kármán model spectrum that is generated based on the given RANS and grid-cut-off length scales. As in SEM, the Cholesky-decomposed Reynolds-stress tensor provides the anisotropic scaling of the induced velocity fluctuations. To provide realistic time correlations if the STG is applied in a volume, a modified position vector and time are introduced and linked with the actual quantities via Taylor's frozen velocity hypothesis, see [8] for details.

The different ST methods are implemented in a unified framework, allowing systematic comparisons as exemplarily shown in Figure (2) (bottom) for a flat-plate flow with  $Re_\theta = 3040$  at the RANS/LES interface ( $x/\delta_0 = 0$ ). The injection of the computed synthetic fluctuations is realized via source terms, which are designed to reproduce the synthetic field in the actual flow solution as accurate as possible. Further implementation details and sensitivity studies can be found in [8], [12].

**Algebraic HRLM Sensors** To prevent unwanted premature switching to LES, common DES variants (e.g. IDDES, ZDES) employ local sensor functions to enforce RANS mode in attached boundary layers. However, as pointed out by different authors [13], [14], this *RANS shielding* may fail in boundary layers with adverse pressure gradients, due to its calibration for the flat plate.

Apart from rather ad-hoc fixes in the sensor formulation [13] we also consider a more rigorous shielding based on non-local algebraic sensors for the boundary-layer state. This is realized in TAU via an additional data structure using wall-normal lines along existing grid points, which allows computing non-local boundary-layer parameters, like the shape factor  $H$  and the boundary-layer thickness  $\delta$ , during run time. With this information at hand (optionally based on running flow time averages), the RANS shielding in (I)DDES is supplemented

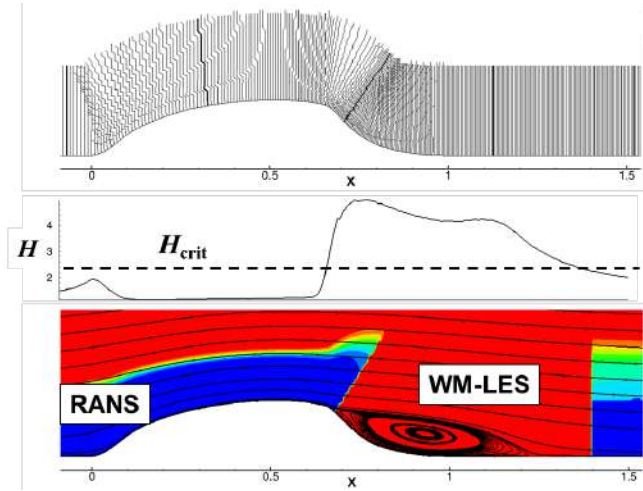


Figure 3: Algebraic HRLM sensors applied to hump flow: Wall-normal lines, computed shape factor, resulting RANS (blue) and WM-LES (red) regions

by strict criteria for attached boundary layers, i.e. set RANS mode if  $d_w < \delta$ , with  $d_w$  being the local wall distance. Moreover, additional criteria for pressure-induced separation ( $H > H_{crit}$  with  $H_{crit} \approx 2.4$ ) and for the detection of resolved turbulent content in the boundary-layer are available in order to control the switch to the LES or WM-LES modes of IDDES, respectively.

Figure (3) provides an illustration for the wall-mounted hump case, showing the lines, the computed shape-factor distribution and the resulting modification of the shielding function. The method is applicable to external aerodynamics and typically causes only small additional effort, thanks to the fully-parallel evaluation of the boundary-layer parameters which, moreover, is performed only once per physical time step.

### 2.3 Hybrid Numerical Scheme

LES methods with explicit modelling of the sub-grid scales are affected by additional dissipation and dispersion errors in the numerical scheme. For this reason, HRLM simulations with TAU employ the *LD2* (low-dissipation low-dispersion) scheme [15], [16] which combines a low-dissipative central flux formulation with a gradient-based reconstruction of face values.

The flux is based on the energy-conserving skew-symmetric operator of Kok [17], which is stabilized by small amounts of matrix-valued artificial dissipation for robustness on unstructured grids. This dissipation operator is extended by low-Mach preconditioning for incompressible flow regions. Its parameters have been optimized in LES of a channel flow [7] for lowest-possible dissipation while retaining robustness (*LD* scheme).

To also improve the dispersion properties of the scheme, the usual assumption in central schemes of constant flow variables within each cell is dropped in favour of a weighted gradient-based extrapolation of the face value (similar to the MUSCL approach). Inspired by [17], but adopted here for a  $2^{nd}$ -order unstructured scheme, the extrapolation parameters have been tuned to minimize the dispersion error in a 1D wave-convection problem. Figure (4) depicts the effect of the low-dispersion property in an inviscid 2D-vortex transport problem on a highly-skewed grid with quad elements (note that similar results were obtained on skewed triangular grids [15]).

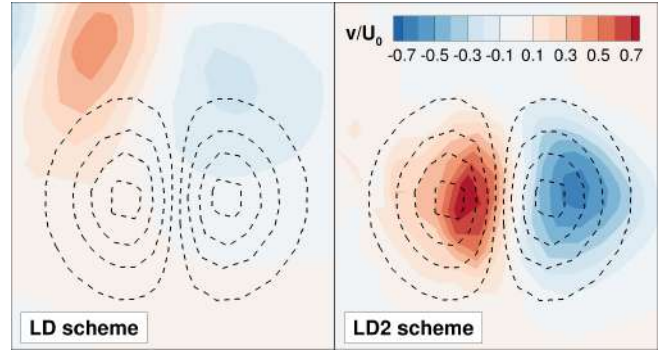


Figure 4: Inviscid vortex transport on a highly-skewed mesh (dashed lines: analytical solution)

In HRLM computations, where large parts of the domain may be coarsely resolved and modelled by RANS, it was found beneficial to apply the *LD2*-scheme in hybrid form, i.e. blending between the *LD2*-scheme in LES regions and more robust (e.g. dissipative) numerical parameters in the non-LES regions. The blending sensor for this *Hybrid LD2* (HLD2) scheme is adopted from [18] which was found to retain robustness and yet accurate results in cases, in which simulations with the globally-applied *LD2*-scheme failed [16]. Additionally, the HLD2 scheme can be controlled via manually-placed RANS/LES zones, which is particularly useful in embedded (WM-)LES simulations.

## 3 HRLM Simulations of Aeronautical Flows

The following section outlines a selection of sample applications of HRLM with the DLR-TAU code, each using at least parts of the methodologies outlined above. In particular, all simulations employ the (hybrid) *LD2* scheme, if not stated otherwise.

### 3.1 3-Element DLR-F15 Airfoil

As geometrically simple, yet relevant aeronautical flow case, we consider the high-lift airfoil DLR-F15 with deployed slat and flap (3-element configuration) close to low-speed stall ( $Ma = 0.15$ ,  $Re = 2.094 \times 10^6$ , angle of attack  $\alpha = 6^\circ$ ). Two different simulation scenarios are compared: first, a standard (*global*) SST-based IDDES with self-adapting RANS/(WM-)LES regions [16] and second, a *zonal* SST-IDDES with a manually-prescribed WM-LES region around the flap and SEM-based synthetic-turbulence injection.

In both simulations, the time-step size was chosen to resolve one convective time unit ( $CTU = c/U_0$ , with  $c$  being the retracted chord length) with 5000 time steps, yielding a convective CFL-number  $< 1$  throughout the resolved flow regions. An overall simulation time of 8 CTU (4 CTU each for initial transient and time-averaging) was found sufficient to obtain meaningful statistics.

Besides a comparative validation of both approaches w.r.t. experimental data, this study was also aimed at demonstrating the potential for grid-point savings with the embedded method. To this end, the original structured grid for the global IDDES with overall  $27 \times 10^6$  grid points was considerably coarsened outside of the embedded WM-LES region, making use of faster growing prismatic elements and spanwise adaptation. The



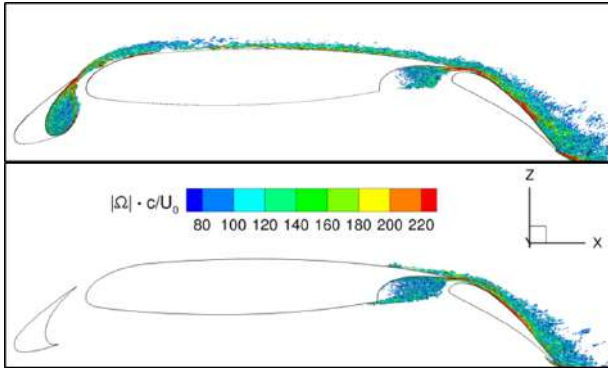


Figure 5: DLR-F15: Resolved turbulence (Q-criterion) in a global IDDES (top) and a *zonal* IDDES with synthetic turbulence injected upstream of the flap (bottom)

resulting grid-point reduction of -62% translates almost completely into computation-time savings, even though two SEM planes on both wing sides are employed.

The locations of the synthetic-turbulence injection are visible in Figure (5) (bottom), showing an instantaneous iso-surface of the Q-criterion in comparison with the global IDDES (top). Although the latter yields much larger resolved (WM-LES) flow parts, the flap shows a similar distribution and level of turbulence content in both simulations. Consequently, good agreement of relevant aerodynamic quantities, such as the mean pressure distribution in Figure (6), is obtained, showing only local deviations between the two simulation approaches and the experimental data (note that wind-tunnel corrections were applied to the measurements).

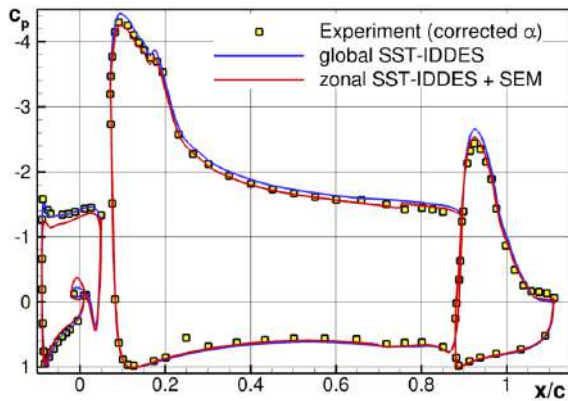


Figure 6: Pressure distributions on DLR-F15 3-element airfoil computed with global and *zonal* IDDES

### 3.2 VFE-2 Delta Wing

To assess the applicability and accuracy of the HLD2 scheme on industrial grids, SST-based DDES simulations of the delta wing from the VFE-2 experiment [19] were conducted on an unstructured (prismatic/tetrahedral) mesh with  $17.4 \times 10^6$  grid points, see [20]. At the given flow conditions ( $Re = 1 \times 10^6$ ,  $Ma = 0.07$ ,  $\alpha = 23^\circ$ ), a pair of primary longitudinal vortices is formed at the sharp leading edge, visible in Figure (7). Also depicted is the HLD2 blending parameter  $\sigma$  which correctly detects the resolved vortical flow regions to be treated with the high-resolution LD2 scheme.

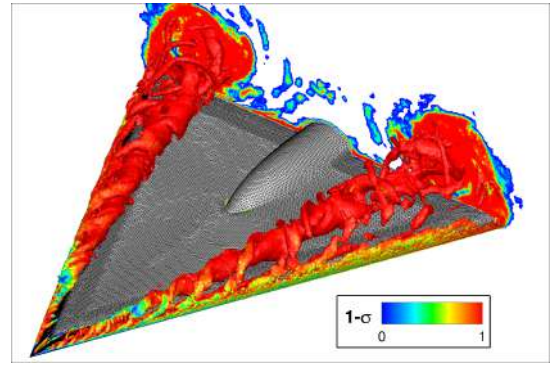


Figure 7: SST-DDES of VFE-2 delta wing: Q-criterion and slice coloured by HLD2 blending parameter

In Figure (8), time-averaged results after a total physical time of 11 CTU are compared with measurements as well as reference results from the standard (RANS) numerics. Note that the global LD2 did not run stable on this industrial grid. Both the mean and root-mean-square values of the surface pressure in selected spanwise slices are predicted in satisfying agreement with the experiment, if the HLD2 scheme is used. Moreover, a clear improvement over the reference scheme is observed.

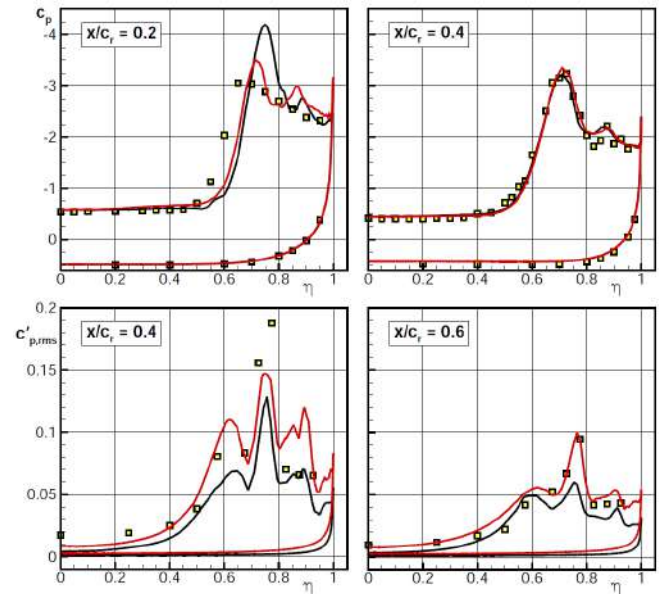


Figure 8: Spanwise mean- and RMS-pressure distributions on the delta wing [20] (symbols: experiment [19], red line: HLD2 scheme, black line: reference scheme)

### 3.3 Airfoil with Disturbed Inflow

While most applications consider statistically time-independent flows, this test case demonstrates the applicability of the presented HRLM methodology to a complex time dependent problem. Figure (9) depicts the setup: A rapidly deflected NACA0021 airfoil generates a two-dimensional lateral vortex that is convected downstream, where it interacts with a DLR-F15 airfoil in two-element configuration [21]. The moving vortex-generator airfoil is accomplished by automated grid deformation. Vortex generation and transport are modeled in RANS mode (using the SST model), which is prescribed in a

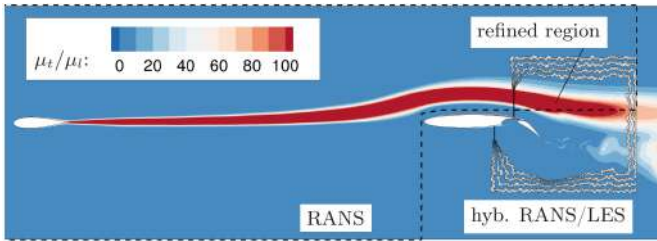


Figure 9: Test case setup for the interaction of a lateral vortex with the DLR-F15 two-element airfoil [21]

user defined region. This RANS region outlined by the dashed lines in Figure (9) is coarsely resolved in the spanwise direction and shows a higher ratio of the modeled eddy viscosity to the laminar viscosity  $\mu_t/\mu_l$ . In the region of detached flow on the flap, where the hybrid mode is active, the grid is fully refined. The algebraic HRLM sensors are applied to shield the attached RANS boundary layers and switch to the WM-LES mode at a user defined position. At this streamwise interface synthetic turbulence is added to accelerate the generation of resolved turbulent structures in the boundary layer.

Figure (10) depicts the temporal impact of the vortex on the leading-edge pressure of the two-element airfoil. In the experiments time-dependent measurements were obtained from an ensemble average over more than 80 pitch cycles. To achieve comparable time-dependent mean values from a single computation, the old mean values are biased with an exponential decay factor yielding a temporal averaging window. However, this approach leads to a certain delay in the response to the vortex in the simulation. Moreover, small inaccuracies in the overall airfoil flow lead to different vortex transport velocities, adding up to the deviation between measurement and simulation. Despite these systematic deviations, the presented HRLM approach is considered well suited to predict this kind of time-dependent vortex interaction.

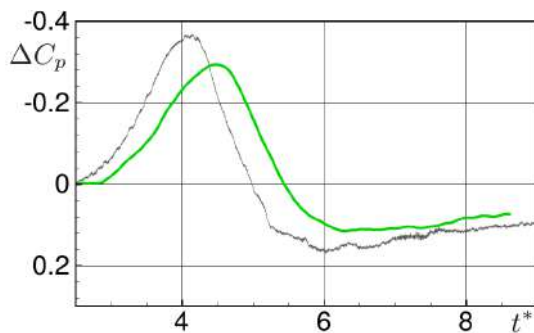


Figure 10: Influence of the lateral vortex on the pressure coefficient of the DLR-F15 two-element airfoil (grey line: experiment, green line: HRLM simulation) [21]

### 3.4 Common Research Model

The NASA Common Research Model (CRM) represents a generic transport aircraft which was experimentally studied at flight Reynolds numbers in the pressurized cryogenic European Transonic Windtunnel (ETW). Simulations using Spalart-Allmaras-based DDES were conducted at low-speed stall conditions, i.e.  $Re = 11.6 \times 10^6$ ,  $Ma = 0.25$ ,  $\alpha = 18^\circ$ , in order to assess TAU's HRLM capabilities for an industrial 3D case. A hybrid mesh of

the aircraft half model with around  $50 \times 10^6$  grid points could be directly adopted from [22]. It contains a structured block downstream of the wing to accurately resolve the wake region, which was one focus of the conducted PIV measurements. The simulations employed the hybrid LD2 scheme, along with the  $\Delta_\omega$ -filter to reduce possible anisotropy-induced grey areas.

At this angle of attack ( $\alpha = 18^\circ$ ), the flow on the wing separates close to the leading edge, yielding a large LES area with resolved turbulence between the wing and the horizontal tail plane, see Figure (11) (top). After a total simulation time of 13 CTU (based on the mean wing chord), statistical flow data was compared with a reference SA-RANS solution and ETW measurement data. Exemplarily, Figure (11) (bottom) shows vertical mean-velocity profiles at two streamwise positions in the wing wake. As compared with RANS, the DDES with TAU agrees clearly better with the experimental data, demonstrating the potential of the present HRLM methodology for complex industrial flows.

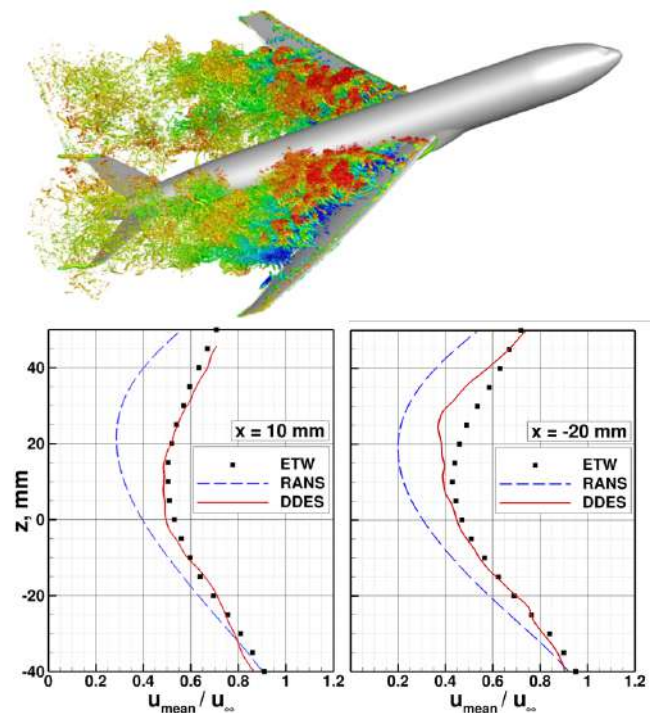


Figure 11: Common Research Model: Resolved turbulence (Q-criterion) in SA-DDES (top) and mean-velocity profiles at two positions in the wing wake (bottom)

## 4 Conclusions

The fundamentals and example applications of the hybrid RANS/LES methodologies in the DLR-TAU code for external aircraft aerodynamics have been presented. The combination of non-zonal IDDES with several modelling extensions and an unstructured low-dissipation low-dispersion numerical scheme offers a high degree of flexibility in applying HRLM to various flow problems. The good agreement with experimental data in exemplary flow cases has demonstrated the growing maturity of these methods for aeronautical applications. Future developments should focus on the automation of complex RANS/LES treatments (e.g. synthetic turbulence), the accuracy of underlying RANS approaches and increased computational efficiency.

## Acknowledgment

We thank our former colleague Dr. Marco Burnazzi, who conducted simulations of the Common Research Model.

## References

- [1] H. Choi and P. Moin, “Grid-Point Requirements for Large Eddy Simulation: Chapman’s Estimates Revisited,” *Center for Turbulence Research, Annual Research Briefs 2011*, pp. 31–36, 2011.
- [2] D. Schwamborn, T. Gerhold, and R. Heinrich, “The DLR TAU-Code: Recent Applications in Research and Industry,” *ECCOMAS CFD, P. Wesseling, E. Oñate, J. Périaux (Eds), TU Delft, The Netherlands* (M. Braza, A. Bottaro, and M. Thompson, eds.), 2006.
- [3] M. L. Shur, P. R. Spalart, M. K. Strelets, and A. K. Travin, “A Hybrid RANS-LES Approach with Delayed-DES and Wall-Modelled LES Capabilities,” *International Journal of Heat and Fluid Flow*, vol. 29, no. 6, pp. 406–417, 2008.
- [4] S. Deck, “Recent improvements in the zonal detached eddy simulation (ZDES) formulation,” *Theoretical and Computational Fluid Dynamics*, vol. 26, no. 6, pp. 523–550, 2012.
- [5] B. Eisfeld, C. Rumsey, and V. Togiti, “Verification and validation of a second-moment-closure model,” *AIAA Journal*, vol. 54, no. 5, pp. 1524–1541, 2016.
- [6] A. Probst, R. Radespiel, and T. Knopp, “Detached-Eddy Simulation of Aerodynamic Flows Using a Reynolds-Stress Background Model and Algebraic RANS / LES Sensors,” *AIAA Paper 2011-3206*, 2011.
- [7] A. Probst and S. Reuß, “Scale-Resolving Simulations of Wall-Bounded Flows with an Unstructured Compressible Flow Solver,” in *Progress in Hybrid RANS-LES Modelling. Notes on Numerical Fluid Mechanics and Multidisciplinary Design*, Springer International Publishing, vol. 130, pp. 481–491, 2015.
- [8] D. G. Francois, R. Radespiel, S. Reuss, and A. Probst, “Computations of Separated Flows with Hybrid RANS/LES Approaches,” in *Advances in Simulation of Wing and Nacelle Stall. Notes on Numerical Fluid Mechanics and Multidisciplinary Design*, vol. 131, 2015.
- [9] N. Chauvet, S. Deck, and L. Jacquin, “Zonal Detached Eddy Simulation of a Controlled Propulsive Jet,” *AIAA Journal*, vol. 45, no. 10, pp. 2458–2473, 2007.
- [10] N. Jarrin, R. Prosser, J.-C. Uribe, S. Benhamadouche, and D. Laurence, “Reconstruction of turbulent fluctuations for hybrid RANS/LES simulations using a Synthetic-Eddy Method,” *International Journal of Heat and Fluid Flow*, vol. 30, pp. 435–442, jun 2009.
- [11] M. L. Shur, P. R. Spalart, M. K. Strelets, and A. K. Travin, “Synthetic Turbulence Generators for RANS-LES Interfaces in Zonal Simulations of Aerodynamic and Aeroacoustic Problems,” *Flow Turbulence and Combustion*, vol. 93, pp. 63–92, 2014.
- [12] A. Probst, “Implementation and Assessment of the Synthetic-Eddy Method in an Unstructured Compressible Flow Solver,” in *Progress in Hybrid RANS-LES Modelling. Notes on Numerical Fluid Mechanics and Multidisciplinary Design*, Springer International Publishing, vol. 137, pp. 91–101, 2018.
- [13] A. Probst, R. Radespiel, C. Wolf, T. Knopp, and D. Schwamborn, “A Comparison of Detached-Eddy Simulation and Reynolds-Stress Modelling Applied to the Flow over a Backward-Facing Step and an Airfoil at Stall,” *AIAA Paper 2010-0920*, 2010.
- [14] M. S. Gritskevich, A. V. Garbaruk, J. Schütze, and F. R. Menter, “Development of DDES and IDDES Formulations for the  $k-\omega$  Shear Stress Transport Model,” *Flow Turbulence and Combustion*, vol. 88, no. 3, pp. 431–449, 2012.
- [15] J. Löwe, A. Probst, T. Knopp, and R. Kessler, “Low-Dissipation Low-Dispersion Second-Order Scheme for Unstructured Finite-Volume Flow Solvers,” *AIAA Journal*, vol. 54, no. 10, pp. 2961–2971, 2016.
- [16] A. Probst, J. Löwe, S. Reuß, T. Knopp, and R. Kessler, “Scale-Resolving Simulations with a Low-Dissipation Low-Dispersion Second-Order Scheme for Unstructured Flow Solvers,” *AIAA Journal*, vol. 54, no. 10, pp. 2972–2987, 2016.
- [17] J. Kok, “A High-Order Low-Dispersion Symmetry-Preserving Finite-Volume Method for Compressible Flow on Curvilinear Grids,” *J. Comp. Phys.*, vol. 228, pp. 6811–6832, oct 2009.
- [18] A. Travin, M. Shur, M. Strelets, and P. R. Spalart, “Physical and Numerical Upgrades in the Detached-Eddy Simulation of Complex Turbulent Flows,” *Advances in LES of Complex Flows*, vol. 65, no. 5, pp. 239–254, 2002.
- [19] A. Furman and C. Breitsamter, “Experimental investigations on the VFE-2 configuration at TU Munich, Germany.,” *Chapter 21 in: Understanding and Modeling Vortical Flows to Improve the Technology Readiness Level for Military Aircraft, RTO-TR-AVT-113, NATO RTO*, 2009.
- [20] A. Probst, “Scale-Resolving Simulations on Unstructured Meshes with a Low-Dissipation Low-Dispersion Scheme,” in *New Results in Numerical and Experimental Fluid Mechanics XI, Notes on Numerical Fluid Mechanics and Multidisciplinary Design 136*, pp. 489–498, Springer International Publishing, 2017.
- [21] S. Probst, “Hybrid RANS/LES Simulation Strategy for High-Lift Applications with Disturbed Inflow,” in *Progress in Hybrid RANS-LES Modelling. Notes on Numerical Fluid Mechanics and Multidisciplinary Design*, Springer International Publishing, vol. 137, pp. 103–112, 2018.
- [22] T. Lutz, P. P. Gansel, A. Waldmann, D. M. Zimmermann, and S. Schulte Am Hülse, “Prediction and measurement of the common research model wake at stall conditions,” *Journal of Aircraft*, vol. 53, pp. 501–514, 2016.

# A QUICK OVERVIEW OF THE CAPABILITIES OF ZDES

S. Deck and N. Renard

*ONERA The French Aerospace Lab, F-92190 Meudon, France*

## Abstract

This paper provides an up-to-date survey of the use of Zonal Detached Eddy Simulations (ZDES) in the frame of applied aerodynamics. The issue of zonal or non-zonal treatment of turbulent flows for engineering applications is discussed. The ZDES method used in this article and based on a fluid problem-dependent zonalization is briefly presented. Some recent landmark achievements featuring massively and thin-layer separated flows are presented. The remaining challenges including wall-turbulence simulation at high Reynolds number are also briefly discussed.

## 1 Introduction

The increasing demand for high-fidelity computational aerodynamics motivates more and more frequently unsteady turbulence modelling. Among the possible approaches, the hybrid RANS/LES paradigm is suited for the industrial needs since it combines a high degree of resolution in the zones of interest, which are treated in LES, with a cost-efficient RANS treatment of the other regions of the flow. The Zonal Detached Eddy Simulation technique (ZDES) [1] developed since 2002 enables a flexible definition of the zones of interest and has been widely validated and used for aerospace engineering applications (see e.g. [2]) as well as for academic research.

In this article, the issue for hybrid RANS-Large Eddy Simulation (LES) approaches to the zonal or non-zonal treatment of turbulent flows is first briefly discussed and the salient features of the Zonal Detached Eddy Simulation (ZDES) method are presented in §2. Some recent landmark achievements featuring massively separated flows are illustrated in §3 while some specific issues concerning the simulation of wall turbulence in the frame of Wall Modelled Large Eddy Simulation (WMLES) approaches are discussed in §4.

## 2 Turbulence modelling

### 2.1 Zonal or non-zonal treatment of turbulence?

As reminded in §1, it is now commonly acknowledged (see Haase *et al* [3]) that hybrid RANS/LES is the main strategy to drastically reduce computational cost (compared to standard WRLES) in a wide range of complex industrial applications. Despite a wide number of approaches (and acronyms!), these methods are close to one another and can often be rewritten as variants of a small group of generic approaches. In practice, these methods differ by their maturity in the sense that many have not been thoroughly validated or widely used on “real” three-dimensional configurations (see the discussions in [4, 5]). At the same time, these methods

raise the important question whether the treatment of turbulence has to be zonal or not.

Indeed, a fully automatic method (i.e. without user input) is desirable to reduce the decision load on the user but “utopian” in a near/mid-term future. In [1] Deck clearly advocates the use of a zonal treatment of turbulence to handle complex configurations, even if the decision load is increased, for several reasons:

- An automatic method (black-box push button) is not desirable (though very tempting!). Indeed, if the fully automatic model fails, the user is helpless (potential reasons for failures include complex geometries and physics on “real-life” grids).

- An automatic method can convey a misleading feeling of easiness. Even perfectly “idiot-proof” models require a significant level of expertise from the user which cannot be replaced by the computer so far (e.g. the design of an hybrid RANS/LES grid is far from being trivial).

- In the frame of wall-turbulence resolving simulations (e.g. on a whole aircraft), the activation of LES content in the TBL will be necessarily embedded in the computational domain (i.e. zonal!).

- A zonal non-automatic approach alleviates the user load during computation monitoring and post-processing since the behaviour of the model is known in advance.

It is worth stressing that a zonal approach also permits operation in an automatic mode (but the reverse is not true). Such a functionality is provided by ZDES mode 2 as will be detailed in the next section. It is worthwhile to notice that current best-practices within the hybrid RANS/LES community suggest the authors’ point of view is now increasingly shared by other teams (see for instance discussions by P. Tucker [6] and NASA [7] as well as the zonal RANS-IDDES technique [8]).

### 2.2 Zonal Detached Eddy Simulation (ZDES)

The Zonal Detached Eddy Simulation (ZDES) technique has been developed by Deck from 2002 onwards. It was first published in [9] and the complete formulation that proposes an efficient solution to prevent delay in the formation of instabilities has been more recently published in Ref. [1]. This approach takes full advantage of its zonal nature, not only to allow the user to specify RANS and LES regions, but also to make possible the use of various formulations within the same calculation (an example is provided in § 4.2).

The ZDES method aims at treating in a single model all classes of flow problems indicated in Figure (1) and typical applications associated. A hybrid length scale  $\bar{d}_{ZDES}$  entering the Spalart-Allmaras model [10] turbulence model is defined:

$$\tilde{d}_{ZDES} = \tilde{d}_{mode} \left( \tilde{\Delta}, d_w, U_{i,j}, \nu, \tilde{\nu}, \frac{\partial \tilde{\nu}}{\partial n}, \frac{\partial \|\omega\|}{\partial n} \right) \quad (1)$$

$$mode = 0, 1, 2, 3 \quad (2)$$

with  $\tilde{\Delta}$  denoting the subgrid length scale entering  $\tilde{d}_{ZDES}$  that depends on the grid cell size,  $U_{i,j}$  the velocity gradients,  $d_w$  the distance to the wall,  $\|\omega\|$  the magnitude of vorticity,  $\nu$  and  $\tilde{\nu}$  the kinematic and pseudo eddy viscosity as well as  $\partial/\partial n$  the derivative in the wall-normal direction. The definition of  $\tilde{d}_{ZDES}$  is not a minor adjustment in the DES framework since the modified lengthscales depend not only on the grid but also on the velocity and eddy viscosity fields and their wall-normal derivatives.

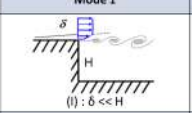
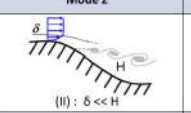
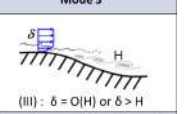
Zonal Detached Eddy Simulation (ZDES)			
	Mode 1	Mode 2	Mode 3
Flow category			
Applications	Base flow, free shear flows, spoilers, steps, slat/flap cove, etc.	Buffet, flaps, duct flows, nacelle intake, etc.	Corner flows, turbulent boundary layer, separation onset on high lift devices, shallow separations, etc.

Figure 1: Classification of typical flow problems, associated ZDES modes and examples of applications. *mode 1*: separation fixed by the geometry, *mode 2*: separation induced by a pressure gradient on a curved surface, *mode 3*: separation strongly influenced by the dynamics of the incoming boundary layer. RANS (*mode 0*) is the default mode (adapted from Deck[1])

Thus, ZDES offers an attractive flexibility in the treatment of turbulent flows in technical applications and has been applied extensively with good results over a range of Mach numbers and configurations as will be illustrated in the following.

## 3 Simulation of massively separated flows

### 3.1 Mode 1

Many applications are concerned with massively separated flows as is the flow in the base region of a space launcher. ZDES is well adapted to simulate massively separated flows which rapidly develop strong instabilities overwhelming the turbulence inherited from upstream boundary layers. Within ZDES mode 1[1], the issue of slow delay in the formation of instabilities has been solved by using a subgrid length that depends not only on the grid but also on the velocity field (see [11]). As reminded earlier, a modern challenge lies in the taking into account of geometrical complexity without spoiling the quality of the results provided by a proven and effective numerical approach. To solve complex flows around realistic configurations in applied aerodynamics, a coupled approach between IBC (Immersed Boundary Conditions) and ZDES is proposed in [12]. This methodology is applied to a full space launcher configuration to assess its capability to return the interactions between the technological details, modeled with IBC, and the simplified afterbody, modeled with a body-fitted (BF) approach consisting in classical no-slip boundary conditions, in the turbulent flow field surrounding the main stage of

the space launcher afterbody. The considered configuration is a full Ariane 5 model with a 1:60 subscale ratio tested in NLR's DNW-HST facility ( $M_0 = 0.8$ ;  $Re_D = 1.18 \times 10^6$ ). The Z-shape sting holding the model in the wind tunnel is also taken into account in order for the simulation to be representative of the experiment [13].

Figure (2) displays the salient features of the turbulent field over the massively separated flow by showing an iso-surface of the Q criterion colored by the streamwise velocity. The several technological devices (DAAR ring, asymmetric struts, helium sphere, etc.) characterizing the afterbody of the Ariane 5 space launcher are taken into account *via* a zonal IBC approach. Indeed, the design of a classical body-fitted structured ZDES grid around such a complex configuration is quite impossible. Besides, this figure also shows that both mean and fluctuating pressure fields are well assessed with this methodology.

More generally, in [12] the authors argued that combining the IBC method in a zonal manner on a structured grid constitutes a serious and valuable alternative to unstructured mesh strategies in a hybrid RANS/LES framework since this preserves the robustness and accuracy of the time-honoured structured grid methods which are strongly validated.

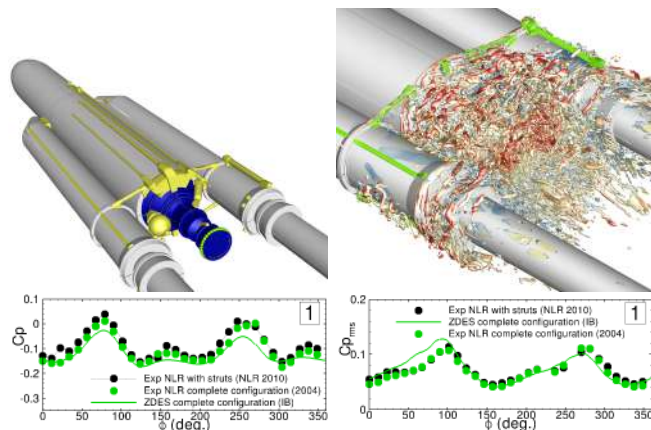


Figure 2: Comparison of the unsteady quantities of interest between NLR's experiments and ONERA's ZDES/IBC. **Top left:** Geometry of the full launcher with technological details (yellow), surface used for side-load integration (blue) and ring on the nozzle used to plot  $C_p$  and  $C_{p_{rms}}$  evolutions (green). **Top right:** Visualization of Q criterion showing the coherent structures ( $Q.D^2/U_\infty^2 = 200$ ) in the afterbody flow region. **Bottom left:** Azimuthal evolution of  $C_p$  at the end of the nozzle. **Bottom right:** Azimuthal evolution of  $C_{p_{rms}}$  at the end of the nozzle. NLR's experiments on Ariane 5 complete configuration (green symbols), NLR's experiments on Ariane 5 with struts linking the main stage to the boosters only (black symbols), ONERA's ZDES/IBC on Ariane 5 complete configuration (green solid lines). Grid details: ( $N_{xyz} = 75 \times 10^6$ , azimuthal refinement:  $\Delta\phi = 1^\circ$ ). Adapted from [12]

### 3.2 Mode 2

ZDES also provides an "automatic" operating option (referred to as mode 2 in the following) for which the switch between RANS and LES regions is dynamically set by the model itself. As an example, mode 2 is retained when the location of separation is not known in advance *i.e.* when it is induced by a pressure gradient.

In practice two main issues arise in any “DES-type” methods. The first one concerns an insufficient protection of the attached boundary layer region on fine grids (*i.e.* when  $C_{DES}\Delta < \delta$ ), while the second one concerns a possible delay in the formation of “LES-content” in free shear layers. While the standard  $f_d$  function entering standard DDES [14] fails for fine meshes (typically when  $C_{DES}\Delta < 0.3\delta$ ) and/or with adverse pressure gradients, the authors [15] have recently proposed a robust ZDES mode 2 mitigating the two aforementioned issues.

A highly challenging and difficult case for hybrid RANS/LES methods is the numerical simulation of transonic buffet because it presents a thin-layer separation that moves significantly in time at a time-scale that is much much slower than the one of the wall-bounded turbulence. The test case retained here is the supercritical airfoil OAT15A in the same flow conditions as in the experiment of Jacquin *et al.* [16] ( $Re_c = 3 \times 10^6$ ,  $M_0 = 0.73$ ,  $\alpha = 3.5^\circ$ ). The salient features of the instantaneous flow field are highlighted by figure 3(a), which shows the isosurface of the Q criterion colored by the streamwise velocity component and  $P/P_0 = 0.57$  isosurface to mark the shock location. The location of the shock is evidenced by plotting an iso-surface of pressure. One can first note that no resolved turbulent content can be seen in the flow upstream of the shock as this boundary layer is treated in URANS mode within ZDES mode 2. Downstream of separation, ZDES mode 2 switches rapidly in its scale resolving mode as no delay in the LES content formation can be depicted. The power spectral densities for two characteristic sensors located respectively on the lower and on the upper side of the airfoil are compared with the experiment in figure 3(b). The first sensor is located at the upper side close to the trailing edge at  $x/c = 0.9$ . The periodic nature of the large-scale self-sustained motion of the shock is evidenced by the strong harmonic peaks in the spectra. On the experimental side, the main peak is at  $69\text{ Hz}$  (or  $f_c/U_0 = 0.065$ ) and is very well reproduced by the present calculations together with the broad-banded spectral distribution at higher frequencies. The second sensor is located at the lower-side of the airfoil where ZDES mode 2 operates in URANS mode owing to its design so that only the high amplitude and low frequency fluctuations can be captured by the calculation.

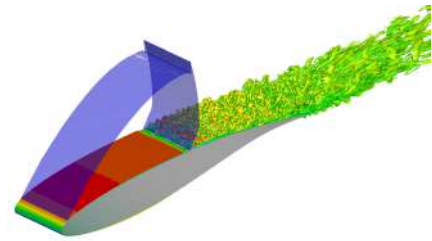
Another example is provided in Figure (4) where a complete aircraft at full scale 1:1 in true flight conditions ( $Re_{AMC} = 50.10^6$ ) is simulated with a focus on the jet flow for an affordable CPU cost since the grid size could be limited to  $200.10^6$  points thanks to the skillfull combination of ZDES together with the Chimera technique.

The new ZDES mode 2[15] can be considered as a case-independent answer to the demand for a general automatic and robust RANS/LES treatment of attached and massively separated flows.

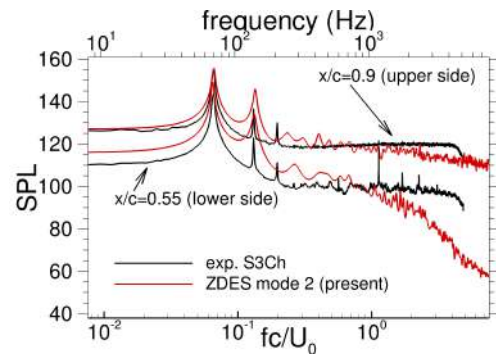
## 4 Towards wall turbulence simulation

### 4.1 High Reynolds number turbulent boundary layer

Boundary layers spatially developing at high Reynolds numbers are ubiquitous in engineering and geophysical flows. Consequently, wall-bounded turbulence plays a



(a) Isosurface of the Q criterion  $Q = 40 \left(\frac{U_0}{c}\right)^2$  colored by the streamwise velocity component and  $P/P_0 = 0.57$  isosurface to mark the shock location



(b) PSD of pressure fluctuations at the lower and upper sides of the airfoil  $SPL = 20 \log_{10} \left( \sqrt{G(f)} / 2.10^{-5} \right)$

Figure 3: ZDES mode 2 of the flow around the OAT15A airfoil in transonic buffet condition. Grid details:  $N_{xyz} = 58 \times 10^6$ ,  $N_z = 148$ ,  $L_z/c = 0.2$ . Adapted from [15]

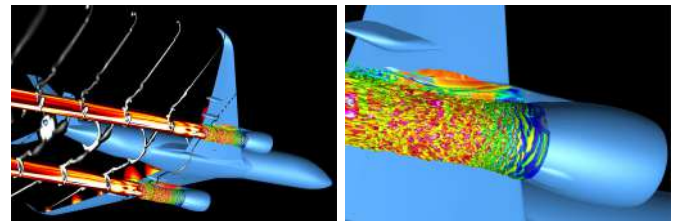


Figure 4: ZDES of the flow around a complete aircraft at scale 1:1 in true flight conditions, with focus on the jet development ( $Re_{AMC} = 50.10^6$ ,  $M = 0.8$ ,  $200.10^6$  points). Mode 2 is used for the whole computational domain. The grid size has been limited to  $200.10^6$  points thanks to the Chimera technique which allows the use of a fine mesh only where it is necessary, namely in the jet development area. Adapted from [2]

key role in many applications, especially because of its impact on friction drag, adverse-pressure-gradient response and incipient flow separation. A RANS averaged description may be insufficient in such cases because of the influence of the turbulent fluctuations from an incoming thick boundary layer on the dynamics of a mild flow separation, but also because of the RANS modelling limitations in presence of strong pressure gradients. Besides, some applications such as aeroacoustic or unsteady load predictions require the explicit resolution of turbulent fluctuations. ZDES mode 3 is devoted to zones where turbulence should be resolved inside attached boundary layers. Turbulence in the outer layer is LES-resolved whereas a near-wall RANS zone plays the role of wall model. With a recommended RANS/LES

interface location near  $d_w = 0.1 \delta_{99}$ , mode 3 becomes the Wall-Modelled LES branch of ZDES [17] with a significant computational cost saving at high Reynolds numbers compared with a Wall-Resolved LES as illustrated in Figure (5). Furthermore, the capacity of ZDES mode 3 to perform as WRLES has also been validated [18, 19]. The resolved fields in WRLES (fine mesh) and WMLES (coarser mesh) are compared in Figure (6) together with the interpolation of the WRLES field on the WMLES grid (showing the best that may be expected from the WMLES simulation). This illustrates the overall good performance of the WMLES use of ZDES.

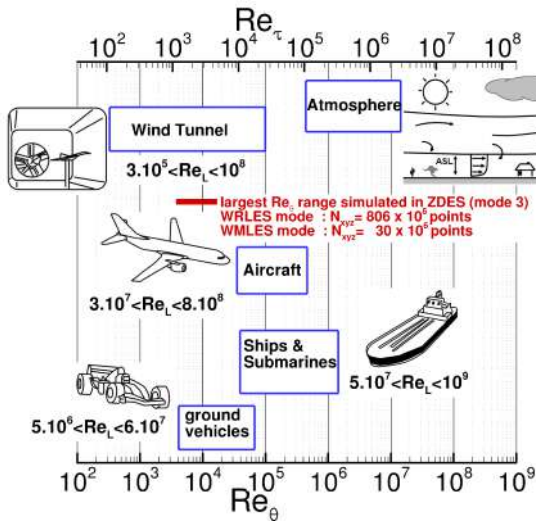


Figure 5: Typical Reynolds numbers in boundary layer applications.  $Re_L$  and  $Re_\tau$  denote the Reynolds numbers based on the streamwise characteristic length and momentum thickness, respectively.  $Re_\tau$  denotes the friction Reynolds number. ASL: Atmospheric Surface Layer; PBL: Planetary Boundary Layer. The largest wall turbulence simulation performed with ZDES (both in WMLES [17] and WRLES[19] operating modes) to date is emphasized along with the corresponding grid size. Note that the Reynolds number range achieved corresponds to the one commonly observed in sub-scale wind tunnels and that the use of WMLES allows a CPU cost reduction factor close to 30 compared to a complete WRLES simulation. Adapted from Deck *et al* [19]

The last evolutions of the RANS/LES interface treatment (outer-scaled positioning and smooth interface function) enable an accurate prediction of mean skin friction within a 5 % error margin [17, 20]. The ZDES technique has been used together with theoretical developments in order to better understand the dynamics of wall-bounded turbulence at high Reynolds numbers, which is an active field of academic research with a wide scope of practical applications (Figure (5)) and relatively recent discoveries such as superstructures [21]. The respective contributions of resolved and modelled turbulence to mean skin friction have been investigated with a focus on the role of the largest scales, leading to a new physical decomposition [19, 22]. Further refinements of the physical analysis have been introduced focusing on the scale dependence of the convection velocity of the velocity fluctuations [23]. These studies have confirmed the dominant role played by the production of turbulent kinetic energy in the logarithmic layer at high Reynolds numbers which ZDES mode 3 aims to resolve (at least partially) in order to attain a higher degree of universality than provided by RANS modelling.

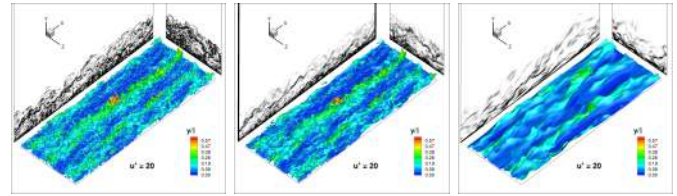
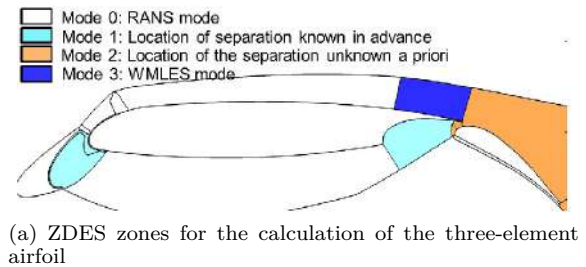
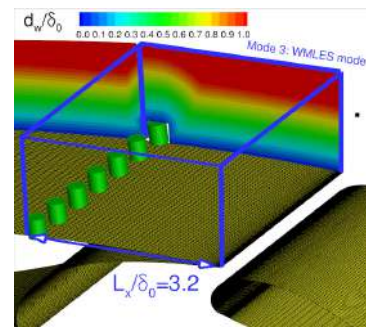


Figure 6: ZDES mode 3 simulations of a zero pressure gradient flat plate turbulent boundary layer. Iso-surface of the streamwise velocity  $u^+ = 20$  coloured by the wall distance  $y/\delta$ , near  $Re_\theta = 13\,000$ , and numerical Schlieren (density gradient magnitude). Left: fine mesh ( $\Delta x = 50^+ / \Delta z = 12^+$ ) WRLES ZDES; Center: Fine mesh ( $50^+ / 12^+$ ) WRLES ZDES interpolated on the WMLES ( $200^+ / 100^+$ ) mesh; Right: WMLES mesh ( $200^+ / 100^+$ ) ZDES,  $y_{interface} = 0.1\delta$



(a) ZDES zones for the calculation of the three-element airfoil



(b) Roughness elements in the WMLES domain

Figure 7: Computational description.  $d_w/\delta_0$  is the normalized distance to the wall where  $\delta_0$  is the boundary thickness at the inlet domain. Adapted from [24]

## 4.2 Low noise turbulent generation

For WMLES of fully turbulent boundary layers, resolved turbulence must be injected into the flow. This means that the ZDES mode 3 technique is used in conjunction with a turbulent injection method. However, in many applications involving compressible flows, the acoustic footprint of this injection may be problematic since the acoustic waves are important and must be predicted accurately at the boundaries and in the interior, especially for aeroacoustic studies.

In [24], the authors present a turbulent inflow for a rapid and low noise switch from RANS to Wall-Modelled LES on curvilinear grids with compressible flow solvers. The new approach relies on roughness elements described as immersed boundaries (ZIBC, Zonal Immersed Boundary Conditions as described in [12]) whose length scales are selected in order to disturb the boundary layer profile and generate large scale vorticity. The fluctuations are then enhanced by a dynamic forcing approach (inspired by Spille-Kohoff & Kaltenbach [25] and adapted to ZDES by [26, 27]), enabling a quick transition from the vorticity generated by the roughness to fully devel-

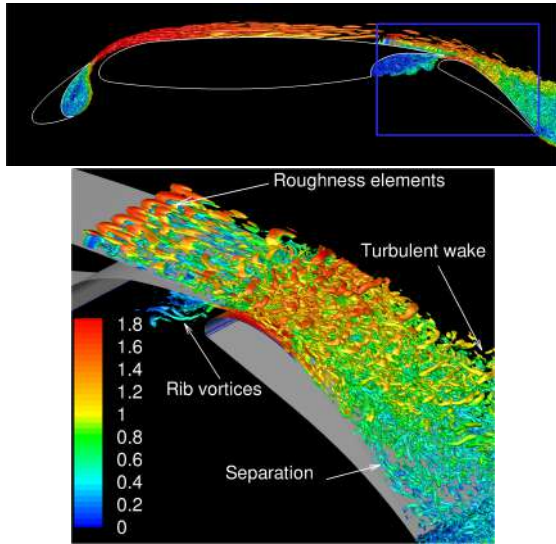


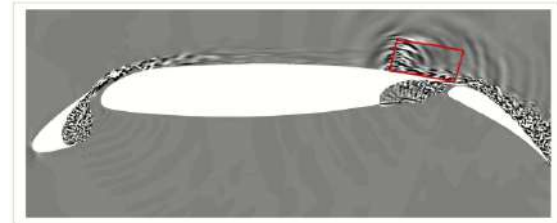
Figure 8: Isosurface of the  $Q$  criterion coloured by the velocity magnitude  $\|\mathbf{u}\|/U_0$  in the flap area (top view:  $Q \frac{c^2}{U_0^2} = 100$ ; zoom:  $Q \frac{c^2}{U_0^2} = 3000$ ). Adapted from [24]

oped realistic turbulence.

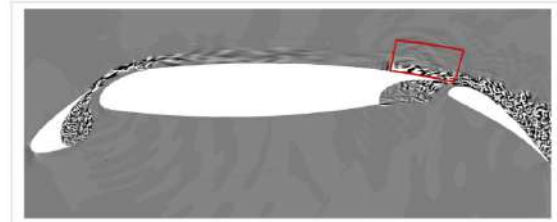
The robustness of the method is tested in the flow around a three-element airfoil with WMLES in the upper boundary layer near the trailing edge of the main element. The proposed modelling methodology has been assessed on the LEISA three-element airfoil designed by DLR[28] for flow conditions corresponding to aircraft approach. The chord Reynolds number is  $Re_c = \frac{U_0 c}{\nu} = 2.09 \times 10^6$  (with  $U_0 = 51 \text{ m.s}^{-1}$  and  $c = 0.6 \text{ m}$ ). In addition, the streamwise (respectively spanwise) grid resolution is  $\Delta x/\delta_0 = 0.086$  (respectively  $\Delta z/\delta_0 = 0.026$ ) corresponding to  $\Delta x^+ = 250$  (respectively  $\Delta z^+ = 75$ ) when expressed in inner scales. Note also that the computational domain length where mode 3 is retained (see figure 7(a)) is  $L_x/\delta_0 = 3.2$  making the WMLES very challenging and thus permits to assess the efficiency of the proposed methodology.

The salient features of the instantaneous flow field are highlighted in Figure (8). The flow in the slat cove displays a large recirculation bubble bounded by a shear layer emanating from the slat cusp and reattaching near the slat trailing edge. Similarly, the flap cove also behaves like a shallow cavity. In spite of the very short relaxation distance allowed, self-sustainable resolved turbulence is generated in the outer layer in the ZDES mode 3 zone with significantly less spurious noise than with an approach involving White Noise instead of ZIBC roughness elements. Both approaches are compared in Figure (9), showing the instantaneous  $-\frac{1}{\rho} \frac{\partial \rho}{\partial t}$  field so that both sound waves and turbulent flow regions are evidenced. The contamination from the white noise application is clearly visible since nearly spherical waves can be seen from the region very near the RANS (mode 0 domain) to WMLES (mode 3 domain) transition (see figure 9(a)). These waves appear to have their highest amplitude near the inlet boundary but contaminate the whole pressure field as discussed in [27]. Conversely, the calculation based on the immersed roughness elements induces significantly less spurious noise at the inlet (see figure 9(b)) since the use of non-moving obstacles has the great advantage of being steady and produces less spurious noise than the inflow method based on the introduction of random velocity fluctuations. Note also that the

ZDES grid count for this latter test case is more than two orders of magnitude lower than the Wall-Resolved LES requirement [29] and a unique mesh is involved, which is much simpler than some multiple-mesh strategies devised for WMLES or turbulent inflow.



(a) ZDES mode 3 - anisotropic White Noise - Dynamic Forcing



(b) ZDES mode 3 - ZIBC - Dynamic Forcing

Figure 9: Instantaneous field of  $-\frac{1}{\rho} \frac{\partial \rho}{\partial t}$ . Grid details:  $N_{xyz} = 50 \times 10^6$ ,  $N_z = 128$ ,  $L_z/c = 0.16$ . Adapted from [24]

## 5 Conclusion

The debate concerning the zonal/non-zonal treatment of turbulence is useful and the authors think that both zonal and non-zonal methods will probably grow because both are needed and one may expect that the next improvements of both approaches of turbulence modelling should be mutually beneficial.

The versatility of ZDES lies in its capability to be used not only in an industrial framework as argued above, but also for academic research. Among the next foreseen challenges in applied numerical aerodynamics, one may cite the capture of the boundary layer dynamics including transition and pressure-gradient-driven separation issues.

## Acknowledgment

The authors are very grateful to their colleagues Pierre-Elie Weiss & Fabien Gand who provided some numerical results shown in this paper.

## References

- [1] S. Deck, "Recent improvements of the Zonal Detached Eddy Simulation (ZDES) formulation.," *Theoretical and Computational Fluid Dynamics*, 26 (6), pp 523–550, doi: 10.1007/s00162-011-0240-z, 2012.
- [2] S. Deck, F. Gand, V. Brunet, and S. Ben Khelil, "High-fidelity simulations of unsteady civil aircraft aerodynamics: stakes and perspectives. Application of zonal detached eddy simulation.,"



- Phil. Trans. R. Soc. A.*, 372: 20130325, (doi: 10.1098/rsta.2013.0325), 2014.
- [3] W. Haase, M. Braza, and A. Revell, “DESider - A European Effort on Hybrid RANS-LES Modelling,” *Notes on Numerical Fluid Mechanics and Multidisciplinary Design*, Vol. 103. Springer, 2009.
- [4] P. Sagaut, S. Deck, and M. Terracol, “Multiscale and multiresolution approaches in turbulence- LES, DES and hybrid RANS/LES methods: applications and guidelines (2nd Edition),” *Imperial College Press, London, UK*, 448 pages, 2013.
- [5] P. Tucker, “Unsteady computational fluid dynamics in aeronautics,” *Springer*, 2013.
- [6] P. Tucker, R. Jefferson-Loveday, J. Tyacke, and V. Rao, “Zonal RANS-LES modeling for turbines in aeroengines,” *Computational Thermal Sciences*, vol. 4, pp. 1–12, 01 2012.
- [7] G.-D. Stich, J. Housman, J. Kocheemoolayil, M. Barad, and C. Kiris, “Application of Lattice Boltzmann and Navier-Stokes Methods to NASA’s Wall Mounted Hump, AIAA paper 2018-3855,” 2018.
- [8] M. L. Shur, P. R. Spalart, M. K. Strelets, and A. K. Travin, “Synthetic turbulence generators for RANS-LES interfaces in zonal simulations of aerodynamic and aeroacoustic problems,” *Flow Turbulence and Combustion*, vol. 93, pp. 63–92, 2014.
- [9] S. Deck, “Zonal-Detached Eddy Simulation of the flow around a high-lift configuration,” *AIAA Journal*, vol 43., No. 11, pp 2372-2384, 2005.
- [10] P. Spalart and S. Allmaras, “A one equation turbulence model for aerodynamic flows,” *La Recherche Aérospatiale*, vol 1., pp 5-21, Jan., 1994.
- [11] N. Chauvet, S. Deck, and L. Jacquin, “Zonal-Detached-Eddy Simulation of a Controlled Propulsive Jet,” *AIAA J.*, vol 45, No. 10, pp 2458-2473, 2007.
- [12] P. Weiss and S. Deck, “On the coupling of a zonal body-fitted/immersed boundary method with ZDES: application to the interactions on a realistic space launcher afterbody flow,” *Computers & Fluids*, vol 176, pp 338-352, doi:10.1016/j.compfluid.2017.06.015, 2017.
- [13] E. Geurts, “Steady and unsteady pressure measurements on the rear section of various configurations of the Ariane 5 launch vehicle,” *6th International Symposium on Launcher Technologies, Munich, Germany, November*, 2005.
- [14] P. Spalart, S. Deck, M. Shur, K. Squires, M. Strelets, and A. Travin, “A new version of Detached-Eddy Simulation, resistant to ambiguous grid densities,” *Theoretical and Computational Fluid Dynamics*, Vol. 20, pp 181-195, July 2006, 2006.
- [15] S. Deck and N. Renard, “Towards an enhanced protection of attached boundary layers in hybrid RANS/LES methods,” *Journal of Computational Physics*, doi=10.1016/j.jcp.2019.108970, 2019.
- [16] L. Jacquin, P. Molton, S. Deck, and D. Soulevant, “Experimental study of shock oscillation over a transonic supercritical profile,” *AIAA J.*, vol. 47, no. 9, pp. 1985–1994, 2009.
- [17] S. Deck, N. Renard, R. Laraufie, and P. Sagaut, “Zonal Detached Eddy Simulation (ZDES) of a spatially developing flat plate turbulent boundary layer over the Reynolds number range  $3150 < Re_\theta < 14000$ ,” *Physics of Fluids*, vol. 26, no. 2, p. 025116, 2014, doi: 10.1063/1.4866180.
- [18] S. Deck, P. Weiss, M. Pamiès, and E. Garnier, “Zonal Detached Eddy Simulation of a spatially developing flat plate turbulent boundary layer,” *Computer & Fluids*, vol 48, pp 1-15, doi:10.1016/j.compfluid.2011.03.09, 2011.
- [19] S. Deck, N. Renard, R. Laraufie, and P. Weiss, “Large scale contribution to mean wall shear stress in high Reynolds number flat plate boundary layers up to  $Re_\theta = 13650$ ,” *Journal of Fluid Mechanics*, vol. 743, pp. 202–248, 2014.
- [20] N. Renard and S. Deck, “Improvements in zonal detached eddy simulation for wall modeled large eddy simulation,” *AIAA J.*, Vol. 53, No. 11, pp 3499-3503, 2015.
- [21] A. Smits, B. McKeon, and I. Marusic, “High Reynolds number wall turbulence,” *Annual Review of Fluid Mechanics*, vol. 43, no. 1, pp. 353–375, 2011, doi: 10.1146/annurev-fluid-122109-160753.
- [22] N. Renard and S. Deck, “A theoretical decomposition of mean skin friction generation into physical phenomena across the boundary layer,” *Journal of Fluid Mechanics*, vol. 790, pp. 339–367, 2016.
- [23] N. Renard and S. Deck, “On the scale-dependent turbulent convection velocity in a spatially developing flat plate turbulent boundary layer at Reynolds number  $Re_\theta = 13000$ ,” *Journal of Fluid Mechanics*, vol. 775, pp. 115–148, 2015.
- [24] S. Deck, P.-E. Weiss, and N. Renard, “A rapid and low noise switch from RANS to WMLES on curvilinear grids with compressible flow solvers,” *Journal of Computational Physics*, vol. 363, pp. 231–255, 2018.
- [25] A. Spille-Kohoff and H. Kaltenbach, “Generation of turbulent inflow data with a described shear-stress profile,” *In Proceedings pp 137-147, third AFOSR Int. Conf. on DNS/LES, Arlington, edited by C.Liu, L. Sakell and T. Beutner, Greyden press, Columbus, OH, 5-9 August*, 2001.
- [26] R. Laraufie, S. Deck, and P. Sagaut, “A dynamic forcing method for unsteady turbulent inflow conditions,” *Journal of Computational Physics*, vol. 230, pp 8647-8663, doi 10.1016/j.jcp.2011.08.012, 2011.
- [27] S. Deck and R. Laraufie, “Numerical investigation of the flow dynamics past a three-element aerofoil,” *Journal of Fluid Mechanics*, vol. 732, pp. 401–444, 2013. doi: 10.1017/jfm.2013.363.
- [28] J. Wild, M. Pott-Pollenske, and B. Nagel, “An integrated design approach for low noise exposing high-lift devices,” *AIAA Paper 2006-2843*, 2006.
- [29] M. Terracol and E. Manoha, “Wall-resolved Large Eddy Simulation of a Three-Element High-Lift Airfoil,” *AIAA J.*, to appear, 2019.

# MATHEMATICAL FRAMEWORK OF THE PITM METHOD FOR THE SIMULATION OF TURBULENT FLOWS

B. Chaouat<sup>1</sup> and R. Schiestel<sup>2</sup>

<sup>1</sup> ONERA, Université Paris-Saclay, 92322 Châtillon, France

<sup>2</sup> IRPHE, 13384, Marseille, France.

## Abstract

We present the mathematical framework of the PITM method in the spectral space of wave numbers from a physical standpoint. This framework is then used to develop subfilter turbulence models accounting for the main physical process such as production, dissipation and transfer of turbulence energy. Then, we present briefly several flows encountered in engineering applications to show that the PITM method gains interest not only from a theoretical point of view but also from a practical point of view for users involved in CFD.

## 1 Background and rationale

Different methods have been developed in the past fifty years for simulating turbulent flows [1, 2]. On the one hand, the direct numerical simulation (DNS) is obviously the best tool to consider but it is out of reach up to present day for practical complex applications, even if using supercomputers. Large eddy simulation (LES) is a promising method but still remains also extremely costly in computer resources at large Reynolds numbers [3]. On the other hand, the Reynolds Averaged Navier-Stokes (RANS) method works relatively well for quasi-steady flows in the mean [4] but shows however some weaknesses in capturing the large scale turbulent eddies [5]. To overcome these difficulties, researchers have developed hybrid RANS/LES methods in the past two-decade to simulate industrial flows on coarse grids with acceptable computer resources. These main schools of hybrid RANS/LES modelling [6] are the very large eddy simulation (VLES) [7], detached eddy simulation (DES) [8], partially integrated transport modelling (PITM) [9, 10, 11], partially averaged Navier-Stokes (PANS) [12] and scale adaptive approach (SAS) [13]. Contrarily to zonal hybrid models often based on empirical techniques with the overwhelming problems caused by the so-called gray zone, the PITM method [9, 10, 11], gains a major interest both from a theoretical and practical point of view because it bridges the RANS and LES methodologies with seamless coupling and allows to perform numerical simulations of turbulent flows out of spectral equilibrium on relatively coarse grids. In this present work, we will focus on the mathematical framework of the PITM method developed in the spectral space [14] and we will briefly present some cases of application to complex flows [15].

## 2 The PITM method

### 2.1 Filtering process

In RANS methodology, each variable  $\phi$  can be decomposed into a statistical part  $\langle\phi\rangle$  and a fluctuating part

$\phi'$  such that  $\phi = \langle\phi\rangle + \phi'$  whereas in large eddy simulation, the variable  $\phi$  is decomposed into a large scale (or resolved part)  $\bar{\phi}$  and a subfilter-scale fluctuating part  $\phi^>$  or modeled part such that  $\phi = \bar{\phi} + \phi^>$ . The instantaneous fluctuation  $\phi'$  contains the large scale fluctuating part  $\phi^<$  and the small scale fluctuating part  $\phi^>$  such that  $\phi' = \phi^< + \phi^>$ . The filtered variable  $\bar{\phi}$  is defined by the filtering operation as the convolution with a filter  $G$  in space  $\bar{\phi} = G * \phi$  that leads to the computation of a variable convolution integral

$$\bar{\phi}(\mathbf{x}, t) = \int_{\Omega} G[\mathbf{x} - \boldsymbol{\xi}, \Delta(\mathbf{x}, t)] \phi(\boldsymbol{\xi}, t) d\boldsymbol{\xi} \quad (1)$$

where in this expression,  $\Delta$  denotes the filter-width that varies in time and space and  $\Omega$  denotes the flow domain. Obviously, the properties of the filtering operator are different from those of the statistical averaging process so that there is no direct connection between the averaged field in a statistical sense and the filtered field in LES. All these difficulties may disappear if considering the tangent homogeneous anisotropic turbulence field at the physical space location  $\mathbf{X}$  within the nonhomogeneous field [14]. In this framework, the variation of the mean velocities  $u_k$  is accounted for by the use of Taylor series expansion in space limited to the linear terms such that  $\langle u_k \rangle(\mathbf{X}_m + \boldsymbol{\xi}_m) = \langle u_k \rangle(\mathbf{X}_m) + \Lambda_{kj} \xi_j$  where  $\Lambda_{kj}$  is a constant tensor and we recover the interesting property establishing the link between the RANS and LES methodologies [14, 17]

$$\overline{\langle u_k \rangle}(\mathbf{X}_m + \boldsymbol{\xi}_m) = \langle u_k \rangle(\mathbf{X}_m) \quad (2)$$

Strictly speaking,  $\overline{\langle\bar{\phi}\rangle} = \langle\bar{\phi}\rangle = \langle\phi\rangle$  stands only in the tangent homogeneous space. In practice however, one can assume that  $\langle\bar{\phi}\rangle \approx \langle\phi\rangle$  if the variation of the flow velocities over the filter width is not too large.

### 2.2 Basic equations in the spectral space

#### 2.2.1 Turbulent velocity fields

The PITM method finds its physical foundation in the spectral space of wave vectors [14]. The theory deals with the dynamic equation of the two-point fluctuating velocity correlations in their extensions to nonhomogeneous turbulence. By using the Fourier transform given by

$$\hat{\phi}(\mathbf{X}, \boldsymbol{\kappa}) = \int \phi(\mathbf{X}, \boldsymbol{\xi}) \exp(-j\boldsymbol{\kappa}\boldsymbol{\xi}) d\boldsymbol{\xi} \quad (3)$$

and performing averaging on spherical shells on the dynamic equation defined as [16]

$$[\phi(\mathbf{X})]^{\Delta}(\boldsymbol{\kappa}) = \frac{1}{A(\boldsymbol{\kappa})} \oint_{A(\boldsymbol{\kappa})} \hat{\phi}(\mathbf{X}, \boldsymbol{\kappa}) dA(\boldsymbol{\kappa}) \quad (4)$$

where  $A(\kappa)$  denotes the spherical shell of radius  $\kappa$ , it is then possible to derive the evolution equation of the spectral velocity correlation tensor in one-dimensional spectral space accounting for the spectral terms of transfer, production and dissipation that play a crucial role in PITM. As a result, the transport equation of the spherical average of the Fourier transform of the two-point correlation tensor  $\varphi_{ij}(\mathbf{X}, \kappa) = \langle u'_i u'_j(\mathbf{X}) \rangle^\Delta(\kappa)$  reads [14]

$$\frac{\partial \varphi_{ij}(\mathbf{X}, \kappa)}{\partial t} + \langle u_k \rangle(\mathbf{X}) \frac{\partial \varphi_{ij}(\mathbf{X}, \kappa)}{\partial X_k} = \mathcal{P}_{ij}(\mathbf{X}, \kappa) + \mathcal{T}_{ij}(\mathbf{X}, \kappa) + \Psi_{ij}(\mathbf{X}, \kappa) + \mathcal{J}_{ij}(\mathbf{X}, \kappa) - \mathcal{E}_{ij}(\mathbf{X}, \kappa) \quad (5)$$

where in this equation, the function  $\varphi_{ij}$  denotes the spherical mean of the Fourier transform of the two-point velocity correlation tensor,  $\mathcal{P}_{ij}$  represents the production term,  $\mathcal{T}_{ij}$  is the total transfer term,  $\Psi_{ij}$  is the redistribution term,  $\mathcal{J}_{ij}$  embodies all the diffusion like terms, and  $\mathcal{E}_{ij}$  denotes the stress dissipation rate,  $\mathbf{X}$  is located midway between the two points and  $\kappa$  is the wave number. In particular, the production term  $\mathcal{P}_{ij}$  is given by

$$\mathcal{P}_{ij}(\mathbf{X}, \kappa) = -\varphi_{ik}(\mathbf{X}, \kappa) \frac{\partial \langle u_j \rangle}{\partial X_k} - \varphi_{jk}(\mathbf{X}, \kappa) \frac{\partial \langle u_i \rangle}{\partial X_k} \quad (6)$$

and the dissipation term  $\mathcal{E}_{ij}$  is defined by

$$\mathcal{E}_{ij}(\mathbf{X}, \kappa) = \frac{\nu}{2} \frac{\partial^2 \varphi_{ij}(\mathbf{X}, \kappa)}{\partial X_l \partial X_l} + 2\nu \kappa^2 \varphi_{ij}(\mathbf{X}, \kappa) \quad (7)$$

where  $\nu$  stands for the molecular viscosity. The equation for the turbulence energy spectrum  $E = \varphi_{jj}/2$  is simply obtained by tensorial contraction of (Eq. (5)) leading to

$$\frac{\partial E(\mathbf{X}, \kappa)}{\partial t} + \langle u_i \rangle(\mathbf{X}) \frac{\partial E_{ij}(\mathbf{X}, \kappa)}{\partial X_j} = \mathcal{P}(\mathbf{X}, \kappa) + \mathcal{T}(\mathbf{X}, \kappa) + \mathcal{J}(\mathbf{X}, \kappa) - \mathcal{E}(\mathbf{X}, \kappa) \quad (8)$$

where  $\mathcal{P} = \mathcal{P}_{mm}/2$ ,  $\mathcal{T} = \mathcal{T}_{mm}/2$ ,  $\mathcal{J} = \mathcal{J}_{mm}/2$  and finally,  $\mathcal{E} = \mathcal{E}_{mm}/2$ . In the following, we will restrict the study to homogeneous flows for sake of clarity and simplification so that the diffusion terms vanishes and the variable  $\mathbf{X}$  is omitted. Exiled in one-dimensional spectral space, the turbulence quantities become only functions of the scalar wave number rather than the full wave vector. The PITM equations are formally obtained from integration of equation (Eq. (5)) in the wave number ranges  $[0, \kappa_c]$ ,  $[\kappa_c, \kappa_d]$  and  $[\kappa_d, \infty[$ , where  $\kappa_c$  is the cutoff wave number linked to the filter size  $\Delta$  by  $\kappa_c = \pi/\Delta$ , and  $\kappa_d$  is the dissipative wave number located at the far end of the inertial range of the spectrum assuming that the energy pertaining to higher wave numbers is negligible [10, 11]. As a result, one then obtain for each spectral region

$$\frac{\partial \tau_{ij}[0, \kappa_c]}{\partial t} = P_{ij}[0, \kappa_c] - \mathcal{F}_{ij}(\kappa_c, t) - \mathcal{K}_{ij}(\kappa_c, t) + \Pi_{ij}[0, \kappa_c] \quad (9)$$

$$\frac{\partial \tau_{ij}[\kappa_c, \kappa_d]}{\partial t} = P_{ij}[\kappa_c, \kappa_d] - \mathcal{F}_{ij}(\kappa_d, t) - \mathcal{K}_{ij}(\kappa_d, t) + \mathcal{F}_{ij}(\kappa_c, t) + \mathcal{K}_{ij}(\kappa_c, t) + \Pi_{ij}[\kappa_c, \kappa_d] \quad (10)$$

$$0 = F_{ij}(\kappa_d, t) - \epsilon_{ij}[\kappa_d, \infty[ \quad (11)$$

where

$$\tau_{ij}[0, \kappa_c] = \int_0^{\kappa_c} \varphi_{ij}(\kappa, t) d\kappa \quad (12)$$

for the large resolved scales and

$$\tau_{ij}[\kappa_c, \kappa_d] = \int_{\kappa_c}^{\kappa_d} \varphi_{ij}(\kappa, t) d\kappa \quad (13)$$

for the smaller modeled scales. The redistribution term  $\Pi_{ij}[\kappa_c, \kappa_d]$  is given by

$$\Pi_{ij}[\kappa_c, \kappa_d] = \int_{\kappa_c}^{\kappa_d} \Psi_{ij}(\kappa, t) d\kappa \quad (14)$$

The subgrid viscous dissipation-rate reads

$$(\epsilon_{ij})_{[\kappa_d, \infty[} = \int_{\kappa_d}^{\infty} \mathcal{E}_{ij}(\kappa, t) d\kappa \quad (15)$$

The total flux of energy transfer through the cutoff  $\kappa_c$ , is obtained from

$$F_{ij}(\kappa_c, t) = \mathcal{F}_{ij}(\kappa_c, t) + \mathcal{K}_{ij}(\kappa_c, t) \quad (16)$$

where

$$\mathcal{K}_{ij}(\kappa_c, t) = -\varphi_{ij}(\kappa_c, t) \frac{\partial \kappa_c}{\partial t} \quad (17)$$

with the definition

$$\mathcal{F}_{ij}(\kappa, t) = \int_{\kappa}^{\infty} \mathcal{T}_{ij}(\kappa', t) d\kappa' = - \int_0^{\kappa} \mathcal{T}_{ij}(\kappa', t) d\kappa' \quad (18)$$

Eq. (11) indicates that the tensorial dissipation-rate can be considered as a spectral flux that is independent of the cutoff wave number  $\kappa_c$ . Its theoretical expression is given by Eq. (15). Combining Eq. (10) with Eq. (11) results in the transport equation for the subgrid scale stress  $\tau_{ij}[\kappa_c, \kappa_d]$  in the statistical sense

$$\frac{\partial \tau_{ij}[\kappa_c, \kappa_d]}{\partial t} = P_{ij}[\kappa_c, \kappa_d] + \mathcal{F}_{ij}(\kappa_c, t) - \varphi_{ij}(\kappa_c, t) \frac{\partial \kappa_c}{\partial t} + \Pi_{ij}[\kappa_c, \kappa_d] - (\epsilon_{ij})_{[\kappa_d, \infty[} \quad (19)$$

This equation allows to single out the role played by the term accounting for the variation of the cutoff wave number  $\mathcal{K}_{ij}(\kappa_c, t)$  on the modeled/resolved scales. The corresponding transfer  $\mathcal{K}(\kappa_c, t)$  associated with the turbulent kinetic energy can be also written [17, 18]

$$\mathcal{K}(\kappa_c, t) = -E(\kappa_c, t) \frac{\partial \kappa_c}{\partial t} = \frac{\partial k_{[\kappa_c, \kappa_d]}}{\partial \Delta} \frac{\partial \Delta}{\partial t} \quad (20)$$

showing clearly that it is a function of the derivative of the subgrid energy to the grid-size. In case the grid-size increases in time  $\partial \Delta(t)/\partial t > 0$  or  $\mathcal{K}(\kappa_c) > 0$ , then a part of the energy contained into the resolved scales is removed and fed into the modeled spectral zone, whereas on the contrary, when  $\partial \Delta(t)/\partial t < 0$  or  $\mathcal{K}(\kappa_c) < 0$ , a part of energy coming from the modeled zone is injected into the resolved scales [17, 18]. It is simple matter to show that  $\tau_{ij}[\kappa_c, \kappa_d]$  corresponds in fact to the statistical averaging of the subgrid scale fluctuating velocities, more precisely

$$\tau_{ij}[\kappa_c, \kappa_d] = \langle (\tau_{ij})_{sfs} \rangle = \langle u_i^> u_j^> \rangle \quad (21)$$

where  $(\tau_{ij})_{sfs}$  and  $k_{sfs} = (\tau_{mm})_{sfs}/2$  denote the subfilter stress and subfilter energy, respectively, in the more general case where the filter is greater than the grid-size (as it has to be). Eq. (19) involving the evolution of

the subfilter-scale stress  $(\tau_{ij})_{sfs}$  can be rewritten in an instantaneous form as

$$\frac{\partial(\tau_{ij})_{sfs}}{\partial t} = (P_{ij})_{sfs} + \frac{\partial(\tau_{ij})_{sfs}}{\partial \Delta} \frac{\partial \Delta}{\partial t} + (\Pi_{ij})_{sfs} - (\epsilon_{ij})_{sfs} \quad (22)$$

where

$$(P_{ij})_{sfs} = (P_{ij})_{[\kappa_c, \kappa_d]} + F_{ij}(\kappa_c) \quad (23)$$

$$(\Pi_{ij})_{sfs} = (\Pi_{ij})_{[\kappa_c, \kappa_d]} \quad (24)$$

$$(\epsilon_{ij})_{sfs} = (\epsilon_{ij})_{[\kappa_d, \infty[} \quad (25)$$

and in a contracted tensor form

$$\frac{\partial k_{sfs}}{\partial t} = P_{sfs} + \frac{\partial k_{sfs}}{\partial \Delta} \frac{\partial \Delta}{\partial t} - \epsilon_{sfs} \quad (26)$$

So, at the wavenumber  $\kappa_d$ , all the preceding hypotheses imply  $F(\kappa_d) = \epsilon \approx \epsilon_{sfs}$ , the turbulence Reynolds number being supposed to be large. Like in the RANS multiscale approach [21], the wavenumber  $\kappa_d$  is defined such that

$$\kappa_d - \kappa_c = \zeta \frac{\epsilon_{sfs}}{k_{sfs}^{3/2}} \quad (27)$$

where the value of the numerical coefficient  $\zeta$  is chosen to ensure that the wavenumber  $\kappa_d$  is always sufficiently large in order to leave the entire inertial region. The dissipation rate equation is then obtained by taking the derivative of Eq. (27) with respect to time. Hence, one can easily obtain [9, 10, 14]

$$\frac{\partial \epsilon_{sfs}}{\partial t} = c_{\epsilon_1} \frac{\epsilon_{sfs}}{k_{sfs}} \left( P_{sfs} + \frac{\partial k_{sfs}}{\partial \Delta} \frac{\partial \Delta}{\partial t} \right) - c_{\epsilon_2} \frac{\epsilon_{sfs}^2}{k_{sfs}} \quad (28)$$

with  $c_{\epsilon_1} = \frac{3}{2}$ . Then, it is also found [9, 10, 14] that

$$c_{\epsilon_2 sfs} = \frac{3}{2} - \frac{k_{sfs}}{(\kappa_d - \kappa_c) E(\kappa_d)} \left[ \left( \frac{\mathcal{F}(\kappa_d) - F(\kappa_d)}{\epsilon} \right) - \frac{E(\kappa_d)}{E(\kappa_c)} \left( \frac{\mathcal{F}(\kappa_c) - F(\kappa_c)}{\epsilon} \right) \right] \quad (29)$$

Setting  $\kappa_d \gg \kappa_c$ , and  $E(\kappa_d) \ll E(\kappa_c)$ , Eq. (29) reduces to

$$c_{\epsilon_2 sfs}(\kappa_c) = \frac{3}{2} - \frac{k_{sfs}(\kappa_c)}{\kappa_d E(\kappa_d)} \left( \frac{\mathcal{F}(\kappa_d) - F(\kappa_d)}{\epsilon} \right) \quad (30)$$

which is valid for any value of  $\kappa_c$ . Considering this equation for  $\kappa_c = 0$  so that  $k_{sfs}(0) = k$  in pure RANS modelling, and combining Eq. (30) with this equation for  $\kappa_c = 0$ , it is then simple matter to show that [9, 10]

$$c_{\epsilon_2 sfs} = \frac{3}{2} + \frac{k_{sfs}}{k} \left( c_{\epsilon_2} - \frac{3}{2} \right) \quad (31)$$

The numerical value  $c_{\epsilon_1} = 3/2$  can be re-adjusted if necessary to a different value and the more general expression for  $c_{\epsilon_2 sfs}$  is [11]

$$c_{\epsilon_2 sfs} = c_{\epsilon_1} + \frac{k_{sfs}}{k} (c_{\epsilon_2} - c_{\epsilon_1}) \quad (32)$$

The ratio  $k_{sfs}/k$  appearing in Eq. (31) can be calibrated as a function of the location of the cutoff wave number.

In the first version of the PITM method [9, 10], this ratio was computed by integrating the Kolmogorov law in the wave number range  $[\kappa_c, \infty[$  taking into account the limiting condition when  $k_{sfs}$  approaches  $k$  leading to

$$c_{\epsilon_2 sfs} = c_{\epsilon_1} + \frac{c_{\epsilon_2} - c_{\epsilon_1}}{1 + \beta \eta_c^{2/3}} \quad (33)$$

where  $\eta_c = \kappa_c L_e$ ,  $L_e = k^{3/2}/\epsilon$  and  $\beta = 2/(3C_K)$ . Then, in more advanced PITM models, the universal spectrum [6]

$$E(\kappa) = \frac{\frac{2}{3} \beta (\kappa L_e)^{\alpha-1} L_e k}{[1 + \beta (\kappa L_e)^\alpha]^{\gamma+1}} \quad (34)$$

where  $\alpha$  and  $\beta$  are constant coefficients given by  $\alpha\gamma = 2/3$  and  $\beta = [2/(3C_K)]^\gamma$  to comply with the Kolmogorov law, was considered to better describe the spectrum at the origin of small wave numbers. As known, in this region, the spectrum behaves like  $E(\kappa) = \propto \kappa^{\alpha-1}$  taking into account the hypothesis of permanence of very large eddies. Using Eq. (34), it is a simple matter to compute the ratio  $k_{sfs}/k$ , leading to the more accurate computation of the coefficient  $c_{\epsilon_2 sfs}$  than Eq. (33) as

$$c_{\epsilon_2 sfs} = c_{\epsilon_1} + \frac{c_{\epsilon_2} - c_{\epsilon_1}}{[1 + \beta \eta_c^\alpha]^\gamma} \quad (35)$$

In practice [5, 6, 19, 20, 22], the coefficients used in Eq. (34) are  $\alpha = 3$  and  $\gamma = 2/9$ . This feature first introduced in [9, 10] was more recently imported into the PANS model [33] allowing decisive improvements. Unlike RANS closures, Eq. (35) sensitizes the model to the filter width [18, 17] (or in practice the grid-size  $\Delta$ ), and tends to draw the spectral distribution towards the prescribed equilibrium distribution given by Eq. (34). The set of the final transport equations for  $(\tau_{ij})_{sfs}$  and  $\epsilon_{sfs}$  accounting for non-homogeneous flows with varying filter width in time and space are given in Refs. [17, 18]. The different contributions appearing in Eq. (22) including the diffusion term read

$$(P_{ij})_{sfs} = -(\tau_{ik})_{sfs} \frac{\partial \bar{u}_j}{\partial x_k} - (\tau_{jk})_{sfs} \frac{\partial \bar{u}_i}{\partial x_k} \quad (36)$$

the redistribution term  $(\Pi_{ij})_{sfs}$  is decomposed into a slow part  $(\Pi_{ij}^1)_{sfs}$  that characterizes the return to isotropy due to the action of subgrid turbulence on itself

$$(\Pi_{ij}^1)_{sfs} = -c_1 \frac{\epsilon_{sfs}}{k_{sfs}} \left( (\tau_{ij})_{sfs} - \frac{1}{3} (\tau_{mm})_{sfs} \delta_{ij} \right) \quad (37)$$

and a rapid part,  $(\Pi_{ij}^2)_{sfs}$  that describes the action of the filtered velocity gradients

$$(\Pi_{ij}^2)_{sfs} = -c_2 \left( (P_{ij})_{sfs} - \frac{1}{3} (P_{mm})_{sfs} \delta_{ij} \right) \quad (38)$$

where  $c_1$  plays the same role as the Rotta coefficient but is no longer constant whereas  $c_2$  is the same coefficient used in RANS modelling. The diffusion terms  $(J_{ij})_{sfs}$  is modeled assuming a well-known gradient law

$$(J_{ij})_{sfs} = \frac{\partial}{\partial x_m} \left( \nu \frac{\partial (\tau_{ij})_{sfs}}{\partial x_m} + c_s \frac{k_{sfs}}{\epsilon_{sfs}} (\tau_{ml})_{sfs} \frac{\partial (\tau_{ij})_{sfs}}{\partial x_l} \right) \quad (39)$$

where  $c_s$  is a constant coefficient. The diffusion term  $(J_\epsilon)_{sfs}$  included in Eq. (28) reads

$$(J_\epsilon)_{sfs} = \frac{\partial}{\partial x_j} \left( \nu \frac{\partial \epsilon_{sfs}}{\partial x_j} + c_\epsilon \frac{k_{sfs}}{\epsilon_{sfs}} (\tau_{jm})_{sfs} \frac{\partial \epsilon_{sfs}}{\partial x_m} \right) \quad (40)$$

where  $c_\epsilon$  is a constant coefficient. In a general way, the derivative  $\partial\bar{\phi}/\partial\Delta$  can be computed is computed by applying a second filtering operation with a larger filter width leading to

$$\frac{\partial\bar{\phi}}{\partial\Delta} = \lim_{\delta\Delta \rightarrow 0} \frac{\bar{\phi}(\bar{\Delta} + \delta\bar{\Delta}) - \bar{\phi}(\bar{\Delta})}{\delta\bar{\Delta}} \approx \frac{\bar{\phi}(\tilde{\Delta}) - \bar{\phi}(\bar{\Delta})}{\tilde{\Delta} - \bar{\Delta}} \quad (41)$$

where  $\bar{\Delta}$  is the filter width of the grid-size  $\Delta$ , and  $\tilde{\Delta}$  denotes the superfilter width of  $\Delta$ . Eq. (41) can be applied easily for the the subfilter scale stress  $(\tau_{ij})_{sfs}$  with respect to the filter width  $\bar{\Delta}$  leading to [17]

$$\begin{aligned} \frac{\partial(\tau_{ij})_{sfs}}{\partial\Delta} &\approx \frac{(\tau_{ij})_{sfs}(\tilde{\Delta}) - (\tau_{ij})_{sfs}(\bar{\Delta})}{\tilde{\Delta} - \bar{\Delta}} \\ &= \frac{(\widetilde{u_i u_j} - \tilde{u}_i \tilde{u}_j) - (\bar{u}_i \bar{u}_j - \bar{u}_i \bar{u}_j)}{\tilde{\Delta} - \bar{\Delta}} \end{aligned} \quad (42)$$

The transfer flux  $\mathcal{K}(\kappa_c)$  can be computed from tensorial contraction of Eq. (42) but also in a theoretical way from Eq. (34) as in [17]

$$\mathcal{K}(\kappa_c) = \frac{2}{3}\beta(\pi L_e)^\alpha \left(\frac{k_{sfs}}{k}\right)^{\frac{\gamma+1}{\gamma}} \frac{k}{\Delta^{\alpha+1}} \frac{\partial\Delta}{\partial t} \quad (43)$$

Note that these commutation terms like in Eq. (26) are needed explicitly only for strong variations in mesh density.

### 2.2.2 Turbulent passive scalar field

It is possible to extend the PITM method developed for dynamic turbulent fields to scalar fields. In the following, we will only indicates the basic guidelines leading to the variance and scalar dissipation equations of a passive scalar. The key is to work in the spectral space. The spectral transport equation of the scalar variance denoted  $E_\theta(\mathbf{X}, \kappa) = \langle \theta' \theta'(\mathbf{X}) \rangle^\Delta(\kappa)/2$  reads [23]

$$\begin{aligned} \frac{\partial E_\theta(\mathbf{X}, \kappa)}{\partial t} + \langle u_k \rangle(\mathbf{X}) \frac{\partial E_\theta(\mathbf{X}, \kappa)}{\partial X_k} &= \mathcal{P}_\theta(\mathbf{X}, \kappa) \\ + \mathcal{T}_\theta(\mathbf{X}, \kappa) + \mathcal{J}_\theta(\mathbf{X}, \kappa) - \mathcal{E}_\theta(\mathbf{X}, \kappa) \end{aligned} \quad (44)$$

where in the right hand side of this equation,  $\mathcal{P}_\theta$  is the production of half the scalar variance by mean gradients of the scalar,  $\mathcal{T}_\theta$  is the spectral transfer driven by the eddying motions in the inertial cascade,  $\mathcal{J}_\theta$  is the diffusion term and  $\mathcal{E}_\theta$  denotes the dissipation term of half the scalar variance. In particular, the production term  $\mathcal{P}_\theta$  is defined by

$$\mathcal{P}_\theta(\mathbf{X}, \kappa) = -\varphi_{j\theta}(\mathbf{X}, \kappa) \frac{\partial \langle \theta \rangle}{\partial X_j} \quad (45)$$

where  $\varphi_{j\theta}(\mathbf{X}, \kappa, t) = \langle u'_j \theta'(\mathbf{X}) \rangle^\Delta(\kappa, t)$  whereas the dissipation term reads

$$\mathcal{E}_\theta(\mathbf{X}, \kappa) = \frac{\sigma}{2} \frac{\partial^2 E_\theta(\mathbf{X}, \kappa)}{\partial X_j \partial X_j} + 2\sigma\kappa^2 E_\theta(\mathbf{X}, \kappa) \quad (46)$$

where  $\sigma$  denotes the molecular diffusivity computed as  $\sigma = \nu/Pr$  using the molecular Prandtl number  $Pr$ . Eq. (44) can be integrated in the same way as Eq. (5) but in the domains  $[0, \kappa_c]$ ,  $[\kappa_c, \kappa_e]$  and  $[\kappa_e, \infty[$  where  $\kappa_e$  denotes here the high end wave number that can be larger

or smaller than  $\kappa_c$  and different from  $\kappa_d$ , leading to the resulting equations

$$\frac{\partial k_{\theta[0, \kappa_c]}}{\partial t} = P_{\theta[0, \kappa_c]} - \mathcal{F}_\theta(\kappa_c, t) - \mathcal{K}_\theta(\kappa_c, t) \quad (47)$$

$$\begin{aligned} \frac{\partial k_{\theta[\kappa_c, \kappa_e]}}{\partial t} &= P_{\theta[\kappa_c, \kappa_e]} - \mathcal{F}_\theta(\kappa_e, t) - \mathcal{K}_\theta(\kappa_e, t) \\ + \mathcal{F}_\theta(\kappa_c, t) + \mathcal{K}_\theta(\kappa_c, t) \end{aligned} \quad (48)$$

$$0 = F_\theta(\kappa_e) - \epsilon_{\theta[\kappa_e, \infty[} \quad (49)$$

where

$$k_{\theta[0, \kappa_c]} = \int_0^{\kappa_c} E_\theta(\kappa, t) d\kappa \quad (50)$$

$$k_{\theta[\kappa_c, \kappa_e]} = \int_{\kappa_c}^{\kappa_e} E_\theta(\kappa, t) d\kappa \quad (51)$$

$$(\epsilon_\theta)_{[\kappa_e, \infty[} = \int_{\kappa_e}^{\infty} \mathcal{E}_\theta(\kappa, t) d\kappa \quad (52)$$

The total flux of variance  $F_\theta(\kappa)$  at the wave number  $\kappa_c$  of the spectrum  $E_\theta$  is then given by

$$F_\theta(\kappa_c, t) = \mathcal{F}_\theta(\kappa_c, t) + \mathcal{K}_\theta(\kappa_c, t) \quad (53)$$

where

$$\mathcal{K}_\theta(\kappa_c, t) = -E_\theta(\kappa_c, t) \frac{\partial \kappa_c}{\partial t} \quad (54)$$

with the definition

$$\mathcal{F}_\theta(\kappa, t) = \int_\kappa^\infty \mathcal{T}_\theta(\kappa', t) d\kappa' = - \int_0^\kappa \mathcal{T}_\theta(\kappa', t) d\kappa' \quad (55)$$

The subfilterscale variance of the passive scalar is defined as  $k_{\theta[\kappa_c, \kappa_e]} = \langle k_{\theta sfs} \rangle = \langle \theta^> \theta^> \rangle / 2$ . Combining these equations, it is simple matter to show that Eq. (48) can be rewritten as in an instantaneous form as

$$\frac{\partial k_{\theta sfs}}{\partial t} = P_{\theta[\kappa_c, \kappa_e]} + F_\theta(\kappa_c, t) - \epsilon_\theta \quad (56)$$

where Eq. (56) expresses simply that the subfilter turbulence scalar variance is computed as the integral of the variance density in the interval  $[\kappa_c, \kappa_e]$ , considering that the variance in the zone  $[\kappa_e, \infty[$  is negligible. As the flux transfer at  $\kappa_e$  approaches the dissipation  $F_\theta(\kappa_e) \approx \epsilon_\theta$ , like in Eq. (27), the wave numbers  $\kappa_e$  and  $\kappa_c$  can be then related in a such way that  $\kappa_e - \kappa_c = \mathcal{O}(1/l_\theta) = \mathcal{O}(\epsilon_\theta/\theta^2 u)$ . Following the same mathematical framework as in the preceding section step by step, considering moreover the counterpart of Eq. (27) transposed to the case of scalar fields, one can derive easily the transport equation of  $\epsilon_\theta$  as for [25]

$$\begin{aligned} \frac{\partial \epsilon_\theta}{\partial t} &= c_{\epsilon_{\theta\theta_1}} P_{\theta sfs} \frac{\epsilon_\theta}{k_{\theta sfs}} + c_{\epsilon_{\theta k_1}} P_{sfs} \frac{\epsilon_\theta}{k_{sfs}} \\ - c_{\epsilon_{\theta k_2}} \frac{\epsilon_\theta \epsilon}{k_{sfs}} - c_{\epsilon_{\theta\theta_2 sfs}} \frac{\epsilon_\theta^2}{k_{\theta sfs}} \end{aligned} \quad (57)$$

with

$$P_{\theta sfs} = P_{\theta[\kappa_c, \kappa_e]} + F_\theta(\kappa_c) \quad (58)$$

and where  $c_{\epsilon_{\theta\theta_1}}$ ,  $c_{\epsilon_{\theta k_1}}$ ,  $c_{\epsilon_{\theta k_2}}$  are constant coefficients whereas  $c_{\epsilon_{\theta\theta_2 sfs}}$  is now a dynamical coefficient involving both the wave numbers  $\kappa_c$  and  $\kappa_e$ . For non-homogeneous flows, the diffusion terms  $\mathcal{J}_\theta$  and  $\mathcal{J}_{\epsilon_\theta}$  modeled assuming the well-known tensorial gradient law hypothesis are included into Eq. (56) and Eq. (57). At least, note that Eq. (22), Eq. (26), Eq. (28), Eq. (56), Eq. (57) to be solved in the PITM method require appropriate numerical schemes both in time and space that are more accurate than schemes used in the traditional RANS method [26].

## 2.3 Illustrations to several typical turbulent flows

### 2.3.1 An overview

Several turbulent flows of complex physics have been performed using the PITM method to this day. Among these flows, it is worth mentioning pulsed flows [9], the mixing of turbulent flow fields of differing scales [27], thermal convection at high Rayleigh numbers [31], rotating flows encountered in turbomachinery at the bulk Reynolds number  $R_b = U_b \delta / \nu = 14000$  and at different rotation numbers  $R_o = \Omega \delta / U_b$  varying from moderate, medium and very high rotation rates  $R_o = 0.17, 0.50$  and  $1.50$  [20], flows with appreciable fluid injection through the surface which correspond to the propellant burning in solid rocket motors [10], flows over periodic hills with separation and reattachment of the boundary layer both at the Reynolds number  $Re = 10595$  [24, 28, 29] and  $Re = 37000$  [5], flow subjected to axisymmetric contraction [22], airfoil flows at the Reynolds number  $Re = 1.64 \times 10^6$  for an angle of attack  $12^\circ$  [30]. In the following, we point out and discuss some results obtained for the flow over periodic hills involving turbulence mechanisms associated with separation, recirculation, reattachment, acceleration and wall effects.

### 2.3.2 The turbulent flow over periodic hills at high Reynolds number

This flow was investigated experimentally at the two Reynolds numbers  $Re = U_b h / \nu = 10595$  and  $37000$  based on the hill height  $h$  and the bulk velocity  $U_b$  about the hill crest [32] and performed by Chaouat [24], Chaouat and Schiestel [5]. Overall, it is found that the PITM re-

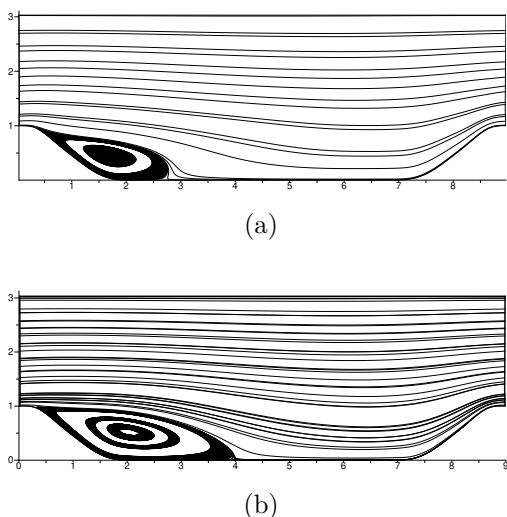


Figure 1: Streamlines of the average flowfield at  $Re=10595$ . (a) RSM computation ( $80 \times 30 \times 100$ ); (b) PITM simulation ( $160 \times 60 \times 100$ )

produced fairly well this flow according to reference data [32] while the RSM computation returned some weakness in the predictions. Figures 1 and 2 show the streamlines plot for the RSM computation and PITM simulation, respectively. For the PITM, the plot are generated in two dimensions and obtained by averaging the velocities both in the homogeneous planes in the spanwise direction and in time. The flow separation that is clearly visible is caused by the adverse pressure gradient resulting from

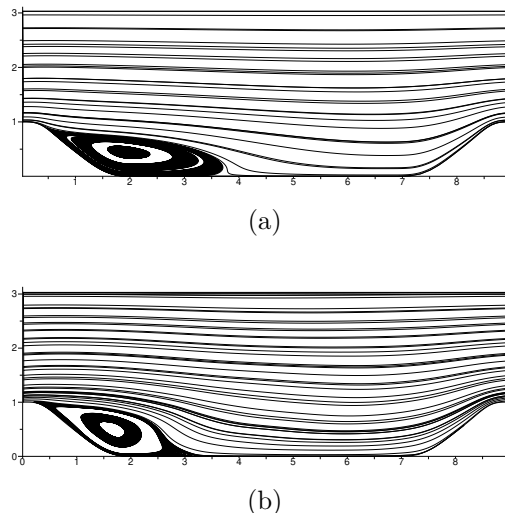


Figure 2: Streamlines of the average flowfield at  $Re=37000$ . (a) RSM computation ( $80 \times 30 \times 100$ ); (b) PITM simulation ( $160 \times 60 \times 100$ )

the strong streamwise curvature of the lower wall. Due to the flow recirculation, a strong turbulence activity is visible near the lower wall and this one is particularly concentrated in the leeward region of the second hill. At  $Re = 10595$ , the RSM model predicted a too small recirculation zone probably because the model cannot capture the large eddies naturally issued from the streamwise curvature of the lower wall that play a major role in this type of flow. At  $Re = 37000$ , the recirculation zone was on the contrary strongly under-predicted in comparison with those measured from the experiment, mainly because the separation is delayed. These flows were investigated in details in Refs [24, 5] showing the mean velocity and turbulent stress profiles in several sections of the channel with a comprehensive study.

## 3 Conclusions

The PITM method allowing seamless coupling between RANS and LES regions has been developed to perform numerical simulations of turbulent flows out of spectral equilibrium on relatively coarse grids to overcome the practical difficulties posed by LES. Unlike almost hybrid RANS/LES models that are built upon empirical techniques, the PITM method relies on a mathematical framework developed in spectral space that provides valuable physical grounds. We hope that this contribution will open promising routes for new future heuristic developments in hybrid RANS/LES modelling.

## References

- [1] R. Schiestel, *Modeling and simulation of turbulent flows*, ISTE Ltd and J. Wiley, 2008.
- [2] K. Hanjalic, B.E. Launder, *Modelling turbulence in engineering and the environment. Second-moment route to closure*, Cambridge University Press, 2011.
- [3] M. Leschziner, M.N. Li and F. Tessicini, Simulating flow separation from continuous surfaces: routes

- to overcoming the Reynolds number barrier, *Phil. Trans. R. Soc. A* **367**, 2885-2903, 2009.
- [4] B. Chaouat, Reynolds stress transport modeling for high-lift airfoil flows, *AIAA Journal*, **44**, 2390-2403, 2006.
- [5] B. Chaouat and R. Schiestel, Hybrid RANS-LES simulations of the turbulent flow over periodic hills at high Reynolds number using the PITM method, *Computers and Fluids* **84**, 279-300, 2013.
- [6] B. Chaouat, The state of the art of hybrid RANS/LES modeling for the simulation of turbulent flows, *Flow, Turbulence and Combustion*, **99**(2), 279-327, 2017.
- [7] C.G. Speziale, Turbulence modeling for time-dependent RANS and VLES: A review, *AIAA Journal*, **36**, 173-184, 1998.
- [8] P.R. Spalart, Detached-eddy simulation, *Annual. Review Fluid Mechanics*, **41**, 181-202, 2009.
- [9] R. Schiestel and A. Dejoan, Towards a new partially integrated transport model for coarse grid and unsteady turbulent flow simulations, *Theoretical and Computational Fluid Dynamics*, **18**, 443-468, 2005.
- [10] B. Chaouat and R. Schiestel, A new partially integrated transport model for subgrid-scale stresses and dissipation rate for turbulent developing flows, *Physics of Fluids*, **17**, 065106, 1-19, 2005.
- [11] B. Chaouat and R. Schiestel, Analytical insights into the partially integrated transport modeling method for hybrid Reynolds averaged Navier-Stokes equations-large eddy simulations of turbulent flows, *Physics of Fluids*, **24**, 085106, 1-34, 2012.
- [12] S.S. Girimaji, Partially-averaged Navier-Stokes method for turbulence: A Reynolds -averaged Navier-Stokes to direct numerical simulation bridging method, *Journal of Applied Mechanics, ASME*, **73**, 413-421, 2006.
- [13] F.R. Menter and Y. Egorov, The scale-adaptive simulation method for unsteady turbulent flow prediction: Part 1: Theory and model description, *Flow, Turbulence and Combustion*, **85**, 113-138, 2010.
- [14] B. Chaouat and R. Schiestel, From single-scale turbulence models to multiple-scale and subgrid-scale models by Fourier transform, *Theoretical and Computational Fluid Dynamics*, **21**, 201-229, 2007.
- [15] B. Chaouat and R. Schiestel, Simulations of turbulent flows out of a spectral equilibrium using the PITM method, *23ème Congrès Français de Mécanique*, 2491-715X, 1-16, 2017.
- [16] C. Cambon, D. Jeandel and J. Mathieu, Spectral modelling of homogeneous non-isotropic turbulence, *Journal of Fluid Mechanics*, **104**, 247-262, 1981.
- [17] B. Chaouat, Commutation errors in PITM simulations, *International Journal of Heat and Fluid Flow*, **67**, 138-154, 2017.
- [18] B. Chaouat and R. Schiestel, Partially integrated transport modeling method for turbulence simulation with variable filters, *Physics of Fluids*, **25**, 125102, 1-39, 2013.
- [19] B. Chaouat and R. Schiestel, Progress in subgrid-scale transport modelling for continuous hybrid non-zonal RANS/LES simulations, *International Journal of Heat and Fluid Flow*, **30**, 602-616, 2009.
- [20] B. Chaouat, Simulation of turbulent rotating flows using a subfilter scale stress model derived from the partially integrated transport modeling method, *Physics of Fluids*, **24**, 045108, 1-35, 2012.
- [21] R. Schiestel, Multiple-time scale modeling of turbulent flows in one point closures, *Physics of Fluids*, **30**, 722-731, 1987.
- [22] B. Chaouat, Application of the PITM method using inlet synthetic turbulence generation for the simulation of the turbulent flow in a small axisymmetric contraction, *Flow, Turbulence and Combustion*, **98**(4), 987-1024, 2017.
- [23] A. S. Monin and A. M. Yaglom *Statistical Fluid Mechanics*, The M.I.T. Press Cambridge, Massachusetts, vols. I and II, 1975.
- [24] B. Chaouat, Subfilter-scale transport model for hybrid RANS/LES simulations applied to a complex bounded flow, *Journal of Turbulence*, **11**, 1-30, 2019.
- [25] B. Chaouat and R. Schiestel, Passive scalar fluctuations in turbulent flows simulation in the framework of the partially integrated transport modeling method. *Submitted paper*, 2019.
- [26] B. Chaouat, An efficient numerical method for RANS/LES turbulent simulations using subfilter scale stress transport equations, *Int. J. Numer. Methods Fluids* **67**, 1207-1233, 2011.
- [27] I. Befeno and R. Schiestel, Non-equilibrium mixing of turbulence scales using a continuous hybrid RANS/LES approach: Application to the shearless mixing layer, *Flow, Turbulence and Combustion*, **78**, 129-151, 2007.
- [28] S. Jakirlic, S. Saric, G. Kadavelil, E. Sirbubalo, B. Basara and B. Chaouat, SGS modelling in LES of wall-bounded flow using transport RANS model: From a zonal to a seamless hybrid LES/RANS method, in *Proceedings of the 6th Symposium on Turbulence Shear Flow Phenomena*, edited by Seoul National University, vol. 3, 1057-1062, 2009.
- [29] C. Friess, R. Manceau and T.B. Gatski, Toward an equivalence criterion for hybrid RANS/LES methods, *Comput. Fluids* **122**, 233-246, 2015.
- [30] M. Stoellinger, R. Roy, and S. Heinz, Unified RANS-LES method based on second-order closure, in *Proceedings of the 9th Symposium on Turbulence Shear Flow Phenomena*, edited by The University of Melbourne, 7B5, 1-6, 2015.
- [31] S. Kenjeres and K. Hanjalic, LES, T-RANS and hybrid simulations of thermal convection at high  $Ra$  numbers, *Int. J. Heat Fluid Flow*, **27**, 800-810, 2006.
- [32] C. Rapp and M. Manhart, Flow over periodic hills - an experimental study, *Experiments in Fluids*, **51**, 247-269, 2011.
- [33] H. Foroutan and S. Yavuzkurt, A partially-averaged Navier-Stokes model for the simulation of turbulent swirling flows with vortex breakdown, *Int J Heat Fluid Flow*, **50**, 402-416, 2014.

# HYBRID TEMPORAL LES: DEVELOPMENT AND APPLICATIONS

R. Manceau

CNRS / Univ Pau & Pays Adour / E2S UPPA  
Laboratoire de mathématiques et de leurs applications de Pau  
Fédération IPRA, UMR 5142, 64000, Pau, France  
and Inria Bordeaux-Sud-Ouest, project-team CAGIRE

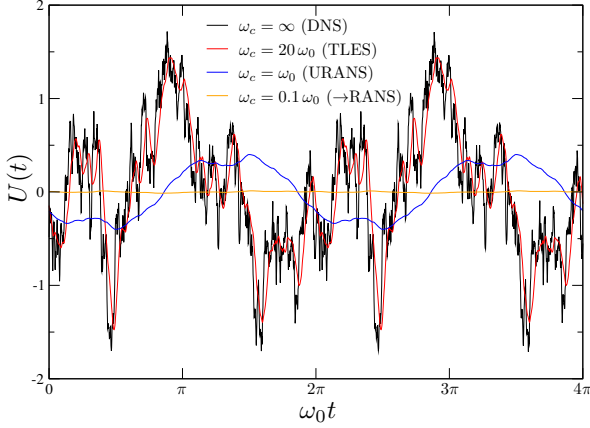


Figure 1: Synthetic turbulent signal. Application of a top-hat temporal filter with several cutoff frequencies  $\omega_c$ .  $\omega_0$  corresponds to the integral scale

## Abstract

The HTLES approach, based on temporal filtering, is a formally consistent way to hybridize (U)RANS and LES. Recent advances are presented as well as applications using industrial codes, which show the strong potential of this approach for industrial CFD.

## 1 Introduction

A rigorous formalism for continuous hybrid RANS/LES methods is highly desirable to favour the modelling of subgrid stresses, comparison with experiments/DNS and understanding of the observed phenomenology. The usual hybrid methods are limited by the fact that statistical averaging (RANS) and spatial filtering (LES) are generally inconsistent [1].

### 1.1 Temporal filtering

Generalized temporal filters, characterized by time integration at a moving application point,

$$\tilde{\mathbf{U}}(\mathbf{x}, t) = \int_{-\infty}^t G_T(t, t') \mathbf{U}(\boldsymbol{\xi}(\mathbf{x}, t, t'), t') dt', \quad (1)$$

are introduced in order to build a consistent formalism for hybrid methods for stationary, inhomogeneous turbulence, since the time-filtered quantities go to the statically-averaged quantities within the limit of an infinite filter width [1]. To satisfy the Galilean invariance, the *uniform temporal filter* [2] is used here,

$$\boldsymbol{\xi}(\mathbf{x}, t, t') = \mathbf{x} + (t' - t) \mathbf{V}_{\text{ref}}, \quad (2)$$

where  $\mathbf{V}_{\text{ref}}$  is an arbitrary velocity. As illustrated by Figure (1), the filtering process leads to temporal LES (TLES), URANS or RANS, depending on the cut-off frequency. The phase shift is due to backward-in-time integration (causal filter).

The equation of the filtered momentum is as follows

$$\frac{\partial \tilde{U}_i}{\partial t} + \tilde{U}_k \frac{\partial \tilde{U}_i}{\partial x_k} = -\frac{1}{\rho} \frac{\partial \tilde{P}}{\partial x_i} + \nu \frac{\partial^2 \tilde{U}_i}{\partial x_j \partial x_j} - \frac{\partial \tau_{ij \text{sfs}}}{\partial x_j} \quad (3)$$

and the transport equation for the subfilter stress (SFS) tensor  $\tau_{ij \text{sfs}}$  is also formally identical to the RANS equation for the Reynolds-stress tensor  $\overline{u_i u_j}$ , and tends exactly towards this equation within the limit of an infinite filter width, which forms a solid foundation for the development of hybrid RANS/LES approaches [1].

### 1.2 Hybridization with URANS

For a filter width of the order of magnitude of the integral time scale of turbulence, the filtered velocity only contains large-scale, quasi-periodic oscillations, Figure (1), similar to URANS solutions. It can be shown that using this filter width leads to the URANS equations (i.e., the RANS system with time derivative) such that URANS can be regarded as a time-filtered approach [2]. As a consequence, the HTLES methodology can also be used to bridge URANS and Temporal LES, which extends the validity of HTLES to non-stationary configurations.

## 2 Subfilter stress model

As in the case of standard LES, a closure problem must be addressed due to the presence of the subfilter stresses  $\tau_{ij \text{sfs}}$  in Eq. (3).

### 2.1 Hybridization method

The HTLES approach is based on the introduction of two filters with characteristic frequencies  $\omega_c$  and  $\omega_d$ , Figure (2). Integrating the equation for the *Eulerian temporal energy spectrum*  $E_T(\mathbf{x}, \omega)$  on the ranges  $[\omega_c; \omega_d]$  and  $[\omega_d; \infty[$ , respectively [1], and using a perturbation method to derive the dissipation term [3], the equation for the subfilter turbulent energy  $k_{\text{sfs}}$  can be written as follows

$$\frac{Dk_{\text{sfs}}}{Dt} = P_{\text{sfs}} + D_{\text{sfs}} - \frac{k_{\text{sfs}}}{T}, \quad (4)$$

where  $P_{\text{sfs}}$  and  $D_{\text{sfs}}$  are the subfilter parts of production and diffusion. The time scale that determines the dissipation term is

$$T(r) = \frac{r}{\psi(r)} \frac{k}{\varepsilon}, \quad (5)$$



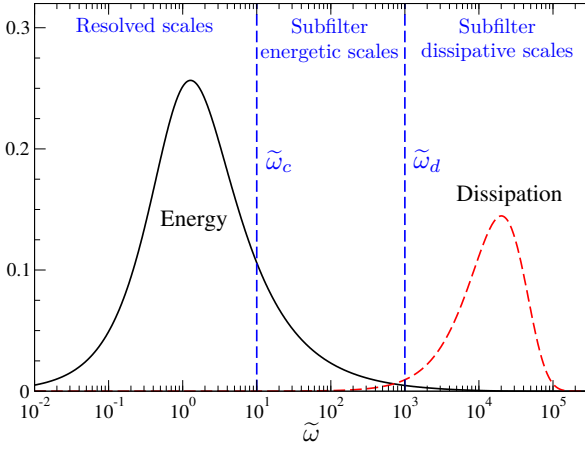


Figure 2: Spectral zones of HTLES. Pre-multiplied energy and dissipation spectra,  $\tilde{\omega}\tilde{E}(\tilde{\omega})$  and  $\tilde{\omega}\tilde{D}(\tilde{\omega})$ , respectively, in units based on the integral scales

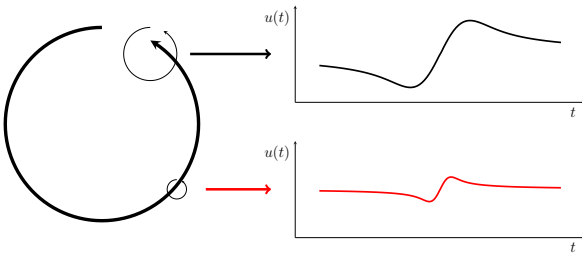


Figure 3: Sweeping mechanism [7]

where

$$r = \frac{\overline{k_{\text{sfs}}}}{k} \quad ; \quad \psi(r) = 1 + \left( \frac{C_{\varepsilon 2}}{C_{\varepsilon 1}} - 1 \right) \left( 1 - r \frac{C_{\varepsilon 1}}{C_{\varepsilon 2}} \right) \quad (6)$$

(the overbar denotes Reynolds averaging). The subfilter-to-total turbulent energy ratio  $r$  goes to unity at the RANS limit, in which case Eq. (4) tends towards the RANS equation. The modified time scale enforces the LES mode for  $r < 1$  by increasing the dissipation term  $k_{\text{sfs}}/T$ , similar to two-equation DES. This method can be applied to two-equation models ([4, 5, 6] or to second moment closures, replacing  $\varepsilon$  in the dissipation tensor with  $k_{\text{sfs}}/T$  [3]. Eq. (4) bears similarities with the corresponding equation in DES, in which the dissipation term writes  $k_{\text{sfs}}^{3/2}/L$ . However, HTLES also differs significantly from DES: it relies on a modified time scale rather than a length scale; Eq. (5) is based on the comparison of averaged quantities ( $r$  and  $k/\varepsilon$ ); DES is an empirical approach, without explicit reference to a particular formalism, although it can be interpreted as a simplified version of HTLES [3].

## 2.2 Switchover criterion

As seen in Eq. (5), the criterion that determines the switchover from RANS to LES is the ratio  $r$ , which must now be linked to the cutoff frequency  $\omega_c$ . It seems optimal to link the cutoff frequency to the Nyquist frequency related to the time step  $dt$ ,

$$\omega_c = \frac{2\pi}{2dt}. \quad (7)$$

However, for a sufficiently small time step, this frequency cannot be observed in the computation, since the corresponding vortices are filtered out by the grid. Frequencies observed at a fixed point are related to the advection

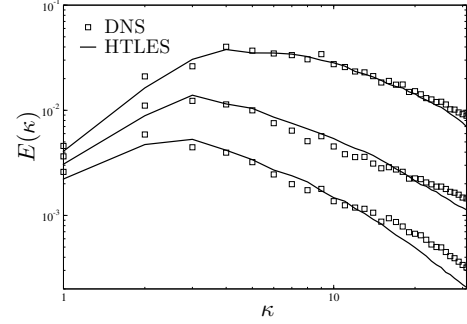


Figure 4: Decaying isotropic turbulence at  $Re_\lambda = 104.5$ . Evolution over time of the energy spectrum predicted by HTLES based on the  $k$ - $\omega$ -SST model [4]

(sweeping) of small scales by large scales [7], Figure (3). The medium-size vortex at the top is swept by the large-scale structure, so that it generates the time-dependent signal at a fixed point shown in the figure at the top right. The small vortex at the bottom generates higher frequencies. However, if the grid is not fine enough, small vortices and their corresponding frequencies are missing, so the maximum observable frequency is

$$\omega_c = \min \left( \frac{\pi}{dt}; \frac{U_s \pi}{\Delta} \right) = \frac{U_s \pi}{\Delta} \min \left( 1; \frac{\Delta}{U_s dt} \right), \quad (8)$$

where  $U_s$  is the sweeping velocity [7], and  $U_s dt/\Delta$  can be called *the sweeping CFL number*. The sweeping velocity is  $U_s = U + u$ , where  $U$  is the mean velocity magnitude and  $u = \gamma\sqrt{k}$  is the characteristic velocity of the energetic eddies, with  $\gamma$  a coefficient usually chosen as unity.

The assumption of an equilibrium Eulerian spectrum [7]

$$E_T(\omega) = C_\kappa \varepsilon^{2/3} U_s^{2/3} \omega^{-5/3}, \quad (9)$$

yields

$$r = \frac{1}{k} \int_{\omega_c}^{\infty} E_T(\omega) d\omega = \frac{1}{\beta} \left( \frac{U_s}{\sqrt{k}} \right)^{2/3} \left( \omega_c \frac{k}{\varepsilon} \right)^{-2/3} \quad (10)$$

As usual for hybrid RANS/LES methods, the coefficient  $\beta = 0.67$  is calibrated in homogeneous isotropic turbulence, so that, as shown in Figure (4), the decay of energy follows the DNS data.

Note that Eq. (10) and Eq. (8) actually define a twofold switchover criterion: if the sweeping CFL number is less than one, the switchover criterion is the ratio of the grid step to the integral length scale; otherwise, it is the ratio of the time step to the integral time scale.

## 2.3 Shielding of the near-wall region

One of the main objectives of hybrid approaches is to treat the near-wall region in RANS mode, in order to avoid the unaffordable cost of wall-resolved LES. Fadai-Ghotbi *et al.* [8] proposed to shield the near-wall region, an idea that was developed independently for the DDES approach [9]. In order to define a shielding function independent of the grid, it is important to base its definition on quantities that are the same in both RANS and LES modes. Duffal *et al.* [6] replaced in Eq. (5) and Eq. (6) the ratio  $r$  by the shielded ratio  $r_s$

$$r_s = 1 - f_s \max[0, 1 - r], \quad (11)$$

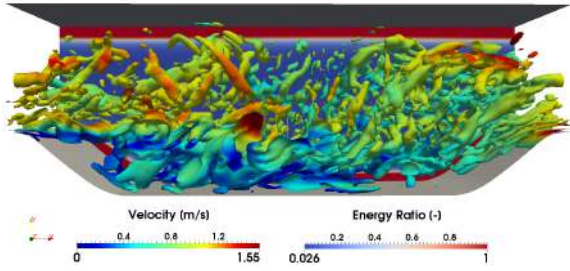


Figure 5: Hill flow. Q-isosurfaces coloured by the velocity magnitude. Background : ratio  $r_s$  [6]

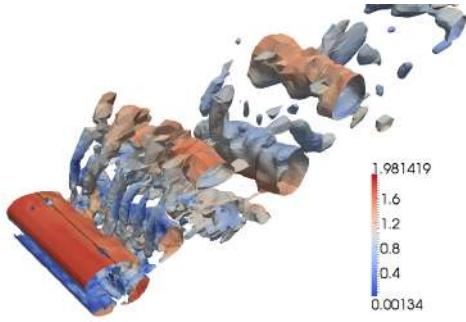


Figure 6: Square-sectioned cylinder. Q-isosurfaces coloured by the velocity magnitude [10]

with the shielding function  $f_s$

$$f_s = 1 - \tanh[\xi^p] \quad \text{where } \xi = C_L \frac{(v^3/\varepsilon)^{1/4}}{d_w}, \quad (12)$$

and  $d_w$  is the distance to the wall. The advantage of using the Kolmogorov scale in  $\xi$  rather than, for example, the integral scale, is that the dissipation rate  $\varepsilon$ , obtained from its transport equation, is reasonably independent of the grid, such that the thickness of the shielded region is also grid-independent [6].

Another possibility is to use the elliptic-blending parameter  $\alpha$  [8, 5], solution of

$$\alpha - L_{\text{sfs}}^2 \nabla^2 \alpha = 1, \quad (13)$$

with  $\alpha = 0$  at the wall and define  $r_s$  as

$$r_s = (1 - \alpha^2) + \alpha^2 r. \quad (14)$$

Another difficulty is that the shielding does not prevent resolved vortices from penetrating into the near-wall RANS region, Figure (5). In order to avoid double-counting, Duffal *et al.* [6] proposed the internal consistency constraint (ICC), which excludes the resolved energy  $k_r$  due to these fluctuations from the total turbulent energy by the use of

$$T = \frac{r}{\psi(r)} \frac{\overline{k_{\text{sfs}}} + c_r k_r}{\varepsilon}, \quad \text{where } c_r = \begin{cases} 0 & \text{if } r_s = 1, \\ f_s & \text{if } r_s < 1. \end{cases} \quad (15)$$

## 3 Some Applications

### 3.1 Square-sectioned cylinder

To illustrate the predictive capabilities of the method, the first case is the flow around a square-sectioned cylinder at  $Re = 21400$ , computed using Code\_Saturne [4].

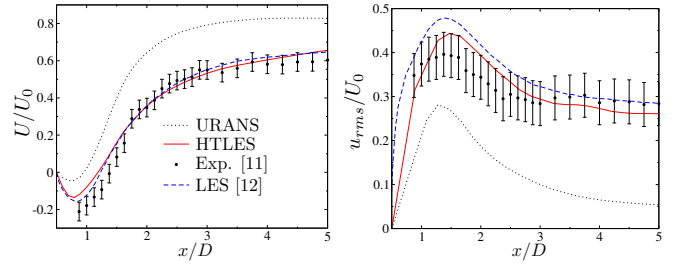


Figure 7: Square-sectioned cylinder. Mean (left) and rms (right) streamwise velocities along the axis of symmetry

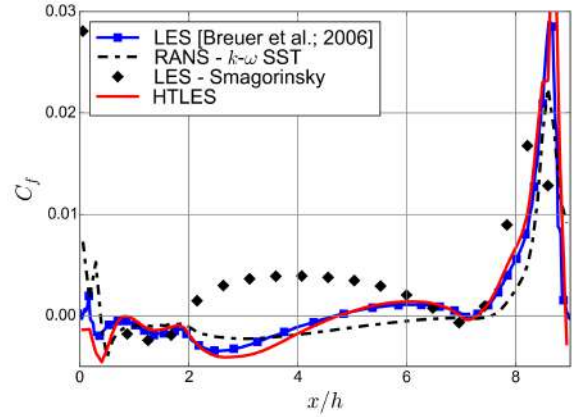


Figure 8: Hill flow. Distribution of skin friction on the lower wall [6]

Figure (6) shows that the flow in the vicinity of the cylinder is smooth and quasi-2D as in URANS computations. In the wake, the model gradually switches to the LES mode.

Figure (7) shows profiles extracted along the symmetry line behind the cylinder. URANS and HTLES are using the same closure, the  $k-\omega$ -SST model, and the same grid. This figure clearly shows the superiority of HTLES over URANS. The HTLES results are also close to the LES results, although the number of cells is reduced by a factor of 145 ( $0.5 \times 10^6$  vs.  $72.9 \times 10^6$ ), because the near-wall region is resolved in URANS mode.

### 3.2 Periodic-Hill Flow

The second case is the periodic hill [13] at  $Re_b = 10600$ . Computations are performed with Code\_Saturne [6], using the hybridized  $k-\omega$ -SST model. Figure (5) displays in the background the ratio  $r$ , which indicates that the hybrid model operates in RANS mode close to the two walls and in LES mode elsewhere.

The skin friction coefficient, Figure (8), is quite well reproduced compared to the results of the refined LES [13], although the number of grid cells is reduced by a factor of 70. RANS, using the same  $k-\omega$ -SST closure, is not able to reproduce the correct reattachment length. LES, using the same mesh as for HTLES does not give acceptable results, which shows the importance of switching to RANS close to the wall. The same conclusion was reached by Afailal *et al.* [5] using a different CFD code, *Converge CFD*: Figure (9) shows the drastic improvement of the velocity profiles.

Another particularly interesting point is that, as shown in Figure (10), HTLES is able to provide information on wall pressure fluctuations at the wall at a CPU cost much lower than LES, with the exception of the

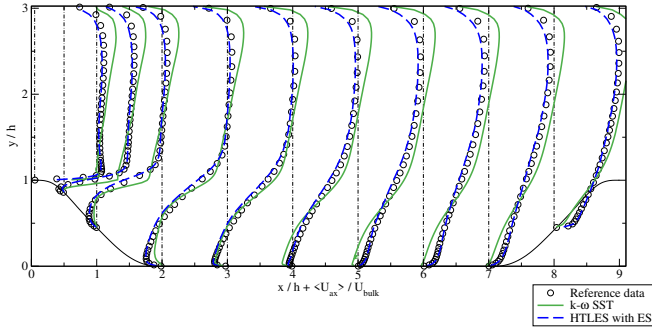


Figure 9: Hill flow. Streamwise velocity profiles. From Afailal *et al.* [5]

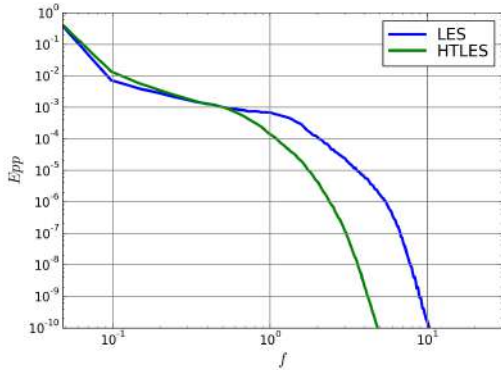


Figure 10: Hill flow. Pressure spectrum at the top of the hill [6]

highest frequencies, which can be very useful for predicting of unsteady pressure loads and mechanical fatigue in industrial applications.

### 3.3 Steady flow rig

The third case is called the *steady flow rig* [14], Figure (11), which is a simplified in-cylinder flow around a valve with a fixed lift at  $Re_b = 30000$ , computed using Converge CFD [5]. It can be seen in Figure (12) that RANS does not correctly reproduce the black-flow and the radial velocity. On the other hand, HTLES provides results similar to those of LES and is in relatively good agreement with the experiments.

But the most interesting result in favour of the hybrid model is the prediction of the pressure drop given

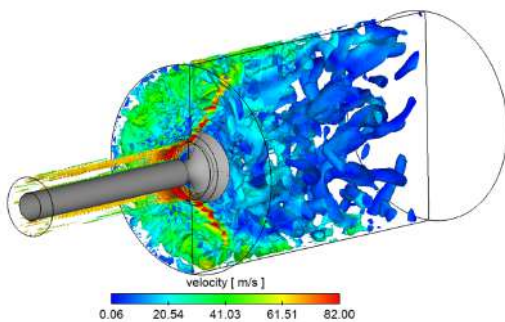


Figure 11: Steady flow rig. HTLES computation. Q-isosurfaces coloured by the velocity magnitude. Only half of the cylinder is shown. From Afailal *et al.* [5]

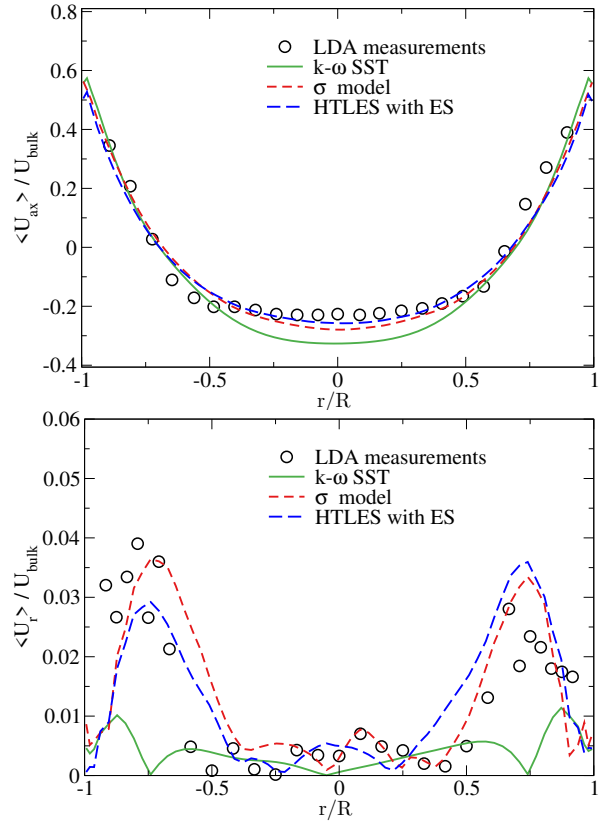


Figure 12: Steady flow rig. Velocity along a radial line located  $5.8D$  downstream the expansion. Top: axial component. Bottom: radial component. From Afailal *et al.* [5]

	EXP	RANS	HTLES	LES
$\Delta P$ [Pa]	1766	1713	1705	1957
Error [%]		-3	-3	+11

Table 1: Steady flow rig. Pressure drop between the inlet pipe and the outlet of the domain [5]

in Table (1). The success of HTLES in this matter compared to LES relies on the use of the RANS mode in the admission pipe and around the valve, where a refined LES would be necessary. This result is probably the best illustration of the main asset of hybrid methods in general, and HTLES in particular: the use of the most appropriate model in each region of the flow.

## 4 Conclusion

Temporal filtering provides a consistent formalism for the hybridization of RANS (or URANS) and LES, either for first or second moment closures. The resulting HTLES approach bears some similarities with DES, but migrates from RANS to LES in a very different way. Recent applications have demonstrated the performance of HTLES, which is able to provide results similar to those of LES, with a drastic cost reduction linked to the use of RANS in the near-wall region. These results also show the potential of hybrid approaches for the prediction of unsteady loads and as a solution to the issue of the prediction of the pressure drop with LES in industrial applications.

## Acknowledgements

Several colleagues and students have contributed over the years to the progress of time-filtered hybrid RANS/LES approaches. They are listed in alphabetical order: H. Afailal, Ch. Angelberger, J. Borée, V. Duffal, A. Fadai-Ghotbi, Ch. Friess, J. Galpin, T.B. Gatski, B. de Laage de Meux, R. Perrin, T.T. Tran, A. Velghe. The author is indebted to T.T. Tran, V. Duffal and H. Afailal for producing the results and figures presented in section 3. A part of this work was supported by ANR within the framework of the MONACO\_2025 project (ANR-17-CE06-0005-01 ACT).

## References

- [1] A. Fadai-Ghotbi, C. Friess, R. Manceau, T. Gatski, and J. Borée, “Temporal filtering: a consistent formalism for seamless hybrid RANS-LES modeling in inhomogeneous turbulence,” *Int. J. Heat Fluid Fl.*, vol. 31, no. 3, pp. 378–389, 2010.
- [2] R. Manceau, “Progress in Hybrid Temporal LES,” vol. 137 of *Notes on Numerical Fluid Mechanics and Multidisciplinary Design*, pp. 9–25, Springer, 2018.
- [3] C. Friess, R. Manceau, and T. Gatski, “Toward an equivalence criterion for hybrid RANS/LES methods,” *Comput. Fluids*, vol. 122, pp. 233–246, 2015.
- [4] T. Tran, R. Manceau, R. Perrin, J. Borée, and A. Nguyen, “A hybrid temporal LES approach. Application to flows around rectangular cylinders,” in *Proc. 9th ERCOFTAC Int. Symp. on Eng. Turb. Modelling and Measurements, Thessaloniki, Greece*, 2012.
- [5] H. Afailal, J. Galpin, A. Velghe, and R. Manceau, “Development and validation of a hybrid temporal LES model in the perspective of applications to internal combustion engines,” *Oil Gas Sci. Technol.*, vol. 74, no. 56, p. 16, 2019.
- [6] V. Duffal, B. de Laage de Meux, and R. Manceau, “Development and validation of a hybrid RANS/LES approach based on temporal filtering,” in *Proc. ASME-JSME-KSME Joint Fluids Eng. Conf. 2019, San Francisco, CA, USA*, 2019.
- [7] H. Tennekes, “Eulerian and Lagrangian time microscales in isotropic turbulence,” *J. Fluid Mech.*, vol. 67, pp. 561–567, 1975.
- [8] A. Fadai-Ghotbi, R. Manceau, and J. Borée, “A seamless hybrid RANS/LES model based on transport equations for the subgrid stresses and elliptic blending,” in *Proc. 5th Int. Symp. Turb. Shear Flow Phenomena, Munich, Germany*, 2007.
- [9] P. Spalart, S. Deck, M. Shur, K. Squires, M. Strelets, and A. Travin, “A new version of detached-eddy simulation, resistant to ambiguous grid densities,” *Theor. Comput. Fluid Dyn.*, vol. 20, no. 3, pp. 181–195, 2006.
- [10] T. Tran, *Développement d’une méthode hybride RANS-LES temporelle pour la simulation de sillages d’obstacles cylindriques*. PhD thesis, ENSMA, Poitiers, France, 2013.
- [11] D. Lyn, S. Einav, W. Rodi, and J.-H. Park, “Laser-Doppler velocimetry study of ensemble-averaged characteristics of the turbulent near wake of a square cylinder,” *J. Fluid Mech.*, vol. 304, pp. 285–319, 1995.
- [12] Y. Cao and T. Tamura, “Large-eddy simulations of flow past a square cylinder using structured and unstructured grids,” *Comput. Fluids*, vol. 137, pp. 36–54, 2016.
- [13] M. Breuer, B. Jaffrézic, N. Peller, M. Manhart, J. Fröhlich, C. Hinterberger, W. Rodi, G. Deng, O. Chikhaoui, S. Jakirlić, *et al.*, “A comparative study of the turbulent flow over a periodic arrangement of smoothly contoured hills,” in *Direct and Large-Eddy Simulation VI*, pp. 635–642, Springer, 2006.
- [14] L. Thobois, G. Rymer, T. Soulères, and T. Poinso, “Large-Eddy Simulation in IC Engine Geometries,” in *2004 SAE Fuels & Lubricants Meeting & Exhibition*, SAE International, 2004.

# NON-ZONAL DETACHED EDDY SIMULATION COUPLED WITH A STEADY RANS SOLVER IN THE WALL REGION

L. Davidson

*Div. of Fluid Dynamics, Dept. of Mechanics and Maritime Science  
Chalmers University of Technology, SE-412 96 Gothenburg, Sweden, www.tfd.chalmers.se/~lada*

## Abstract

Xiao *et al.* [1] proposed an interesting hybrid LES/RANS method in which they use two solvers and solve the RANS and LES equations in the entire computational domain. In the present work this method is simplified and used as a hybrid RANS-LES method, a *wall-modeled* LES. The two solvers are employed in the entire domain. Near the walls, the flow is governed by the steady RANS solver; drift terms are added to the DES equations to ensure that the time-integrated DES fields agree with the steady RANS field. Away from the walls, the flow is governed by the DES solver; in this region, the RANS field is set to the time-integrated LES field. The disadvantage of traditional DES models is that the RANS models in the near-wall region – which originally were developed and tuned for steady RANS – are used as URANS models where a large part of the turbulence is resolved. In the present method – where steady RANS is used in the near-wall region – the RANS turbulence models are used in a context for which they were developed. In this method, it may be worth while to use an accurate, advanced RANS model. The EARSM model is used in the steady RANS solver in the present work. The new method is called **N-Z S-DES**.

## 1 Introduction

DES (Detached-Eddy Simulation) uses unsteady RANS near walls (URANS region) and LES further away from walls (LES region). The resolved turbulence in the URANS region is often larger than the modeled part. But the RANS models used in the URANS region were originally developed and tuned in steady RANS simulations. Hence the accuracy and the validity of the RANS models in the URANS region can be questioned. In the present work, DES is coupled with *steady* RANS near the walls. We denote the method N-Z S-DES (**N**on-**Z**onal approach using **S**teady RANS coupled to **DES**).

Xiao *et al.* [1] proposed a new method in which they solve both the LES and RANS equations in the entire domain. The flow is in the near-wall region governed by the RANS equations and in the outer region it is governed by the LES equations. This is achieved by adding drift terms in the LES and RANS equations. In the interface region(s), the drift terms are modified by a linear ramp function. Drift terms are used in all equations in the RANS equations (momentum equations, the pressure equation (PISO is used)) and in the modelled turbulent equations ( $k$  and  $\epsilon$ ). Two drift terms are added in the LES momentum equations; one to ensure that the mean velocity fields in the RANS and LES equations are the same and one to ensure that the total turbulent kinetic energies are the same.

In [2] they extended the method to account for non-

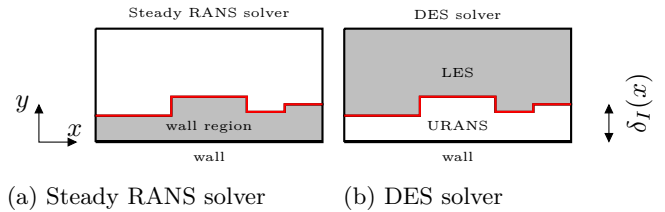


Figure 1: Grey color indicates the solver that drives the flow. The interface,  $I$ , is shown in red

conformal meshes. They used a Cartesian mesh for the LES equations and a body-fitted mesh for the RANS equations. They applied the method to fully developed channel flow and the flow over periodic hills. The paper shows how an accurate academic solver – massively parallel – can be combined with industrial, flexible RANS solvers.

Tunstall *et al.* [3] implement and use the method in [1] and modify it (different ramp function, different constants, reducing the number of case-specific constants etc). They apply it to fully developed channel flow and a rather complex flow consisting of a pipe junction including heat transfer. Hence, they have to introduce drift terms also in the energy equations.

Laage de Meux *et al.* [4] use forcing to achieve resolved Reynolds stress profiles equal to target modeled RANS stress profiles. The resolved Reynolds stresses are integrated in time in the same way as in [1, 3].

Breuer and Schmidt [5] use an advanced RANS turbulence model – the Explicit Algebraic Reynolds Stress Model, EARSM – in an hybrid LES-RANS methodology. However, as mentioned above, the disadvantage is that the RANS equations are solved in transient mode, where a large part of the large-scale turbulence is resolved.

Davidson [6] use the same model as in the present study. In [6], however, the interface is defined along a pre-selected gridline and the grid in the hump flow simulations is much coarser upstream the hump and in the outlet region. Moreover, the present work uses a different timescale in the drift term as well as evaluates different locations of the interface (see Eq. 6).

In the present study, the steady RANS equations are solved. Here it makes sense to use advanced RANS turbulence models, since these models were developed for steady RANS. The EARSM [7] is used in the RANS solver. The present method is in many aspects similar to that proposed in [1, 3] but it is simplified: the RANS equations are used in steady mode, a more advanced RANS turbulence model is used and the present method includes fewer drift terms and tuning constants.

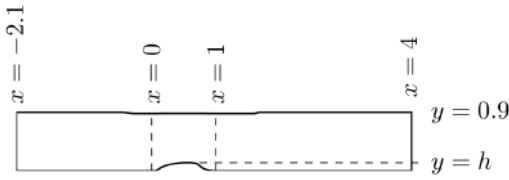


Figure 2: The domain of the hump.  $z_{max} = 0.3$

## 2 Numerical solvers

The momentum equations with an added turbulent viscosity read

$$\frac{\partial \bar{u}_i}{\partial t} + \frac{\partial \bar{u}_j \bar{u}_i}{\partial x_j} = \delta_{1i} - \frac{1}{\rho} \frac{\partial \bar{p}}{\partial x_i} + \frac{\partial}{\partial x_j} \left( (\nu + \nu_t) \frac{\partial \bar{u}_i}{\partial x_j} \right) \quad (1)$$

where the first term on the right side is the driving pressure gradient in the streamwise direction, which is used in the fully-developed channel flow simulations.

### 2.1 DES solver

An incompressible, finite volume code is used [8, 9]. The convective terms in the momentum equations are discretized using central differencing. Hybrid central/upwind is used for the  $k$  and  $\omega$  equations. The Crank-Nicolson scheme is used for time discretization of all equations. The numerical procedure is based on an implicit, fractional step technique with a multigrid pressure Poisson solver [10] and a non-staggered grid arrangement.

### 2.2 RANS solver

An incompressible, finite volume code – CALC-BFC [11] – is used. The transient term in Eq. 1 (the first term on the left side) is not included. The convective terms in the momentum equations are discretized using the second-order bounded scheme, MUSCL [12]. Hybrid central/upwind is used for the  $k$  and  $\omega$  equations. The numerical procedure is based on SIMPLEX and a staggered grid arrangement.

## 3 The N-Z S-DES methodology

Two sets of equations are solved (steady RANS solver, see Fig. 1a and DES solver, see Fig. 1b) in the entire domain on identical grids. The steady RANS solver may be two dimensional (as in the present work). Drift terms are added in the DES equations,  $S_i^{DES}$ , in the wall region, see Fig. 1a. The drift terms in the DES velocity equations read

$$S_i^{DES} = \frac{\langle v_i^{RANS} \rangle_T - \langle \bar{v}_i^{DES} \rangle_T}{\tau_r} \quad (2)$$

where  $\tau_r = \max(0.1k/\varepsilon, \Delta t)$  following [3]. No drift term is used in the pressure equation.  $\langle \cdot \rangle_T$  indicates integration over time,  $T$ , i.e.

$$\langle \phi(t) \rangle_T = \frac{1}{T} \int_{-\infty}^t \phi(\tau) \exp(-(t-\tau)/T) d\tau \Rightarrow \langle \phi \rangle_T^{n+1} \equiv \langle \phi \rangle_T = a \langle \phi \rangle_T^n + (1-a) \phi^n, \quad (3)$$

where  $a = 1/(1+\Delta t/T)$  and  $n$  denotes the timestep number. Note that although the flow cases in the present

work include homogeneous direction(s), no space averaging is made in Eq. 3. It may be noted that although the velocity field in the RANS solver is steady, it is time integrated when used in Eqs. 2 and 4 because it varies slightly in time. This time integration may not be necessary.

In the LES region, the RANS velocities are prescribed as  $v_i^{RANS} = \langle v_i^{LES} \rangle_T$  by adding a large source term, i.e.

$$S_i^{RANS} = \frac{\langle v_i^{LES} \rangle_T - \langle \bar{v}_i^{RANS} \rangle_T}{\epsilon} \quad (4)$$

where  $\epsilon = 10^{-10}$ . The pressure is simply set as  $\bar{p}^{RANS} = \langle p^{LES} \rangle_T$  and the pressure correction is set to zero. This means that, in reality, the steady RANS solver needs to be solved only in the wall region. In the LES region the momentum equations in the RANS solver are merely transporting the turbulence quantities,  $k$  and  $\omega$ , to ensure that correct values of  $k$  and  $\omega$  are transported into the RANS region through the LES-RANS interface at  $y = \delta_I$ , see Fig. 1. The pressure,  $\langle \bar{p}_{j+1}^{LES} \rangle_T$ , and the streamwise velocity,  $\langle \bar{u}_{j+1}^{LES} \rangle_T$ , at the LES-RANS interface are used as a boundary condition for the RANS equations in the wall region, see Fig. 3. The wall-normal velocity,  $\bar{v}_j^{RANS}$ , is solved for using the pressure at node  $j+1$ .

### 3.1 The $k - \omega$ model

The Wilcox  $k - \omega$  turbulence model reads

$$\begin{aligned} \frac{dk}{dt} &= P^k - \frac{k^{3/2}}{\ell_t} + \frac{\partial}{\partial x_j} \left[ \left( \nu + \frac{\nu_t}{\sigma_k} \right) \frac{\partial k}{\partial x_j} \right] \\ \frac{d\omega}{dt} &= C_{\omega 1} \frac{\omega}{k} P^k - C_{\omega 2} \omega^2 + \frac{\partial}{\partial x_j} \left[ \left( \nu + \frac{\nu_t}{\sigma_\omega} \right) \frac{\partial \omega}{\partial x_j} \right] \end{aligned} \quad (5)$$

where  $d/dt = \partial/\partial t + \bar{v}_j \partial/\partial x_j$  ( $\partial/\partial t = 0$  in the RANS solver). The standard coefficients are used, i.e.  $C_{\omega 1} = 5/9$ ,  $C_{\omega 2} = 3/40$ ,  $\sigma_k = \sigma_\omega = 2$  and  $C_\mu = 0.09$ . The location of the interface is defined as

$$C_I C_{DES} \Delta_{max} = \frac{k^{1/2}}{C_\mu \omega}. \quad (6)$$

$C_I = 1.0$  is the standard DES value. Here we use two different values,  $C_I = 1.0$  and  $C_I = 1.4$ . The result of the latter value is that the interface location is moved further away from the wall compared with standard DES.

### 3.2 The $k - \omega$ model in the DES solver

The DES equations are solved in the entire region, but they govern the flow only in the LES region, see Fig. 1. In the RANS regions, the lengthscale in Eq. 5 is computed as  $\ell_t = k^{1/2}/(C_\mu \omega)$  and in the LES region it is taken from the standard DES model, i.e.

$$\ell_t = C_{DES} \Delta_{max}, \quad \Delta_{max} = \max\{\Delta x, \Delta y, \Delta z\} \quad (7)$$

with  $C_{DES} = 0.67$ . The location of the interface in the DES solver is defined in the same way as between the RANS solver and the DES solver, i.e. by Eq. 6.

### 3.3 The $k - \omega$ EARSM model in the RANS solver

The steady RANS equations are solved in the entire region, but they govern the flow only in the RANS region, see Fig. 1. The Reynolds stresses,  $\bar{v}_i' v_j'$ , are computed from the two-dimensional explicit algebraic Reynolds stress model (EARSM) [7].

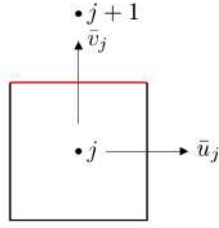


Figure 3: Control volume,  $j$ , in the wall region (RANS solver) adjacent to the interface,  $I$  (in red)

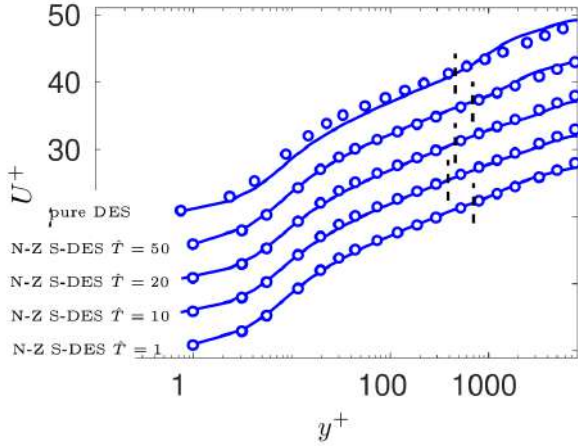


Figure 4: N-Z S-DES using different integration time  $\hat{T}$  compared with pure *DES*.  $\circ$ : Reichardt's law,  $U^+ = \frac{1}{\kappa} \ln(1 - 0.4y^+) + 7.8 [1 - \exp(-y^+/11) - (y^+/11) \exp(-y^+/3)]$ . Vertical black lines show DES interface

### 3.4 Initialization

The simulations are initialized as follows: first the 2D RANS equations are solved. Anisotropic synthetic fluctuations,  $(\mathcal{V}'_i)_m$ , are then superimposed to the 2D RANS field which gives the initial LES velocity field. The initial time integrated fields,  $\langle v_i^{LES} \rangle_T$  and  $\langle v_i^{RANS} \rangle_T$ , are also set from the 2D RANS field.

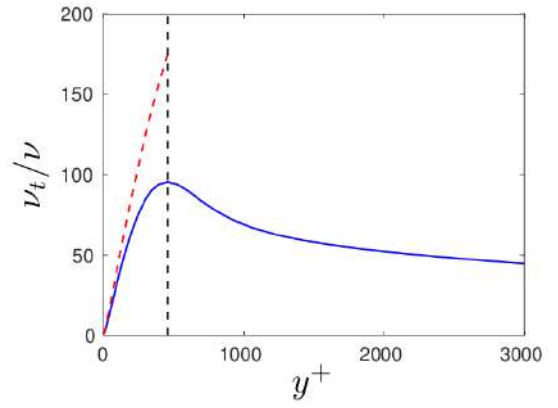
In order to compute  $(\mathcal{V}'_i)_m$ , synthetic fluctuations,  $v'_{i,synt}$ , are computed plane-by-plane ( $y-z$ ) in the same way as prescribing inlet boundary conditions. The synthetic fluctuations in the  $y-z$  planes are coupled with an asymmetric space filter

$$(\mathcal{V}'_i)_m = a(\mathcal{V}'_i)_{m-1} + b(v'_{synt,i})_m \quad (8)$$

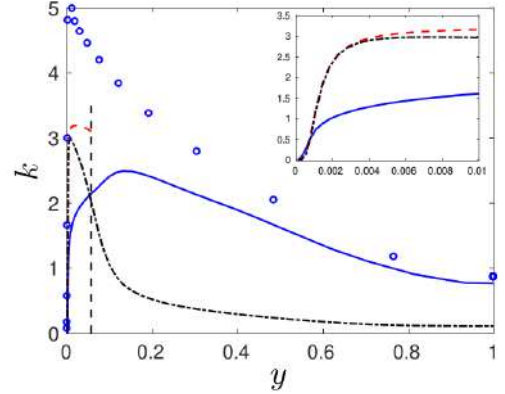
where  $m$  denotes the index of the  $x_1$  location and  $a = \exp(-\Delta x_1/L_{int})$  and  $\Delta x_1$  and  $L_{int}$  denote the grid size and the integral length scale, respectively ( $L_{int} = 0.2$ ).

## 4 Results

The first test case is fully developed channel flow with periodic boundary conditions in streamwise ( $x$ ) and spanwise ( $z$ ) directions. The Reynolds number,  $Re_\tau = u_\tau h/\nu$ , is 8000 where  $h$  denotes half-channel width. The size of the domain is  $x_{max} = 3.2$ ,  $y_{max} = 2$  and  $z_{max} = 1.6$ . The mesh has  $32 \times 96 \times 32$  ( $x, y, z$ ) cells. The interface between the wall region and LES is defined by Eq. 6. Four different integration times,  $T$  (see Eq. 3), are evaluated. It is important that the sampling time is

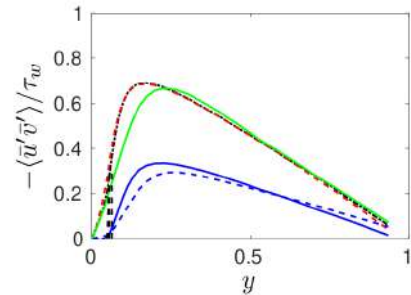


(a) Turbulent viscosity. —: DES solver; - - : RANS solver

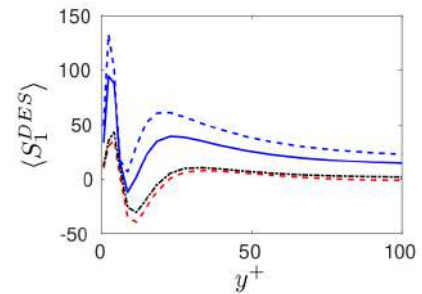


(b) Turbulent kinetic energy.  $\circ$ : DNS [13] at  $Re_\tau = 5,200$ ; - - : DES solver, modeled turbulence; —: DES solver, resolved turbulence; - - : RANS solver, modeled turbulence

Figure 5: Viscosity and turbulence. Vertical black lines show DES interface



(a) Resolved shear stresses. —: pure DES



(b) Drift term,  $\langle S_1^{DES} \rangle$ , see Eq. 2

Figure 6: Channel flow. —:  $\hat{T} = 1$ ; - - :  $\hat{T} = 10$ ; - - - :  $\hat{T} = 20$ ; - - - :  $\hat{T} = 50$ . Vertical black lines show DES interface

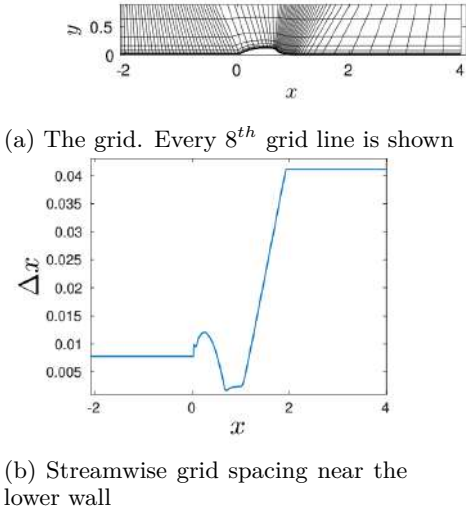


Figure 7: Grid and grid spacing

much larger than the integration time. If it is too small, it often gives an asymmetric time-averaged flow field. The time,  $\mathcal{T}$ , to reach fully developed condition and sampling time are both set to  $\hat{T} \equiv \mathcal{T}U_b/h = 1000$  except for  $\hat{T} = 50$  for which they are set to  $\hat{T} \equiv \mathcal{T}U_b/h = 2000$ . The switch is set to  $C_I = 1.4$  (Eq. 6) both for N-Z S-DES and pure DES.

Figure 4 compares the velocity profiles obtained with N-Z S-DES with that of pure DES. The velocity profiles predicted with N-Z S-DES for  $\hat{T} = 1, 10$  and  $20$  agree all very well with Reichardt's law but  $\hat{T} = 50$  shows a small log-layer mismatch. Pure DES exhibits the usual log-layer mismatch (larger than that for  $\hat{T} = 50$ ).

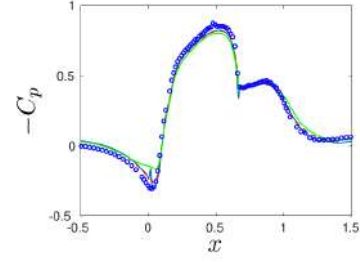
The turbulent viscosity and turbulent kinetic energies are presented in Figure 5. Figure 5a confirms that steady RANS gives a much larger turbulent viscosity than does the DES, i.e. steady RANS give much larger turbulent viscosity than URANS. The reason is that in DES, low  $k$  is transported into the URANS region from the LES region (the magnitudes of  $\omega$  at the interface are similar in steady RANS and DES). It can, however, be noted that close to the wall (for  $y < 0.01$ , see zoom), steady RANS and URANS give almost identical modeled kinetic energy, see Fig. 5b.

Figure 6a shows the resolved shear stresses. It can be seen that the peak of  $-\langle \bar{u}'\bar{v}' \rangle$  decreases for large ( $\hat{T} = 50$ ) and small ( $\hat{T} = 1$ ) integration time. In fully developed channel flow, the total (resolved plus modeled) shear stress is given by

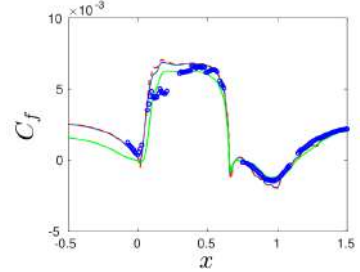
$$\tau_{tot} = \tau_w \left(1 - \frac{y}{h}\right). \quad (9)$$

Normally,  $\tau_w = 1$  because the driving pressure gradient is equal to one (the first term on the right side of Eq. 1). However, for small and large integration times, it turns out that the drift term in the DES momentum equation increases (see Fig. 6b) because  $\langle v_i^{RANS} \rangle_T$  is slightly larger than  $\langle \bar{v}_i^{DES} \rangle_T$ . Hence, in this case the wall shear stress,  $\tau_w$ , balances not only the driving pressure gradient but also the drift term. As a result,  $\tau_w$  increases. Xiao *et al.* [2] also report that the drift term affects the resolved shear stresses.

The second test case is the flow over a two-dimensional hump, see Fig. 2. The Reynolds number of the hump flow is  $Re_c = 936000$ , based on the hump length,  $c = 1$ , and the inlet mean velocity at the centerline,  $U_{in,c} = 1$ . The



(a) Pressure coefficient



(b) Skinfriction

Figure 8:  $T = 10h/U_{in}$ . — : N-Z S-DES, DES solver; - - : N-Z S-DES, RANS solver; — : pure DES

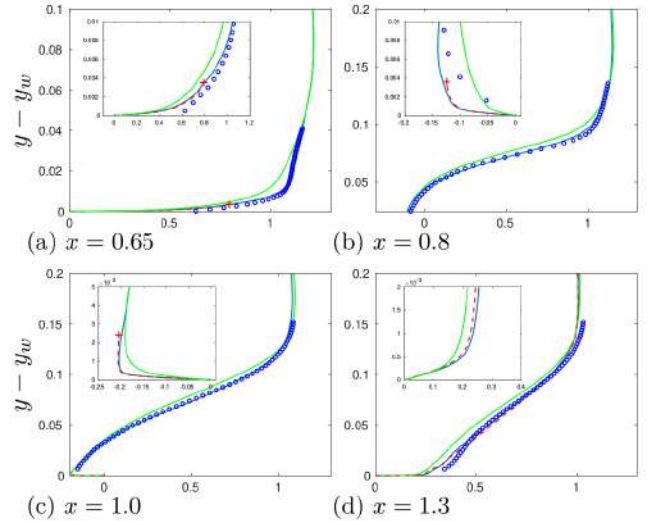


Figure 9: Velocities.  $T = 10h/U_{in}$ . — : N-Z S-DES, DES solver; - - : N-Z S-DES, RANS solver; — : pure DES; o : exp; +

inlet is located at  $x = -2.1$  and the outlet at  $x = 4.0$ , see Fig. 2. The mesh has  $650 \times 110 \times 66$  cells ( $x, y, z$ ) and it is based on the mesh from the NASA workshop<sup>1</sup> but it is refined upstream of the hump and in the outlet region, see Fig. 7a. The spanwise extent of the domain is set to  $0.3$  so that  $\Delta z = 0.3/64 = 0.0047$ . The required resolution for an LES away from the wall (in the log-region) is  $\Delta x/\delta \simeq 10$ ,  $\Delta z/\delta \simeq 20$ . The streamwise spacing,  $\Delta x$ , near the wall is shown in Fig. 7b. The inlet boundary layer thickness is  $\delta_{in} = 0.08$  which means that the resolution in the inlet region reasonable ( $\Delta x/\delta_{in} \simeq 10$ ,  $\Delta z/\delta_{in} \simeq 17$ ). The boundary layer thickness after the recirculation bubble ( $x > 1.3$ ) is  $\delta \simeq 0.13$  (see Fig. 9d) so that  $\Delta x/\delta \simeq 3$  which is somewhat too small; this region is, however, believed to be less critical than the inlet and hump region.

The inlet profiles are taken from a separate 2D RANS

<sup>1</sup>[https://turbmodels.larc.nasa.gov/nasahump\\_val.html](https://turbmodels.larc.nasa.gov/nasahump_val.html)



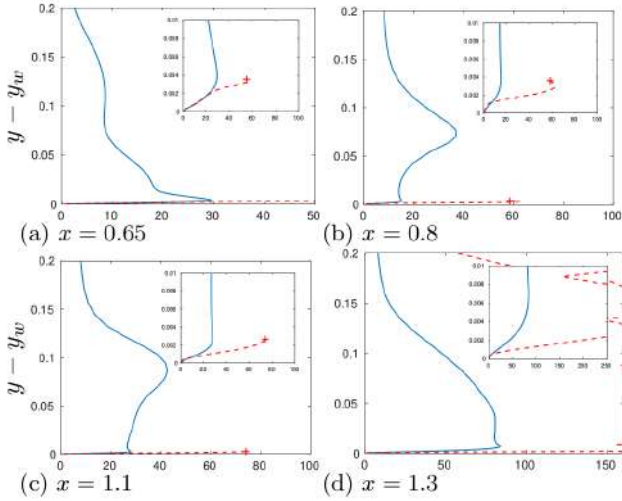


Figure 10: Turbulent viscosity.  $T = 10h/U_{in}$ . — : DES solver; - - : RANS solver

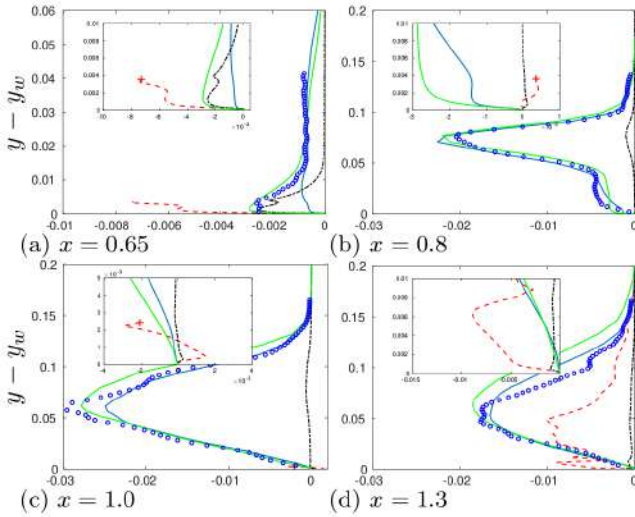
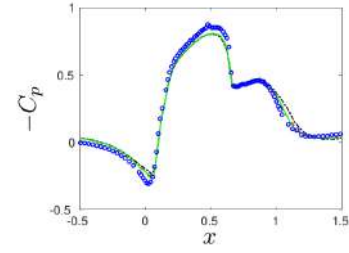


Figure 11: Shear stresses.  $T = 10h/U_{in}$ . — : DES solver, resolved; - - : RANS solver; - · - : DES solver, modeled; — : DES solver, resolved

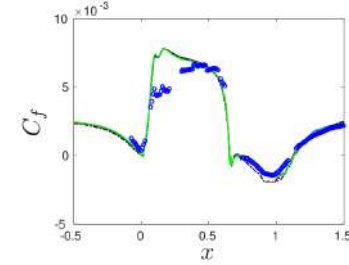
simulation with the same momentum thickness as the experimental velocity profiles. Anisotropic synthetic fluctuations are superimposed to the inlet velocity profile (for more detail, see [14]). Periodic boundary conditions are used in the spanwise direction ( $z$ ). The interface between the wall region and the LES domain as well as that between the steady RANS solver and the DES solver is defined by Eq. 6.

The pressure coefficient and skin friction are presented in Fig. 8. As can be seen, the agreement with experiments is good for both N-Z S-DES and pure DES except that the pure DES predicts slightly too low a skinfriction upstream of the hump. For the channel flow it was found that for too large and too small  $\hat{T}$ , the drift term in the DES equation was comparable to the driving pressure gradient. Figure 8a shows no such problems for the hump flow with  $\hat{T} = 10$ ; the pressure from the RANS and DES solvers are virtually identical (there are small differences at  $x \simeq 0$  and  $x \simeq 0.66$ ).

Figure 9 compares the predicted velocity profiles with experiments. The S-Z S-DES gives a better agreement with experiments than pure DES; in particular, the latter gives a worse velocity profile of the boundary layer at



(a) Pressure coefficient



(b) Skinfriction

Figure 12: N-Z S-DES, RANS solver.  $C_I = 1.0$ . — :  $T = 10$ ; - - :  $T = 20$ ; - · - :  $T = 5$ ; — :  $T = 40$

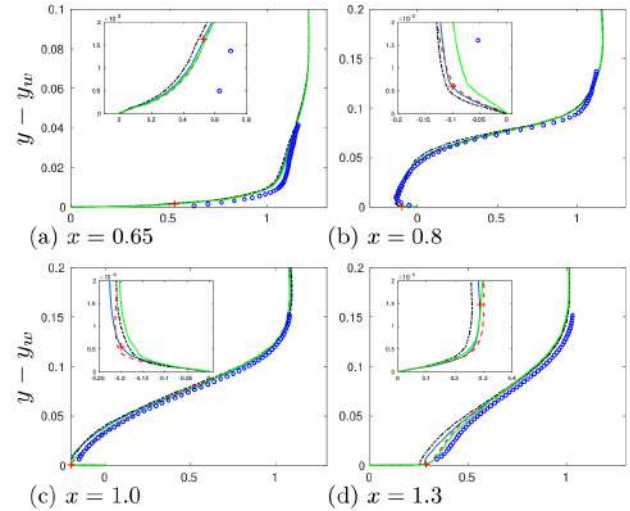


Figure 13: Velocities. N-Z S-DES.  $C_I = 1.0$ . — :  $T = 10$ ; - - :  $T = 20$ ; - · - :  $T = 5$ ; — :  $T = 40$

$x = 0.65$ . The velocity profiles of the RANS solver are also included. The RANS solver velocity profiles in the wall region match those of the DES solver as they should. The locations of the interface is shown with a red plus sign. It may be noted that the location of the interface at  $x = 1.3$  is not seen and it seems that it is located at  $y > 0.2$ . This will be discussed below.

The turbulent viscosity is shown in Fig. 10. As for the channel flow, the turbulent viscosity predicted by the RANS solver is much larger than that predicted by the DES solver, especially in the recirculation region. Again, as was seen in Fig. 9d, it seems that the interface is located at  $y > 0.2$ ; this is also seen for the turbulent shear stress in Fig. 11d.

Figure 11 presents the predicted and measured shear stresses. The agreement between the resolved shear stresses and the measured is good downstream of the separation point. What is somewhat surprising is that at  $x = 0.65$  the N-Z S-DES models most of the turbulence rather than resolving it (the magnitude of the modeled shear is much larger than the resolved one). This should

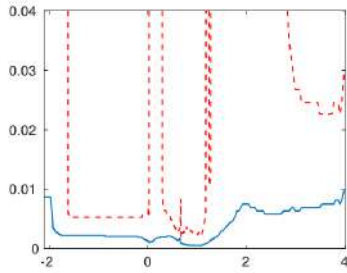


Figure 14: Location of interface.  $\hat{T} = 10$ . — :  $C_I = 1.0$ ; - - :  $C_i = 1.4$

probably be viewed as a drawback of the N-Z S-DES.

Figures 12 – 13 present simulations using four different values  $\hat{T} = 5$ ,  $\hat{T} = 10$ ,  $\hat{T} = 20$  and  $\hat{T} = 40$ . The time,  $\mathcal{T}$ , to reach fully developed condition and sampling time are set to  $\hat{T} \equiv \mathcal{T}U_b/h = 175$  and 90, respectively, for all integration times,  $\hat{T}$  ( $h$  denotes hump height, see Fig. 2). This is much smaller than for the channel flow. It is believed that the channel flow is particularly sensitive because of the streamwise periodic boundary conditions which lacks a stabilizing inlet boundary condition. Figures 12 – 13 show that the flow is only weakly dependent to the integration time,  $\hat{T}$ . The lowest value,  $\hat{T} = 5$ , gives somewhat worse agreement than the other three.

The switch between RANS and DES (i.e. the interface) is in Figs. 8 – 11 defined by  $C_I = 1.4$  (see Eq. 6). In Figs. 12 – 13 the switch is defined by  $C_I = 1.0$ , i.e. the standard switch in pure DES. Figure 14 presents the location of the interface for the hump simulations. When the switch is defined as  $C_I = 1.4$  it is seen that there are three regions where the interface is located at  $y > 0.04$ : near the inlet ( $x < -1$ ), at  $x \simeq 0.12$  and at  $1.26 < x < 1.8$ . The interface in these three regions is actually located at the upper boundary, i.e. the entire region is covered by the RANS solver. However, as seen in Figs. 12 – 13, the influence of the location is not large (compare the blue solid lines in Figs. 12 – 13 with Figs. 8 – 9). The largest differences are found in the skinfriction at  $x \simeq 0.18$  and as a result the velocity profile is less full in Fig. 13a than in Fig. 9a.

## 5 Conclusions

A new non-zonal model based on a steady RANS solver in the wall region coupled to a DES solver which covers the entire region. The steady RANS solver is called very 10th timestep. The RANS solver dictates the flow in the wall region. A drift term in the wall region in the DES solver forces the time-integrated DES flow to match that of the RANS flow. The steady RANS solver velocity field is set to that of the time-integrated DES flow in the off-wall region. The only object of the steady RANS field in the off-wall region is to transport the modeled turbulent quantities ( $k$  and  $\omega$ ) into the wall region. They –  $k$  and  $\omega$  – could instead be transported by the time-integrated DES flow.

The new model is evaluated in fully developed channel flow and the hump flow. Very good agreement with experiments is obtained. However, three issues are identified. First, the drift term in the DES solver in the wall region – which is the ratio of the difference between the steady RANS velocity field and that of the time-integrated DES to a turbulent relaxing timescale –

is non-zero which acts as an additional driving pressure gradient. No such problem is seen in the hump flow. Second, the time integration is chosen over a certain time,  $T = \hat{T}h/U_b$ , where values of  $\hat{T}$  between one and 50 have been evaluated. For the channel flow simulations, too large ( $\hat{T} = 50$ ) or too small ( $\hat{T} = 1$ ) values act as an additional driving pressure gradient. For the hump flow, the influence of  $\hat{T}$  is small. Third, in the attached boundary layer over the hump, the modeled turbulence in the DES solver is larger than the resolved one. In the near future, the reason for this will be analyzed by making simulations of developing flat-plate boundary layers.

## References

- [1] H. Xiao and P. Jenna, “A consistent dual-mesh framework for hybrid LES/RANS modeling,” *Journal of Computational Physics*, vol. 231, pp. 1848–1865, 2012.
- [2] H. Xiao, Y. Sakai, R. Henniger, M. Wild, and P. Jenna, “Coupling of solvers with non-conforming computational domains in a dual-mesh hybrid LES/RANS framework,” *Computers & Fluids*, vol. 88, pp. 653–662, 2013.
- [3] R. Tunstall, D. Laurence, R. Prosser, and A. Skillen, “Towards a generalised dual-mesh hybrid les/rans framework with improved consistency,” *Computers & Fluids*, vol. 157, pp. 73–83, 2017.
- [4] B. de Laage de Meux, B. Audebert, R. Manceau, and R. Perrin, “Anisotropic linear forcing for synthetic turbulence generation in large eddy simulation and hybrid RANS/LES modeling,” *Physics of Fluids A*, vol. 27, no. 035115, 2015.
- [5] M. Breuer and S. Schmidt, “Hybrid LES-RANS modeling of complex turbulent flows,” *PAMM – Proc. Appl. Math. Mech.*, vol. 14, pp. 647–650, 2014.
- [6] L. Davidson, “Zonal detached eddy simulation coupled with steady RANS in the wall region,” *ECCOMAS MSF 2019 Thematic Conference, Minisymposium “devoted to 80th birthday of Prof. Kemo Hanjalic”*, Sarajevo, 2019.
- [7] S. Wallin and A. V. Johansson, “A new explicit algebraic Reynolds stress model for incompressible and compressible turbulent flows,” *Journal of Fluid Mechanics*, vol. 403, pp. 89–132, 2000.
- [8] L. Davidson and S.-H. Peng, “Hybrid LES-RANS: A one-equation SGS model combined with a  $k - \omega$  for predicting recirculating flows,” *International Journal for Numerical Methods in Fluids*, vol. 43, no. 9, pp. 1003–1018, 2003.
- [9] L. Davidson, “CALC-LES: A Fortran code for LES and hybrid LES-RANS,” tech. rep., Division of Fluid Dynamics, Dept. of Mechanics and Maritime Sciences, Chalmers University of Technology, Gothenburg, 2018.
- [10] P. Emvin, *The Full Multigrid Method Applied to Turbulent Flow in Ventilated Enclosures Using Structured and Unstructured Grids*. PhD thesis, Chalmers University of Technology, Göteborg, 1997.
- [11] L. Davidson and B. Farhanieh, “CALC-BFC: A finite-volume code employing collocated variable arrangement . . .” Rept. 95/11, Chalmers University of Technology, Gothenburg, 1995.
- [12] B. van Leer, “Towards the ultimate conservative difference scheme. V. A second-order sequel to godonov’s method,” *Journal of Computational Physics*, vol. 32, pp. 101–136, 1979.
- [13] M. Lee and R. D. Moser, “Direct numerical simulation of turbulent channel flow up to  $Re_\tau \approx 5200$ ,” *Journal of Fluid Mechanics*, vol. 774, pp. 395–415, 2015.
- [14] L. Davidson, “Zonal PANS: evaluation of different treatments of the RANS-LES interface,” *Journal of Turbulence*, vol. 17, no. 3, pp. 274–307, 2016.

# HYBRID RANS/LES APPLICATIONS AT DASSAULT AVIATION

F. Billard\*, F. Chalot, F. Dagrau, L. Daumas  
M. Mallet, P.E. Normand and P. Yser†

**DASSAULT AVIATION**

78, quai Marcel Dassault. 92552 Saint-Cloud Cedex, France

## Abstract

The following provides an update on recent developments and applications of hybrid RANS/LES methods at Dassault-Aviation. The in-house solver Aether is first introduced, with a focus on the stabilised finite element method applied to the entropy formulation of the Navier Stokes equation. Then, two applications are presented: the effect of space-scheme order and mesh refinement on the M219 cavity; and the wall-modelling effect on the buffeting prediction on a supercritical laminar airfoil. Finally a new hybrid RANS/LES high-order modelling strategy hybridising variational multi-scale with a near-wall model is introduced, with an application to the LEISA II slat-noise prediction.

## 1 Introduction

The range of hybrid RANS/LES applications in daily aeronautical engineering has significantly widened over the past decade, not only because of a constant growth of available CPU capacity. Indeed the aeronautical sector has never been so competitive and is subject to increasingly tougher environmental regulations. To shape tomorrow's innovative designs and reduce margins the need for reliable CFD predictions is therefore of the utmost importance, in particular at the limits of the flight envelope, where cheaper steady RANS modelling is often inaccurate. Not to mention flows dominated by large scale unsteadiness, such as buffet, buzz at supersonic intake, intake at high angle of attack, massively separated flows, and aero-acoustics assessment.

At Dassault-Aviation, hybrid RANS/LES methods have been used for over two decades [1, 2] and developments have been kept up-to-date through active participation in several European project, such as LESFOIL, DESIDER and ATAAC, related to hybrid RANS/LES modelling, as well as ADIGMA, IDIHOM and TILDA on high-order method; and several PhD topics on variational multi-scale modelling [3], high-order methods [4], and high-order VMS [5]. Some of these developments and applications will now be presented in this paper.

## 2 The Navier-Stokes solver

The following provides a brief description of the in-house unstructured stabilised finite element code Aether.

\*flavien.billard@dassault-aviation.com

†Authors are given in alphabetical order

## 2.1 Entropy variables and symmetry

The conservative form of the continuity, momentum and energy equations can be written in the following matrix form:

$$\underline{\mathbf{U}}_{,t} + \underline{\mathbf{A}}_i \underline{\mathbf{U}}_{,i} = (\underline{\mathbf{K}}_{ij} \underline{\mathbf{U}}_{,j})_{,i} \quad (1)$$

Where  $\underline{\mathbf{U}}$  represents the conservative variables,  $\underline{\mathbf{A}}_{ij} = \mathcal{F}_{i,\underline{\mathbf{U}}}$  is the  $i^{\text{th}}$  advective Jacobian matrix and  $\underline{\mathbf{K}}_{ij}$  is the diffusive matrix defined such as  $\underline{\mathbf{K}}_{ij} \underline{\mathbf{U}}_{,j} = \mathcal{F}^{\text{diff}}$ . These matrices are defined with the following vectors

$$\underline{\mathbf{U}} = \rho \begin{pmatrix} 1 \\ u_1 \\ u_2 \\ u_3 \\ e + \frac{1}{2}u^2 \end{pmatrix}; \quad \mathcal{F}_i = \rho u_i \underline{\mathbf{U}} + p \begin{pmatrix} 0 \\ \delta_{1i} \\ \delta_{2i} \\ \delta_{3i} \\ u_i \end{pmatrix}$$

$$\mathcal{F}^{\text{diff}} = \begin{pmatrix} 0 \\ \sigma_{1i}^D \\ \sigma_{2i}^D \\ \sigma_{3i}^D \\ \sigma_{ji}^D u_i - q_j^T \end{pmatrix}$$

with  $\rho$  the density,  $u_i$  the velocity in the  $i^{\text{th}}$  direction,  $e = p/(\gamma - 1)$ ,  $u^2 = u_i u_i$ ,  $q_j^T$  the thermal flux evaluated using the Fourier's law,  $\underline{\sigma}^D = 2\mu \underline{\mathbf{S}}^D$ , the Stokes hypothesis is used, and  $\underline{\mathbf{S}}^D$  is the deviatoric part of the strain tensor defined as  $\underline{\mathbf{S}}^D = \underline{\mathbf{S}} - 1/3 \text{tr}(\underline{\mathbf{S}}) \underline{\mathcal{I}}$  where  $\underline{\mathbf{S}} = 1/2 (\underline{\text{grad}}(\underline{\mathbf{u}}) + \underline{\text{grad}}(\underline{\mathbf{u}})^T)$  is the symmetric part of the strain tensor,  $\underline{\mathcal{I}}$  the identity matrix and  $\mu$  the dynamic viscosity.

As proposed in [6], the generalised entropy function  $\mathcal{H}$  given by ( $s$  the entropy per unit mass and  $\gamma$  the specific heat ratio):

$$\mathcal{H} = \mathcal{H}(\underline{\mathbf{U}}) = -\rho s \text{ with } s = c_v \ln \frac{p}{\rho^\gamma} + s_0$$

is used in the following change of variable  $\mathcal{V} : \underline{\mathbf{U}} \rightarrow \underline{\mathbf{V}}$  defined as

$$\underline{\mathbf{V}} = \mathcal{V}(\underline{\mathbf{U}}) = \frac{\partial \mathcal{H}^T}{\partial \underline{\mathbf{U}}} \quad (2)$$

Using the variable  $\underline{\mathbf{V}}$  the equations can be reformulated as follows:

$$\tilde{\underline{\mathbf{A}}}_0 \underline{\mathbf{V}}_{,t} + \tilde{\underline{\mathbf{A}}}_i \underline{\mathbf{V}}_{,i} = (\tilde{\underline{\mathbf{K}}}_{ij} \underline{\mathbf{V}}_{,j})_{,i} \quad (3)$$

Where  $\tilde{\underline{\mathbf{A}}}_0$  is the change of variable matrix and  $\underline{\mathbf{V}}$  is defined by

$$\underline{\mathbf{V}} = \frac{1}{T} \begin{pmatrix} g - \frac{u^2}{2} \\ u_1 \\ u_2 \\ u_3 \\ -1 \end{pmatrix} \quad (4)$$

where  $g = h - Ts$  is the Gibbs free enthalpy and  $T$  the temperature. The matrices  $\tilde{\underline{\mathbf{A}}}_0$ ,  $\tilde{\underline{\mathbf{A}}}_i$ ,  $\tilde{\underline{\mathbf{K}}}_i = [\tilde{\underline{\mathbf{K}}}_{ij}]$  are symmetric,  $\tilde{\underline{\mathbf{A}}}_0$  is positive definite and  $\tilde{\underline{\mathbf{K}}}$  is positive semi-definite. The entropy formulation has numerous interesting mathematical properties (symmetric operators with positivity properties, efficient preconditioning, ...) very useful for the numerical resolution of the problem.

## 2.2 Stabilised Finite element method

The variational formulation of Eq. (3) is obtained by multiplying this equation with the weighting functions  $\underline{\mathbf{W}}$  taken in the same functional space as  $\underline{\mathbf{V}}$ . This yields

$$\int_{\Omega} \underline{\mathbf{W}} \cdot \left( \tilde{\underline{\mathbf{A}}}_0 \underline{\mathbf{V}}_{,t} + \tilde{\underline{\mathbf{A}}}_i \underline{\mathbf{V}}_{,i} - \left( \tilde{\underline{\mathbf{K}}}_{ij} \underline{\mathbf{V}}_{,j} \right)_{,i} \right) d\Omega = 0 \quad (5)$$

where  $\tilde{\underline{\mathbf{A}}}_0 \underline{\mathbf{V}}_{,t} + \tilde{\underline{\mathbf{A}}}_i \underline{\mathbf{V}}_{,i} - \left( \tilde{\underline{\mathbf{K}}}_{ij} \underline{\mathbf{V}}_{,j} \right)_{,i}$  is defined as the residual part of Eq. (5) and  $\Omega$  denotes the volume of the computational domain. Using the Galerkin method, the Navier-Stokes equations are known to be numerically unstable for convection dominated flows ( $Pe = uL/\nu \gg 1$ ). This approach is therefore stabilised using the Petrov-Galerkin method, which consists in adding a perturbation  $P$  to the weighting function  $\underline{\mathbf{W}} \rightarrow \underline{\mathbf{W}} + \underline{\mathbf{P}}(\underline{\mathbf{W}})$ . The Galerkin/Least-Square method is used herein where the perturbation function is chosen as  $\underline{\mathbf{P}} = \underline{\tau} \underline{\mathcal{L}}(\underline{\mathbf{W}})$  where  $\underline{\mathcal{L}} = \tilde{\underline{\mathbf{A}}}_i \partial / \partial \underline{\mathbf{x}}_i - \left( \tilde{\underline{\mathbf{K}}}_{ij} \partial / \partial \underline{\mathbf{x}}_i \right)_{,i}$  is the Navier-Stokes operator of Eq. (3). To control the convection, an artificial dissipation is added to the equation by the mean of the intrinsic time scale matrix  $\underline{\tau}$  which is based on the eigenvalues of  $\tilde{\underline{\mathbf{A}}}_0$ ,  $\tilde{\underline{\mathbf{A}}}_i$  and  $\tilde{\underline{\mathbf{K}}}_{ij}$ . The aim is to correct the unbalanced convection solved in Galerkin method numerical scheme, by comparing this term to the overall dissipation of the computation. The stabilised equations of the entropy formulation are then given by

$$\int_{\Omega} (\underline{\mathbf{W}} + \underline{\tau} \underline{\mathcal{L}}(\underline{\mathbf{W}})) \cdot \left( \tilde{\underline{\mathbf{A}}}_0 \underline{\mathbf{V}}_{,t} + \underline{\mathcal{L}}(\underline{\mathbf{V}}) \right) d\Omega = 0 \quad (6)$$

This is strictly equivalent to the *Streamline Upwind Petrov-Galerkin* (SUPG) stabilisation (where only the convective term is kept in the first  $\underline{\mathcal{L}}$  operator) when linear interpolation functions are used, as the diffusive contribution to  $\underline{\mathcal{L}}$  is then zero. This formulation is employed in the Aether code.

## 2.3 Turbulence closure

Several RANS models are available in Aether, ranging from one and two-equation formulations (Spalart Allmaras, two-layer  $k-\varepsilon$ , SST  $k-\omega$  and  $k-kL$  [7],  $BL-\bar{v}^2/k$  [8]) to Reynolds Stress Models (EB-RSM [9], SSG/LRR [10]). For unsteady simulations several strategies are used:

- Second and third order LES, with Smagorinsky or VMS models
- Zonal DES [11] available with Spalart Allmaras,  $k-\varepsilon$ ,  $k-\omega$  and  $k-kL$  as underlying near-wall RANS model.
- Third order VMS hybridised with the Spalart Allmaras model[12] in the near-wall region.

## 3 High-order LES of cavity flows

Simulation results on the transonic M219 QinetiQ cavity flow [13, 14] are summarised below. The geometry is a simplified model of an aircraft bay at approximately  $1/10^{th}$  scale. The cavity has a length/depth ratio of 5 and a width/depth ratio of unity. No bay doors are present. The Mach number is  $M = 0.85$  and the unit Reynolds number is 13 million  $m^{-1}$ . The main focus of this study [14] was the low-frequency aero-acoustic coupling between upward shear-layer vortices and acoustic waves retroaction (Rossiter modes) which can be detrimental to the structure. The study covered the influence of several simulation parameters (order of the space interpolation functions, mesh refinement and variants of the Smagorinsky sub-grid scale modelling). The flow structures (iso-surfaces of the Q-criterion) are shown on Figure (1) and Figure (2) for LES with order 2 and order 3 spatial scheme (O2 and O3). The scheme order directly influences the nature of resolved turbulent content, allowing the development of thinner and more 3-D structures. The vortex breakdown throughout the cavity shear layer is better captured with the O3 scheme. This is also confirmed when looking at the overall frequency integration of the resolved kinetic energy along the cavity shear layer Figure (3), where the level of resolved kinetic energy is higher by almost one order of magnitude in the beginning of the shear layer. Figure (3) also shows that O3 simulation is less dissipative than O2 simulation on a refined mesh, thus stressing the beneficial effect of using high-order scheme with finite element method, in terms of efficiency (higher accuracy for lower CPU cost).

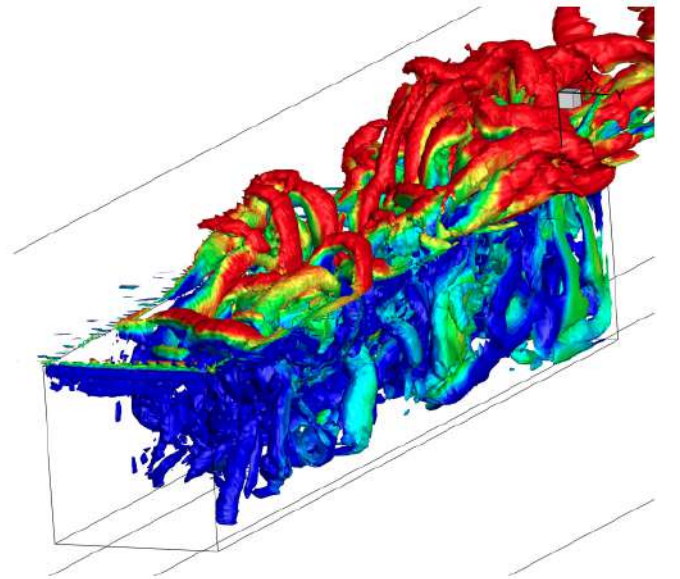


Figure 1: M219 Cavity: Q-criterion standard-order structures

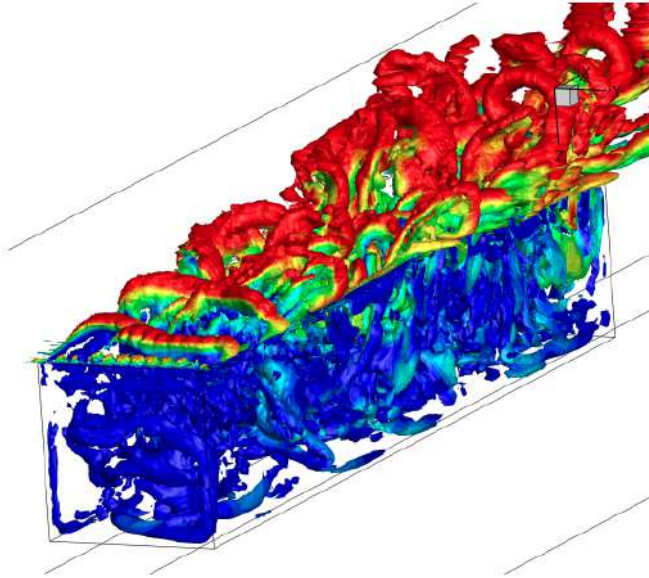


Figure 2: M219 Cavity: Q-criterion high order structures

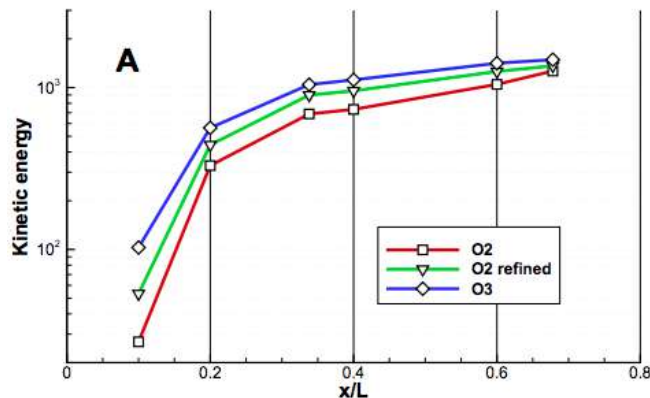


Figure 3: M219 Cavity: Band integration (50Hz - 200Hz) of resolved kinetic energy  $\|V^2\|$  along the shear layer

## 4 Transitional buffeting

Application of the ZDES method for simulation of transitional buffet was undertaken in the framework of the European TFAST project<sup>1</sup> (<http://tfast.eu>). The configuration is the V2C airfoil (see Figure (4)) which is a supercritical laminar profile designed by Dassault Aviation for numerical benchmark purpose across partners. Reference data both experimental [15, 16] and numerical [17] (highly resolved implicit LES) were produced within the extent of the project for comparison with CFD. The aim is to compare the buffet characteristics (course of the shock and pressure fluctuation magnitude) between fully turbulent, transitional and laminar shock / boundary layer interaction. The flow parameters are  $M = 0.7$  and  $\alpha = 7^\circ$ . Simulations using ZDES [11] coupled with the 2-layer  $k - \varepsilon$  and Spalart Allmaras models were produced with fully turbulent boundary layer from the leading edge. The  $k - \varepsilon$ -ZDES was repeated with a boundary layer tripping at 24% chord (*i.e.* the production term of the turbulent kinetic energy is switched off before the tripping point), which corresponds to the most upstream shock position.

A time step of  $10^{-6}s$  was used and the mesh was extruded over 33% chord on the spanwise direction with

<sup>1</sup>Transition Location Effect on Shock Wave Boundary Layer Interaction

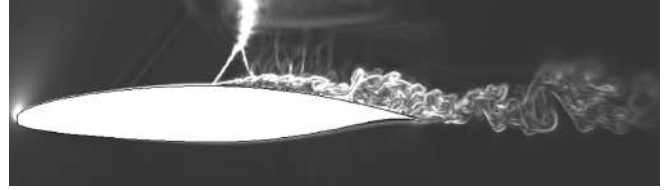


Figure 4: V2C: Schlieren for the ZDES- $k - \varepsilon$  with tripped BL

80 grid points. One of the outcomes of the benchmark was that mesh resolution around the profile plays a major role in the overall flow prediction quality. In the present simulation, around 2000 grid points were clustered around the profile which is as many as for the 500+ million nodes mesh of the ILES [17], while retaining a mere 13 millions grid points mesh in total. This was possible thanks to the present unstructured meshing strategy, which allows focussing the grid refinement in the region of interest. The typical mesh spacing in wall unit are given below

	Near-wall region	LES region
$\Delta X^+$	150	150
$\Delta Y^+$	0.25	150
$\Delta Z^+$	410	410

The flow pattern is shown on the Schlieren visualisation  $\|\nabla\rho\|$  (Figure (4)) and the Q-criterion (Figure (5)): the flow separates at the shock; Kelvin-Helmholtz (KH) instabilities appear right from the beginning of the separated shear layer downstream of the shock-induced separation; the Von Kármán pattern (VK) is well captured in the wake. However a strong influence of the underlying RANS model in the present ZDES simulations was observed:

- The shock oscillates between 15% and 42% of the chord length for the SA-ZDES (that is a 27% chord length amplitude), and between 25% and 40% of the chord length for the  $k - \varepsilon$ -ZDES (that is a 15% chord length amplitude).
- The buffeting frequency is 106Hz and 119Hz, respectively for the SA-ZDES and the  $k - \varepsilon$ -ZDES (corresponding Strouhal numbers  $St = 0.093$  and  $St = 0.104$ ), which are only slightly above the reference value [18].
- KH are more noticeable for the  $k - \varepsilon$ -ZDES model than for the SA-ZDES with characteristic frequency of about 10kHz, whereas the VK are stronger for the SA-ZDES results.
- VK frequency is 1970Hz and 2700Hz for the SA-ZDES and the  $k - \varepsilon$ -ZDES respectively.

The spectral map in Figure (6) evidences the sustenance of instabilities at buffeting frequency throughout the separated shear layer, suggesting a coupling phenomenon between the buffeting, KH and VK mechanisms, as supported by [17].

The effect of boundary layer tripping was only to shift further downstream the averaged shock position. It did not change the oscillation amplitude. The buffeting frequency, VK and KH were not noticeably affected, unlike what is observed for transitional buffeting [19] (much higher oscillation frequency,  $St \simeq 1$  and smaller

oscillation amplitude). To properly capture transitional buffeting characteristics in a ZDES framework, the boundary layer tripping location should be updated at each time step to follow the shock location.

This studies showed the strong influence of the underlying RANS model in hybrid RANS/LES calculations when the flow is not massively separated. It was not possible, with the given reference data, to ascertain which model amongst SA or  $k - \varepsilon$ -ZDES was performing the best, but it gives an idea of the dispersion in the simulation results. This motivates further work to minimise the influence of the simplest RANS models shortcomings on the overall ZDES predictions, for instance by using more accurate models, such as EARSM or DRSM coupled with LES.

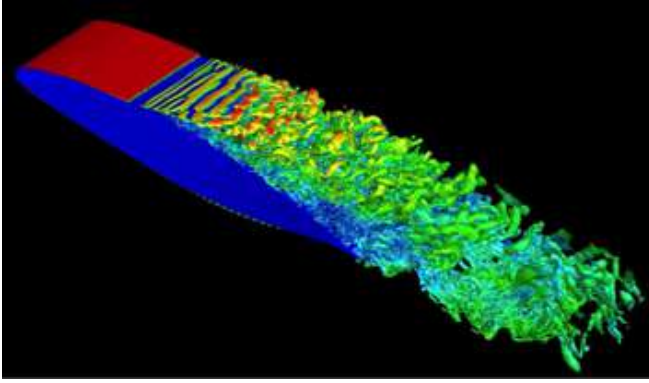


Figure 5: V2C: Iso-Q criterion visualisation

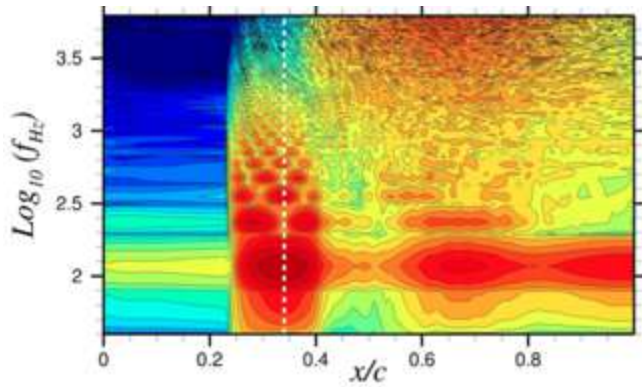


Figure 6: V2C: Surface pressure PSD for the  $k - \varepsilon$ -ZDES model. Dashed white line indicates average shock position

## 5 Variational multi-scale model

In order to improve sub-grid scale modelling in a LES or ZDES framework, the variational multiscale modelling (VMS) [20] was adapted to the Aether code [3], for standard-order and higher-order schemes [5]. The VMS, based on an explicit filtering, will be presented first. The application to the LEISA II slat noise prediction will be then briefly exposed.

### 5.1 Methodology and explicit filtering

The filtered Navier-Stokes equations for the resolved unknown field  $\underline{\mathbf{U}}^R$  are

$$\underline{\mathbf{U}}_{,t}^R + \underline{\mathbf{A}}_i^R \underline{\mathbf{U}}_{,i}^R = \left( \underline{\mathbf{K}}_{ij}^R \underline{\mathbf{U}}_{,j}^R \right)_i + \underline{\mathbf{T}}_{SGS} \quad (7)$$

With the Smagorinsky model expressed as follows

$$\underline{\mathbf{T}}_{SGS} = \left( \underline{\mathbf{K}}_{ij}^R (\nu_{SGS}, \underline{\mathbf{U}}^R) \underline{\mathbf{U}}_{,j}^R \right)_i$$

$$\nu_{SGS} = (C_S \Delta_m)^2 \sqrt{2 \underline{\mathbf{S}}^D(\underline{\mathbf{U}}^R) : \underline{\mathbf{S}}^D(\underline{\mathbf{U}}^R)}$$

This model is known to be much dissipative and over-predicts the energy transfer from the resolved to the modelled scales. In order to address this problem, a VMS model is introduced. The aim is to decrease the velocity spectral composition used for the sub-grid scale model, *i.e.* considering only the smallest resolved eddies  $\underline{\mathbf{U}}''$  in the Smagorinsky model by taking out the largest resolved eddies  $\tilde{\underline{\mathbf{U}}}$  from the full resolved field  $\underline{\mathbf{U}}^R$  (see Figure (7)). In the LES-filtered Navier Stokes equations the sub-grid scale tensor  $\underline{\mathbf{T}}_{SGS}$  is then replaced by  $\underline{\mathbf{T}}_{VMS}$  with:

$$\underline{\mathbf{T}}_{VMS} = \left( \underline{\mathbf{K}}_{ij}^R (\nu_t, \underline{\mathbf{U}}'') \underline{\mathbf{U}}_{,j}'' \right)_i$$

$$\nu_t = (C_{VMS} \Delta_m)^2 \sqrt{2 \underline{\mathbf{S}}^D(\underline{\mathbf{U}}'') : \underline{\mathbf{S}}^D(\underline{\mathbf{U}}'')}$$

$$C_{VMS} \Delta_m \simeq C_S \Delta_f \left[ \left( \frac{\Delta_f}{\Delta_m} \right)^{4/3} - 1 \right]^{-3/4}$$

where  $\delta_m$  and  $\delta_f$  are respectively the length of the element and the length of the filter. These will be taken as the cubic-root of the element volume, and the cubic-root of the macro element volume, defined as the element build on elements which share a common node. The VMS model therefore only impacts the high wave numbers and it changes the local intensity of the turbulent viscosity to be adapted to the real presence of sub-grid structures and to the mesh refinement through the definition of  $\nu_{VMS}$ .

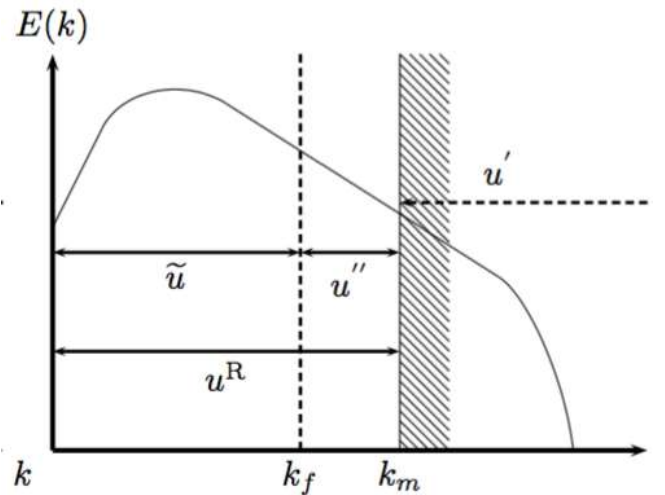


Figure 7: VMS methodology: the separation of VMS resolved scales.  $k_m$  is the mesh cut-off wave number and  $k_f$  is the filter cut-off wave number

The smallest scales of the resolved field  $\underline{\mathbf{U}}''$  are obtained using an explicit filtering. When high-order simulations are performed,  $\tilde{\underline{\mathbf{U}}}$  is computed by interpolating the high-order solution on lower order functions.

When coupled with a near-wall RANS model in the ZDES framework, the VMS model is progressively switched off towards the wall to recover the URANS mode of the ZDES. The following blending is proposed:

$$\underline{\mathbf{U}}'' = (1 - f_c) \underline{\mathbf{U}}'' + f_c \underline{\mathbf{U}}^R \quad (8)$$

$$\frac{\partial \underline{\mathbf{U}}''}{\partial \underline{\mathbf{x}}} = (1 - f_c) \frac{\partial \underline{\mathbf{U}}''}{\partial \underline{\mathbf{x}}} + f_c \frac{\partial \underline{\mathbf{U}}^R}{\partial \underline{\mathbf{x}}} \quad (9)$$

$$\nu_t^{VMS} = (1 - f_c) \nu_t^{VMS} + f_c \nu_t^{DES} \quad (10)$$

Where  $f_c$  is based on the  $f_d$  function of the Spalart DDES model.

## 5.2 The LEISA II configuration

The methodology was applied to the LEISA-II benchmark, Figure (8), both for unsteady flow and aero-acoustics predictions. The flow parameters are the Mach number  $M_\infty = 0.1804$  and the angle of attack  $\alpha = 6.15^\circ$ . The study focuses on the slat cavity flow, where the lower shear layer is subjected to Kelvin-Helmholtz vortices development, which convect, breakdown, and impact the cavity upper surface, that being considered as the dominant noise source. The flow phenomena is well captured by the simulation (Schlieren visualisation  $||\nabla\rho||$  presented on Figure (10)), thanks to the unstructured meshing strategy using local refinement based on user-prescribed metrics, Figure (9), and the VMS formulation. Indeed using an explicit filtering in the VMS to remove the largest scales from the energy transfer process allows leaving unaffected large areas in the outer region of the cavity, otherwise influenced by a much more diffusive Smagorinsky model.

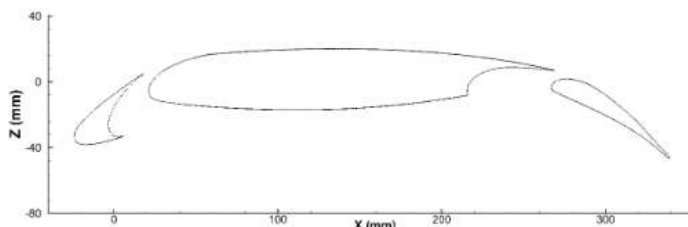


Figure 8: LEISA II configuration

Figure (11) shows the longitudinal velocity PSD at probe just before impact on the cavity upper surface (measurements from ONERA F2 wind tunnel), showing a good agreement with the experimental probe, both in high and low frequencies. Aero-acoustics results are presented on Figure (12), for the pressure PSD measured on a microphone located right under the profile. The measurements from F2 wind tunnel are compared to the far field propagated VMS results using the integral formulation of Curle [21]. The comparison is satisfactory both in energy and frequency. The spectrum shows tonal peaks at  $f = 2000\text{Hz}$  and  $f = 3000\text{Hz}$  and a wide acoustic activity around  $f = 4000\text{Hz}$ .

## 6 Conclusions

These examples of recent hybrid RANS/LES applications at Dassault Aviation show that this technology is now mature to meet tomorrow's engineering requirements. The growing use of high-order schemes allows

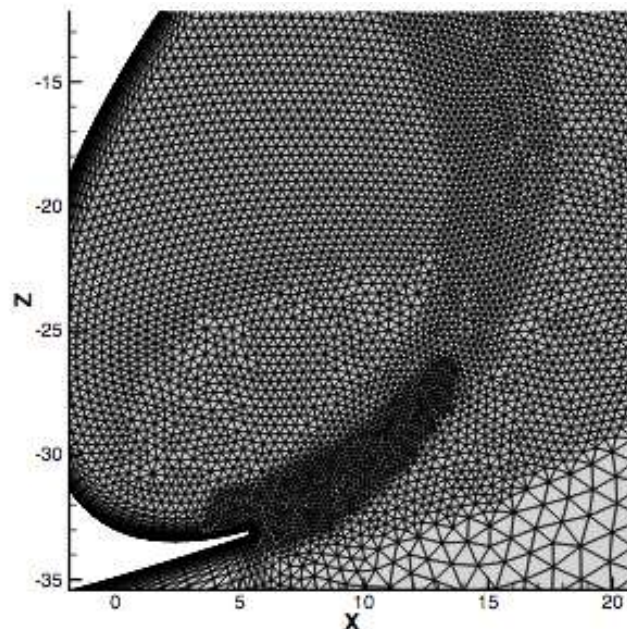


Figure 9: LEISA II: Exemple of unstructured mesh refinement at the slat trailing edge

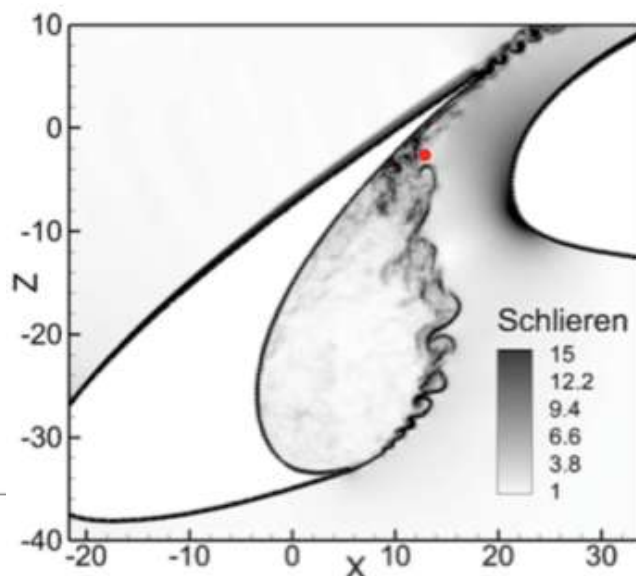


Figure 10: LEISA II: VMS simulation results. Schlieren plot

to increase the level of accuracy and flow description while retaining a reasonable CPU cost; alternatives to the Smagorinsky model have been developed, such as the variational multi-scale modelling, to allow for a more physical representation of energy transfer from resolved to modeled scales; and the hybrid RANS/LES framework in Aether, using the Zonal DES method, was adapted to several RANS near-wall models providing the engineer with several modelling options.

## References

- [1] F. Chalot, B. Marquez, M. Ravachol, F. Ducros, F. Nicoud, and T. Poinot, "A consistent finite element approach to large eddy simulation," in *29th AIAA, Fluid Dynamics Conference*, p. 2652, 1998.

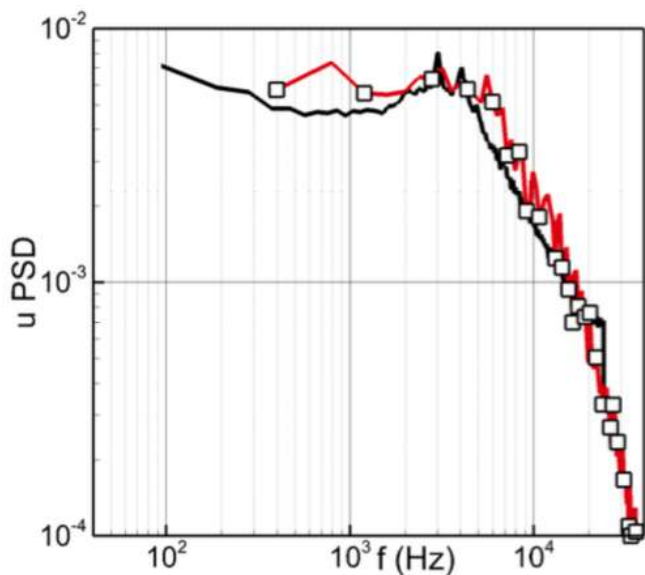


Figure 11: LEISA II: PSD of longitudinal velocity at probe 11108-9-2 (position indicated on Figure (10))

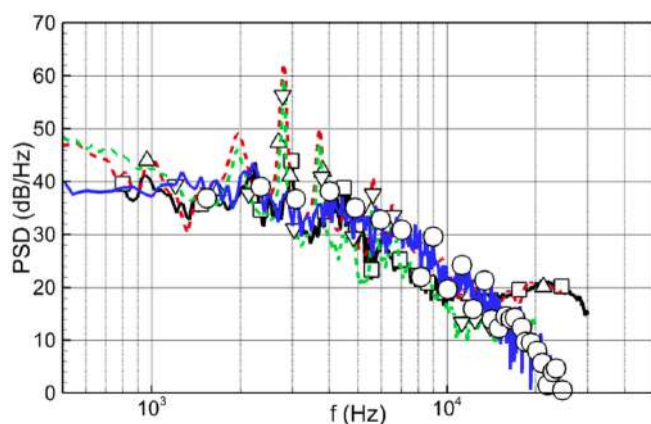


Figure 12: LEISA II: Pressure PSD on microphone 4. Square symbols / solid black line: F2 measurement. Circle symbols with solid blue line: VMS results

[2] F. Chalot, B. Marquez, M. Ravachol, F. Ducros, and T. Poinsot, "Large eddy simulation of a compressible mixing layer-study of the mixing enhancement," in *14th Computational Fluid Dynamics Conference*, p. 3358, 1999.

[3] V. Levasseur, *Simulation des grandes échelles en éléments finis stabilisés: une approche variationnelle multi-échelles*. PhD thesis, Paris 6, 2007.

[4] P.-E. Normand, *Application de méthodes d'ordre élevé en éléments finis pour l'aérodynamique*. PhD thesis, Bordeaux 1, 2011.

[5] P. Yser, *Simulation numérique aéroacoustique d'écoulements par une approche LES d'ordre élevé en éléments finis non structurés*. PhD thesis, Lyon, 2017.

[6] M. Mallet, *A finite element method for computational fluid dynamics*. PhD thesis, Stanford University Stanford, CA, 1985.

[7] T. Daris and H. Bezar, "Four-equation models for reynolds stress and turbulent heat flux predictions," in *International Heat Transfer Conference Digital Library*, Begel House Inc., 2002.

[8] F. Billard and D. Laurence, "A robust  $k-\varepsilon-v2/k$  elliptic blending turbulence model applied to near-wall, separated and buoyant flows," *International Journal of Heat and Fluid Flow*, vol. 33, no. 1, pp. 45–58, 2012.

[9] R. Manceau and K. Hanjalić, "Elliptic blending model: A new near-wall reynolds-stress turbulence closure," *Physics of Fluids*, vol. 14, no. 2, pp. 744–754, 2002.

[10] R.-D. Cécora, R. Radespiel, B. Einfeld, and A. Probst, "Differential reynolds-stress modeling for aeronautics," *AIAA Journal*, vol. 53, no. 3, pp. 739–755, 2014.

[11] S. Deck, "Numerical simulation of transonic buffet over a supercritical airfoil," *AIAA journal*, vol. 43, no. 7, pp. 1556–1566, 2005.

[12] P. Yser and C. Bailly, "High-order variational multi-scale model in finite elements applied to the LEISA-2 configuration," *AIAA Journal*, vol. 56, no. 12, pp. 5000–5012, 2018.

[13] L. Dumas, F. Chalot, V. Levasseur, M. Mallet, and N. Réau, "LES and DES aeroacoustic simulations for inflight opened weapon bay," in *IFASD International Forum on Aeroelasticity and Structural Dynamics, At Seattle, USA*, 2009.

[14] P. Yser, S. Barré, F. Chalot, and F. Dagrau, "High-order and subgrid model effects on finite elements DES-LES computations of a transonic cavity experiment," 2015.

[15] T. S. Davidson and H. Babinsky, "Transition location effects on normal shock wave-boundary layer interactions," in *53rd AIAA aerospace sciences meeting*, p. 1975, 2015.

[16] R. Placek and W. Stryczniewicz, "Identification of the boundary layer shock wave interaction type in transonic flow regime," *Journal of KONES*, vol. 23, 2016.

[17] A. Memmolo, M. Bernardini, and S. Pirozzoli, "Scrutiny of buffet mechanisms in transonic flow," *International Journal of Numerical Methods for Heat & Fluid Flow*, vol. 28, no. 5, pp. 1031–1046, 2018.

[18] L. Jacquin, P. Molton, S. Deck, B. Maury, and D. Soulevant, "Experimental study of shock oscillation over a transonic supercritical profile," *AIAA journal*, vol. 47, no. 9, pp. 1985–1994, 2009.

[19] J. Dandois, I. Mary, and V. Brion, "Large-eddy simulation of laminar transonic buffet," *Journal of Fluid Mechanics*, vol. 850, p. 156–178, 2018.

[20] T. J. Hughes, L. Mazzei, and K. E. Jansen, "Large eddy simulation and the variational multi-scale method," *Computing and visualization in science*, vol. 3, no. 1-2, pp. 47–59, 2000.

[21] N. Curle, "The influence of solid boundaries upon aerodynamic sound," *Proceedings of the Royal Society of London. Series A. Mathematical and Physical Sciences*, vol. 231, no. 1187, pp. 505–514, 1955.



# USE OF ANISOTROPIC LINEAR FORCING FOR COMPLEX SCALE-RESOLVING SIMULATION

S. Lardeau and L. Erbig

*Siemens Digital Industries Software, Nordostpark 3, 90411 Nuremberg, Germany*

## Abstract

A modified version of the Anisotropic Linear Forcing (ALF), originally proposed by [1], is presented. The objective of the modification is to make the ALF easier to use for industrial applications, but also improves its robustness, and to decrease its sensitivity to mesh changes and user-input. A simple validation case of a turbulent channel flow is used to illustrate the benefits of that new method over more classical inlet perturbations methods. Then, we outline how ALF was recently used to simulate turbulent boundary layer induced gap noise in the literature.

## 1 Introduction

Industrial CFD software have been based, for the past 35 years, on solving the conservation equations (momentum, mass, energy) for mean flow quantities (ie using the Reynolds-averaging procedure). Additional information about the effect of turbulent motion on the mean flow field needs to be modeled, and requires solving additional transport equations, for mean quantities, such as mean turbulent kinetic energy  $k$  or mean flow dissipation rate  $\varepsilon$ .

Although it is hard to overestimate the benefits of this method for industrial applications, it also has limited values for applications that require either time-accurate data (e.g. aeroacoustics), or for application where the RANS approach is simply not accurate enough (e.g. flow separation on smooth surfaces under adverse pressure gradients). The only option is then to turn to scale-resolving simulation (SRS), whereby all or part of the turbulent motion is resolved. A prerequisite for performing an accurate SRS is to ensure that the mesh resolution is fine enough to resolve most of the turbulence motion, so that only the smallest parts are modeled. In this context, detached-Eddy Simulation (DES) has become one of the most popular SRS models in the industry, because of its ease of use, and because it is derived from well-known RANS models. But it also has severe limitations. The one that has proven to be the most problematic is referred to in the literature as the *grey-area problem*: this happens in the early stages of flow separation, for instance, when the model switches theoretically from RANS to a subgrid-scale-like model. This is where the modeled turbulence should be converted instantaneously into resolved motion with similar statistical properties. For those cases, LES is often found to be a better alternative.

Another important difficulty when performing SRS is to prescribe accurate boundary conditions. Wall-boundaries, symmetries, and periodicities are usually treated as in RANS, but inlet and outlet need special considerations. Outlet boundary conditions should allow the flow to cross without any disturbances (e.g. specific

non-reflective boundary conditions for pressure), and for inlets, just like in RANS, the correct level of turbulent kinetic energy, as well as the correct turbulence length-scales need to be prescribed. While for RANS only the mean values are needed (and those could vary in space, but tend to be stationary), for SRS, the inlet needs to correctly represent not only the mean value, but also the correct energy spectra (e.g. having a Kolmogorov spectrum if the flow is fully turbulent).

Several methods are available in the literature to solve this problem, ranging from advanced recycling methods (Lund, etc.) to more complex ones such as digital-filtering based methods (Xie et al. [2]) or synthetic-eddy methods (e.g. Jarrin et al. [3] and subsequent work from Skillen et al. [4]). Although useful to generate inlet perturbations with prescribed length-scale, they can only be used at interfaces, thus lacking 3D information of the perturbations, or cannot be used in complex flow configurations (e.g. Lund's recycling model).

The objective of this paper is to present a modified version of the ALF (De Laage de Meux et al. [1]) that can be easily applied to industrial applications, with minimum user input, and can potentially be used to perform accurate embedded RANS/LES calculations.

## 2 Model Formulation

### 2.1 Original ALF model

The ALF [1] is effectively a body-force (source term)  $F_i$  that is added on the R.H.S. of the filtered momentum equation:

$$\frac{\partial \tilde{u}_i}{\partial t} + \frac{\partial \tilde{u}_i \tilde{u}_j}{\partial x_j} = -\frac{1}{\rho} \frac{\partial \tilde{p}}{\partial x_i} + \nu \frac{\partial^2 \tilde{u}_i}{\partial x_j \partial x_j} - \frac{\partial \tilde{\tau}_{ij}}{\partial x_j} + F_i \quad (1)$$

In the following,  $\tilde{\cdot}$  is used to denote resolved quantities (e.g. filtered quantities for LES). Furthermore, two additional notation types need to be introduced:

- Averaged quantities are denoted using  $\hat{\cdot}$ , and the difference between the averaged quantity and the instantaneous filtered quantity is denoted with a  $()'$ , ie

$$\tilde{\phi} = \hat{\phi} + \tilde{\phi}' \quad (2)$$

- Target quantities (in this case, target quantities are coming from additional RANS calculations) are noted with superscript  $()^t$ .

De Laage de Meux et al [1] proposed a general definition of the volumetric forcing using a tensorial linear function

$$F_i = A_{ij} \tilde{u}_j + B_i \quad (3)$$

where  $A_{ij}$  and  $B_i$  are a deterministic second-order tensor and a vector, respectively.

The elegant idea of ALF is to derive the definition of  $\mathbf{A} := (A_{ij})$  and  $B_i$  from physical considerations. First, as for other variables, the forcing term  $F_i$  can be decomposed into mean and fluctuating parts

$$F_i = \widehat{F}_i + F'_i \quad (4)$$

which gives, using Eq. (3)

$$\widehat{F}_i = A_{ij}\widehat{u}_j + B_i \quad (5)$$

$$F'_i = A_{ij}\tilde{u}'_j \quad (6)$$

By applying Reynolds averaging to the conservation equation (Eq. (1)), the contribution of the forcing to the mean flow equation would then be simply  $\widehat{F}_i$ , and the contribution of the forcing term to the Reynolds-stress equations (not shown here, but easily found in any turbulence textbook) would just be an additional production term, which has the exact form:

$$P_{ij}^F = \widehat{F'_i\tilde{u}'_j} + \widehat{F'_j\tilde{u}'_i} \quad (7)$$

or, given Eq. (6),

$$P_{ij}^F = A_{ik}\widehat{\tilde{u}'_k\tilde{u}'_j} + A_{jk}\widehat{\tilde{u}'_k\tilde{u}'_i} \quad (8)$$

For simplicity, we will denote the stress-tensor calculated from the resolved flow field  $\mathbf{R} := (R_{ij}) := (\widehat{\tilde{u}'_k\tilde{u}'_j})$ .

The main desired effect of the forcing is to force the flow statistics (mainly mean velocity, and Reynolds-stresses) towards pre-defined target state. How these pre-defined statistical (target) states are obtained will be discussed in the next section. Let's note those targets velocity and stress fields  $U_i^t$  and  $\mathbf{R}^t = (R_{ij}^t)$ .

The resolved flow field can be forced towards a target mean-flow state by imposing

$$\widehat{F}_i = \frac{1}{T_v} (U_i^t - \widehat{u}_i) \quad (9)$$

where  $T_v$  is a relaxation time-scale.

The contribution to the Reynolds-stress equation can also be formulated as an under-relaxed state of the resolved stresses towards a pre-defined state:

$$P_{ij}^f = \frac{1}{T_r} (R_{ij}^t - R_{ij}) \quad (10)$$

and by combining Eq. (5) and Eq. (9) on one hand, and Eq. (8) and Eq. (10),  $A_{ij}$  and  $B_i$  are the solution of

$$A_{ij}\widehat{u}_j + B_i = \frac{1}{T_v} (U_i^t - \widehat{u}_i) \quad (11)$$

$$A_{ik}R_{kj} + R_{ik}A_{kj} = \frac{1}{T_r} \underbrace{(R_{ij}^t - R_{ij})}_{:=H_{ij}} \quad (12)$$

Eq. (12) is a second order tensorial algebraic equation, which general solution is given by

$$\begin{aligned} \mathbf{A} = \frac{1}{C} \quad [ & I_R\mathbf{R}^2\mathbf{H}\mathbf{R}^2 - I_R^2(\mathbf{R}^2\mathbf{H}\mathbf{R} - \mathbf{R}\mathbf{H}\mathbf{R}^2) \\ & + (I_R\mathbf{I}\mathbf{I}_R - \mathbf{I}\mathbf{I}\mathbf{I}_R)(\mathbf{R}^2\mathbf{H} + \mathbf{H}\mathbf{R}^2) \\ & + (I_R^3 + \mathbf{I}\mathbf{I}\mathbf{I}_R)\mathbf{R}\mathbf{H}\mathbf{R} - I_R^2\mathbf{I}\mathbf{I}_R(\mathbf{R}\mathbf{H} + \mathbf{H}\mathbf{R}) \\ & + (I_R^2\mathbf{I}\mathbf{I}\mathbf{I}_R + \mathbf{I}\mathbf{I}_r(I_R\mathbf{I}\mathbf{I}_R - \mathbf{I}\mathbf{I}\mathbf{I}_R))\mathbf{H} \quad ] \quad (13) \end{aligned}$$

where  $\mathbf{H} := (H_{ij})$ ,  $C := 2\mathbf{I}\mathbf{I}\mathbf{I}_R(I_R\mathbf{I}\mathbf{I}_R - \mathbf{I}\mathbf{I}\mathbf{I}_R)$ , and  $I_R$ ,  $\mathbf{I}\mathbf{I}_R$  and  $\mathbf{I}\mathbf{I}\mathbf{I}_R$  are the first, second and third order principal invariants of the resolved stress-tensor  $\mathbf{R}$ , respectively.

The vector  $B_i$  is then obtained from rearranging Eq. (11)

$$B_i = \frac{1}{T_v} (U_i^t - \widehat{u}_i) - A_{ij}\widehat{u}_j \quad (14)$$

The ALF model thus provides a way to force the statistical properties of a scale-resolving flow field, using two different information: one about the mean flow statistics, which in essence forces the mean flow part of the simulation, and one about the turbulence statistics, which will drive the smaller scales content (fluctuations). It requires however three more ingredients to be complete:

1. Sensible target velocity  $U_i^t$  and stress fields  $R_{ij}^t$
2. Sensible relaxation time-scales  $T_r$  and  $T_v$ .
3. Sensible averaging procedure to calculate  $\widehat{u}_i$  and  $R_{ij}$

The following subsections address these requirements in order.

## 2.2 Target velocity and target stresses

Target values are mean flow quantities that can be used to drive the scale-resolving simulation towards a specific statistical state. In most industrial applications, this is achieved by performing a precursor RANS calculation of the flow, and extract a volume, usually upstream of the region of interest, in which the forcing term  $F_i$  will be added to the filtered momentum equation. The target Reynolds-stress  $R_{ij}^t$  can either be obtained directly using a Reynolds-stress model [5], or can be calculated from eddy-viscosity models using the Boussinesq approximation.

Those target values are then mapped onto the same region of the scale-resolving simulation, and used to solve Eq. (13) and Eq. (14). The target quantities are also used in the next step, to calculate the two relaxation time-scales for the mean flow and turbulence.

## 2.3 Relaxation time-scales

[1] proposed some definitions for the two relaxation time-scales ( $T_r$ , the time-scale related to the Reynolds-stress term and  $T_v$ , related to the velocity forcing term). For the velocity time-scale, they assumed that it should be related to the integral length-scale of the flow, which is equivalent, for a simple boundary layer to

$$T_v = 5h/U_b \quad (15)$$

where  $h$  is the typical length-scale of the flow (e.g. the boundary layer thickness or channel-half height for instance) and  $U_b$  is a typical velocity scale (e.g free-stream or bulk velocity). For  $T_r$ , they just used a constant value, varying from 0.01 to 0.05 (in the case of a channel), and obtained good results. Those definitions are not general enough for an industrial CFD software, and thus need to be generalized. The statistical data available from the precursor simulation can be used to define those scales: The fluctuating time-scale  $T_r$  should be related to the turbulence time-scale of the precursor simulation, ie.

$$T_r \propto \frac{k^t}{\varepsilon^t} \quad (16)$$

This needs to be limited, however, by the time-step  $\Delta t$  of the scale-resolving simulation

$$T_r = \max \left( 2\Delta t, C_r \frac{k^t}{\varepsilon^t} \right) \quad (17)$$

where  $k^t$  and  $\varepsilon^t$  are target data, extracted from the precursor simulation (alternatively, the dissipation can be computed by imposing a target length-scale  $L^t$  and using  $\varepsilon = k^{t3/2}/L^t$ ). It was also found necessary to clip the turbulent time-scale  $T_r$  in the near-wall region, to avoid large values of the forcing itself. As in classical RANS model (e.g. [6]), the Kolmogorov time-scale is used as the lower time limit

$$T_r = \max \left[ 2\Delta t, \max \left( C_r \frac{k^t}{\varepsilon^t}, C_t \sqrt{\frac{\nu}{\varepsilon^t}} \right) \right] \quad (18)$$

Preliminary calibration in channel flows showed that the constant  $C_r$  should be of the order of 10.

A local definition of the velocity time-scale  $T_v$  was also proposed by [1]

$$T_v = C_v \frac{d}{\|\mathbf{U}^t\|} \quad (19)$$

where  $d$  is the wall-distance, and  $C_v = 5$ . However Eq. (19) is not Galilean invariant and the wall-distance dependency of Eq. (19) can be problematic for complex flow configurations. A more natural large-eddy time-scale, usually used in RANS modeling, is based on the inverse of the magnitude of the strain-rate tensor ( $S^t$ ) of the target velocity field.

$$T_v = \frac{1}{C_v S^t}, \quad S^t = \sqrt{2S_{ij}^t S_{ij}^t} \quad (20)$$

$$S_{ij}^t = \frac{1}{2} \left( \frac{\partial U_i^t}{\partial x_j} + \frac{\partial U_j^t}{\partial x_i} \right)$$

It is Galilean invariant, and it also has another advantage: because the time-scale  $T_v$  appears in the denominator of the drift term in Eq. (14), it means that a zero strain-rate will give a zero-mean velocity forcing in the free-stream.

## 2.4 Averaging procedure

The last step to perform the ALF is to provide sensible mean values of the resolved flow field. For this, and following [1], we use the Exponentially Weighted Average (EWA) method. Here again, a more general approach is introduced. The assumption is that the time-step is set properly for the LES. In that case, the EWA is computed over about 500 to 750 time-steps (noted  $n_{\text{EWA}}$ ), which was found to be sufficient for most cases.

A computationally efficient way to compute EWA mean and variance of the velocity was proposed by [7],

$$\hat{u}_i^n = \hat{u}_i^{n-1} + \alpha (\tilde{u}_i^n - \hat{u}_i^{n-1}) \quad (21)$$

where the exponential weighted factor is

$$\alpha = 1 - \exp \left( -\frac{\Delta t}{T} \right) \quad (22)$$

with  $T = n_{\text{EWA}} \Delta t$ , and  $\Delta t$  is the simulation time-step. For the stress-tensor, we use the formulation

$$R_{ij}^n = (1 - \alpha) \left[ R_{ij}^{n-1} + \alpha (\tilde{u}_i^n - \hat{u}_i^{n-1})(\tilde{u}_j^n - \hat{u}_j^{n-1}) \right] \quad (23)$$

## 2.5 Formulation of the new ALF model

For general practical application, it was also necessary to add several limiters, such that the ALF is deactivated in regions where the grid would not be able to support the fluctuations. A robust and accurate forcing method should thus include the following length-scales

1. The integral length-scale:  $l = k^{t3/2}/\varepsilon^t$ ,
2. The Taylor micro-scale:  $\lambda = \sqrt{10\nu \frac{k^t}{\varepsilon^t}}$ ,
3. A mesh-related length-scale:  $L_{\text{vol}} = \sqrt[3]{V_{\text{ol}}}$ .

The forcing should be prevented if the mesh size is larger than the integral length-scale (ie the mesh will not be able to support the fluctuations that are about to be created). The forcing is also only active when the ratio  $\frac{\lambda}{l} \approx \sqrt{\frac{\nu}{\nu_t}} < 0.5$ .

The full forcing term can then be recast as the combination of a mean-flow forcing component and a fluctuating one

$$F_i = \underbrace{A_{ij} \phi (\tilde{u}_j - \hat{u}_j)}_{\text{Fluctuating}} + \underbrace{C_v \phi S^t (U_i^t - \hat{u}_i)}_{\text{Mean}} \quad (24)$$

where  $A_{ij}$  is obtained using Eq. (13),  $\phi$  is a scaling function that prevents a too strong flow acceleration at each time step

$$\phi = \min \left( 1, \frac{L_{\text{vol}}}{\Delta t \|\tilde{u}_i\|} \right) \quad (25)$$

and the EWA values are computed using Eq. (21) and Eq. (23). The constants are given in Table (1).

Table 1: Constants for the ALF model.

$C_r$	$C_v$	$C_t$	$n_{\text{EWA}}$
10	1	1	750

## 3 Numerical methods

The ALF has been implemented in Simcenter STAR-CCM+, which is a general purpose, finite-volume-based, commercial CFD software, which offers a large range of physics and numerical models.

Although ALF could be easily used to perform a real hybrid RANS/LES (and potentially a full embedded RANS/LES, as suggested by [8]), we use here, for presentation purpose, only a fully segregated approach, where the target velocity and target stress fields are pre-computed using a separate simulation, exported to a file, and then reimported into the simulation (ie using a steady state approach or data mappers). But the framework can be easily extended to a dual mesh approach, using for instance co-simulation or data mapping.

## 4 Results

Two different application cases are presented here. The first one, a channel flow at  $Re_\tau = 550$  is used to assess the performance of the ALF in a simple flow configuration, compared with the Synthetic Eddy Method [4]. The industrial problem of turbulent boundary layer induced gap-noise, studied by Erbig et al. [9, 10, 11, 12], is then introduced briefly to show the benefits of ALF to reduce the computational cost of an otherwise very complex and costly problem and to discuss how ALF could be applied to such problems.

## 4.1 Channel flow at $Re_\tau = 550$

Two LES of a spatially developing channel flow are performed, using either the ALF or the SEM. The LES are based on the WALE model [13]. The domain is long enough ( $40H$ ) to allow instabilities to develop even without perturbation, and the results are compared with DNS data in a periodic channel [14]. The inflow profile for the LES is also extracted from this DNS database. For the ALF calculation, the target velocity  $U_i^t$  and target Reynolds-stresses  $R_{ij}^t$  are extracted from a precursor RANS calculation, using the EB-RSM model of [5]). For the SEM calculation, the inlet length-scale and intensity are also extracted from the same RANS calculation. The comparison between the SEM, the ALF, the RANS and the DNS data are shown on Figure (1)-Figure (4).

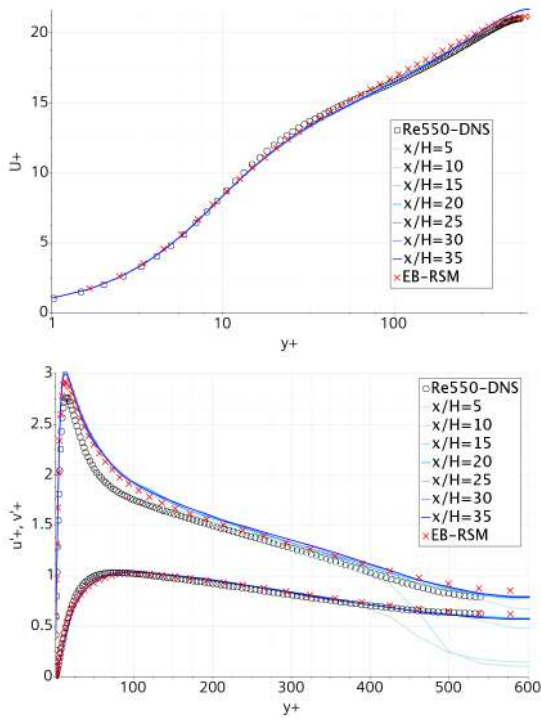


Figure 1: Profiles of the mean streamwise velocity (top) and two components of the Reynolds-stress tensor (bottom) at different positions in the streamwise direction of spatially developing channel using ALF

Velocity and Reynolds-stress profiles (Figure (1)-Figure (2)) at different streamwise locations show that the ALF results reach the target values very quickly, with the only difference being observed in the center of the channel, and only up to  $x/H > 10$ , while the SEM does not reach a completely fully developed state before  $x/H = 25$ . Even then, the LES solution does not match completely the DNS solution (note here that we use the theoretical DNS value to normalize the velocity and the Reynolds-stresses, rather than the local value).

For the SEM case, this delay in generating significant perturbations is also illustrated in Figure (3), which shows the streamwise variation of the normalized mean wall-shear stress (with respect to the DNS value), as well as the spread of the instantaneous wall-shear stress (shades of grey). The results from the ALF show a much better agreement, and this is almost entirely due to the fact that the target fields (shown with crosses on Fig. Figure (1)) also match the DNS data almost perfectly. In this particular case, the ALF is even used to overcome a deficiency of the underlying LES model (the log-layer

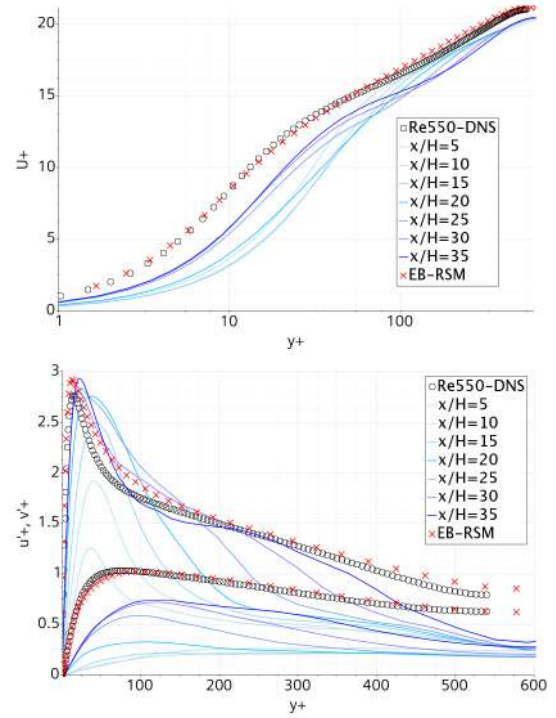


Figure 2: Profiles of the mean streamwise velocity (top) and two components of the Reynolds-stress tensor (bottom) at different positions in the streamwise direction of spatially developing channel using SEM

mismatch).

The magnitude of the forcing  $F_i$  for the ALF case is presented in Figure (4). It shows how the fluctuations are generated mainly at the wall, and reaches the center of the channel by  $xH = 10$ , and how the forcing itself reduces as the perturbed flow moves downstream. This is in contrast to the SEM, which shows that the fluctuations are generated mostly at the center of the channel and only diffuse very slowly to the wall, thus explaining the slow rise of the wall-shear stress observed on Figure (3).

## 4.2 Application to gap noise

A possible industrial application for ALF is the aeroacoustic simulation of gap noise of passenger cars, as discussed in [11, 12]. It has been shown in [15] that rear door gap noise is typically generated by an amplification mechanism of boundary layer fluctuations that are convected above the gap's opening. Accordingly, resolved boundary layer turbulence is required to simulate this problem, but it is also only of interest in the vicinity of the gap. Using ALF it was possible to separate the simulation in two parts, first a precursor RANS to calculate target fields for ALF and second a LES in a sub-domain around the gap. For this specific purpose three main practical challenges needed to be investigated:

1. The accuracy of the target fields from the precursor RANS determines the quality of the synthesized turbulence,
2. Spurious noise of the pressure fluctuations of the synthesized turbulence must be small enough for the problem,
3. A suitable location for the ALF forcing needs to be specified.

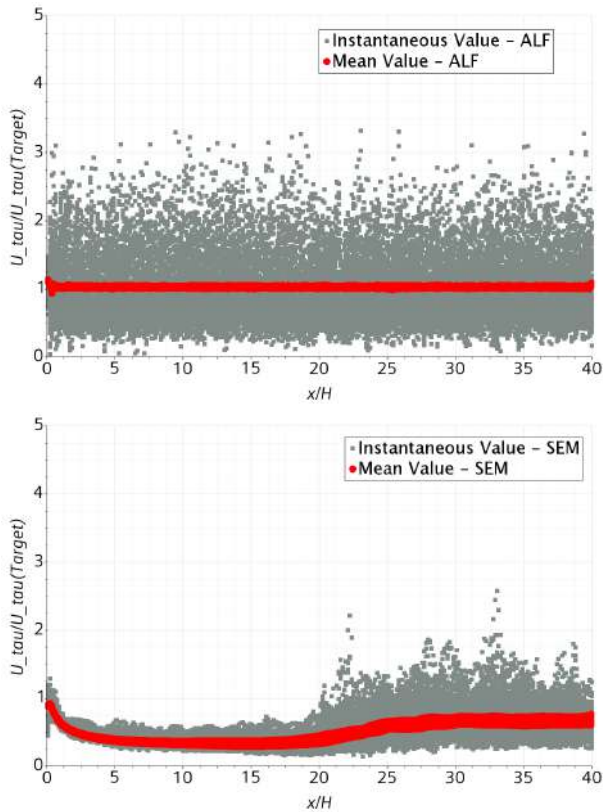


Figure 3: Streamwise evolution of the mean and fluctuating streamwise wall-shear stress components, normalized by the theoretical DNS value for the ALF (top) and the SEM (bottom) calculations

A validated workflow for this problem was derived by successive investigation of different cases:

- Zero pressure gradient (ZPG) and adverse pressure gradient (APG) turbulent boundary layers that were experimentally studied by Hu and Herr, [16], in [10, 12],
- Gap noise generated by a simplified, partially covered, rectangular gap beneath a ZPG or APG turbulent boundary layer in [9, 12]
- Gap noise generated by the rear door gap of a Mercedes-Benz E-Class Estate in [11, 12].

While a calculation of accurate target fields for the ZPG cases was straightforward with the EB-RSM turbulence model, the setup for the LES needed some consideration. As discussed for the turbulent channel flow, ALF helped to overcome deficiencies of the underlying LES model. This advantage principally allowed to use slightly under-resolved meshes compared to the literature. But as soon as ALF is only used as a turbulence synthetization method upstream of a region of interest it was reported that a drop of the wall shear stress, that significantly depended on the mesh resolution, occurred at the transition between the ALF forcing region and the unforced LES. It was also found that the streamwise extent  $\ell_{ALF}$  of the ALF application region had a significant influence on the accuracy of the stresses and the wall pressure spectra in the region of interest. In a convergence study excellent results were obtained for  $\ell_{ALF} > 15\delta$  and  $\Delta x^+ = \Delta z^+ < 36$ ,  $y^+ = 1$  where  $\delta$  is the local boundary layer thickness.

For adverse pressure gradient cases the situation turned out to be more complex. In the experiments

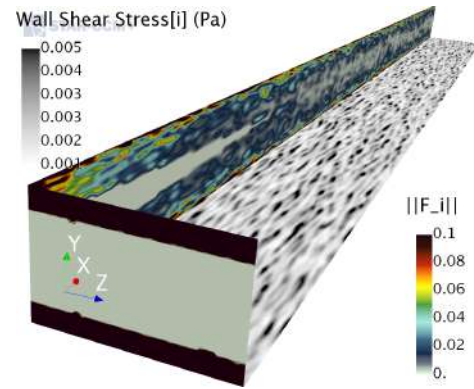


Figure 4: Contours of the forcing magnitude  $\|F_i\|$

from [16] and [12] a pressure gradient was imposed by positioning a NACA-0012 airfoil at a non-zero angle of attack above a flat plate configuration, see Figure (5). As this configuration led to a deflection of the wind-tunnel's open jet shear layer and a contraction of the free-stream core between the flat plate and the airfoil, a RANS of the whole wind-tunnel setup was already required to obtain accurate mean velocity target fields in the desired LES sub-domain. Despite these efforts, the EB-RSM turbulence model still over-predicted at the line probe at  $x = 1210$  mm, in the APG region below the airfoil. Consequently it was necessary to avoid the use of ALF in that region and restrict it to the flow acceleration region below the stagnation point, as shown in Figure (5).<sup>1</sup> Despite these potential deficiencies of the target fields an excellent match of the wall pressure spectra and the mean velocity profiles at  $x = 1128$  mm and  $x = 1210$  mm and the stresses at  $x = 1210$  mm was obtained with the LES. It was also shown that an isotropic forcing also generated good results which could remove the dependency on Reynolds-stress models. In [12], two cases were discussed where the gap was positioned downstream of the airfoil. Although this configuration potentially increased the impact of the target stress over-prediction by the EB-RSM a good match of the wall pressure spectra and gap acoustics to the experimental data was found for both cases.

Finally, the application to the car model was relatively straightforward as the pressure gradient along the car's roof was found to be close to zero. With these pressure gradient conditions the EB-RSM RANS obtained accurate mean velocity profiles along the roof and the target stresses could be assumed well predicted. It was thus decided to apply ALF within a streamwise extent of  $\ell_{ALF} \approx 15\delta$  along the roof. Due to the larger dimensions of the problem and the thicker boundary layer it was additionally necessary to coarsen the mesh to  $\Delta x^+ = \Delta z^+ = 92$  to keep the computational costs as small as possible. Despite this compromise it was still possible to obtain good quality turbulent boundary layer wall pressure spectra and noise spectra inside the gap. The successful prediction of the aeroacoustics of the rear door gap can be considered as a first step towards a prediction of gap noise inside the cabin. For this purpose the described simulations would have to be combined with models of the acoustic transfer path from the gap's interior into the cabin. This path would especially include

<sup>1</sup>As the mesh under-resolution is more critical in a flow acceleration region, the LES subgrid model was not able to correctly predict the flow here. It was thus necessary to apply ALF in that region and to employ ALF's potential to overcome LES modeling deficiencies.

the sealings and the structural response of the body.

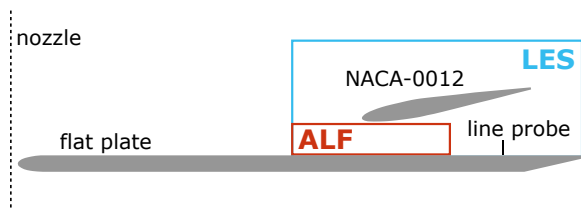


Figure 5: Setup used in [10] for the simulation of the APG-10 case by Hu and Herr, [16], relative dimensions based on published data from [16, 10]. The line probe is located at  $x = 1210$  mm

## 5 Conclusions

A generalized form of ALF, originally proposed in [1], was described. Especially, a generalization of the required relaxation time scales and the exponential averaging procedure provide a link between target fields from a precursor RANS and the forcing.

An application to a turbulent channel flow at  $Re_\tau = 550$  showed that ALF successfully recovered both the target fields expected and values of  $u_\tau$ , and generated fluctuations mostly close to the walls. This was not the case for turbulence synthetization with SEM at the inlet. Accordingly, ALF helped to overcome deficiencies of the underlying LES model.

We also provided a review of recent simulations of turbulent boundary layer induced gap noise for passenger cars that were based on ALF turbulence synthetization. In these simulations it was possible to successfully apply ALF to complex aeroacoustic problems involving zero and adverse pressure gradient conditions and an industrial geometry. In all cases it was also possible to use a coarser mesh than typically required for wall resolved LES. Although the generation of the anisotropic target fields was challenging for the considered adverse pressure gradient conditions it was always possible to determine a suitable setup for ALF. In such a setup, especially the streamwise extent of the ALF application region turned out to be important if ALF was used for aeroacoustics. Even in cases where the calculation of anisotropic target fields might be impossible it was shown that also an isotropic target stress tensor for ALF could deliver appropriate results.

Consequently, ALF could be used to simulate cases that require resolved boundary layer turbulence in defined areas of industrial problems. These problems could be separated into a RANS of the full setup and a LES in the defined area of interest where ALF is used to synthesize turbulence based on the target fields from the precursor RANS.

## References

- [1] B. de Laage de Meux, B. Audebert, R. Manceau, and R. Perrin, “Anisotropic linear forcing for synthetic turbulence generation in large eddy simulation and hybrid rans/les modeling,” *Physics of Fluids (1994-present)*, vol. 27, no. 3, p. 035115, 2015.
- [2] Z.-T. Xie and I. P. Castro, “Efficient generation of inflow conditions for large eddy simulation of street-scale flows,” *Flow, turbulence and combustion*, vol. 81, no. 3, pp. 449–470, 2008.

- [3] N. Jarrin, S. Benhamadouche, D. Laurence, and R. Prosser, “A synthetic-eddy-method for generating inflow conditions for large-eddy simulations,” *International Journal of Heat and Fluid Flow*, vol. 27, no. 4, pp. 585–593, 2006.
- [4] A. Skillen, A. Revell, and T. Craft, “Accuracy and efficiency improvements in synthetic eddy methods,” *International Journal of Heat and Fluid Flow*, vol. 62, pp. 386–394, 2016.
- [5] S. Lardeau and R. Manceau, “Computations of canonical and complex flow configurations using a robust formulation of the elliptic-blending reynolds-stress model to cite this version: using a modified elliptic-blending reynolds-stress model,” in *10th engineering turbulence modelling and measurement conference (ETMM10)*, 2014.
- [6] R. Manceau and K. Hanjalić, “Elliptic blending model: A new near-wall reynolds-stress turbulence closure,” *Physics of Fluids*, vol. 14, no. 2, pp. 744–754, 2002.
- [7] T. Finch, “Incremental calculation of weighted mean and variance,” *University of Cambridge*, vol. 4, pp. 11–5, 2009.
- [8] H. Xiao and P. Jenny, “A consistent dual-mesh framework for hybrid les/rans modeling,” *Journal of Computational Physics*, vol. 231, no. 4, pp. 1848–1865, 2012.
- [9] L. Erbig, N. Hu, and S. Lardeau, “Experimental and numerical study of passive gap noise,” in *2018 AIAA/CEAS Aeroacoustics Conference*, 2018. AIAA 3595-2018.
- [10] L. Erbig and S. Lardeau, “Hybrid rans/les of an adverse pressure gradient turbulent boundary layer using an elliptic blending reynolds stress model and anisotropic linear forcing,” in *Notes on Numerical Fluid Mechanics and Multidisciplinary Design*, 2018.
- [11] L. Erbig and M. Maihöfer, “A hybrid rans/les for automotive gap noise simulations,” in *25th AIAA/CEAS Aeroacoustics Conference*, 2019. AIAA 2445-2019.
- [12] L. Erbig, *Aeroacoustic Simulation of Turbulent Boundary Layer Induced Automotive Gap Noise*. Phd thesis, Institute of Aerodynamics and Gas Dynamics, University of Stuttgart, 2019. Submitted to the thesis committee.
- [13] F. Nicoud and F. Ducros, “Subgrid-scale stress modelling based on the square of the velocity gradient tensor,” *Flow, turbulence and Combustion*, vol. 62, no. 3, pp. 183–200, 1999.
- [14] M. Lee and R. D. Moser, “Direct numerical simulation of turbulent channel flow up to  $re_\tau \approx 5200$ ,” *Journal of Fluid Mechanics*, vol. 774, pp. 395–415, 2015.
- [15] S. Schimmelpfennig, *Aeroakustik von Karosseriespalten*. Phd thesis, Friedrich-Alexander-Universität Erlangen-Nürnberg, 2015.
- [16] N. Hu and M. Herr, “Characteristics of wall pressure fluctuations for a flat plate turbulent boundary layer with pressure gradients,” in *22nd AIAA/CEAS Aeroacoustics Conference*, 2016. AIAA 2016-2749.

# A FINITE-ELEMENT VISCOSITY BASED NON-SLIP WALL MODELLING STRATEGY FOR THE SIMULATION OF INDUSTRIAL TURBULENT FLOWS

H. Owen, S. Radhakrishnan, S. Gomez and O. Lehmkuhl

*Barcelona Supercomputing Center, Spain*

## Abstract

The current status of WMLES and its readiness for aerospace applications were recently discussed in the NASA CFD Vision 2030 report [1]. The report recognized WMLES as one of the pacing items "for developing a visionary CFD capability required by the notional year 2030." However, at the same time, the report stated that "WMLES requires additional development of the wall-modelling capability that is currently at a very low technology-readiness level (TRL)." The present work aims to help the increase the TRL of WMLES by proposing a novel finite-element viscosity based non-slip wall modelling strategy able to work on complex geometries. The strategy is compared with the traditional slip wall approach for finite-elements and benchmarked with the flow over a NACA4412 at  $Re_c = 10^6$  and a DrivAer car at  $Re = 4.87 \times 10^6$ . The proposed method has been proven to be more robust and insensitive to the geometry imperfections, achieving good accuracy when compared with the available reference data.

## 1 Mathematical formulation

In this work the spatially filtered Navier-Stokes equations governing the fluid flow are used:

$$\frac{\partial \bar{u}_i}{\partial x_i} = 0 \quad (1)$$

$$\frac{\partial \bar{u}_i}{\partial t} + \frac{\partial}{\partial x_k} (\bar{u}_k \bar{u}_i) = -\frac{\partial \bar{P}}{\partial x_i} + \frac{1}{Re} \nabla^2 \bar{u}_i - \frac{\partial \tau_{ik}}{\partial x_k}. \quad (2)$$

The equations are normalized using a reference length  $L$  and velocity  $U_0$ , which define the Reynolds number  $Re = U_0 L / \nu$ . The filtered velocity is  $\bar{u}_i$ ,  $\bar{P} = \bar{p} / \rho$  is the modified pressure, and  $\tau_{ik} = \bar{u}_i \bar{u}_k - \bar{u}_i \bar{u}_k$  is the subgrid scale stress (SGS) tensor.

These equations are solved by means of a low-dissipation finite-element method implemented into the code Alya [2]. Alya is a parallel multi-physics/multi-scale simulation code developed at the Barcelona Supercomputing Centre to run efficiently on high-performance computing environments. The convective term is discretized using a Galerkin finite element (FEM) scheme recently proposed [3], which conserves linear and angular momentum, and kinetic energy at the discrete level. Both second- and third-order spatial discretizations are used. Neither upwinding nor any equivalent momentum stabilization is employed. In order to use equal-order elements, numerical dissipation is introduced only for the pressure stabilization via a fractional step scheme [4], which is similar to approaches for pressure-velocity coupling in unstructured, collocated finite-volume codes [5].

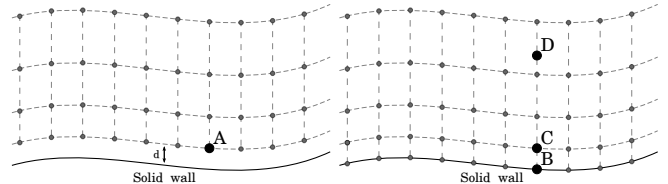


Figure 1: Wall modelling approach in different spatial discretization methods. Left) Classical finite element; right) Owen et al. [9] method

The set of equations is integrated in time using a third-order Runge-Kutta explicit method combined with an eigenvalue-based time-step estimator [6].

This approach has been shown to be significantly less dissipative than the traditional stabilized FEM approach [7]. This low-dissipation strategy has been recently tested in different massively separated flows with success [8].

The SGS stresses tensor is modelled using an eddy viscosity approach. Its deviatoric part is parametrized as

$$\tau_{ij}^a = \tau_{ij} - \frac{\delta_{ij}}{3} \tau_{kk} = -2\nu_{\text{sgs}} \bar{S}_{ij} \quad (3)$$

where  $\delta_{ij}$  is the Kronecker delta and

$$\bar{S}_{ij} = \frac{1}{2} \left( \frac{\partial \bar{u}_i}{\partial x_j} + \frac{\partial \bar{u}_j}{\partial x_i} \right) \quad (4)$$

is the strain-rate tensor. The formulation is closed by an appropriate expression for the subfilter-scale viscosity,  $\nu_{\text{sgs}}$ .

Finally, since the size of the dynamically important vortices at high Reynolds numbers becomes too small close to the wall to be grid resolved, a wall model to impose the boundary conditions for the LES equations is needed. In this study, a finite element extension [9] of the wall law of Reichardt [10] is used:

$$u^+ = \frac{1}{\kappa} \ln(1 + \kappa y^+) + 7.8 \left( 1 - e^{-y^+/11} - \frac{y^+}{11} e^{-0.33y^+} \right) \quad (5)$$

where  $u_\tau = \tau_w^{1/2}$ ,  $y^+ = y u_\tau / \nu$  and  $u^+ = u / u_\tau$ .

## 2 Slip wall modelling strategy

The analytical expression for the shear stress parallel to the wall at a distance  $y = d$  from the wall is:

$$\overline{\tau(d)} = \overline{(\nu + \nu_{\text{sgs}}) \frac{\partial u_x}{\partial y}} \Big|_{y=d} - \overline{u'_x u'_y} \Big|_{y=d} \quad (6)$$

where  $x$  and  $y$  correspond to the streamwise and wall-normal directions respectively, while  $\nu_{sgs}$  refers to the turbulent viscosity introduced by the subgrid-scale model. The first term of the RHS of Eq. (6) refers to the viscous and the modelled stresses, while the second term refers to the resolved stress. It is worth noting at this point that an open integration rule is used in the simulations, i.e., the calculations are performed at the boundary gaussian points and the corresponding exchange location points. However, we refer to grid points in the following as if a closed (nodal) integration rule was used, in order to make an easier comparison between the finite element and finite difference approaches.

The most commonly approach used for wall modelling in finite elements is to consider a mesh that does not extend all the way to the wall, as shown in Figure (1) (see also [11, 12, 13, 14]). In this approach, the layer between the wall and the first grid point (A) is not directly resolved. Instead, it is modelled through a wall function. The velocity at point A and the so-called “wall distance” between that point and the wall (denoted by  $d$  in Figure (1)) are typically used to calculate the shear stress ( $\tau(d)$ ), which is then imposed at point A. In addition, a no-penetration condition is imposed at that point.

This method sets the following conditions on point A ( $y = d$ ):

$$\overline{\tau(d)} = \overline{(\nu + \nu_{sgs}) \frac{\partial u_x}{\partial y}} \Big|_{y=d} \quad (7)$$

$$u_y = 0 \quad (8)$$

where the no-penetration condition (Eq. (8)) means the resolved stress is equal to zero. Comparing Eq. (6) and Eq. (7), we see that the classical approach does not account for the effect of the resolved stress at  $y = d$ . Since the total shear stress is well calculated due to momentum conservation, this leads to an inaccurate prediction of the velocity gradient, i.e., the method suffers from severe log-layer mismatch (see Owen et al [9]).

Similar to finite differences and finite volumes [15, 16, 17, 18, 19], Owen et al. [9] have recently proposed the following slip approach, to be used in the present paper. In this approach, the grid extends all the way to the solid wall (Figure (1)) and we are, in fact, imposing the wall shear stress at  $y = 0$ , in terms of the velocity evaluated at  $y = d$ , where  $d$  denotes the distance between the first grid point (B), which coincides with the wall, and the first grid point off the wall (C). Due to the fact that this velocity has a non-zero vertical component, the problem outlined in the previous paragraph in regards to the resolved stress being zero at a distance  $y = d$  from the wall is solved. It is worth noting that, since in this case we actually are resolving the near-wall part of the domain, the following shear stress at point B are indirectly imposed:

$$\overline{\tau(d)} = \overline{(\nu + \nu_{sgs}) \frac{\partial u_x}{\partial y}} \Big|_{y=d} - \overline{u'_x u'_y} \Big|_{y=d} \approx \overline{\tau(y=0)} + \frac{\partial p}{\partial x} \quad (9)$$

where the last approximation stems from integrating the Navier-Stokes equations in the near-wall elements. As opposed to the classical finite element approach, this method is equivalent to a wall-stress model (following the classification of [18]), where a wall model is solved over a layer of thickness  $d$ .

A further improvement of the slip method is to include an exchange location method (as explained in [20]) to reduce numerical errors. A very typical problem of wall modelling is that, even with a perfect wall model, the

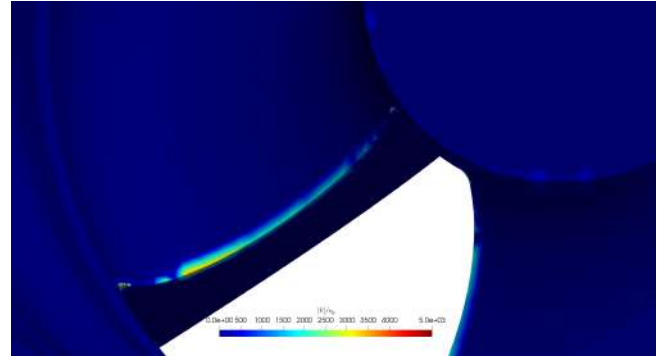


Figure 2: Slip wall artefacts at the edge of sharp surface in a realistic car wheel geometry

results would still be inaccurate, since the LES is under-resolved in the near-wall part of the domain (e.g. at the first grid point off the wall) and thus provides inaccurate information to the wall model. There is, however, no requirement for the velocity to be evaluated at the first grid point off the wall. As mentioned earlier, the only requirement is that the velocity is evaluated at a point located within the inner part of the boundary layer, where the wall functions are typically valid. The use of the exchange location method allows us to place the exchange interface (i.e. the point where the LES feeds information to the wall model) further away from the wall (such as point D in Figure (1)), where the LES is more accurately resolved and, therefore, can provide a more accurate prediction for the wall shear stress. In our slip wall model we carry out this technique at the 3<sup>rd</sup> off-grid node.

### 3 Non-slip wall modelling strategy

Despite the method presented in the previous Section provides highly accurate results for moderately complex geometries it can suffer from robustness issues as the geometry becomes more complex. The difficulties are associated to particularities of the finite element method for the application of no penetration in the normal direction and slip conditions in the tangential direction. These, plus an external force in the opposite direction to the velocity are the main ingredients of the wall law presented in the previous Section. In order to apply slip no penetration boundary conditions at a wall node the normal at that node must be defined. When all the boundaries that surround the node have the same normal, the definition of the normal at the node is straightforward. When the geometry is complex, the normal at a node is defined in such a way that the total flow through the boundaries surrounding the node is zero when the normal velocity at the node is zero [21]. This works well on most curved boundaries but introduces difficulties at sharp edges. The most basic example where this problem arises is the flow around a 2D symmetric airfoil with a sharp trailing edge at zero angle of attack. If both boundaries touching the node at the trailing edge have the same size, the normal at the trailing edge node turns out to be aligned with the incoming flow. The no penetration boundary condition, zero velocity in the normal direction, creates a spurious stagnation point and an unphysical rise of the pressure at the node (see Figure (2) for a more complex example). When such situation arises in a finite element grid, two possible solutions are



adopted. The first one is to smoothen out the geometry so that the sharp trailing edge is removed, but this is not always possible or desired. The second solution is to modify the boundary condition at the trailing edge node so that penetration is allowed. This results in a non zero flow through the airfoil boundary and is therefore not an optimal solution but it usually provides better results than using the no penetration boundary condition. Moreover, the main disadvantage with this approach is that it is only feasible for simple geometries, since the nodes where the boundary condition needs to be modified have to be selected by the user.

Within the finite volume community two different implementations of the wall law exists. The first one introduces the traction calculated from wall law as a source term in the momentum equations similarly to what we described in the previous Section. The second approach [22] modifies the viscosity in the first element so that the modified viscosity times the velocity gradient equals the traction calculated from the wall law. In the finite volume context the gradient is approximated from the velocity difference between the wall and the velocity at the cell center and the distance from the cell center to the wall. Contrary to what happens with typical finite volumes, in finite elements there are unknowns located at the boundary. When adapting the method proposed in [22] to finite elements we prescribe the velocity to zero at the wall and introduce a modified viscosity in the elements close to the wall that is obtained from the velocity gradients and the traction provided by the wall law. Having a zero velocity at the wall eliminates the problems that we have described previously and thus provides a much more robust approach. According to our knowledge, this method has not been used in the finite element context before despite it eliminates well known problems when the no penetration slip boundary condition is used with complex geometries.

At the elements that are in contact with the wall the viscosity is modified with an additional viscosity,  $\nu_{ad}$ . The traction at the wall is then

$$\tau(0) = (\nu + \nu_{sgs} + \nu_{ad}) \left. \frac{\partial u_x}{\partial y} \right|_{y=0},$$

where  $\tau(0)$  is obtained from the wall law (usually by means of the exchange location method explained in the previous Section) and  $\frac{\partial u_x}{\partial y}$  is the normal derivative of the velocity in the element. The additional viscosity is therefore obtained from

$$\nu_{ad} = \tau(0) \left. \frac{\partial u_x}{\partial y} \right|_{y=0}^{-1} - (\nu + \nu_{sgs}).$$

## 4 Numerical experiments

### 4.1 NACA4412

In order to test the presented wall modelling strategies, the flow over a NACA4412 at  $Re_c = U_0 C / \nu = 10^6$  and  $AoA = 5^\circ$  is selected. This particular configuration has been recently studied by Vinuesa et al. [23] by means of well-resolved LES using the spectral-element code Nek5000 and 2.28 billion grid points. Being a very nice data base to validate wall models for LES on adverse pressure gradients (APG), more specifically, we compare wall shear stress, boundary layer (BL) profiles and pressure distribution (here comparing to the experimental data available [24]).

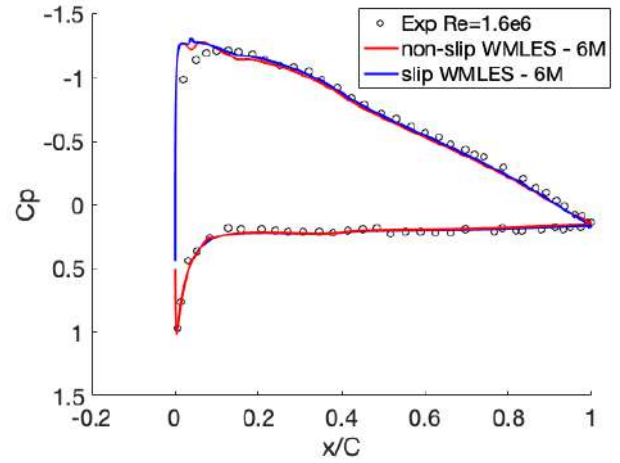


Figure 3: NACA4412 at  $Re_c = 10^6$  and  $AoA = 5^\circ$ . Non-dimensional pressure at the airfoil surface, WMLES results vs. experimental data [24]

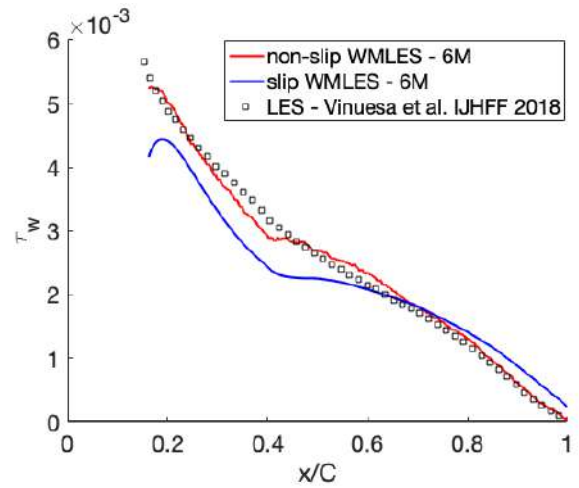


Figure 4: NACA4412 at  $Re_c = 10^6$  and  $AoA = 5^\circ$ . Wall shear stress at the suction side, WMLES results vs wall resolved results from Vinuesa et al. [23]

A mesh of 6 million grid points is used for our calculations, the grid is representative for wall model LES being the first grid point of  $y^+ \approx 30$  and having at least 10 elements inside the BL region. Additionally, bump of the size of the  $\delta$  is located at  $x/C = 0.1$  to trigger the turbulence transition, similarly to the experiments and previous LES works. The ILSA subgrid scale eddy viscosity model [25] is used in this study.

First, we compare the results of both wall shear approaches to predict the pressure at the airfoil surface (see Figure (5)). No apparent differences for this quantity are observed when compared with the experimental data [24]. More interesting is the prediction of the wall shear stress at the suction side of the NACA4412, here the viscosity based non-slip approach outperforms the slip wall model. Although the non-slip wall models does not present a fully turbulent BL until  $x/C = 0.5$  the error with the wall resolved data is less than 10% for all the positions. This is a good proof of the capability of WMLES to work in APG even using equilibrium correlations. This is related with the fact that a WMLES resolves the energy containing scales of the BL out-layer. As seen in Figure (4), the slip wall approach has more difficulties to predict the wall shear, although obtained

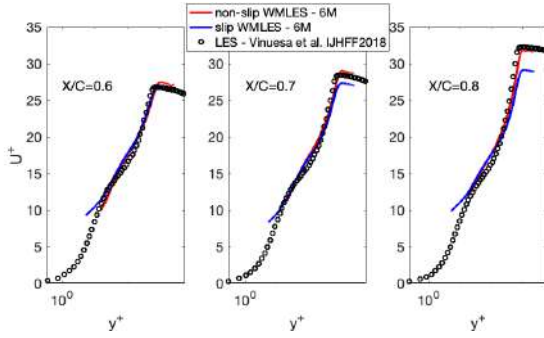


Figure 5: NACA4412 at  $Re_c = 10^6$  and  $AoA = 5^\circ$ . Mean velocity profiles in wall units at position  $x/C = 0.6, 0.7$  and  $0.8$ , WMLES results vs wall resolved LES results from Vinuesa et al. [23]

results are rather fair.

Finally, the mean velocity profiles in wall units at position  $x/C = 0.6, 0.7$  and  $0.8$  are also assessed. Agreement is perfect for the viscosity non-slip approach, however the slip wall approach has much more difficulties to predict the mean velocity profile in wall units as it gets closer to the trailing-edge. It is important to remember that the error of the slip wall model is bigger in sharp surfaces, exactly like the ones encountered in this area of the airfoil.

## 4.2 DrivAer car

The selected test case is a realistic generic car model called the DrivAer body that has become widely accepted within the aerodynamics community (see for instance [26]). The model has been developed at TUM, where it has been experimentally tested using a 40% scaled model at  $Re = 4.87 \times 10^6$ . In the Munich wind tunnel, cases with and without moving ground have been simulated taking advantage of the belted wind tunnel. We choose to focus our work on the moving ground cases, since the physics are closer to real industrial conditions. Three different geometries are available where the back part of the geometry is changed: fastback, estateback and notchback (see Figure (6)).

The computational domain has a length of  $10L$ , a height of  $8H$  and a width of  $11W$ , where the vehicle is situated at  $2L$  from the inlet boundary at the symmetry. A top hat laminar profile is imposed at the inlet and pressure based condition is imposed at the outlet. A slip velocity at the reference velocity is prescribed at the ground boundaries, a tangential velocity is set at the wheel car surface and the wall model is imposed at the car body surface. A final mesh of 80M elements is used with a resolution in the car surface of 1 mm in the wall normal direction and between 1 and 10 mm in the tangential directions. Here, the mesh is more challenging for a WMLES simulation, and the resolution in BL is from 3 to 10 elements. Therefore, the out-layer may not be resolved in some of the car regions, however this is a representative mesh for an industrial application with the current computational power. The Vreman subgrid scale eddy viscosity model [27] is used in this study.

The instantaneous  $Q$ -isosurfaces are depicted in Figure (7) for the fastback geometry and the non-slip wall model. Similar features are observed using the slip wall model and in the other two geometries. The flow remains attached in the central part of the body and detaches with the interaction of the wheels, the side mirror and the back region.

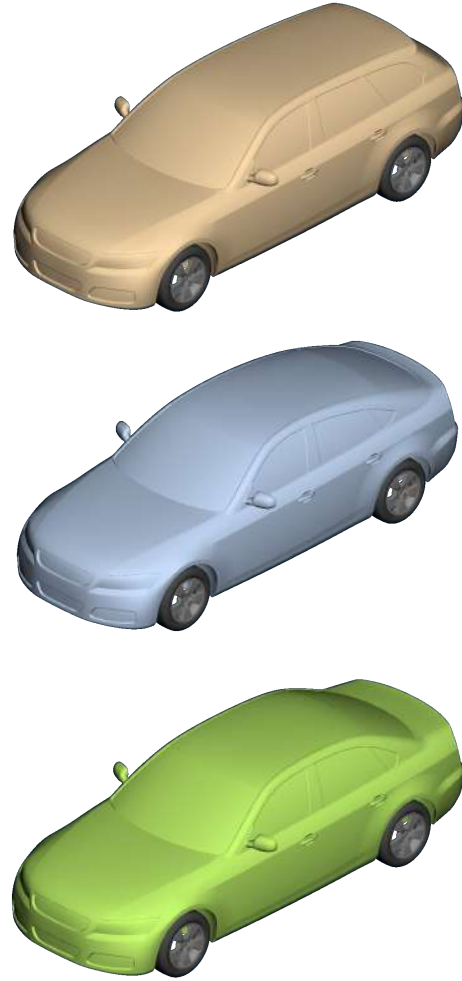


Figure 6: DrivAer geometries. Top) estateback ; middle) fastback ; bottom) notchback

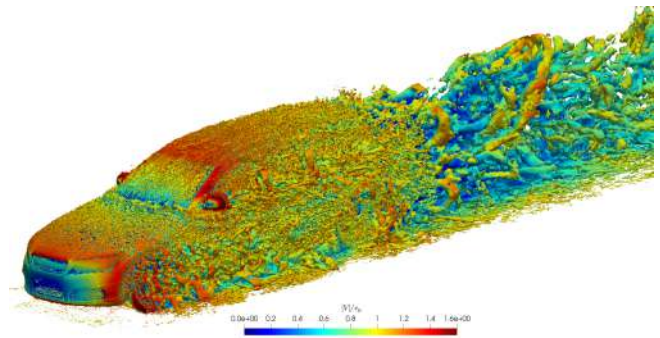


Figure 7: DrivAer fastback with ground simulation ( $Re = 4.87 \times 10^6$ ). Instantaneous  $Q = 100$  isosurfaces coloured by velocity magnitude

Table 1: Drivaer with ground simulation ( $Re = 4.87 \times 10^6$ ). Aerodynamic force coefficient. Drag coefficient,  $C_D$  and lift coefficient,  $C_L$ , respectively.

		$C_D$	$C_L$
Fastback	slip	0.252	-0.040
	no-slip	0.259	-0.063
	experiment [26]	0.258	-0.060
Estateback	slip	0.334	0.104
	experiment [26]	0.316	-0.201
Notchback	slip	0.268	-0.063
	no-slip	0.258	-0.058
	experiment [26]	0.270	-0.080

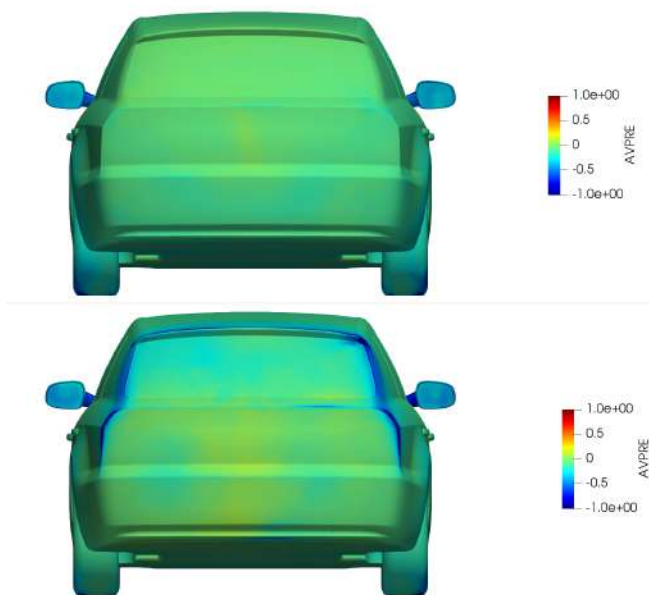


Figure 8: DrivAer estateback with ground simulation ( $Re = 4.87 \times 10^6$ ). Averaged non-dimensional pressure at the car surface. Top) viscosity based non-slip wall model; bottom) slip wall model

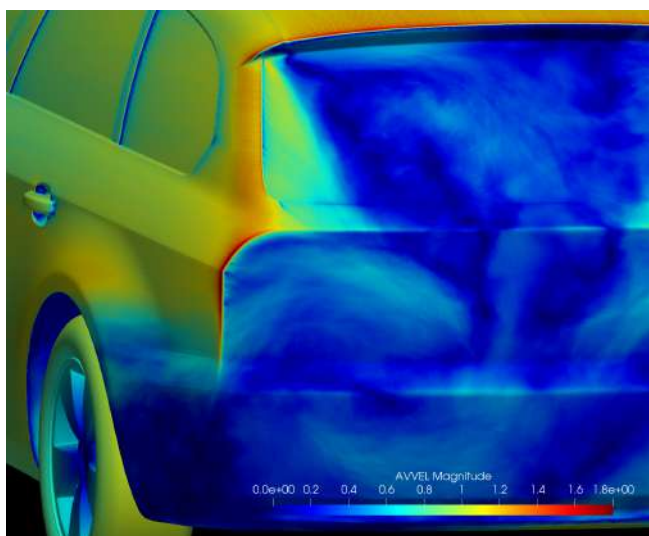


Figure 9: DrivAer estateback with ground simulation ( $Re = 4.87 \times 10^6$ ) with slip wall model. Detail of the averaged non-dimensional slip wall velocity at the back of the car

The inspection of the averaged forces over the car is very interesting (see Table (1)). First, when the car geometry is smooth (i.e, fastback and notchback), little differences between the two considered methodologies are observed, and differences might just be related to sampling errors. This later point will be studied in a future work. However, for the estateback geometry, where sharp corners in the back surface of the car are present, the slip velocity based strategy has larger differences versus the experimental data[26]. Here, the drag coefficient is overestimated with a bigger error respect to the other geometries, but the more problematic aspect is that the lift coefficient is no longer negative, having a relative error around 150%. These results are very different from the ones obtained with the viscosity non-slip model with errors around 6% and 4% for the drag and lift coefficients, respectively.

In order to understand why the slip wall model is failing, the pressure at the back region of the estateback car is presented in Figure (8) for both wall modelling approaches. An un-physical pressure depression in the sharp edge features of the back geometry is observed for the slip wall model, this is not observed in the non-slip wall model results, where the pressure remains approximately constant in the rear part of the car. More clues related to this un-physical behaviour can be found in the Figure (9), where the averaged mean slip wall velocity is shown. Here, spikes of velocity around the sharp edges are observed, most likely generated by the ambiguous definition of the nodal normal vector in those edges.

## 5 Conclusions

In this work, a novel finite-element viscosity based non-slip wall modelling strategy for LES has been proposed and compared with the traditional slip wall velocity (see [9]). First, the two different wall modelling approaches have been validated with the flow over a NACA4412 at  $Re_c = 10^6$  and  $AoA = 5^\circ$  by direct comparison with well-resolved LES results from Vinuesa et al. [23]. Good results are obtained for both approaches, but the wall shear stress is better predicted by the non-slip wall strategy. Finally, the DrivAer car at  $Re = 4.87 \times 10^6$  is used in order to asses the performance of the wall modelling strategies in realistic geometries. As conclusion, the present results with the DrivAer configuration are a very nice example of the limitations of the traditional slip wall velocity approach, that is capable of giving accurate results but is limited to smooth surfaces. Hence, it is not a good method towards large scale WMLES of industrial applications, where to have sharp edges in the geometry model is very common. Fortunately, the novel method proposed in this work based on an elemental viscosity and resulting in a non-slip wall model, has been proven to be more robust and insensitive to the geometry details, achieving good accuracy when compared with the wind tunnel results.

## Acknowledgment

We acknowledge the financial support by the the Ministerio de Economía y Competitividad, Secretaría de Estado de Investigación, Desarrollo e Innovación, Spain (ref. TRA2017-88508-R). We also acknowledge Barcelona Supercomputing Center for awarding us access to the MareNostrum IV machine based in Barcelona, Spain. OL acknowledges Prof. I. Rodriguez, Dr. A. Lozano-

Duran and Prof. R. Vinuesa for the discussions and data analysis of the NACA4412. In addition, the NACA4412 results are funded in part by the Coturb program of the European Research Council.

## References

- [1] J. Slotnick, A. Khodadoust, J. Alonso, D. Darmofal, W. Gropp, E. Lurie, and D. Mavriplis, “Cfd vision 2030 study: A path to revolutionary computational aerosciences,” *Technical Report, NASA/CR-2014-218178, NF1676L-18332*, 2014.
- [2] A. M. Vazquez, G. Houzeaux, S. Koric, A. Artigues, J. Aguado-Sierra, R. Aris, D. Mira, H. Calmet, F. Cucchietti, H. Owen, E. Casoni, A. Taha, E. D. Burness, J. M. Cela, and M. Valero, “Alya: Multiphysics engineering simulation towards exascale,” *J. Comput. Sci.*, vol. 14, pp. 15–27, 2016.
- [3] S. Charnyi, T. Heister, M. A. Olshanskii, and L. G. Rebholz, “On conservation laws of Navier-Stokes Galerkin discretizations,” *Journal of Computational Physics*, vol. 337, pp. 289 – 308, 2017.
- [4] R. Codina, “Pressure stability in fractional step finite element methods for incompressible flows,” *J. Comput. Phys.*, vol. 170, pp. 112–140, 2001.
- [5] L. Jofre, O. Lehmkuhl, J. Ventosa, F. Trias, and A. Oliva, “Conservation properties of unstructured finite-volume mesh schemes for the Navier-Stokes equations,” *Numerical Heat Transfer, Part B: Fundamentals*, vol. 54, no. 1, pp. 53–79, 2014.
- [6] F. X. Trias and O. Lehmkuhl, “A self-adaptive strategy for the time integration of Navier-Stokes equations,” *Numerical Heat Transfer. Part B*, vol. 60, no. 2, pp. 116–134, 2011.
- [7] O. Lehmkuhl, G. Houzeaux, H. Owen, G. Chrysokentis, and I. Rodriguez, “A low-dissipation finite element scheme for scale resolving simulations of turbulent flows,” *Journal of Computational Physics*, vol. 390, pp. 51 – 65, 2019.
- [8] O. Lehmkuhl, H. Owen, G. Chrysokentis, S. Gomez, and G. Houzeaux, “On the large-eddy simulation with wall modelled support for massive separated flows at high Reynolds numbers,” in *Seventh European Conference on Computational Fluid Dynamics (ECFD7)*, (Glasgow (UK)), 11-15 June 2018.
- [9] H. Owen, G. Chrysokentis, M. Avila, D. Mira, G. Houzeaux, R. Borrell, J. C. Cajas, and O. Lehmkuhl, “Wall-modeled large-eddy simulation in a finite element framework,” *International Journal for Numerical Methods in Fluids*, 2019.
- [10] H. Reichardt, “Vollständige darstellung der turbulenten geschwindigkeits- verteilung in glatten leitungen,” *ZAMM-Z. Angew. Math. Me.*, vol. 31, pp. 208–219, 1951.
- [11] D. Lacasse, E. Turgeon, and D. Pelletier, “On the judicious use of the k-epsilon model, wall functions and adaptivity,” *Int. J. Therm. Sci.*, vol. 43, pp. 925–938, 2004.
- [12] T. C. Rebollo, M. G. Marmol, and S. Rubino, “Numerical analysis of a finite element projection-based vms turbulence model with wall laws,” *Computer Methods in Applied Mechanics and Engineering*, vol. 285, pp. 379–405, 2015.
- [13] A. Lew, G. Buscaglia, and P. Carrica, “A note on the numerical treatment of the k-epsilon turbulence model,” *International Journal of Computational Fluid Dynamics*, vol. 14, no. 3, pp. 201–209, 2001.
- [14] D. Kuzmin, O. Mierka, and S. Turek, “On the implementation of the k-epsilon turbulence model in incompressible flow solvers based on a finite element discretisation,” *International Journal of Computing Science and Mathematics*, vol. 1, no. 2-4, pp. 193–206, 2007.
- [15] P. Sagaut, *Large eddy simulation for incompressible flows - An introduction*. Springer, 3 ed., 2006.
- [16] U. Piomelli and E. Balaras, “Wall-layer models for large-eddy simulations,” *Annu. Rev. Fluid Mech.*, vol. 34, pp. 349–374, 2002.
- [17] U. Piomelli, “Wall-layer models for large-eddy simulations,” *Prog. Aerosp. Sci.*, vol. 44, no. 6, pp. 437–446, 2008.
- [18] J. Larsson, S. Kawai, J. Bodart, and I. Bermejo-Moreno, “Large eddy simulation with modelled wall stress: recent progress and future directions,” *Mech. Eng. Rev.*, vol. 3, no. 1, 2016.
- [19] S. T. Bose and G. I. Park, “Wall-modeled large-eddy simulation for complex turbulent flows,” *Annu. Rev. Fluid Mech.*, vol. 50, pp. 535–561, 2018.
- [20] S. Kawai and J. Larsson, “Wall-modeling in large eddy simulation: Length scales, grid resolution, and accuracy,” *Phys. Fluids*, vol. 24, no. 015105, 2012.
- [21] R. L. S. P. M. Gresho, *Incompressible flow and the finite element method*. John Wiley & sons, 2000.
- [22] L. Davidson and B. Farhanieh, “CALC-BFC. Report 95/1,” tech. rep., Department of Thermo and Fluid Dynamics, Chalmers University of Technology, Gothenburg, 1995.
- [23] R. Vinuesa, P. Negi, M. Atzori, A. Hanifi, D. Henningson, and P. Schlatter, “Turbulent boundary layers around wing sections up to  $re_c = 1000000$ ,” *International Journal of Heat and Fluid Flow*, vol. 72, pp. 86 – 99, 2018.
- [24] R. C. Hastings and B. R. Williams, “Studies of the flow field near a naca 4412 aerofoil at nearly maximum lift,” *The Aeronautical Journal (1968)*, vol. 91, no. 901, pp. 29–44, 1987.
- [25] O. Lehmkuhl, U. Piomelli, and G. Houzeaux, “On the extension of the integral length-scale approximation model to complex geometries,” *International Journal of Heat and Fluid Flow*, vol. 78, p. 108422, 2019.
- [26] A. I. Heft, *Aerodynamic Investigation of the Cooling Requirements of Electric Vehicles*. PhD thesis, Technische Universitat Munchen, 2014.
- [27] A. W. Vreman, “An eddy-viscosity subgrid-scale model for turbulent shear flow: Algebraic theory and applications,” *Phys. Fluids*, vol. 16, no. 10, pp. 3670–3681, 2004.

# COUPLED HYBRID RANS-LES RESEARCH AT THE UNIVERSITY OF MANCHESTER

A. Revell\*, I. Afgan, A. E. A. Ali, M. C. Santasmasas, T. Craft, A. De Rosis, J. Holgate, D. Laurence, B. E. O. Iyamabo, A. Mole, B. Owen, M. Savoie, A. Skillen, J. Wang and X. Zhang

*Multiscale & Multifidelity Modelling for CFD (M3CFD)*

*Department of Mechanical, Aerospace & Civil Engineering, The University of Manchester, UK*

## Abstract

This short communication summarises recent developments and ongoing work on Hybrid RANS-LES Methods (HRLM) at The University of Manchester. Our work is focussed primarily on the development of coupled zonal methods, investigating improvements and novel applications of embedded turbulence simulation via the Synthetic Eddy Method. These activities are centred around the premise that no single modelling methodology will be generally applicable. Not only does this apply to different test cases, but for particular regions of the flow within a single test case. Similarly, when factoring in the computational resources available to the modern-day CFD practitioner, a framework for multifidelity approaches seems pragmatic. The work presented herein is intended primarily as a window through which we outline our current activities, mostly driven by PhD projects, many of which with industrial projects in mind. We also introduce recent developments focused on using the lattice Boltzmann method as part of a coupled Hybrid RANS LES approach.

## 1 Introduction

Hybrid RANS-LES Methods offer compromise to the accuracy-cost-speed trilemma for simulations at moderate-to-high Reynolds number, and can generally be separated into two distinct classes, 1) Zonal and 2) Non-Zonal (Global). The latter has become more widely used than the former over the past decades, in particular due to the prevalence of Detached Eddy Simulation proposed by Strelets et al. [1], which has received a lot of attention for industrial applications [2]. On the other hand, Zonal approaches such the framework proposed by Deck [3] can offer different advantages. These methods generally employ sub-domains which are then solved individually with a separate set of transport equations. Unlike non-zonal methods, there is a clear and conscious demarcation between mean RANS and transient LES regions. In the transfer to LES regions, instantaneous fluctuations must be generated using information taken from the upstream flow; whereas the mean/modelled turbulent quantities must be recovered from the LES field upon re-entering a RANS region.

At Reynolds numbers of practical engineering interest, the incoming flow will often be turbulent. The generation of turbulent inflow boundary conditions for scale-resolving simulations poses a formidable challenge. A popular solution to this problem is the Synthetic Eddy Method (SEM) of Jarrin et al. [4] whereby Lagrangian spots (or synthetic eddies) are generated to represent

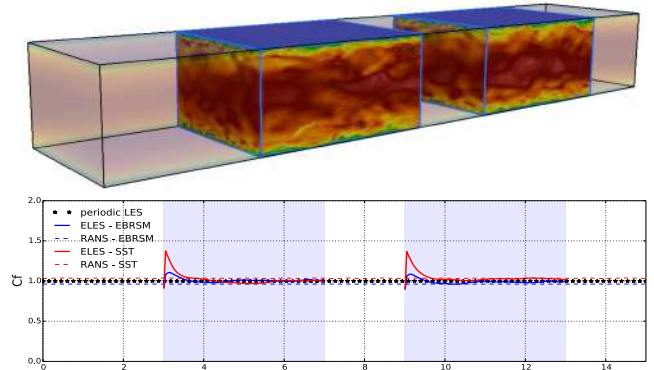


Figure 1: Proof of concept for ELES, **Top**) Two-region nested LES computation coloured by instantaneous velocity. **Bottom**) Skin friction coefficient normalised by periodic LES value through the entire channel

fluctuations, with the intensity and sign set to satisfy prescribed first and second order statistics. In practise, these low-order statistics may be obtained by experiment, theoretical approximation, or as is perhaps the most common, by a separate or precursor RANS study. Embedded LES (ELES) is a natural evolution of this concept, whereby the RANS data generated in one mesh is used directly for the generation of synthetic turbulence and subsequent turbulent simulation in another. An early implementation of ELES is presented by Cokljat et al. [5] who considered a number of internal flow applications and a number of more recent implementations have followed. Notably Li et al. [6] validated a two-region ELES solver consisting of a single RANS and implicit LES region and Anupindi & Sandberg [7] implemented an ELES model within OpenFOAM. In a slightly different approach, Vonlanthen et al. [8] introduced a one-way nesting procedure which embeds a highly-resolved LES within a low-resolution LES. For an extensive review of Embedded LES approaches the reader is referred to Holgate et al. [9].

Through work at the University of Manchester, the SEM has evolved in several directions; a divergence-free version was proposed by Poletto et al. [10] and a more efficient formulation was presented by Skillen et al. [11]. More recent work has focused on the code-code coupling aspects, wherein mixed fidelity solvers can be used interchangeably. In particular we have developed ideas based on the Two-Velocity method of Uribe et al. [12], and the consistent Dual-Mesh approach of Xiao and Jenny [13]. These methods solve RANS and LES models simultaneously on separate grids, with added ‘drift terms’ in the momentum, pressure and turbulent transport equations used to relax the flow statistics towards a consistent solution.

\*contact: alistair.revell@manchester.ac.uk

As a final point, it is worth noting that in all the above, zonal methods are enhanced when the upstream prediction of turbulent Reynolds stresses is good. As such there is a rational case for the use and further refinement of advanced turbulence modelling tools in this framework. We have been using the Elliptic Blending model of Manceau and Hanjalić [14] with its demonstrated advantages complex flows [15], as well as models based on the stress-strain lag approach of Revell et al. [16], recently reformulated for elliptic blending [17]. This is highlighted in recent work demonstrating potential for multiple embedded regions, as shown in Figure (1), where faster recovery is observed with the more advanced turbulence model.

## 2 Recent work with the SEM

As recently demonstrated by Skillen et al. [11], with improved normalisation of the fluctuations on the inlet plane, the Synthetic Eddy Method (SEM) can accomplish a short recovery of the turbulent statistics. However, it remains sensitive to the prescribed variation of the length scale  $\sigma$  to produce realistic turbulence. The length scale of the eddies is generally assigned the following form where  $C_\sigma$  is a scaling factor, discussed further below.  $\sigma_i = \min(C_\sigma R_{ii}^{3/2} / \varepsilon, \sigma_{\max})$ .

Defining the term Eddy Simulation (ES) as applying to both DES and LES methods, and following extensive testing for internal flows, we now consider application to a spatially developing boundary layer case in the fully turbulent regime. A schematic showing how the domain is split between mean and resolved (ES) domain is shown in Figure (2). In this case we use Improved Delayed Detached Eddy Simulations (IDDES) in place of the LES in order to further reduce the computational cost according to Shur et al. [18]. The Reynolds number based on the momentum thickness at the start of the LES region is  $Re_\theta = 3040$ .

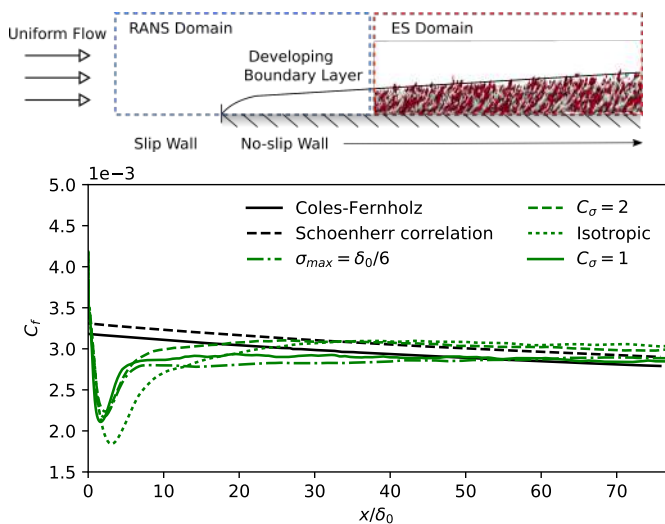


Figure 2: **Top)** Schematic of TBL domain. **Btm)** Downstream recovery of skin friction coefficient  $C_f$

In order to assess the development length, the evolution of the skin friction coefficient,  $C_f$ , along the length of the ES domain is shown in Figure (2). Some sensitivity to imposed length scale variation is observed as also identified in earlier work for internal flows [9], in an attempt to minimise the development length. In this instance increasing the length scale by setting  $C_\sigma = 2$  improved the

development length. The figure also demonstrates that using an anisotropic length scale definition is a significant improvement over an isotropic definition.

First and second order statistics of the flow at a location downstream of the SEM were also assessed. These are given for a Reynolds number based on the momentum thickness of  $Re_\theta = 5200$  and compared to experimental data of DeGraaff & Eaton [19]. Although a degree of log-layer mismatch is present, the close agreement of the statistics suggest that the relationship between the IDDES and the SEM is working.

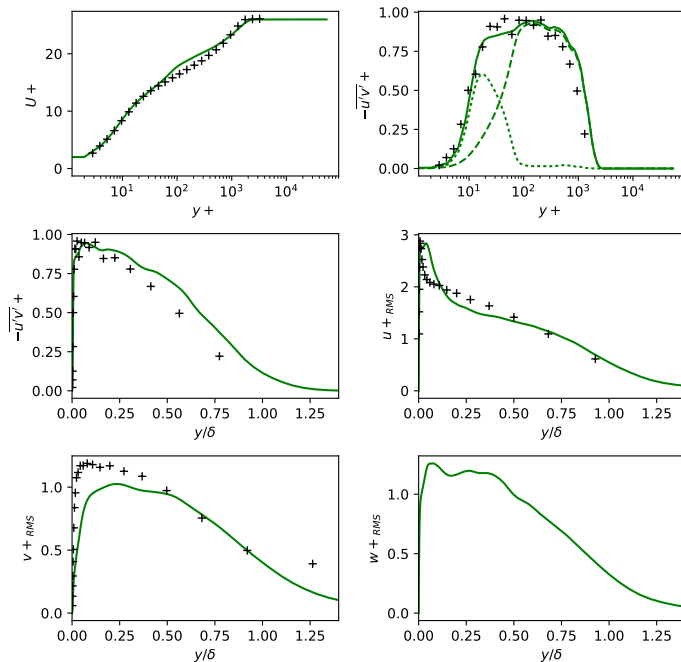


Figure 3: Velocity and Reynolds stress profiles at  $Re_\theta = 5200$ . *Solid:* Total stress, *Dashed:* Resolved stress, *Dotted:* Modelled stress

As an example of a more complex test for SEM, we consider the case defined by Liu et al. [20] for the superposition of a pair of counter-rotating vortices in a turbulent boundary layer, directly relevant to flow downstream of vortex generators and other flow control devices. Initial work has been performed on a ‘Common Flow Down’ vortex pair, generated by superimposing Batchelor vortices onto the boundary layer inlet before applying the SEM. Figure (4) shows a visualisation of the flow for this case using Q-iso surfaces.

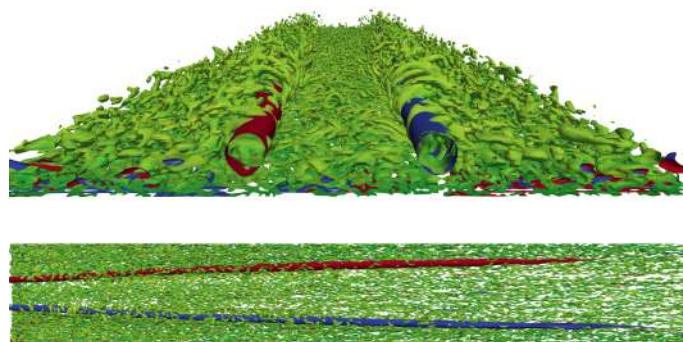


Figure 4: Q-iso surfaces. *Top:* View from inlet, *Bottom:* Side view. *Green:* Instantaneous, *Red and blue:* Mean

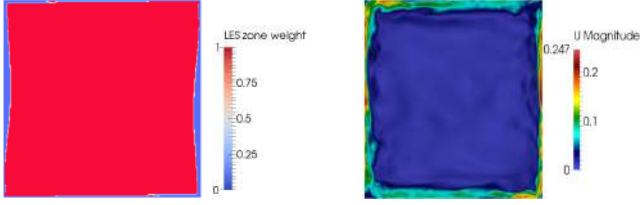


Figure 5: Square Cavity Case. Distribution of the LES zone weight and Instantaneous Velocity

### 3 Dual Mesh with Heat transfer

In this work, the dual-mesh approach [13] was extended and applied for the first time to natural convection flows, following work by Tunstall et al. [21]. The two cases reported here are a high Rayleigh number differentially heated square cavity flow and the flow in a cylindrical annuli. Detailed descriptions of these test cases can be found in [22] and [23].

In the dual-mesh approach, two separate meshes are produced, tailored to the specific needs of each solver; the RANS grid is refined in the near-wall regions and the LES grid is designed to be under-resolved near the walls of the domain. The two simulations are ‘drifted’ towards each other using source terms added to the momentum, temperature and turbulence equations of the RANS and the LES. A novel criterion is introduced to predict the locations at which the LES is under-resolved. At these locations, the mean velocity and temperature, total turbulent kinetic energy and total temperature variance (the latter two including resolved and modelled contributions) of the LES solution are corrected towards the corresponding RANS quantities. At remaining locations, the RANS solution is corrected towards the solution of the LES. More details about the formulation of the method can be found in [13] and [21].

A new criterion has been introduced based on the ratio of the turbulence length scales to the grid size; designed to account for the presence of both turbulent and laminar regions within the flow domain. Reasonable results for the square cavity and cylindrical annuli flows were obtained when the new criterion was used. Results for the square cavity are shown in Figure (5) which displays the LES zone weight ( $\sigma^L$ ) as well as the instantaneous velocity. This quantity is equal to 0 at locations where RANS drives the LES, and equals unity at all other locations. It can be observed that the new criterion returns a rational variation, with  $\sigma^L=0$  restricted to the near-wall regions of the boundary layers. This is in contrast with the original formulation of the model and demonstrates the criteria’s ability to discern near-wall flow from laminarization that occurs in the core of the cavity due to the stable stratification.

With regards to the cylindrical annuli flow, a schematic of the flow geometry is shown in Figure (6). In this figure, the tangential velocity component at a line located at an angle of  $60^\circ$  is also shown and compared to quasi-direct numerical simulation data from [23]. It can be seen that RANS and LES results from the dual-mesh framework (solid lines) offer improved prediction when compared to the RANS and LES results computed alone (dashed lines).

### 4 Subdomain Wall Function

In addition to the work presented in the previous section, we are developing a modified approach wherein

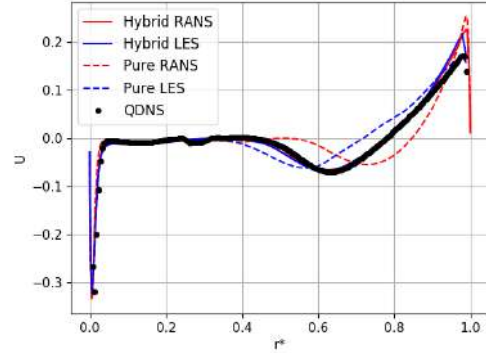
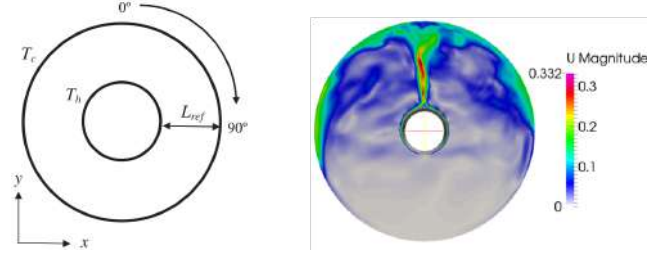


Figure 6: **Top**) Schematic of the cylindrical annuli and Instantaneous Velocity from simulation. **Bottom**) Tangential velocity along radius at  $60^\circ$

the RANS mesh covers only a narrow near wall region, termed a subdomain wall function (SWF). This method shares much with the previous section and is similar to the wall-modelled LES (WMLES) of Balaras et al. (1996)[24]. As portrayed in Figure (3), the primary domain covers the entire region of the flow field and computes the transport equations of LES. The second domain, termed here the subdomain, overlaps the near-wall area of the coarse LES grid and solves the RANS equations. The two domains are coupled to exchange information between grids. The SWF makes use of ideas of Xiao and Jenny[13] by applying the wall function as a weak volumetric source term in the near-wall LES region beyond the first cell at the wall. This source term corrects the under-resolved near-wall LES fields. In return, the LES grid supplies information to the interface of the RANS grid to complete the boundary conditions of the RANS subdomain. A consistent coupling at the interface is established by computing the partial time average of the instantaneous LES fields. The use of the partial mean differentiates the method from previous WMLES approaches which instead couple instantaneous LES directly to the RANS values.

The partial time-average of LES fields of interest is computed using the exponentially weighed average (EWA), where the averaging time period is sufficiently long to ensure the assumption that the partial time-averaged filtered LES velocity is equivalent to the Reynolds-averaged velocity ( $\langle \bar{U}_i \rangle^{EWA} \approx \langle U_i \rangle^{RANS}$ ). This assumption enables the calculation of the resolved fluctuations about the EWA of the filtered velocity as  $u_i'' = \bar{U}_i - \langle \bar{U}_i \rangle^{EWA}$ . The LES stress tensor is determined as the summation of the resolved and modelled stresses about the EWA of the filtered velocity  $\tau_{ij} = u_i'' u_j'' + \tau_{ij}^r$ . Hence, the LES stress tensor is assumed to be equivalent to the RANS stress tensor as  $\langle \tau_{ij} \rangle^{EWA} \approx \langle u_i u_j \rangle^{RANS}$ .

The momentum transport equation for the LES domain is defined as:

$$\frac{\partial \bar{U}_i}{\partial t} + \frac{\partial \bar{U}_i \bar{U}_j}{\partial x_j} = -\frac{\partial P}{\partial x_i} + 2\nu \frac{\partial}{\partial x_j} \bar{S}_{ij} - \frac{\partial \tau_{ij}^r}{\partial x_j} + Q_i, \quad (1)$$

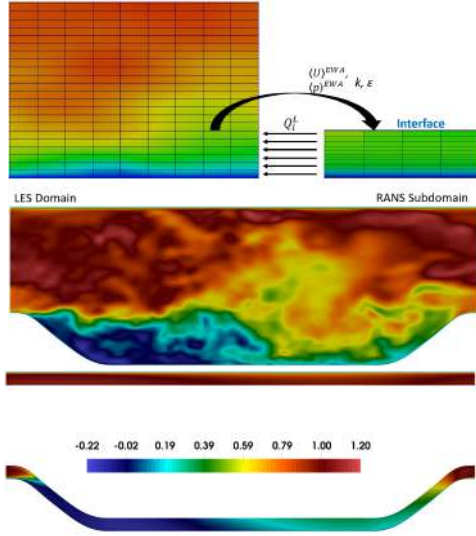


Figure 7: **Top)** Schematic of the subdomain wall function for LES. **Bottom)** Contours of the LES and RANS domains predicted by the subdomain wall function

where  $Q_i$  is the drift term which is defined as:

$$Q_i = (1 - \sigma^L) \left[ \frac{\langle U_i \rangle^{RANS} - \langle \bar{U}_i \rangle^{EWA}}{\gamma_{l1}} + \frac{G_i}{\gamma_{l2}} \right]. \quad (2)$$

The variable  $\sigma^L$  is the zoning parameter that determines the areas of the LES grid that are under-resolved. The drift term is only active in the area of the LES grid that overlaps the RANS subdomain. The left term in the square bracket of the drift term relaxes the partial mean filtered LES velocity towards the velocity field of the RANS subdomain. Also, the right term  $G_i$  rescales the trace of the LES stress tensor towards the RANS turbulent kinetic energy. The RANS subdomain sends information to the LES grid to enable the computation of the drift term. On the other hand, the subdomain receives partial time-averaged LES fields of velocity and pressure at the interface to complete the boundary conditions of the RANS. This work makes use of eddy viscosity models in the subdomain, and so the interface receives the trace of the LES stress tensor ( $k^{RANS} = 0.5 \langle \tau_{ij} \rangle^{EWA}$ ) and the LES dissipation rate ( $\epsilon^{LES} = 2\nu S_{ij} S_{ij} - \tau_{ij}^{SGS} S_{ij}$ ).

The performance of the new method is applied to the  $Re_\tau = 10,595$  flow through periodic hills as shown in Figure (7), which displays contour plots for both LES and RANS regions. Present results are then compared on Figure (8) with wall-resolved LES of Breuer et al. (2009)[25] which employed a mesh of 13M cells; noting that the present mesh as less than 0.6M cells, a factor of 20 less. For reference results for LES using the same coarse grid without the SWF are also included. The benefit of the wall function is clear in the near-wall velocity field of the LES towards the RANS, and overall SWF results are in excellent agreement with the reference data.

## 5 Turbulence with LBM

Nowadays, the lattice Boltzmann method (LBM) is a consolidated approach to simulate fluid flows. Its popularity at least in part stems from the intrinsic simplicity of the Bhatnagar-Gross-Krook (BGK) collision operator [27], where all the populations are forced to relax towards a discrete equilibrium state derived by applying a Gauss-Hermite quadrature to the continuous

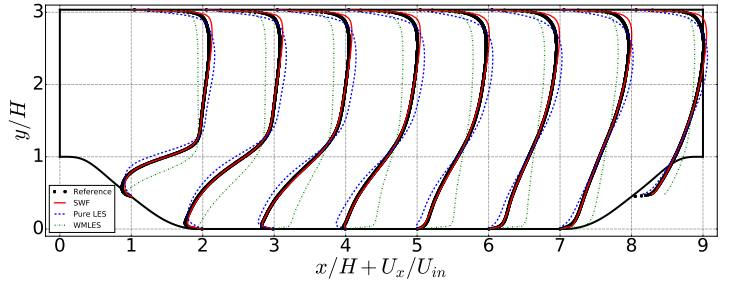


Figure 8: Profiles of the mean streamwise velocity in the LES domain. Red line: SWF; Green line: Pure LES; Blue line: WMLES; Black markers: reference data

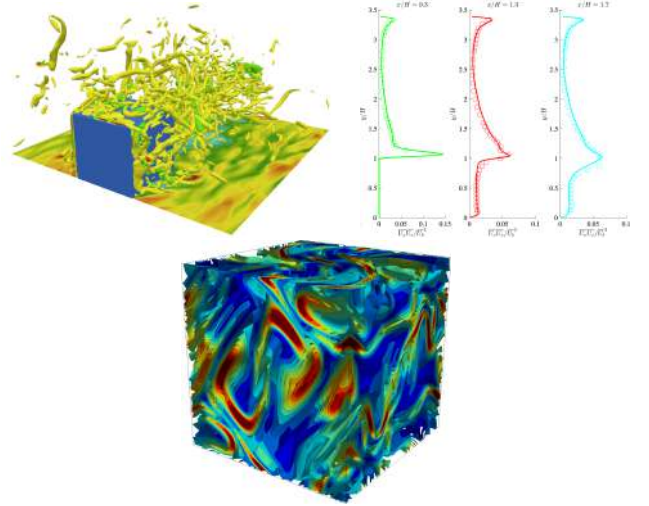


Figure 9: **Top)** LUMA validation for turbulent flow over cube array of [26], Q-criterion and profiles of streamwise normal Reynolds stress. **Bottom)** Simulation of a magneto-hydrodynamic vortex in three dimensions for  $Re = 570$

Maxwellian distribution. However, the BGK model is well known to be prone to numerical instability in the low-viscosity regime, thus becoming unsuitable for the prediction of turbulent flows. To cope with this problem, a family of collision models based on the relaxation of central moments (CMs) was introduced in 2006 [28]. Here, the collision process shows pyramidal hierarchical topology, where the post-collision state of CMs is constructed starting from the lowest order, and then proceeding in ascending sequence, hence the name *cascaded* lattice Boltzmann method. It has been demonstrated to outperform both BGK and multiple-relaxation-time [29] LBM in terms of stability (the latter based on absolute moments).

More recently, we approached central moments from a different viewpoint. Given a certain lattice, our methodology consists of building a transformation matrix allowing us to move from the space of populations to the one of central moments and vice-versa. The resultant algorithm loses the above-mentioned pyramidal cascaded structure and, as a consequence, it can be interpreted as a *non-cascaded* way to apply the collision step in CMs space [30, 31]. Interestingly, it is also shown that the present method recovers the behaviour of the cascaded LBM while allowing the derivation of forcing terms in an a systematic and straightforward manner. This was thoroughly demonstrated by successfully recovering different sets of governing equations with this approach, hence allowing the simulation of a rich variety of physics



problems such as magnetohydrodynamics [32] and multicomponent flows [33] among others. As an example, Figure (9) shows an instantaneous snapshot from a turbulent magnetohydrodynamics case.

The group has recently developed a lattice Boltzmann (LB) code primarily for the purpose of testing new approaches. LUMA (LBM at The University of Manchester) [34] offers grid refinement, turbulence and fluid-structure interaction, and a GPU version is now in development based on our earlier work [35]. Validation results for turbulent flow are displayed in Figure (9) for the periodic cube array case of [26]. Ongoing work is in progress to further develop our LBM capabilities in the context of hybrid RANS LES methods.

## 6 A Dual-Solver using LBM

A natural evolution of the dual mesh approach is to use different codes for each region. In this work, focused on developing fast prediction for turbulent flow around urban geometries, the solver in the region of interest is a lattice Boltzmann (LB) solver based on [34] running on GPUs. Since the LB region is a small volume of the domain the hybrid model overcomes the mesh and memory related drawbacks of using GPU accelerated LB, while maintaining its inherent speed and accuracy. The solver for the remainder of the domain is a finite volume RANS solver running on CPU, which takes advantage of the mesh flexibility and lower memory consumption of the NS algorithm. Moreover, the RANS-LBLES model exploits the availability of heterogeneous CPU/GPU hardware on consumer devices.

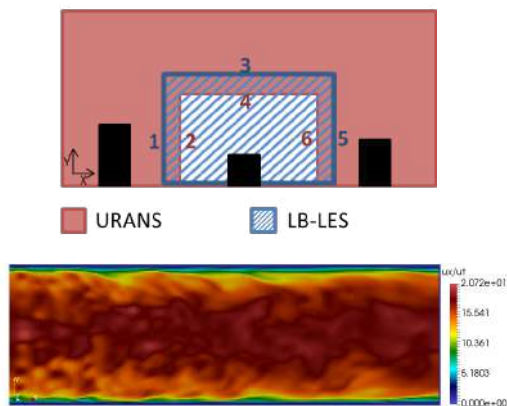


Figure 10: **Top)** Dual solver concept **Bottom)** Streamwise instantaneous velocity on vertical section of a channel flow using SEM with LBM

The method uses two fully-coupled sub-domains as shown in Figure (10), wherein the LBLES and the RANS regions exchange required information at overlapping interfaces, marked with numbers in Figure (10). Odd numbers denote the LBLES boundaries that receive data from the RANS solver, while the even numbers denote RANS boundaries that receive data from the LBLES solver. The volume between them is the overlap region, which is part of both sub-domains. The external boundaries (boundaries 1, 3 and 5) incorporate the Synthetic Eddy Method (SEM) to generate the instantaneous velocity as needed by the LES. The two subdomains are coupled using the parallel explicit algorithm in the preCICE libraries [36]. In this framework it is noted that eventually unsteady mean flow i.e. URANS could be coupled with LES in the same way.

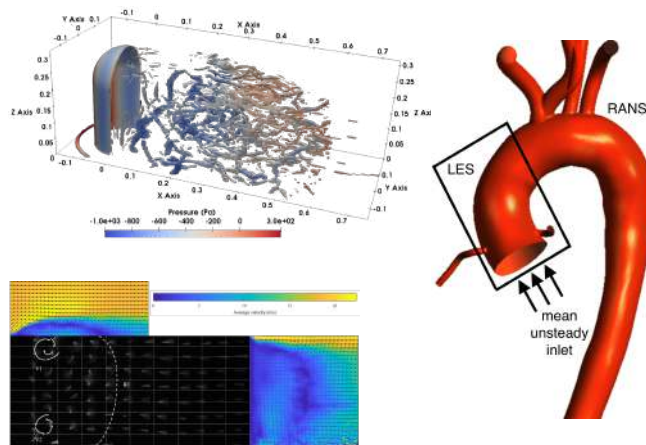


Figure 11: Ongoing work: **Top)** Isosurface of Q-criterion for flow around GSM, **Bottom)** Experimental validation case for truck aerodynamics, Embedded simulation for cardiovascular flow

The SEM inlet boundary has been implemented within a lattice Boltzmann solver for the first time, and tested for a channel flow at  $Re_\tau = 180$ , where the domain is discretised using a uniform Cartesian grid with  $y^+ = 4$ . Figure (10) displays the streamwise components of the instantaneous velocity  $u_x/u_\tau$ .

## 7 Conclusions and Ongoing work

This communication has provided a brief overview of recent and ongoing activities in our group at The University of Manchester in the context of Hybrid RANS LES methods; the interested reader is invited to contact us where more details are desired. These activities underpin our primary objective to develop a set of computational tools which enable fast and efficient coupling between different levels of modelling fidelity. The resulting series of coupled Hybrid RANS LES methods are applicable across a range of applications. Furthermore, we have demonstrated the potential for combining lattice Boltzmann method in this framework, particularly given its inherent scalability on GPU processors.

Work in our group is also in progress on the more applied side, in particular testing their potential for application to complex configurations which cover a range of lengthscales. Examples include the assessment of wind turbines on environmental landscapes [37], assessment of individual buildings in context of city-scale flows, application to ground vehicles aerodynamics [38, 39] and cardiovascular flow in and around the heart [40, 41]. One ongoing study is motivated by noise levels in road vehicles, wherein we will apply the dual solver approach in section 6 to a generic side mirror (GSM) model [42], consisting of a quarter sphere mounted on a half cylinder. Thus far, work has focused on using Delayed Detached Eddy Simulation (DDES) but will soon incorporate LBM also; initial results are displayed in Figure (11). Other ongoing work will apply these methods to truck 0 in tandem, with an experimental campaign. Finally, we are also starting to apply coupled HRLM to cardiovascular flows as proposed in Figure (11).

## Acknowledgment

We acknowledge support from the UK Turbulence Consortium (EPSRC Grant EP/G069581/1) and The UK

Consortium on Mesoscale Engineering Sciences (Grant No. EP/L00030X/1), both of which provided computational access to ARCHER, UK. The authors also acknowledge assistance from IT Services and the use of the Computational Shared Facility at The University of Manchester.

## References

- [1] M. Strelets, "Detached eddy simulation of massively separated flows," in *39th AIAA Aero. sciences meet*, p. 879, 2001.
- [2] W. Haase, M. Braza, and A. Revell, *DESider-A European Effort on Hybrid RANS-LES Modelling: Results of the European-Union Funded Project, 2004-2007*, vol. 103. Springer Science & Business Media, 2009.
- [3] S. Deck, "Zonal-detached-eddy simulation of the flow around a high-lift configuration," *AIAA journal*, vol. 43, no. 11, pp. 2372–2384, 2005.
- [4] N. Jarrin, S. Benhamadouche, D. Laurence, and R. Prosser, "A synthetic-eddy-method for generating inflow conditions for large-eddy simulations," *International Journal of Heat and Fluid Flow*, vol. 27, no. 4, pp. 585–593, 2006.
- [5] D. Cokljat, D. Caridi, S. Sheffield, G. Link, F. Menter, and A. G. Gmbh, "Embedded LES Methodology for General-Purpose CFD Solvers," *6th International Symposium on Turbulence and Shear Flow Phenomena*, pp. 1191 – 1196, 2009.
- [6] Z. Li, H. Chen, and Y. Zhang, "Validation of a Window-Embedded RANS/LES Method Based on Synthetic Turbulence," *54th AIAA Aero. Sciences Meet.*, pp. 1–8, jan 2016.
- [7] K. Anupindi and R. Sandberg, "Implementation and Evaluation of an Embedded LES-RANS Solver," *Flow, Turbulence and Combustion*, 2016.
- [8] M. Vonlanthen, J. Allegrini, and J. Carmeliet, "Assessment of a one-way nesting procedure for obstacle resolved large eddy simulation of the ABL," *Computers & Fluids*, vol. 140, pp. 136–147, nov 2016.
- [9] J. Holgate, A. Skillen, T. Craft, and A. Revell, "A review of embedded large eddy simulation for internal flows," *Archives of Comp. Methods in Engineering*, vol. 5, pp. 1–18, 2018.
- [10] R. Poletto, T. Craft, and A. Revell, "A New Divergence Free Synthetic Eddy Method for the Reproduction of Inlet Flow Conditions for LES," *Flow, Turbulence and Combustion*, vol. 91, pp. 519–539, jul 2013.
- [11] A. Skillen, A. Revell, and T. Craft, "Accuracy and efficiency improvements in synthetic eddy methods.," *Int. J. of Heat and Fluid Flow*, vol. 62, pp. 386–394, 2016.
- [12] J. Uribe, A. Revell, and C. Moulinec, "Computation of flow in a 3d diffuser using a two-velocity field hybrid rans/les," in *Turbulence and Interactions*, pp. 385–391, Springer, 2010.
- [13] H. Xiao and P. Jenny, "A consistent dual-mesh framework for hybrid LES/RANS modeling," *Journal of Computational Physics*, vol. 231, pp. 1848–1865, feb 2012.
- [14] R. Manceau and K. Hanjalić, "Elliptic blending model: A new near-wall reynolds-stress turbulence closure," *Physics of Fluids*, vol. 14, no. 2, pp. 744–754, 2002.
- [15] F. Billard, A. Revell, and T. Craft, "Application of recently developed elliptic blending based models to separated flows," *International Journal of Heat and Fluid Flow*, vol. 35, pp. 141–151, 2012.
- [16] A. J. Revell, T. J. Craft, and D. R. Laurence, "Turbulence modelling of unsteady turbulent flows using the stress strain lag model," *Flow, Turbulence and Combustion*, vol. 86, no. 1, pp. 129–151, 2011.
- [17] S. Lardeau and F. Billard, "Development of an elliptic-blending lag model for industrial applications," in *54th AIAA Aerospace Sciences Meeting*, p. 1600, 2016.
- [18] M. L. Shur, P. R. Spalart, M. K. Strelets, and A. K. Travin, "A hybrid rans-les approach with delayed-des and wall-modelled les capabilities," *International Journal of Heat and Fluid Flow*, vol. 29, no. 6, pp. 1638–1649, 2008.
- [19] D. DeGraaf and J. Eaton, "Reynolds number scaling of the flat-plate turbulent boundary layer," *Journal of Fluid Mechanics*, vol. 422, pp. 319–346, 2000.
- [20] J. Liu, U. Piomelli, and P. R. Spalart, "Interaction between a spatially growing turbulent boundary layer and embedded streamwise vortices," *Journal of Fluid Mechanics*, vol. 326, pp. 151–179, 1996.
- [21] R. Tunstall, *CFD and turbulence modelling for Nuclear Plant Thermal hydraulics systems*. PhD thesis, University of Manchester, 2016.
- [22] F. Sebilliau, R. Issaa, S. Lardeau, and S. Walker, "Direct Numerical Simulation of an air-filled differentially heated square cavity with Rayleigh numbers up to 1011," *Int. J. of Heat and Mass Transfer*, pp. 297–319, 2018.
- [23] Y. Addad, I. Zaidi, and D. Laurence, "Quasi-DNS of natural convection flow in a cylindrical annuli with an optimal polyhedral mesh refinement," *Computers and Fluids*, vol. 118, p. 444–452, 2015.
- [24] E. Balaras, C. Benocci, and U. Piomelli, "Two-layer approximate boundary conditions for large-eddy simulations," *AIAA Journal*, vol. 34, pp. 1111–1119, 1996.
- [25] M. Breuer, N. Peller, C. Rapp, and M. Manhart, "Flow over periodic hills - Numerical and experimental study in a wide range of Reynolds numbers," *Computers and Fluids*, vol. 38, no. 2, pp. 433–457, 2009.
- [26] E. Meinders and K. Hanjalić, "Vortex structure and heat transfer in turbulent flow over a wall-mounted matrix of cubes," *International Journal of Heat and fluid flow*, vol. 20, no. 3, pp. 255–267, 1999.
- [27] P. Bhatnagar, E. Gross, and M. Krook, "A model for collision processes in gases. I. small amplitude processes in charged and neutral one-component systems," *Phys. Rev.*, vol. 94, no. 3, p. 511, 1954.
- [28] M. Geier, A. Greiner, and J. Korvink, "Cascaded digital lattice Boltzmann automata for high Reynolds number flow," *Phys. Rev. E*, vol. 73, no. 6, p. 066705, 2006.
- [29] D. d'Humières, I. Ginzburg, M. Kravczyk, P. Lallemand, and L.-S. Luo, "Multiple-relaxation-time lattice Boltzmann models in three dimensions," *Phil. Trans. R. Soc. A*, vol. 360, pp. 437–451, 2002.
- [30] A. De Rosis, "Nonorthogonal central-moments-based lattice boltzmann scheme in three dimensions," *Phys. Rev. E*, vol. 95, no. 1, p. 013310, 2017.
- [31] A. De Rosis and K. H. Luo, "Role of higher-order hermite polynomials in the central-moments-based lattice boltzmann framework," *Phys. Rev. E*, vol. 99, no. 1, p. 013301, 2019.
- [32] A. De Rosis, E. Lévêque, and R. Chahine, "Advanced lattice boltzmann scheme for high-reynolds-number magneto-hydrodynamic flows," *J. Turbul.*, pp. 446–462, 2018.
- [33] S. Saito, A. De Rosis, A. Festuccia, A. Kaneko, Y. Abe, and K. Koyama, "Color-gradient lattice boltzmann model with nonorthogonal central moments: Hydrodynamic melt-jet breakup simulations," *Phys. Rev. E*, vol. 98, 2018.
- [34] A. R. G. Harwood, J. O'Connor, J. S. M. noz, M. C. Santasmasas, and A. J. Revell, "LUMA: A many-core, Fluid-Structure Interaction solver based on the Lattice-Boltzmann Method," *SoftwareX*, vol. 7, pp. 88–94, 2018.
- [35] M. J. Mawson and A. J. Revell, "Memory transfer optimization for a lattice boltzmann solver on kepler architecture nvidia gpus," *Computer Physics Communications*, vol. 185, no. 10, pp. 2566–2574, 2014.
- [36] H. J. Bungartz, F. Lindner, B. Gatzhammer, M. Mehl, K. Scheufele, A. Shukaeve, and B. Uekermann, "pre-CICE A fully parallel library for multi-physics surface coupling.," *Computers and Fluids*, vol. 141, pp. 250–258, 2016.
- [37] S. Hewitt, L. Margetts, and A. Revell, "Building a digital wind farm," *Archives of Computational Methods in Engineering*, vol. 25, no. 4, pp. 879–899, 2018.
- [38] N. Ashton and A. Revell, "Key factors in the use of ddes for the flow around a simplified car," *International Journal of Heat and Fluid Flow*, vol. 54, pp. 236–249, 2015.
- [39] N. Ashton, A. West, S. Lardeau, and A. Revell, "Assessment of rans and des methods for realistic automotive models," *Computers & Fluids*, vol. 128, pp. 1–15, 2016.
- [40] M. G. Al-Azawy, A. Turan, and A. Revell, "Assessment of turbulence models for pulsatile flow inside a heart pump," *Computer methods in biomechanics and biomedical engineering*, vol. 19, no. 3, pp. 271–285, 2016.
- [41] B. Owen, C. Lowe, N. Ashton, P. Mandal, S. Rogers, W. Wein, C. McCollum, and A. Revell, "Computational hemodynamics of abdominal aortic aneurysms: three-dimensional ultrasound versus computed tomography," *Proceedings of the Institution of Mechanical Engineers, Part H: Journal of Engineering in Medicine*, vol. 230, no. 3, pp. 201–210, 2016.
- [42] R. Siegert, V. Schwarz, and J. Reichenberger, "Numerical Simulation of aeroacoustic sound generated by generic bodies placed on a plate: Part II - Prediction of Radiated Sound Pressure," *5th AIAA/CEAS Aeroacoustics Conference and Exhibit*, no. May, 1999.

# GREY-AREA MITIGATION IN SCALE-RESOLVING SIMULATIONS WITH HYBRID RANS-LES METHODS

S-H. Peng<sup>1,2</sup>

<sup>1</sup> Department of Aerospace Engineering, Swedish Defence Research Agency, FOI, Stockholm, Sweden

<sup>2</sup> Department of Mechanics and Maritime Sciences, Chalmers University of Technology, Göteborg, Sweden

## Abstract

For Grey-Area Mitigation (GAM) in hybrid RANS-LES computations, apart from turbulence reconstruction superimposed at the RANS-LES interface, alternative GAM methods have also been developed for enhanced LES-resolving capabilities by justifying turbulence energy transfer between resolved and modelled scales. Two GAM methods are briefly introduced here, including a method incorporating energy backscatter in SGS modelling, and a method adopting commutation term in the modelled turbulent transport equations of LES. Both methods have are able to enforce turbulent fluctuations resolved in the grey area. The capabilities of the methods in mitigating grey area are exemplified in hybrid RANS-LES computations of turbulent mixing layer.

## 1 Introduction

Pragmatically, hybrid RANS-LES modeling abandons full LES resolution of near-wall turbulent structures, which are instead modelled in the context of (unsteady) RANS approaches, usually as a whole in terms of *mean* turbulence scales. Away from the wall layer and in regions where the flow undergoes massive separation, e.g. in the wake region after a bluff body, the capability of LES in resolving coherent vortical structures is well deployed. A modelling approach as such has been increasingly invoked over the past two decades in CFD-based analysis of engineering flow problems.

Being facilitated by industrial needs, the development of hybrid RANS-LES modelling approaches has undergone continuous evolution, since the pioneering work of Spalart et al. [1] about Detached Eddy Simulation (DES). This concerns not only of improved variants of the original DES method but also of a variety of different types of hybridization of RANS and LES models [2, 3, 4]. It is recognized, nevertheless, that the most challenging issue in hybrid RANS-LES modelling has been the formulation of the interface between the LES and RANS modes incorporated. Indeed, the interface concerns a hybridization of flow variables stemmed from two different types of decomposition of flow properties, adopted respectively in RANS and LES modelling. Such a hybridization often leads to the so-called “grey-area” problem.

A “grey area” in hybrid RANS-LES computations refers typically to regions where the RANS mode is switching to, and interacting with, the LES mode. As mentioned, it happens due to the inherent modelling formalism by which the RANS-modelled turbulent flow properties, when being fed into the LES computation, are unable to support an appropriate LES resolution of large-scale turbulent fluctuations. Consequently, the LES region neighboring to the RANS-LES interface be-

comes a “grey area”, where the LES-resolved turbulent contents are usually not *saturated* as otherwise it should be in a full LES computation. The evolution of turbulent structure is often delayed over the grey area for a re-establishment of LES-resolved turbulent properties. As a consequence, the LES prediction may become erroneous in the grey area and further downstream.

Over the recent years, a set of collaborative initiatives have been dedicated to the development of advanced hybrid RANS-LES modelling approaches, of which some have placed a primary focus on the mitigation of the grey-area problem. Typical examples include the EU FP7 project Go4Hybrid (2015-2017) and the GARTEUR AG54 project (2015-2019). This short note provides a brief introduction of some related effort made by the author and co-workers in these projects to address the grey-area problem for improved hybrid RANS-LES modelling.

## 2 Grey-area mitigation (GAM)

In the context of hybridizing the RANS and LES modes, most of existing hybrid RANS-LES modelling approaches may usually be cast into two major categories, namely, the *zonal* and *non-zonal* methods. A zonal method is often referred to a hybrid modelling approach in which the RANS-LES interface is prescribed. Embedded LES is a typical example in this category. A non-zonal method, on the other hand, is of a seamless type in hybridization of the RANS and LES modes. As exemplified by the DES model and its variants, the RANS-LES interface in a non-zonal method is instead accomplished due to inherent modelling formulation by means of a justification of local grid resolution in relation to local turbulent flow properties.

With a zonal hybrid RANS-LES model, a GAM method, as adopted commonly in specifying turbulent inflow conditions in full LES, has been to superimpose turbulent fluctuations onto the RANS-computed mean flow at the prescribed interface. They are then taken as fed-in turbulent flow properties for the LES computation. The imposed turbulent fluctuations are usually generated from precursor LES or DNS of a fully developed turbulent flow relevant to the interface boundary (e.g., boundary layer, channel flow or duct flow), or using a synthetic-turbulence method, e.g., the synthetic eddy method by Jarrin et al. [5].

For a seamless non-zonal hybrid method, the RANS-LES interface is often justified by means of a modelled adaption of the near-wall RANS length scale to a LES length scale away from the wall. Instead of superimposing turbulent fluctuations at the RANS-to-LES interface, a variety of GAM methods proposed for non-zonal hybrid methods have been targeting to enforce LES-resolved turbulence by means of manipulating the turbulent energy transfer between resolved and modelled

scales via SGS modelling, see e.g. Refs [6, 7, 8, 9]. We introduce here two GAM methods using, respectively, energy backscatter or commutation term for enhancing LES-resolving capabilities in the grey area.

## 2.1 GAM with energy backscatter

SGS modelling in LES plays an essential role in representing the energy drain between the resolved large scales and the sub-filtered scales. While the energy drain in a statistic framework is directed from resolved large scales to under-resolved small scales, it is known that instantaneous reverse energy transfer may also occur from small to large scales, namely, the so-called “energy backscatter” phenomenon. A typical example of SGS models with energy backscatter is the scale-similarity model [10], which has usually been used in conjunction with an eddy viscosity based SGS model (e.g. the Smagorinsky model) in the form of a mixed model to enable sufficient energy dissipation.

With the scale-similarity model, double-filtering operation has to be invoked, which may become rather complicated and time-consuming in actual LES of flows with complex geometry for unstructured grid. It was shown that, by applying the Leonard expansion to the residual stress tensor in the spatial-filtered Navier-Stokes equations, the first two leading terms may actually be cast in a form similar to a mixed model [11], of which the scale-similarity part (the first term or the Leonard term) is approximated by velocity-gradient tensor. The computation of the Leonard term is much easier in engineering LES than for the similarity model that requires a second filtering operation.

The resulting two-term SGS model is similar to a mixed model and takes the form of [12]

$$\tau_{ij} = L_{ij} + R_{ij} = (C_L \Delta)^2 f_L \frac{\partial \bar{u}_i}{\partial x_k} \frac{\partial \bar{u}_j}{\partial x_k} - 2f_D \nu_{sgs} \bar{S}_{ij} \quad (1)$$

In Eq. (1)  $C_L = \sqrt{1/12}$  is a model constant,  $\Delta$  is the width of the filter and  $\nu_{sgs}$  is the SGS eddy viscosity. The first term,  $L_{ij}$ , is the Leonard term, which may induce instantaneous turbulent energy backscatter, and the second term,  $R_{ij}$ , is the conventional eddy viscosity based formulation. When the Smagorinsky model was employed, the details of the formulation of the two-term SGS model were given in Peng [12].

In LES for turbulent channel flows, the energy backscatter induced by the Leonard term was explored with the two-term SGS model in which the Smagorinsky model was employed in the second term of Eq. (1). By sampling the forward and backward energy transfer,  $\varepsilon_L^+ = \max(-L_{ij} \bar{S}_{ij}, 0.0)$  and  $\varepsilon_L^- = \min(-L_{ij} S_{ij}, 0.0)$ , respectively, in statistic analysis, it was shown that  $\varepsilon_L^-$  is about (15 – 20)% of the total energy transfer due to the Leonard term, taking place usually in the viscous sub-layer and in the buffer layer, as illustrated in Figure (1). Instantaneously, the reverse energy transfer may raise up to about the same amount of the forward energy transfer. Note that in Figure (1) the turbulent energy transfer rate,  $\varepsilon$ , has been normalized by  $(u_\tau^3/h)$  but not  $(u_\tau^4/\nu)$  ( $h$  is the half-channel width) for illustrative purpose. The primary component that has contributed to the energy backscatter in the Leonard stresses is  $L_{11}$ . The other components,  $L_{12}$  and  $L_{22}$ , are usually smaller than  $L_{11}$  in the wall layer.

The energy-backscatter function is desired for the LES mode in the grey area immediately neighbouring the RANS-LES interface in order to enhance the resolved

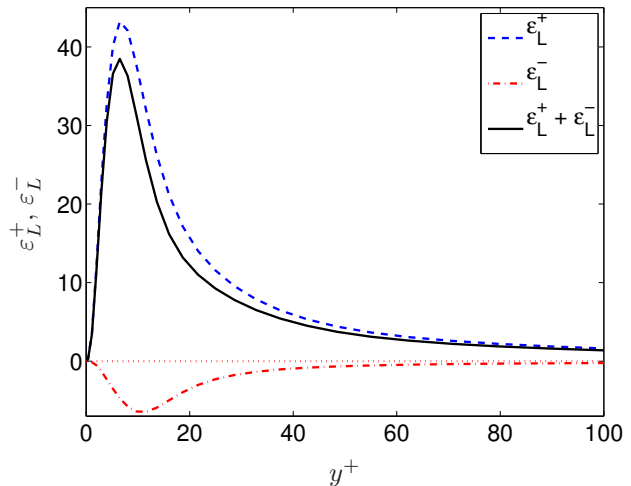


Figure 1: Turbulent energy dissipation and backscatter by the Leonard term estimated in LES for turbulent channel flow ( $Re_\tau = 550$ )

turbulence energy, whereas the modelled energy dissipation is often over-estimated. The two-term SGS model was verified in hybrid RANS-LES modelling [13] and being cast in the following form.

$$\tau_{ij} = f_d L_{ij} - 2\nu_h S_{ij}, \quad (2)$$

where the first term,  $L_{ij}$ , is the Leonard term in the LES mode, given in Eq. (1). Note that the overbar is now removed for the hybrid RANS-LES formulation, which indicates otherwise a filtered flow quantity in LES. The function,  $f_d$ , is designed in such a way that  $f_d = 0$  to deactivate the Leonard term in the near-wall RANS region and  $f_d = 1$  in off-wall LES region. In Eq. (2) the hybrid eddy viscosity,  $\nu_h$ , usually takes the RANS eddy viscosity,  $\nu_h = \nu_t$  for the RANS mode and  $\nu_h = \nu_{sgs}$  for LES. The Leonard term is thus exploited only by the LES mode in hybrid RANS-LES modelling for grey-area mitigation. The energy backscatter due to this term is expected to enforce the resolved large-scale turbulent fluctuations.

It is indicated here that the modelling of  $\tau_{ij}$ , given in Eq. (2), can be readily generalized for any hybrid RANS-LES models by relating it to the production term of turbulent generation. For the SA-based DES formulation, for example, the production term in the  $\tilde{\nu}$ -equation is re-written as

$$P_{\tilde{\nu}} = C_{b1} \tilde{\nu} \tilde{S} = -C_{b1} \left( \frac{\tau_{ij} S_{ij}}{S} - f_{\nu 2} \frac{\tilde{\nu}^2}{\kappa^2 d^2} \right) \quad (3)$$

In Eq. (3),  $\tau_{ij}$  is estimated by Eq. (2), and thus the SA RANS one-equation model is rendered in the near-wall layer, while the Leonard term is incurred in the off-wall LES mode.

It is noted that the energy transfer between the resolved and subgrid scales is determined by  $\varepsilon = -\tau_{ij} S_{ij}$ . While the Leonard term is able to induce instantaneous reverse turbulence energy transfer, it may also lead to numerical instabilities for too a large energy backscatter that may be dominant over the energy dissipation. To eliminate the numerical instability problem in the computation, the Leonard term is split into two parts, namely,

$$L_{ij} = L_{ij}^* + L_{ij}^d \quad (4)$$

The first part in Eq. (4),  $L_{ij}^*$ , is responsible for the overall energy transfer due to the Leonard term and is formulated with an effective viscosity,  $\nu^*$ , in the form of

$L_{ij}^* = -2\nu^* S_{ij}$ . The effective eddy viscosity,  $\nu^*$ , is computed by a contraction of Eq. (4) multiplying with  $S_{ij}$  on both sides, and let  $L_{ij}^d S_{ij} = 0$ . This gives

$$\nu^* = -\frac{L_{ij}^d S_{ij}}{2S_{ij} S_{ij}} \quad (5)$$

The second term in Eq. (4) is then estimated by  $L_{ij}^d = L_{ij} - L_{ij}^*$ . It is noted that energy backscatter takes place instantaneously when the effective viscosity,  $\nu^*$ , becomes negative. In this case, to avoid numerical problem, the negative value of  $\nu^*$  has to be limited by the sum of the molecular viscosity and the hybrid eddy viscosity, namely,  $\nu^* \geq -(\nu + \nu_h)$ .

## 2.2 GAM with commutation term

A commutation term may raise in hybrid RANS-LES modelling since the hybrid filter does not commute with the spatial derivative. This leads to an additional term when computing the spatial derivative of a filtered quantity  $f$ , namely,

$$\frac{\overline{\partial f}}{\partial x_i} = \frac{\partial \bar{f}}{\partial x_i} - \frac{\partial \Delta}{\partial x_i} \frac{\partial \bar{f}}{\partial \Delta} \quad (6)$$

The GAM method using the commutation term has been motivated by the fact that over the RANS-to-LES interface the commutation error may become rather large [14]. Arvidson et al. [15] explored the effect of the commutation term in hybrid RANS-LES modelling to serve grey-area mitigation.

The GAM function was verified in simulations using a  $k - \omega$ -based hybrid RANS-LES model [16]. The commutation term was introduced respectively in the  $k$ -,  $\omega$ - and momentum equations and only imposed at the RANS-LES interface.

Using Eq. (6), the commutation term in the modelled  $k$ -equation takes the form of

$$\frac{\overline{\partial u_i k}}{\partial x_i} = \frac{\partial \bar{u}_i k}{\partial x_i} - \underbrace{\frac{\partial \Delta}{\partial x_i} \frac{\partial \bar{u}_i k}{\partial \Delta}}_{S_k^c} \quad (7)$$

A corresponding term in the  $\omega$ -equation reads

$$\frac{\overline{\partial u_i \omega}}{\partial x_i} = \frac{\partial \bar{u}_i \omega}{\partial x_i} + \underbrace{\frac{\omega}{k} S_k^c}_{S_\omega^c} \quad (8)$$

By adding the commutation terms in the  $k$ - and  $\omega$ -equations at the RANS-LES interface, the aim is to alleviate the grey area in LES. The source term added to the  $k$ -equation acts as a destruction term to reduce the modelled turbulent kinetic energy for a flow directed across the interface from RANS to LES. Since the source term in the  $\omega$ -equation has the opposite sign to that of the source term in the  $k$ -equation, the commutation term increases the specific dissipation rate. Consequently, for a flow over the interface from RANS to LES, a reduction of the modelled SGS viscosity is attained with a possibility to mitigate the grey area.

The commutation term introduced in the  $k$ -equation entails a change in the modelled turbulent kinetic energy across the RANS-LES interface. This change should correspond to a change of the resolved turbulent kinetic energy. For example, when the modelled turbulent kinetic energy is reduced across a RANS-to-LES interface

due to  $S_k^c$ , the resolved turbulent kinetic energy should be increased by the same amount across the interface. This energy transfer is achieved by introducing a source term in the momentum equations, which should represent a commutation term in the transport equation for resolved turbulent kinetic energy.

It is noted that the transport equation for the resolved turbulent kinetic energy is obtained with the dynamic equations for fluctuating velocity components,  $u'_k$ . Here the derivation of the source term in the momentum equations has been based on the source term  $S_k^c$ , representing the commutation error for the convection term in the  $k$ -equation. The time-averaged source term in the dynamic equations for  $u'_j$ , multiplied further by  $u'_j$  should thus be rendered as well in the transport equation for resolved turbulent kinetic energy, i.e. in the form of  $\langle S_k^c \rangle$ .

The source term introduced in the momentum equations should take the same sign of the velocity fluctuations to enforce the resolved turbulence at the RANS-LES interface, and is thus cast in the following form [15].

$$S_{mom,i}^c = \text{sign}(u'_i) \left\langle S_k^c \frac{u'_i}{\langle u'_m u'_m \rangle} \right\rangle \quad (9)$$

The source terms introduced in the momentum equations, Eq. (9), are added only on the LES side of the interface, i.e. it is added only when the local flow direction is from RANS to LES across the RANS-LES interface.  $S_{mom,i}^c$  is ensured to have the same sign as the velocity fluctuation on the LES side of the interface to enforce the turbulent fluctuations. This consequently leads to increased resolved turbulent kinetic energy and, at the same time, the modelled turbulent kinetic energy (and the turbulent viscosity) are reduced accordingly by the source term introduced in the  $k$ - (and  $\omega$ -) equation on the LES side of the interface.

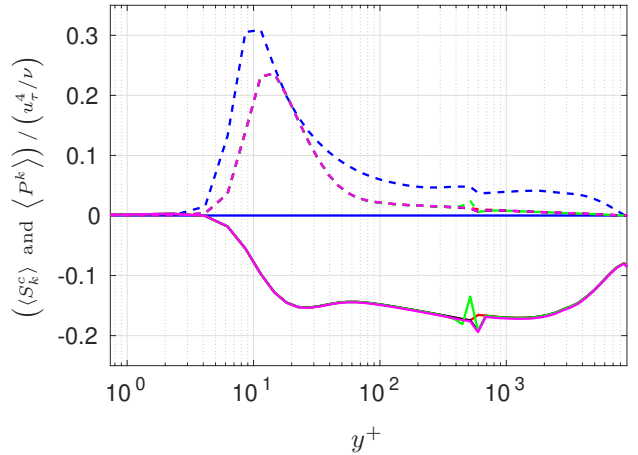


Figure 2: GAM with commutation term in hybrid RANS-LES computations of channel flow ( $Re_\tau = 8000$ ). Commutation (solid) and production (dashed) terms in the  $k$  equation. The purple lines indicate simulations with commutation terms applied only in the  $k$  and  $\omega$  equations at the wall-normal interface, and blue lines with no momentum equations [15]

The GAM function of the commutation term has been verified in hybrid RANS-LES computations of turbulent flows [15]. The source term at the interface is exemplified for a turbulent channel flow at  $Re_\tau = 8000$ , where the RANS mode in the upstream is coupled with downstream LES over a vertical interface, and further a wall-parallel RANS-LES interface is also prescribed with the RANS

mode patched in the wall layer up to  $y^+ = 550$ . Figure (2) illustrates a comparison of  $S_k^c$  with the production term,  $P^k$ , in the  $k$  equation at the wall-normal interface. The commutation term at the wall-normal interface is stronger than the commutation term added at the wall-parallel interfaces. Except at the peak of the production term in the  $k$  equation, the commutation term at the wall-normal interface is as large as 10 to 15 times of the production term, which leads to a strong reduction of the turbulent viscosity across the interface. Moreover, a much reduced magnitude of the production term in the  $k$  equation is observed when the commutation terms in the  $k$  and  $\omega$  equations are applied at the wall-normal interface than in the reference simulation with no commutation terms applied.

### 3 Verification of GAM methods

Both GAM methods introduced above have aimed to enforce the LES-resolved turbulent kinetic energy, although having been argued with different physic mechanisms to attain grey-area mitigation. Reduced energy dissipation from resolved large scales to modelled scales can also be achieved by reducing the modelled SGS eddy viscosity. This strategy has been used to mitigate the grey area in LES of mixing layer by re-adapting the LES length scale to, for example, a vorticity-based length scale,  $\Delta_\Omega$ , as proposed by Chauvet et al. [6].

$$\begin{aligned} \Delta_\Omega &= \sqrt{N_\xi^2 \Delta_\eta \Delta_\zeta + N_\eta^2 \Delta_\xi \Delta_\zeta + N_\zeta^2 \Delta_\xi \Delta_\eta} \\ \mathbf{N} &= \frac{\boldsymbol{\Omega}}{\|\boldsymbol{\Omega}\|}, \quad \boldsymbol{\Omega} = \nabla \times \mathbf{u} \end{aligned} \quad (10)$$

The LES length scale  $\Delta_\Omega$ , adapts to the local vorticity field in order to minimize the excess of modelled SGS turbulent viscosity. In Eq. (10),  $\Delta_\xi$ ,  $\Delta_\eta$ , and  $\Delta_\zeta$  are the sizes in the  $\xi$ ,  $\eta$  and  $\zeta$  directions, respectively, of the local control volume in a curvilinear grid with hexahedral cells.  $\mathbf{N}$  is the direction of the spin axis of the local vorticity. Obviously,  $\Delta_\Omega$  is actually a characteristic length scale of the cross section perpendicular to the orientation of the resolved turbulent vortex structure. On unstructured grids, the vorticity-based length scale,  $\Delta_\Omega$ , at an arbitrary node can be calculated by means of

$$\Delta_\Omega = \left( \frac{1}{2} \sum_{k=1}^m \mathbf{N} \cdot A_k \mathbf{n}_k \right)^{1/2} \quad (11)$$

where  $m$  is the number of surfaces of the control volume for the node,  $A_k$  is the area of surface  $k$  with a normal direction  $\mathbf{n}_k$ , and  $\mathbf{N}$  is the unit (normalized) vorticity vector at the node, as given in Eq. (10).

In previous work [16], several different LES length scales were comparatively investigated in zonal RANS-LES modelling, including  $\Delta_\Omega$ ,  $\Delta_{\max}$  and  $(\delta V)^{1/3}$ . For two-dimensional (2D) wall-bounded flows (namely, the flow over the third direction is homogeneous), it was shown that around the RANS-LES interface in the wall layer  $\Delta_\Omega$  is very similar to  $(\delta V)^{1/3}$  [16]. In the computation reported here, the length scale  $\Delta_\Omega$  has been used in the zonal hybrid RANS-LES modelling with the commutation term for GAM, while  $\Delta_{max}$  has been used in all other computations.

For the GAM method with energy backscatter, as given in Eq. (2), the results present here have been taken from computations based on the zero-equation algebraic hybrid RANS-LES model (HYB0) by Peng [17]. The

Leonard term is incorporated into the LES mode but shielded from the near-wall RANS layer. This is achieved by means of an empirical function,  $f_d$  (see Eq. (2)), which takes the form of  $f_d = \tanh[(R_l/2)^8]$  with  $R_l = \tilde{l}_\mu/\Delta$ , where  $\tilde{l}_\mu$  and  $\Delta$  are the RANS and LES length scale, respectively, defined in the HYB0 model [17]. With the energy backscatter incorporated, the resulting hybrid model is termed here the **HYB0M** model.

The GAM method with the commutation term has been verified using a two-equation zonal hybrid RANS-LES model as the base model [16]. The details for verifying the GAM function can be found in Arvidson et al [15]. We present here the results computed using the zonal model with and without the commutation term for GAM.

As mentioned, a grey area arises in regions where RANS-modelled flow is fed into the LES-resolved flow field over a RANS-LES interface. An example is the turbulent mixing layer, stemming from the confluence of two RANS-modelled boundary layers at the trailing edge of a (very) thin flat plate. The initial stage of such a mixing layer is a typical grey area, of which the resolved initial shear-layer instabilities are often delayed. The primary purpose has been to present a verification of the GAM methods in reproducing the initial shear-layer instabilities in comparison with the computation without a GAM function incorporated.

The mixing layer measured by Delville [18] has been used in the verification. The bulk velocity of the two boundary layers is, respectively,  $U_h = 41.54$  m/s and  $U_l = 22.4$  m/s. In the computation, the flow in the spanwise direction is assumed of homogeneity with an extension of  $150\theta_h$  ( $\theta_h$  is the momentum thickness of the boundary layer with  $U_h = 41.54$  m/s). Periodic boundary conditions are imposed on the spanwise boundaries. The origin,  $x = 0$ , of the coordinate system is set at the trailing edge of the flat plate. To match the velocity profile at the trailing edge of the plate, the inflow locations have been specified, respectively, at  $x_h = -0.82$  m for the upper boundary layer and  $x_l = -0.46$  m for the lower boundary layer, as shown in Figure Figure (3). The flow domain has a downstream extension of  $x = 2$  m from the plate trailing edge and a relatively large vertical extension of  $L_y = \pm 1.0$  m. Euler wall boundary conditions are used at the top and bottom boundaries. The region of  $x \in [0, 1]$  m is focused in the analysis of computed results. The details of the computational settings can be found in [9].

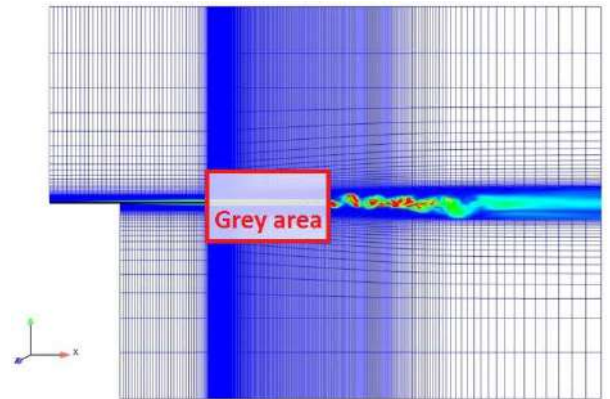


Figure 3: Schematic of the grey area of a mixing layer in hybrid RANS-LES modelling

The improvement of turbulence-resolving capabilities, and thus the effectiveness of the GAM method, for the

hybrid RANS-LES modelling is indicated by a rich presence of resolved turbulent structures and, quantitatively, being reflected in the resolved mixing-layer thickness and turbulent quantities.

In Figure (4), the resolved turbulent structure is illustrated with the iso-surface of the second invariant,  $Q_{cr}$ , of velocity gradient tensor. The results have been taken from the computations based on the HYB0 model with and without energy backscatter incorporated for GAM. It is clearly shown that the energy backscatter (HYB0M computation) has sensibly enriched the resolved structures in the initial stage of the mixing layer, as compared to the HYB0 computation with no energy backscatter incorporated. It is noted here that, although not shown, the zonal modelling with the commutation term for GAM has rendered similar improvement of enabling rich turbulent structures resolved in the grey area.

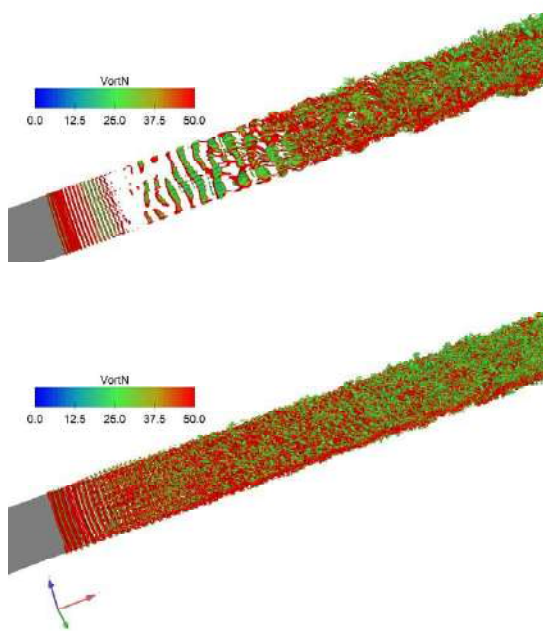


Figure 4: Resolved turbulent structure, iso-surface of  $Q_{cr}$ . Upper: HYB0 computation (no energy backscatter); Lower: HYB0M computation (with energy backscatter)

The mixing layer growth, in terms of respectively the momentum ( $\delta_m$ ) and vorticity ( $\delta_\omega$ ) thickness, is presented in Figure (5) for the computation based on the HYB0 model with and without energy backscatter, and in Figure (6) for the zonal model with and without commutation term invoked for GAM. Corresponding to the resolved turbulence structures in the grey area, the GAM capability is well reflected in the HYB0M computation for both  $\delta_m$  and  $\delta_\omega$ , comparing to the HYB0 computation, as shown in Figure (5).

For the zonal hybrid RANS-LES modelling, as shown in Figure (6), the GAM effect of the commutation term in combination with  $\Delta_{max}$  is stronger than with  $\Delta_\Omega$ . Nonetheless, when  $\Delta_{max}$  is used with no commutation terms added at the RANS-LES interface, a poor mixing layer growth is predicted. Not shown here though, it is noted that the growth prediction is improved when adding the commutation terms in the  $k$  and  $\omega$  equations. The best agreement with experimental data is given when commutation terms are also added in the momentum equations in combination with  $\Delta_{max}$ .

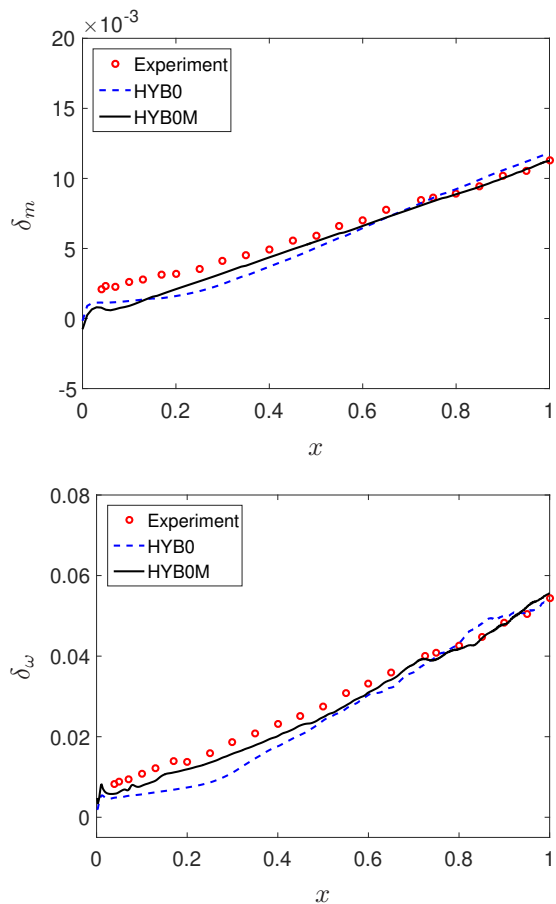


Figure 5: Mixing layer growth computed with energy backscatter incorporated for GAM in the HYB0 model. Upper: Momentum thickness; Lower: Vorticity thickness

## 4 Summary and conclusions

Two methods for grey-area mitigation in hybrid RANS-LES modelling are briefly introduced. Both methods have aimed at enforcing LES-resolved turbulent fluctuations by improving SGS modelling in relation to turbulent energy transfer between resolved and modelled scales. The GAM method with energy backscatter is similar to a scale-similarity SGS model in conjunction with a SGS eddy viscosity model. An instantaneous reverse energy transfer from modelled to resolved scales is expected to support enforcing resolved turbulent fluctuations in the grey area. The GAM method with commutation terms taken as source terms renders a reduced modelled eddy viscosity (and leading consequently to a reduced energy dissipation) via the turbulent transport equations of LES and, furthermore, an enhancing resolving velocity fluctuations through the momentum equations. As demonstrated in the computation of a turbulent mixing layer both methods have shown promising capabilities in mitigating the grey area for improved hybrid RANS-LES computations in comparison with available experimental data.

## Acknowledgments

The GAM method with commutation term was also reported in the PhD thesis work by S. Arvidson at Chalmers. The author is grateful for the collaboration with Dr S. Arvidson (Saab Aeronautics) and Prof L. Davidson (Chalmers).

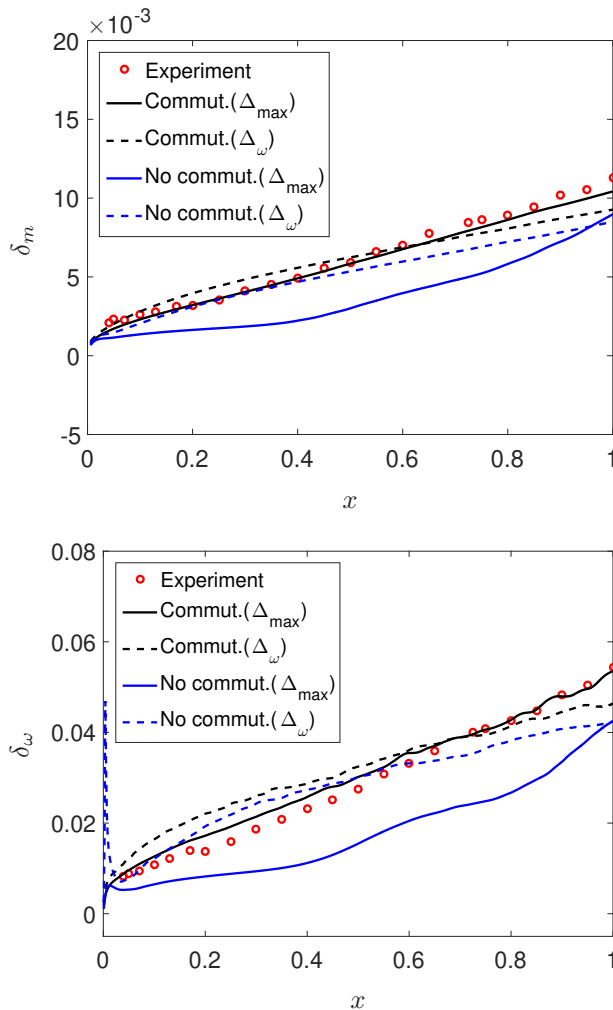


Figure 6: Mixing layer growth computed with commutation term incorporated for GAM using the zonal  $k - \omega$ -based hybrid RANS-LES model [15]. Upper: Momentum thickness; Lower: Vorticity thickness

## References

- [1] P. R. Spalart, W.-H. Jou, M. Strelets, and S. R. Allmaras, “Comments on the feasibility of les for wings and on a hybrid 0RANS/LES approach,” in *Advances in DNS/LES: Proceedings of the First AFOSR International Conference on DNS/LES* (C. Liu and Z. Liu, eds.), Greyden Press, Columbus, 1997.
- [2] P. R. Spalart, S. Deck, M. L. Shur, K. D. Squires, M. Strelets, and A. Travin, “A new version of DES, resistant to ambiguous grid densities,” *Theoretical and Computational Fluid Dynamics*, vol. 20, pp. 181–195, 2006.
- [3] M. L. Shur, P. R. Spalart, M. K. Strelets, and A. Travin, “A hybrid RANS-LES approach with delayed-des and wall-modelled LES capabilities,” *International Journal of Heat and Fluid Flow*, vol. 29, pp. 1638–1649, 2008.
- [4] P. R. Spalart, “Detached-eddy simulation,” *Annual Review of Fluid Mechanics*, vol. 41, pp. 181–202, 2009.
- [5] N. Jarrin, R. Prosser, J.-C. Uribe, S. Benhamadouche, and D. Laurence, “Reconstruction of turbulent fluctuations for hybrid RANS/LES simulations using a synthetic-eddy method,” *Int. J. Heat and Fluid Flow*, vol. 30, pp. 435–442, 2009.
- [6] N. Chauvet, S. Deck, and L. Jacquin, “Zonal-detached-eddy simulation of a controlled propulsive jet,” *AIAA J.*, vol. 45, pp. 2458–2473, 2007.
- [7] S. Deck, “Recent improvement in the zonal detached eddy simulation (ZDES) formulation,” *Theor. Comput. Fluid Dyn.*, vol. 26, pp. 523–550, 2012.
- [8] J. Kok, “A stochastic backscatter model for grey-area mitigation in detached eddy simulations,” *Flow, Turbulence and Combustion*, vol. 99, pp. 119–150, 2017.
- [9] S.-H. Peng, “Adaptation of LES subgrid scale to grey-area mitigation in hybrid RANS-LES modelling,” AIAA Paper 2017-4283, Denver, CO, 2017.
- [10] J. Bardina, J. Ferziger, and W. Reynolds, “Improved subgrid scale models for large eddy simulation,” AIAA Paper 80-1357, Snomass, Colorado, 1980.
- [11] S.-H. Peng and L. Davidson, “Some remarks on approximation for subgrid scale modeling in large eddy simulation,” Scientific Report, FOI-R-0381-SE, FFA, Swedish Defence Research Agency, FOI, Stockholm, 2001.
- [12] S.-H. Peng and L. Davidson, “Approximation of subgrid-scale stresses based on the Leonard expansion,” in *Proceedings of the 6th International Symposium on Turbulent Heat and Mass Transfer* (K. Hanjalic, Y. Nagano, and S. Jakirlic, eds.), Begell House, Inc., Roma, Italy, 2009.
- [13] S.-H. Peng, “Hybrid RANS-LES modelling with an energy-backscatter function incorporated in the LES mode,” in *Proceedings of the 7th International Symposium on Turbulent Heat and Mass Transfer* (K. Hanjalic, Y. Nagano, D. Borello, and S. Jakirlic, eds.), Begell House, Inc., Parlemo, Italy, 2012.
- [14] F. Hamba, “Analysis of filtered Navier-Stokes equation for hybrid RANS/LES simulation,” vol. 23, 2011.
- [15] S. Arvidson, L. Davidson, and S.-H. Peng, “Interface methods for grey-area mitigation in turbulence-resolving hybrid RANS-LES,” *International Journal of Heat and Fluid Flow*, vol. 73, pp. 236–257, 2018.
- [16] S. Arvidson, L. Davidson, and S.-H. Peng, “Hybrid Reynolds-averaged Navier-Stokes/large-eddy simulation modeling based on a low-Reynolds-number  $k - \omega$  model,” *AIAA Journal*, vol. 54, pp. 4032–4037, 2016.
- [17] S.-H. Peng, “Hybrid RANS-LES modelling based on zero- and one-equation models for turbulent flow simulation,” in *Proceedings of 4th Int. Symp. Turb. and Shear Flow Phenomena* (J. Humphrey, T. Gatski, J.K.Eaton, R. Friedrich, N. Kasagi, and M. Leschziner, eds.), vol. 3, pp. 1159–1164, 2005.
- [18] J. Delville, L. Ukeiley, L. Cordier, J. P. Bonnet, and M. Glauser, “Examination of large-scale structures in a turbulent plane mixing layer. part 1. proper orthogonal decomposition,” *J. Fluid Mech.*, vol. 391, pp. 91–112, 1999.



---

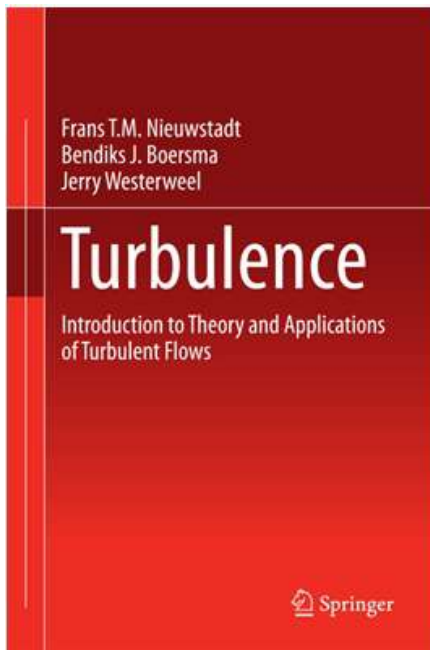
## *Recommended literature*

---

### TURBULENCE

#### Introduction to Theory and Applications of Turbulent Flows

Frans T.M. Nieuwstadt, Bendiks J. Boersma, Jerry Westerweel



- **Winner of the 2017 Most Promising New Textbook Award from the Textbook & Academic Authors Association**
- Proven to be an excellent course-text over many years
- Combines theory with practical applications
- Avoids lengthy mathematical descriptions

This book provides a general introduction to the topic of turbulent flows. Apart from classical topics in turbulence, attention is also paid to modern topics. After studying this work, the reader will have the basic knowledge to follow current topics on turbulence in scientific literature. The theory is illustrated with a number of examples of applications, such as closure models, numerical simulations and turbulent diffusion, and experimental findings. The work also contains a number of illustrative exercises

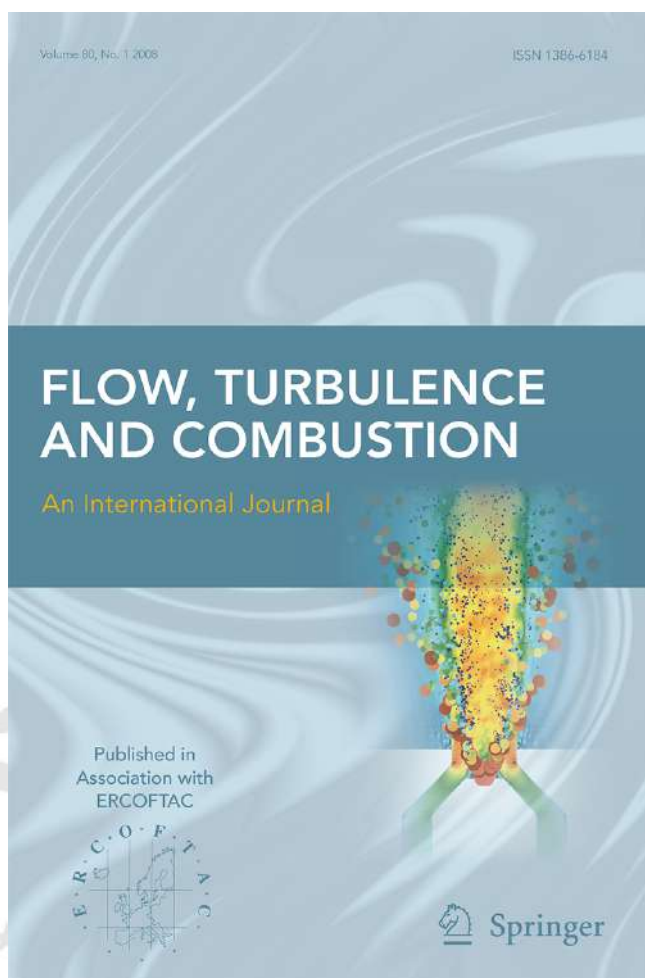
## *ERCOFTAC Workshops and Summer Schools*

### ERCOFTAC Workshops, Conferences – 2019/20

Title	Location	Date	Coordinators	Organiser
Workshop on Frontiers of Uncertainty Quantification in Fluid Dynamics	Pisa, Italy	11-13/09/2019	Lucot D.	SIG 45
Fundamental Understanding and Modelling of High Pressure Turbulent Premixed Combustion	Munich, Germany	19-20/09/2019	Klein, M., Pfitzner, M., Creta, F., Chakraborty, N. Roekaerts, D.	
Modelling of wall-bounded turbulent natural convection: A re-assessment using state-of-the-art massively parallel DNS	Ljubljana, Slovenia	15-16/10/2019	Jakirlic, S.	SIG 15
3rd Workshop on Modelling of Biological Cells, Fluid Flow and Microfluidics 2020	Vratna, Slovakia	09-13/02/2020	Kovalcikova K.	SIG 37
Multiscale and directional approach to single-phase and two-phase flows	France	4-7/05/2020	Cambon, C., Gorokhovski M., Casciola C. M.	SIGs 35, 39, 50, Henry Bénard PC
Reconstruction methods for complex flows and porous media	Sheffield, UK	22-23/06/2020	Yi Li	SIG 42, 14
3rd Workshop and Challenge on Data Assimilation & CFD Processing for PIV and Lagrangian Particle Tracking	Lisbon, Portugal	11-12/07/2020	Sciacchitano A.	SIG 32

### ERCOFTAC Summer Schools, Courses - 2020

Title	Location	Date	Coordinators	Organiser
Course on Particle Image Velocimetry	Delft, Netherlands	8-12/06/2020	Sciacchitano A.	SIG 32
Fluids under Control	Prague, Czech Republic	24-28/08/2020	Bodnar T.	PC Czech Republic



<http://link.springer.com/journal/10494>

**2018 Impact Factor: 2.371**

**Editor-in-Chief**

Michael Leschziner,  
Imperial College London, UK,  
E-mail: [mike.leschziner@imperial.ac.uk](mailto:mike.leschziner@imperial.ac.uk)

**Editors** - all international authorities in specific subject areas central to FTaC

**Andreas Dreizler**, Technical University of Darmstadt, Germany

**Koji Fukagata**, Keio University, Japan

**Ephraim Gutmark**, University of Cincinnati, USA

**Andreas Kempf**, University of Duisburg-Essen, Germany

**Suresh Menon**, Georgia Institute of Technology, USA

**Wolfgang Rodi**, Karlsruhe Institute of Technology, Germany

**Thierry Schuller**, Institut de Mécanique des Fluides de Toulouse, France

**Berend van Wachem**, University of Magdeburg, Germany

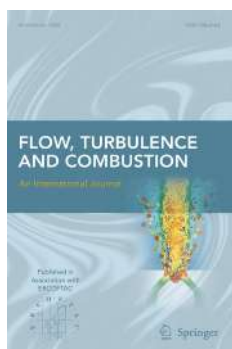
**Richard Sandberg**, University of Melbourne, VIC, Australia

As stated on its cover, **Flow, Turbulence and Combustion (FTaC)** is published in association with ERCOFTAC. The expectation is, therefore, that FTaC would be a primary medium for disseminating the most innovative and highest-quality scientific output of ERCOFTAC-supported technical events.

In addition to contributed articles constituting the large majority of FTaCs published output FTaC publishes *special issues* arising from major ERCOFTAC conferences, notably **ETMM** and (in 2017) **DLES**. However, there are many other opportunities that are, arguably, not sufficiently exploited in particular, in respect of original contributions to theme issues of the Bulletin and papers arising from SIG events, such as workshops and summer schools.

Both the Editor-in-Chief of FTaC and the Scientific Programme Committee of ERCOFTAC wish to see more contributions channelled from ERCOFTAC sources to FTaC. Such contributions in the form of high-quality technical papers within the scope of FTaC are most welcome. They will be subjected to the same rigorous review process as any other contributed manuscript.

FTaC provides a forum with global reach for the publication of original and innovative research results that contribute to the solution of fundamental and applied problems encountered in single-phase, multi-phase and reacting flows, both in idealized and real systems. This includes topics in fluid dynamics, scalar transport, multi-physics interactions and flow/turbulence control. Contributions may report research that falls within the broad spectrum of analytical, computational and experimental methods, including research pursued in academia, industry and the variety of environmental and geophysical sectors. The emphasis is on originality, timeliness, quality and thematic fit, as identified by the title of the journal and the above qualifications. Relevance to real-world problems and industrial applications will be regarded as strengths. Contributions may be full-length research and review manuscripts or short communications (of no more than 6 printed pages). The latter may report new results, address contentious topics or contain discussions of full-length papers previously published in the journal. Short communications will benefit from rapid publication. All contributed manuscripts, as well as any invited contributions to special or theme issues, will undergo rigorous peer review by three expert reviewers prior to decisions on acceptance or rejection.



RECENT TABLE OF CONTENTS OF FLOW TURBULENCE AND COMBUSTION

AN INTERNATIONAL JOURNAL PUBLISHED BY SPRINGER

IN ASSOCIATION WITH ERCOFTAC

EDITOR-IN-CHIEF: M. A. LESCHZINER

EDITORS: A. DREIZLER, K. FUKAGATA, E. GUTMARK, A. KEMPF, S. MENON, W. RODI, T.

SCHULLER, B. VAN WACHEM, R. SANDBERG

FOUNDING EDITOR: F. NIEUWSTADT

**VOLUME 103, NUMBER 1, JUNE 2019**

**Turbulence in a Localized Puff in a Pipe**

*A. Yakhot, Y. Feldman, D. Moxey, S. Sherwin, G.E. Karniadakis*

**Synthetic Freestream Disturbance for the Numerical Reproduction of Experimental**

**Zero-Pressure-Gradient Bypass Transition Test Cases** *B. Pinto, G. Lodato*

**Large Eddy Simulation Requirements for the Flow over Periodic Hills**

*X. Gloerfelt, P. Cinnella*

**Zonal Eddy Viscosity Models Based on Machine Learning**

*R. Matai, P.A. Durbin*

**Flow Characteristics of Curved Rotor Stator Systems Using Large Eddy Simulation**

*M.D. Damavandi, A. Nejat*

**Numerical Investigation and Experimental Comparison of the Gas Dynamics in a Highly Underexpanded Confined Real Gas Jet**

*C.-N. Xiao, B. Fond, F. Beyrau, C. T'Joen, R. Henkes, P. Veenstra, B. van Wachem*

**A Correlation for the Discontinuity of the Temperature Variance Dissipation Rate at the Fluid-Solid Interface in Turbulent Channel Flows**

*C. Flageul, I. Tiselj, S. Benhamadouche, M. Ferrand*

**Large Eddy Simulations of a Set of Experiments with Water Spray-Hot Air Jet Plume Interactions**

*S. Ebrahimzadeh, G. Maragkos, T. Beji, B. Merci*

**Effects of Integral Scale on Darrieus-Landau Instability in Turbulent Premixed Flames**

*W. Zhang, J. Wang, S. Guo, Q. Yu, W. Jin, M. Zhang, Z. Huang*

**Experimental Investigation of the Flame Front Propagation Characteristic During Light-round Ignition in an Annular Combustor**

*Y. Xia, C. Linghu, Y. Zheng, C. Ye, C. Ma, H. Ge, G. Wang*

**Measuring Rotating Detonation Combustion Using Cross-Correlation**

*M.D. Bohon, R. Bluemner, C.O. Paschereit, E.J. Gutmark*

**VOLUME 103, NUMBER 2, AUGUST 2019**

**Fractal Reconstruction of Sub-Grid Scales for Large Eddy Simulation**

*E.O. Akinlabi, M. Wactawczyk, S.P. Malinowski, J.P. Mellado*

**Effect of Nozzle Spacing on Turbulent Interaction of Low-Aspect-Ratio Twin Rectangular Jets** *R. Naseri Oskouie, M.F. Tachie, B.-C. Wang*

**Influence of the Prandtl Number on Wall-to-Fluid Thermal Transfer Rate in a Cubic Cavity**

*B.A. de Freitas Duarte, R. Serfaty, A. da Silveira Neto*

**On the Measurement of Wall-Normal Velocity Derivative in a Turbulent Boundary Layer**

*Z.X. Qiao, S.J. Xu, Y. Zhou*

**Subgrid Reaction-Diffusion Closure for Large Eddy Simulations Using the Linear-Eddy Model**

*S. Arshad, E. Gonzalez-Juez, A. Dasgupta, S. Menon, M. Oevermann*

**An Efficient Method to Reproduce the Effects of Acoustic Forcing on Gas Turbine Fuel Injectors in Incompressible Simulations**

*N.C.W. Treleaven, J. Su, A. Garmory, G.J. Page*

**Evolution of Flame Curvature in Turbulent Premixed Bunsen Flames at Different Pressure Levels**

*A. Alqallaf, M. Klein, C. Dopazo, N. Chakraborty*

**Large Eddy Simulation of Pre-Chamber Ignition in an Internal Combustion Engine**

*Q. Malé, G. Staffelbach, O. Vermorel, A. Misdariis, F. Ravet, T. Poinso*

**Progress Variable Variance and Filtered Rate Modelling Using Convolutional Neural Networks and Flamelet Methods**

*Z.M. Nikolaou, C. Chrysostomou, L. Vervisch, S. Cant*

**Decomposition of Turbulent Fluxes from Filtered Data and Application to Turbulent Premixed Combustion Modelling**

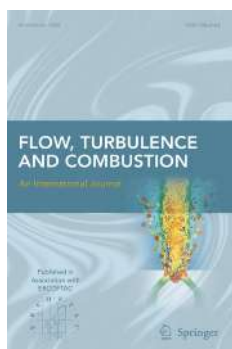
*M. Klein, C. Kasten, M. Germano*

**Modelling Sub-Grid Passive Scalar Statistics in Moderately Dense Evaporating Sprays**

*B. Wang, A. Kronenburg, O.T. Stein*

**LES Study of a Turbulent Spray Jet: Mesh Sensitivity, Mesh-Parcels Interaction and Injection Methodology**

*D. Alessandro, I. Stankovic, B. Merci*



RECENT TABLE OF CONTENTS OF FLOW TURBULENCE AND COMBUSTION

AN INTERNATIONAL JOURNAL PUBLISHED BY SPRINGER

IN ASSOCIATION WITH ERCOFTAC

EDITOR-IN-CHIEF: M. A. LESCHZINER

EDITORS: A. DREIZLER, K. FUKAGATA, E. GUTMARK, A. KEMPF, S. MENON, W. RODI, T.

SCHULLER, B. VAN WACHEM, R. SANDBERG

FOUNDING EDITOR: F. NIEUWSTADT

VOLUME 103, NUMBER 3, SEPTEMBER 2019

**Modelling of Soot Aerosol Dynamics in Turbulent Flow**

*S. Rigopoulos*

**An Analysis of Turbulent Mixing Effects on the Soot Formation in High Pressure n-dodecane Sprays**

*M.F.A. Razak, F. Salehi, M.A. Chishty*

**Statistics of Scalar Dissipation and Strain/Vorticity/Scalar Gradient Alignment in Turbulent Nonpremixed Jet Flames**

*A. Attili, F. Bisetti*

**Filtered Reaction Rate Modelling in Moderate and High Karlovitz Number Flames: an a Priori Analysis**

*T. Nilsson, R. Yu, N.A.K. Doan, I. Langella, N. Swaminathan, X.-S. Bai*

**Investigation of Reactive Scalar Mixing in Transported PDF Simulations of Turbulent Premixed Methane-Air Bunsen Flames**

*H. Zhou, Z. Ren, M. Kuron, T. Lu, J.H. Chen*

**Large Eddy Simulation of Combustion and Heat Transfer in a Single Element  $GCH_4GO_x$  Rocket Combustor**

*D. Maestro, B. Cuenot, L. Selle*

**Flameless Combustion Characteristics of Producer Gas Premixed Charge in a Cyclone Combustor**

*L. Chanphavong, K.A. Al-Attab, Z.A. Zainal*

**Impact of the Acoustic Forcing Level on the Transfer Matrix of a Turbulent Swirling Combustor with and Without Flame**

*R. Gaudron, M. Gatti, C. Mirat, T. Schuller*

**Noise Sources of Lean Premixed Flames**

*K. Pausch, S. Herff, F. Zhang, H. Bockhorn, W. Schröder*

**Effects of Nozzle Geometry on Turbulent Characteristics and Structure of Surface Attaching Jets**

*M.S. Rahman, G.F.K. Tay, M.F. Tachie*

**Integral Quantities of Axisymmetric Synthetic Jets Evaluated from a Direct Jet Thrust Measurement**

*J. Kordk, Z. Trávníček*

Further articles can be found at [www.springerlink.com](http://www.springerlink.com)

**Abstracted/Indexed** in Science Citation Index, Science Citation Index Expanded (SciSearch), Journal Citation Reports/Science Edition, SCOPUS, INSPEC, Chemical Abstracts Service (CAS), Google Scholar, EBSCO, CSA, ProQuest, Academic OneFile, ASFA, Current Abstracts, Current Contents/Engineering, Computing and Technology, Earthquake Engineering Abstracts, EI Encompass, Ei Page One, EI-Compendex, EnCompassLit, Engineered Materials Abstracts, Gale, OCLC, PASCAL, SCImago, STMA-Z, Summon by Serial Solutions, VINITI - Russian Academy of Science.

**Instructions for Authors** for Flow Turbulence Combust are available at <http://www.springer.com/10494>.

---

## ERCOFTAC Special Interest Groups

---

### 1. Large Eddy Simulation

Salvetti, M.V.  
University of Pisa, Italy.  
Tel: +39 050 221 7262  
mv.salvetti@ing.unipi.it

### 4. Turbulence in Compressible Flows

Dussauge, Jean-Paul  
IUSTI, Marseille  
jean-paul.dussauge  
@polytech.univmrs.fr

### 5. Environmental Fluid Mechanics

Armenio, V.  
Universit di Trieste, Italy  
Tel: +39 040 558 3472  
armenio@dica.units.it

### 10. Transition Modelling

Dick, E.  
University of Ghent, Belgium  
Tel: +32 926 433 01  
erik.dick@ugent.be

### 12. Dispersed Turbulent

#### Two Phase Flows

Sommerfeld, M.  
University of Magdeburg, Germany  
Tel: +49 345 552 3680  
martin.sommerfeld@ovgu.de

### 14. Stably Stratified and Rotating Flows

Redondo, J.M.  
UPC, Spain  
Tel: +34 934 017 984  
redondo@fa.upc.edu

### 15. Turbulence Modelling

Jakirlic, S.  
Darmstadt University of Technology,  
Germany  
Tel: +49 615 116 3554  
s.jakirlic@sla.tu-darmstadt.de

### 20. Drag Reduction and Flow Control

Choi, K-S.  
University of Nottingham, England  
Tel: +44 115 951 3792  
kwng-so.choi@nottingham.ac.uk

### 24. Variable Density Turbulent Flows

Anselmet, F.  
IMST, France.  
Tel: +33 491 505 439  
anselmet@irphe.univ-mrs.fr

### 28. Reactive Flows

Roekaerts, D.  
Delft University of Technology,  
The Netherlands.  
Tel: +31 152 782 470  
D.J.E.M.Roekaerts@tudelft.nl

### 32. Particle Image Velocimetry

Scarano, F., Sciacchitano, A.  
Delft University of Technology,  
The Netherlands.  
F.Scarano@tudelft.nl  
A.Sciacchitano@tudelft.nl

### 33. Transition Mechanisms, Prediction and Control

Hanifi, A.  
FOI, Sweden  
Tel: +46 855 503 197  
ardeshir.hanifi@foi.se

### 34. Design Optimisation

Giannakoglou, K.  
NTUA, Greece  
Tel: +30 210 772 1636  
kgianna@central.ntua.gr

### 35. Multipoint Turbulence Structure and Modelling

Cambon, C.  
ECL Ecully, France.  
Tel: +33 472 186 161  
claude.cambon@ec-lyon.fr

### 36. Swirling Flows

Braza, M.  
IMFT, France  
Tel: +33 (0) 561 285 839  
braza@imft.fr

### 37. Bio-Fluid Mechanics

Nicoud, F.  
Université de Montpellier, France  
franck.nicoud@umontpellier.fr

### 39. Aeroacoustics

Bailly, C.  
Ecole Centrale de Lyon, France  
Tel: +33 472 186 014  
christophe.bailly@ec-lyon.fr

### 40. Smoothed Particle Hydrodynamics

Rogers, B. D.  
University of Manchester, UK  
Tel: +44 (0) 161 306 6000  
Benedict.Rogers@manchester.ac.uk

### 41. Fluid Structure Interaction

Braza, M.  
IMFT, France  
Tel: +33 (0) 561 285 839  
marianna.braza@imft.fr  
Lacazedieu, E.  
EDF R&D, France  
Tel: +33 (1) 30 87 80 87  
elisabeth.lacazedieu@edf.fr

### 42. Synthetic Models in Turbulence

Nicolleau, F.  
University of Sheffield, England  
Tel: +44 114 222 7867  
f.nicolleau@sheffield.ac.uk

### 43. Fibre Suspension Flows

Lundell, F.  
The Royal Institute of Technology,  
Sweden  
Tel: +46 87 906 875  
fredrik@mech.kth.se

### 44. Fundamentals and Applications of Fractal Turbulence

Fortune, V.  
Université Pierre et Marie Curie, France  
Tel: +33 549 454 044  
veronique.fortune  
@lea.univ-poitiers.fr

### 45. Uncertainty Quantification in Industrial Analysis and Design

Lucor, D.  
d'Alembert Institute, France  
Tel: +33 (0) 144 275 472  
didier.lucor@upmc.fr

### 46. Oil, Gas and Petroleum

Sommerfeld, M.  
Otto von Guericke-Universität  
Germany  
martin.sommerfeld@ovgu.de  
Khanna, S.  
BP Global, USA

### 47. 3D Wakes

Morrison, J.F.  
Imperial College, London  
Tel: +44 (0) 20 7594 5067  
j.morrison@imperial.ac.uk  
Cadot, O.  
ENSTA Paris Tech,  
Université Paris-Saclay  
Tel: +33 (0) 16 931 9756  
cadot@ensta.fr

### 48. Respiratory Aerosols

Kassinis, S.  
University of Cyprus  
kassinis@ucy.ac.cy  
Sznitman, J.  
Biofluids Laboratory, Israel  
sznitman@bm.technion.ac.il

### 49. Non-Ideal Comp. Fluid Dynamics

Guardone, A.  
Politecnico di Milano, Italy  
alberto.guardone@polimi.it  
Pini, M.  
Delft University of Technology,  
The Netherlands  
M.Pini@tudelft.nl

## ERCOFTAC Pilot Centres

### Alpe - Danube - Adria

Steiner, H.  
Inst. Strömungslehre and  
Wärmeübertragung  
TU Graz, Austria  
kristof@ara.bme.hu

### Belgium

Hillewaert, K.  
Bâtiment Eole,  
6041 Gosselies,  
Belgium.  
Tel: +32 71 910 942  
Fax: +32 495 385 030  
koen.hillewaert@cenaero.be

### Brasil

Rodriguez, O.  
Department of Mechanical Engineering,  
Sao Carlos School of Mechanical  
Engineering,  
Universidade de Sao Paulo,  
Brasil.  
oscarmhr@sc.usp.br

### Czech Republic

Bodnar, T.  
Institute of Thermomechanics AS CR,  
5 Dolejskova,  
CZ-18200 Praha 8,  
Czech Republic.  
Tel: +420 224 357 548  
Fax: +420 224 920 677  
bodnar@marian.fsik.cvut.cz

### Iberia

Onate, E.  
Universitat Politècnica de Catalunya,  
Valero, E.  
Universidad Politécnica de Madrid,  
Spain.  
onate@cimne.upc.edu  
eusebio.valero@upm.es

### France South

Braza, M.  
IMF Toulouse,  
CNRS UMR - 5502,  
Allée du Prof. Camille Soula 1,  
F-31400 Toulouse Cedex, France.  
Tel: +33 534 322 839  
Fax: +33 534 322 992  
Braza@imft.fr

### France West

Danaila, L.  
CORIA, University of Rouen,  
Avenue de l'Université BP12,  
76801 Saint Etienne du Rouvray  
France.  
Tel: +33 232 953 702  
luminita.danaila@coria.fr

### Germany North

Sommerfeld, M.  
University of Magdeburg,  
Germany  
Tel: +49 345 552 3680  
martin.sommerfeld@ovgu.de

### Germany South

Becker, S.  
Universität Erlangen, IPAT  
Cauerstr. 4  
91058 Erlangen  
Germany  
Tel: +49 9131 85 29451  
Fax: +49 9131 85 29449  
sb@ipat.uni-erlangen.de

### Greece

M. Founti.  
National Tech. University Of Athens,  
School of Mechanical Engineering,  
Lab. of Steam Boilers and  
Thermal Plants,  
Heroon Polytechniou 9,  
15780 Zografou, Athens, Greece  
Tel: +30 210 772 3605  
Fax: +30 210 772 3663  
mfou@central.ntua.gr

### Switzerland

Gallaire, F.  
EPFL-STI-LTCM  
Station 9,  
CH-1015 Lausanne,  
Switzerland.  
francois.gallaire@epfl.ch

### Italy

Rispoli, F.  
Tel: +39 064 458 5233  
franco.rispoli@uniroma1.it  
Borello, D.  
Tel: +39 064 458 5263  
domenico.borello@uniroma1.it  
Sapienza University of Rome,  
Via Eudossiana, 18  
00184 Roma, Italy

### Netherlands

Van Heijst, G.J.  
J.M. Burgerscentrum,  
National Research School for Fluid  
Mechanics, Mekelweg 2,  
NL-2628 CD Delft, Netherlands.  
Tel: +31 15 278 1176  
Fax: +31 15 278 2979  
g.j.f.vanheijst@tudelft.nl

### Nordic

Wallin, S.  
KTH, Dept. of Mechanics,  
SE-100 44 Stockholm,  
Sweden  
Tel: +46 733 303 453  
stefanw@mech.kth.se

### Poland

Szumbarski J.  
Warsaw University of Technology,  
Inst. of Aero. & App. Mechanics,  
ul. Nowowiejska 24,  
PL-00665 Warsaw, Poland.  
Tel: +48 22 234 7444  
Fax: +48 22 622 0901  
jasz@meil.pw.edu.pl

### France - Henri Bénard

Godefert, F.S.  
Ecole Centrale de Lyon.  
Fluid Mechanics and Acoustics Lab.,  
F-69134 Ecully Cedex,  
France.  
Tel: +33 4 72 18 6155  
Fax: +33 4 78 64 7145  
fabien.godefert@ec-lyon.fr

### United Kingdom

Juniper, M.  
Department of Engineering,  
Trumpington Street,  
Cambridge, CB2 1PZ  
United Kingdom.  
Tel: +44 (0) 1223 332 585  
mpj1001@cam.ac.uk



# Best Practice Guidelines for Computational Fluid Dynamics of Dispersed Multi-Phase Flows

## Editors

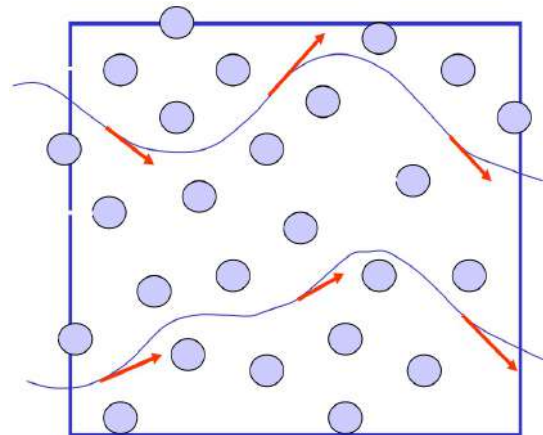
Martin Sommerfeld, Berend van Wachem  
&  
René Oliemans

The simultaneous presence of several different phases in external or internal flows such as gas, liquid and solid is found in daily life, environment and numerous industrial processes. These types of flows are termed multiphase flows, which may exist in different forms depending on the phase distribution. Examples are gas-liquid transportation, crude oil recovery, circulating fluidized beds, sediment transport in rivers, pollutant transport in the atmosphere, cloud formation, fuel injection in engines, bubble column reactors and spray driers for food processing, to name only a few. As a result of the interaction between the different phases such flows are rather complicated and very difficult to describe theoretically. For the design and optimisation of such multiphase systems a detailed understanding of the interfacial transport phenomena is essential. For single-phase flows Computational Fluid Dynamics (CFD) has already a long history and it is nowadays standard in the development of air-planes and cars using different commercially available CFD-tools.

Due to the complex physics involved in multiphase flow the application of CFD in this area is rather young. These guidelines give a survey of the different methods being used for the numerical calculation of turbulent dispersed multiphase flows. The Best Practice Guideline (BPG) on Computational Dispersed Multiphase Flows is a follow-up of the previous ERCOFTAC BPG for Industrial CFD and should be used in combination with it. The potential users are researchers and engineers involved in projects requiring CFD of (wall-bounded) turbulent dispersed multiphase flows with bubbles, drops or particles.

## Table of Contents

1. Introduction
2. Fundamentals
3. Forces acting on particles, droplets and bubbles
4. Computational multiphase fluid dynamics of dispersed flows
5. Specific phenomena and modelling approaches
6. Sources of errors
7. Industrial examples for multiphase flows
8. Checklist of 'Best Practice Advice'
9. Suggestions for future developments



Copies of the Best Practice Guidelines can be acquired electronically from the ERCOFTAC website:

[www.ercoftac.org](http://www.ercoftac.org)

Or from:

ERCOFTAC (CADO)  
PO Box 53877  
London, SE27 7BR  
United Kingdom

Tel: +44 208 117 6170

Email: [admin@cado-ercoftac.org](mailto:admin@cado-ercoftac.org)

The price per copy (not including postage) is:

ERCOFTAC members

First copy	Free
Subsequent copies	75 Euros
Students	75 Euros

Non-ERCOFTAC academics	140 Euros
Non-ERCOFTAC industrial	230 Euros
EU/Non EU postage fee	10/17 Euros